4-2016

Preliminary design tools in turbomachinery: Non-uniformly spaced blade rows, multistage interaction, unsteady radial waves, and propeller horizontal-axis turbine optimization

Yujun Leng
Purdue University

Graduate School Form
30 Updated 12/26/2015

PURDUE UNIVERSITY
GRADUATE SCHOOL
Thesis/Dissertation Acceptance

This is to certify that the thesis/dissertation prepared

By Yujun Leng

Entitled

Preliminary Design Tools in Turbomachinery: Non-uniformly Spaced Blade Rows, Multistage Interaction, Unsteady Radial Waves, and Propeller Horizontal-Axis Turbine Optimization

For the degree of Doctor of Philosophy

Is approved by the final examining committee:

Sanford Fleeter
Chair

Gregory A. Blaisdell

John S. Bolton

Jun Chen

To the best of my knowledge and as understood by the student in the Thesis/Dissertation Agreement, Publication Delay, and Certification Disclaimer (Graduate School Form 32), this thesis/dissertation adheres to the provisions of Purdue University's "Policy of Integrity in Research" and the use of copyright material.

Approved by Major Professor(s): Sanford Fleeter

Approved by: Jay P. Gore 4/26/2016

Head of the Departmental Graduate Program Date

PRELIMINARY DESIGN TOOLS IN TURBOMACHINERY: NON-UNIFORMLY SPACED BLADE ROWS, MULTISTAGE INTERACTION, UNSTEADY RADIAL WAVES, AND PROPELLER HORIZONTAL-AXIS TURBINE OPTIMIZATION

A Dissertation

Submitted to the Faculty

of

Purdue University

by

Yujun Leng

In Partial Fulfillment of the

Requirements for the Degree

of

Doctor of Philosophy

May 2016

Purdue University

West Lafayette, Indiana

ACKNOWLEDGEMENTS

Frist, I would like to give thanks to my advisor Prof. Sanford Fleeter for introducing me into the research of turbomachinery and for giving me a lot of freedom and patience to do what I am interested in doing. I am also grateful to take class from and/or work with several great professors at Purdue, Prof. J. Stuart Bolton, Prof. John Sullivan, Prof. Gregory Blaisdell, Prof. Chen Jun, Prof. Steven Schneider and Prof. Carl Wassgren. I am impressed by their knowledge and also their willingness to help students to learn and succeed. In addition, I would like to thank Dr. Rita Saerens and Dr. Dominic Naughton for training me and giving me teaching jobs in the Math Department.

I feel very fortunate to have several good friends during my time at Purdue such as my labmate Brandon Ennis, and my fellow graduate students at Zucrow lab and Herrick lab, Fangyuan Lou, Yanfan Liu and Bin Yang. My friendships with Math Department colleagues, Eduardo Garcia, Hongshan Li and Dr. Lizhen Qin, bring many colorful and pleasant memories of my PhD study. In particular, I am extremely grateful to know Dr. Dana Gottfried. He gave me a lot of help in my research and in my personal life during my entire time at Purdue University. His encouragements made me feel my work is meaningful and worthy.

Finally, thank you to my parents and Yongxi for your constant love, support and encouragement.

TABLE OF CONTENTS

Page

Page

Page

LIST OF TABLES

Table Page

Table Page

LIST OF FIGURES

Figure Page

Figure Page

Figure Page

Figure Page

Figure Page

Figure Page

Figure Page

Figure Page

Figure Page

NOMENCLATURE

Symbol	Description
a_0	sound speed
A_h	unsteady lift due to bending motion of the blade
A_G	unsteady lift due to vorticity wave
A_u	unsteady lift due to upstream going pressure wave
A_d	unsteady lift due to downstream going pressure wave
B_α	unsteady moment due to torsion motion of the blade
B_G	unsteady moment due to vorticity wave
B_u	unsteady moment due to upstream going pressure wave
B_d	moment due to downstream going pressure wave
B	number of blades in a blade row
c	chord length
C_h	structural damping for bending
C_α	structural damping for torsion
C_T	thrust coefficient
C_Q	torque coefficient
C_P	power coefficient
F_i	inviscid lifting force

Symbol	Description
F_v	viscous drag force
F	total force
h	bending deflection.
I_α	mass moment of inertia
K_h	structural stiffness for bending
K_α	structural stiffness for torsion
L	unsteady lift
m	mass
ND	nodal diameter
P^+	strength of upstream going pressure wave
P^-	strength of downstream going pressure wave
p	pressure
Q	torque
r_h	rotor hub radius
s	tangential blade spacing
T	trust
$\vec{u}$	unsteady velocity
u_a^*	axial induced velocity
u_t^*	tangential induced velocity
$\overline{u}_a$	axial induced velocity influence function
$\overline{u}_t$	tangential induced velocity influence function
$\overline{u}_a^*$	axial induced velocity horseshoe influence function
$\overline{u}_t^*$	tangential induced velocity horseshoe influence function
$\vec{U}_0$	steady mean velocity

Symbol	Description
V_a	axial inflow velocity
V_t	tangential inflow velocity
V^*	total velocity
V_f	free flow incoming velocity
z	chordwise position

Greek

α	angular deflection
α	axial wavenumber
β_w	helical wake pitch angle
β_i	total flow angle
β	total flow angle without induced velocities.
β	tangential wavenumber
γ	bound vortex in the flat plate cascade model
γ	free shedding vortex in the lifting line model
Γ	bound vortex strength in the flat plate cascade model
Γ	bound circulation in the lifting line model
ζ	strength of vorticity wave
η	propeller efficiency
ρ	density
σ	interblade phase angle
φ	potential perturbation
Θ	unsteady moment
ω	frequency in the flat plate cascade model
ω	angular rotational speed in the lifting line model

Symbol	Description
ω_h	bending mode natural frequency
ω_α	torsion mode natural frequency
Ω	angular rotational speed of a blade row

Superscript & subscript

'	unsteady perturbation
–	complex perturbation amplitude
$_x$	axial component
$_y$	tangential component
$_r$	radial component
$_\theta$	circumferential component
$_a$	potential component related to acoustic pressure wave
$_v$	vortical component related to vorticity wave
$_0$	steady mean flow

ABSTRACT

Leng, Yujun. Ph.D., Purdue University, May 2016. Preliminary Design Tools in Turbomachinery: Non-uniformly Spaced Blade Rows, Multistage Interaction, Unsteady Radial Waves, and Propeller Horizontal-axis Turbine Optimization. Major Professor: Sanford Fleeter.

Turbomachinery flow fields are inherently unsteady and complex which makes the related CFD analyses computationally intensive. Physically based preliminary design tools are desirable for parametric studies early in the design stage, and to provide deep physical insight and a good starting point for the later CFD analyses. Four analytical/semi-analytical models are developed in this study: 1) a generalized flat plate cascade model for investigating the unsteady aerodynamics of a blade row with non-uniformly spaced blades; 2) a multistage interaction model for investigating rotor-stator interactions; 3) an analytical solution for quantifying the impeller wake convection and pressure wave propagating between a centrifugal compressor impeller and diffuser vane; and 4) a semi-analytical model based Lifting line theory for unified propeller and horizontal-axis turbine optimization. Each model has been thoroughly validated with existing models.

With these models, non-uniformly spaced blade rows and vane clocking are investigated in detail for their potential use as a passive control technique to reduce forced response, flutter and aeroacoustic problems in axial compressors. Parametric

studies with different impeller blade numbers and back sweep angles are conducted to investigate their effect on impeller wake and pressure wave propagation. Results show that the scattered pressure waves with high circumferential wave numbers may be an important excitation source to the impeller as their amplitude grows much faster as they travel inwardly than the lower order primary pressure waves. Detailed analysis of Lifting line theory reveals the mathematical and physical equivalence of Lifting line models for propellers and horizontal-axis turbines. With a new implementation, the propeller optimization code can be used for horizontal-axis turbine optimization without any modification. The newly developed unified propeller and horizontal-axis turbine optimization code based on lifting line theory and interior point method has been shown to be a very versatile tool with the capability of hub modelling, working with non-uniform inflow and including extra user specified constraints

CHAPTER 1. INTRODUCTION

Computational fluid dynamics (CFD) has developed rapidly due to the advances in computational power, numerical analysis and algorithms, and due to improvement in physical models. CFD as a flow physics simulator has been used widely to provide detailed flow information for engineers and designers to improve their products. However, there are still certain limitations of CFD that make it hard to be applied in certain areas. The two major limitations are: 1) heavy computational burden and 2) inaccurate physical models. Transonic flow, unsteady flow, fluid structure interactions, and problems with complex geometry and scales are generally computationally intensive. The models used in viscous flows, in boundary layers and for turbulence may be inaccurate. In addition, good meshing and a reasonable understanding of the physical problem itself are also essential for CFD analysis. These limiting factors become more important in the preliminary design phase when parametric studies and optimizations are performed extensively. Typically CFD is used as a high fidelity tool in the last design phase to provide understanding, validation, diagnostic and final improvement of the product. A relatively accurate preliminary design is essential to maximize the effectiveness of resource-intensive CFD analyses.

Turbomachinery machines (axial and centrifugal compressors, turbines, propellers, etc.) play a fundamental role in providing power in modern society. However, the flow through turbomachinery is inherently complex and unsteady which prevents CFD from being used in the early design cycle. If viscosity is neglected, the Navier–Stokes equations solved numerically in CFD are reduced to Euler equations which can be solved in some analytical and semi-analytical ways. In this study, preliminary design tools based on the Euler equations are developed for solving unsteady aerodynamic problems in axial and centrifugal compressors (internal flow), and for optimizing propellers and

horizontal-axis turbines (external flow). In particular: 1) a generalized flat plate cascade model is developed for investigating the unsteady aerodynamics of a blade row with non-uniformly spaced blades; 2) a multistage interaction model is developed for investigating rotor-stator interactions; 3) an analytical solution is derived for quantifying the centrifugal compressor impeller wake convection and pressure wave propagation between the impeller and diffuser vanes; 4) a semi-analytical model based on lifting line theory is developed for unified propeller and horizontal-axis turbine optimization. These physically based analytical/semi-analytical models developed in this study not only provide a good starting point for the later CFD analysis, but also give the user deeper physical insights of the problem.

A literature review and background introduction for each problem is given in this following parts of this chapter. The theories and numerical implementation behind the preliminary design tools are given in Chapter 2. The validation and case studies of the generalized flat plate cascade model are conducted in Chapter 3. The validation and case studies of the multistage interaction model are conducted in Chapter 4. The validation and case studies involving non-uniformly spaced blade row in a multistage environment are conducted in Chapter 5. Case studies for impeller wake convection and pressure wave propagation behavior in the vaneless space are conducted in Chapter 6. The validation and case studies of the unified propeller and horizontal-axis turbine optimization code are given in Chapter 7. The conclusion and future perspective are given in Chapter 8. The corresponding codes in Matlab are given in the Appendices.

1.1 Aeromechanic and Aeroacoustic Problem in Axial Compressors

The flow in both axial and centrifugal compressors is inherently unsteady due to the relative motion between rotors and stators. In addition, it can be shown that a compressor can only do work through unsteady flow processes. However, the unsteady flow produces unsteady loading on the blade rows and causes both aeromechanic problems and noise. The two major types of the aeromechanic problems are forced response and flutter. Forced response is caused by external excitations, such as the wake from an upstream blade row and potential field of adjacent blade rows. When the

excitation frequency matches the natural frequency of the blade, resonant vibrations occur. Flutter is a self-excited oscillation due to the blade vibration itself. When the unsteady loading due to the blade vibration produces a negative damping on the blade motion, flutter occurs and the blade vibration amplitude gets larger and larger until non-linear phenomenon come into play. Both forced response and flutter cause premature blade failure by High Cycle Fatigue (HCF). In order to reduce size and weight, current trends in compressor design are higher loading per stage, smaller gaps between rotors and stators, and the use of integrally bladed rotors (IBR). Such modern design requirements lead to stronger blade row interaction, lower structural damping and thus a higher probability of premature blade failure.

The most commonly used method to avoid forced response problems in the early design stage is the Campbell diagram. Every crossing on the diagram represents a resonant vibration of a certain mode at a certain rotation speed. In reality, the excitations could be at many different engine orders and a rotor could have many different vibration modes. This leads to many crossings on the diagram. Each crossing leads to a possible resonant vibration that should be avoided in the design. Unfortunately, this method cannot provide the amplitude of the vibration at the resonant frequency, which is critical to identify the importance of each resonant mode. To avoid the flutter problem, the aerodamping due to blade vibration at all possible interblade phase angles needs to be calculated. Any negative aerodamping indicates a possible flutter condition that should be avoided. The unsteady loading on the blade row also acts as dipole sources that generate discrete frequency noise at the excitation frequency. The scattering effect of each blade row causes much additional discrete frequency noise. Depending on the axial wave number, only the propagating pressure waves are of interest in any effort to reduce the noise in the far field.

Two passive control techniques, aerodynamic mistuning and vane clocking are investigated to minimize the aeromechanic and aeroacoustic problem using the preliminary design tools developed in this study.

1.1.1 Aerodynamic Mistuning and Non-uniformly Spaced Blade Row

Most computational methods and physical models for aeromechanic studies are based on the assumption that all the blades in a certain blade row have the same structural and aerodynamic properties. However, there are small blade-to-blade variations that result from manufacturing tolerances, operational wear and damage. The variation in structural properties (natural frequency, stiffness and damping) is termed structural mistuning. The variation in aerodynamic properties (chord length, stagger angle, blade spacing and etc.) is termed aerodynamic mistuning. It is well known that both structural mistuning and aerodynamic mistuning can greatly affect the forced response and flutter stability of blade rows. Intentional structural mistuning (in terms of blade-to-blade frequency variation) and intentional aerodynamic mistuning (in terms of the blade-to-blade spacing variation) have been proposed and studied as passive control techniques to reduce the blade forced response amplitude and flutter instability. Most of turbomachinery mistuning research in the past concentrated on structural mistuning. Both Finite Element Analysis (FEA) investigation and lumped parameter method have been applied to structure mistuning problem [1-3]. On the other hand, a CFD analysis for aerodynamic mistuning is usually very computationally intensive because whole blade rows need to be modeled due to the breakdown of the symmetry. There are fewer studies addressing aerodynamic mistuning. To avoid the high computational cost of a CFD simulation, Sawyer and Fleeter [4] developed a detuned flat plate cascade model with alternating chord length and blade spacing and analyzed this aerodynamic mistuning effect on flutter. Ekici, Kielb and Hall [5] used a time-linearized harmonic balance method to study the effect of alternating stagger angle and blade spacing effect on flutter. However, the detuned blade row was treaded as aerodynamically tuned with symmetry groups involving two blades, and thus is not a general aerodynamically mistuned pattern. The most applicable intentional blade row aerodynamically mistuned patterns are in the form of sinusoidal blade-to-blade spacing and half-half blade-to-blade spacing [6-8]. These general aerodynamically mistuned patterns contain no symmetry groups. A generalized flat plate cascade model is developed in this study to investigate the unsteady aerodynamics of blade rows with any aerodynamically mistuned pattern.

1.1.2 Vane Clocking and Multistage Interactions

Most previous unsteady aerodynamic analyses of blade rows were conducted assuming the blade row is isolated in an infinitely long duct. However in an actual axial compressor, the axial spacing between adjacent blade rows is usually only a fraction of a chord. The axial spacing tends to be further reduced in new designs in order to minimize the overall size and weight of the gas turbine engine. Due to the involvement of several blade rows, it is very computationally expensive to simulate multistage interactions using time-marching CFD methods. Hanson [9] modeled two blade rows of flat plate airfoils in compressible flow using a time-linearized method to incorporate several harmonics. Buffum [10] used Smith's flat plate cascade model [11] and developed a similar method to include multiple spinning modes but neglected all the cut-off pressure waves. Hall and Sikowaski [12-13] developed an influence coefficient method termed the Coupled Mode Method that represents each airfoil row and inter-row space as a matrix. Different blade rows are coupled together by using unsteady pressure and vorticity waves in the flow field. The Coupled Mode Method's modular structure has great flexibility and provides more physical insight into multi-row interactions. The multistage interaction model developed in this study is based on the formulation of the Coupled Mode Method.

Vane clocking is the circumferential indexing of adjacent stators with the same vane numbers. Physically, vane clocking changes the relative phase between the excitations from the upstream stator and the downstream stator. In addition to the benefit of increasing compressor performance [14], the relative phase change has a large impact on the unsteady aerodynamic forces on the rotor. Capece and Fleeter [15] showed that indexing the upstream stators could change the unsteady aerodynamic forcing function to the rotor based on experiments in a three stage low-speed compressor. Experimental work by Choi [16] showed that vane clocking had a significant effect on the resonant vibration amplitude of the rotor blades in the Purdue 3 Stage Research Compressor. To understand the vane clocking effect on the unsteady loading on the rotor, Salontay and Key [17] used an implicit nonlinear unsteady compressible flow solver AU3D to simulate the resonant vibration amplitude of rotor2 at different stator1-stator2 clocking configurations in the Purdue 3 Stage Research Compressor. The results showed good

agreement with the trend of the relative response from experimental data. However, the long set up time and computational time required by such a coupled nonlinear unsteady simulation hinder it from being an effective tool used routinely in the design process. The linearized multistage interaction model is used to explore the potential of vane clocking as a passive control technique for reducing forced response, flutter and the associated noise problem of blade rows in a multistage environment.

1.1.3 Aerodynamically Mistuned Blade Rows in Multistage Environment

The major excitation of a rotor comes from the wake of the upstream stator. For a normal uniformly spaced stator row, the wake excitation is at discrete frequencies including the fundamental frequency and its higher harmonics. A non-uniformly spaced stator row is able to reduce the discrete wake excitation by spreading the excitation energy over a broad range of frequencies. Non-uniformly spaced stator rows have already been used in real engines to reduce the forced repose problem of rotor vibration. PSM (Power Systems Mfg., LLC.) incorporated non-uniform spacing vanes into S0 and S1 stator rows to reduce the vibratory response of R0 and R1 rotor blades of the GE 7FA+e gas turbine. However, the CFD multistage study with aerodynamically mistuned blade rows can be very computationally expensive. No research regarding the effect of a non-uniformly spaced stator row on rotor stability in a multistage environment has been done. To close this gap, the non-uniformly spaced blade model and multistage interaction model are combined to quantify the effect of aerodynamic mistuning (in terms of non-uniform spacing) in a multistage environment.

1.2 Radial Waves in Centrifugal Compressor

Traditionally, centrifugal compressors have relatively fewer aeromechanic issues as compared to axial compressors. However, in recent years, effort is being directed at developing the next generation high power density centrifugal compressors. In these advanced designs, a vaned diffuser is frequently used to increase the compressor efficiency. The vaneless space between the impeller exit and vaned diffuser is small so as

to increase the diffuser's performance and decrease weight. However, the impeller wakes hitting the diffuser vanes generate a series of strong pressure waves that propagate upstream and affect the impeller trailing edge. Both experimental [18] and computational simulations [19] have shown that under certain operating conditions, these pressure waves generated by the impeller-diffuser vane interaction are large enough to cause impeller failure. Bryan [20] investigated unsteady impeller-diffuser interactions in the Purdue Low-Speed Centrifugal Research Compressor. Gottfried and Fleeter [21] developed a small perturbation model to predict the unsteady aerodynamic response of impeller blades to the diffuser vane potential field. However, no analytical model has been developed to predict the impeller excitation by the pressure wave resulting from impeller wake-diffuser vane interactions.

1.3 Horizontal-axis Turbine Optimization

Wind turbines and propellers work in a very similar way aerodynamically, except that wind turbines extract kinetic energy from the flow field and generate torque while propellers absorb torque and accelerate the flow. In fact, Actuator Disk theory used to predict the maximum theoretical wind turbine power coefficient, known as Betz limit [22], was developed for analyzing propeller performance by Betz [23]. In the propeller community, there is a 3-level design process: 1) blade element momentum theory, or BEM; 2) the Lifting line/surface method; and 3) advanced CFD methods. However, in the wind turbine community, the lifting line method is missing. CFD analyses usually start from the results from BEM or empirical results. The BEM method does not include the effect of tip loss due to a finite number of blades and the aerodynamic interaction between blade elements. The large errors from the BEM method mean much more time and effort is required for the CFD analysis to find an optimized blade design at a specified operating condition. A preliminary wind turbine design tool is needed to fill the gap by providing the middle level design method. It should run fast enough for design optimization and parametric studies, and be accurate enough to provide a good starting point for high-level CFD analyses.

Many efforts have been made to provide such a mid-level design tool for optimized turbine blade design. Wald [24] summarized the classical propeller design method using Goldstein factors [25] to account for tip loss, and suggested that the same method may be used for turbine design. Okulov and Sørensen [26] modified the Goldstein factors method by introducing a new analytical solution to the wake vortex model and used it for predicting the maximum power coefficient for a turbine with a finite number of blades. However, the Goldstein factors method has many restrictions and has been superseded by the Lifting line method in propeller design [27]. Epps [28] developed a unified rotor Lifting line model for both propeller and horizontal-axis turbine blade optimization. However, his turbine blade optimization is done by "hard-wired' flow perpendicularity requirement in the General Momentum Theory [29-30] which is only valid for a turbine operating in uniform inflow conditions.

In this study, a unified propeller and horizontal-axis turbine design code (with emphasis on wind turbine blade design) is developed based on the Lifting line model. It is able to optimize turbine blade design for non-uniform inflow conditions. A hub model is included and extra constraints on the blade loading can also be specified. Through a detailed analysis of the Lifting line model, this study also shows that the classic propeller design method based on Lerbs criterion [31] can be used for turbine design directly but through a new implementation.

CHAPTER 2. THEORIES AND MODEL DETAIL

In this chapter, the theories, models and the numerical implementation of each preliminary design tool are discussed in detail. The first five sections deal with the aeromechanic and aeroacoustic problems in compressors. The last section deals with the rotor blade optimization problem. The blade structural dynamic properties are derived using a spring-mass model in Section 2.1, with the unsteady aerodynamic loading represented using the influence coefficients. The unsteady flow field in both axial and centrifugal compressors are solved by linearizing the Euler equations in Section 2.2. The uniformly spaced flat plate cascade model is explained in Section 2.3. The extension to the generalized uniformly spaced flat pate cascade model is given in Section 2.4. The detail of the multistage interaction model is discussed in Section 2.5. In Section 2.6, both propeller and horizontal-axis turbine optimization based the Lifting line model and with different optimization methods are discussed in detail.

2.1 Structural Dynamics

A two dimensional blade section analysis is used in this study to develop the preliminary design tools. The blade row is “unwrapped” from annular cascades into a linear 2D cascade at a constant radius slice. It is assumed that the 2D airfoil section in the flow field has two degrees of freedoms (bending and torsion). Figure 2.1 shows a schematic of the system and the deflected position of the airfoil.

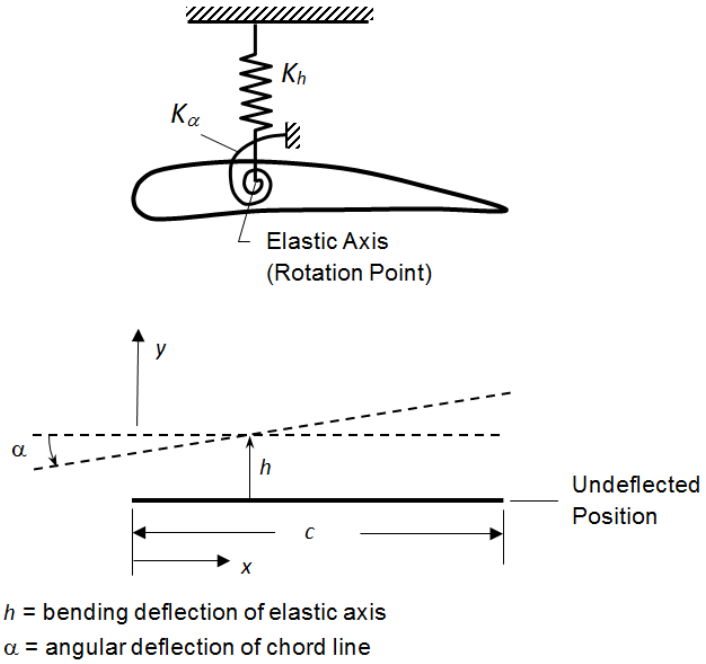

Figure 2.1. Mass-spring model of a two dimensional airfoil section.

For most unshrouded turbomachinery blade rows, the bending mode and torsion mode are uncoupled from each other. The equations of motion are:

$$m\ddot{h} + C_h\dot{h} + K_h h = L \tag{2.1}$$

$$I_\alpha\ddot{\alpha} + C_\alpha\dot{\alpha} + K_\alpha\alpha = \Theta \tag{2.2}$$

where in the bending mode, h is bending deflection, m is mass, C_h and K_h are the structural damping and stiffness for bending, and L is the unsteady lift. In the torsion mode, α is angular deflection, I_α is mass moment of inertia, C_α and K_α are the structural damping and stiffness for torsion, and Θ is the unsteady moment.

The unsteady lift and moment acting on an airfoil result from both external excitations (vorticity wave ζ, upstream going pressure wave P^+ and downstream going pressure wave P^-) and internal excitations (bending deflection h and angular deflection α). The unsteady lift and moment can be calculated using unsteady aerodynamic influence coefficients. The unsteady aerodynamic influence coefficients for the unsteady

lift due to the bending motion of the airfoil, due to the vorticity wave, due to the upstream going pressure wave and due to the downstream going pressure wave are A_h, A_G, A_u and A_d respectively. The unsteady aerodynamic influence coefficient for unsteady moment due to the torsional motion of the airfoil, due to the vorticity wave, due to the upstream going pressure wave and due to the downstream going pressure wave are B_α, B_G, B_u and B_d respectively. The equations of motion can be written as,

$$m\ddot{h} + C_h\dot{h} + K_h h = A_h h + A_G\zeta + A_u P^+ + A_d P^- \tag{2.3}$$

$$I_\alpha\ddot{\alpha} + C_\alpha\dot{\alpha} + K_\alpha\alpha = B_\alpha a + B_G\zeta + B_u P^+ + B_d P^- \tag{2.4}$$

Assuming both the excitation and blade vibration are harmonic in time with frequency ω, then $\zeta = \bar{\zeta}e^{i\omega t}$, $P^+ = \overline{P^+}e^{i\omega t}$, $P^- = \overline{P^-}e^{i\omega t}$, $h = \bar{h}e^{i\omega t}$ and $\alpha = \bar{\alpha}e^{i\omega t}$. In addition, bending stiffness $K_h = m\omega_h{}^2$ and torsion mode stiffness $K_\alpha = I_\alpha\omega_\alpha{}^2$, where ω_h and ω_α are bending natural frequency and torsion natural frequency of the blade, respectively. Thus, the time linearized equations of motion become,

$$-m\omega^2\bar{h} + i\omega C_h\bar{h} + m\omega_h{}^2\bar{h} - A_h\bar{h} = A_G\bar{\zeta} + A_u\overline{P^+} + A_d\overline{P^-} \tag{2.5}$$

$$-I_\alpha\omega^2\bar{\alpha} + i\omega C_a\bar{\alpha} + I_\alpha\omega_\alpha{}^2\bar{\alpha} - B_\alpha\bar{\alpha} = B_G\bar{\zeta} + B_u\overline{P^+} + B_d\overline{P^-} \tag{2.6}$$

The blade vibration amplitude can be calculated as,

$$\bar{h} = \frac{-\left[A_G\bar{\zeta} + A_u\overline{P^+} + A_d\overline{P^-}\right]}{m\omega^2 - m\omega_h^2 - i\omega C_h + A_h} \tag{2.7}$$

$$\bar{\alpha} = \frac{-\left[B_G\bar{\zeta} + B_u\overline{P^+} + B_d\overline{P^-}\right]}{I_\alpha\omega^2 - I_\alpha\omega_\alpha^2 - i\omega C_\alpha + B_\alpha} \tag{2.8}$$

Both the blade vibration amplitude and unsteady loading are important quantities of interest in the forced response analysis.

Without external excitation, the time linearized equations of motion can be written as,

$$\left[-m\omega^2 + m\omega_h{}^2 - \mathrm{Re}(A_h)\right]\bar{h} + i\left[\omega C_h - \mathrm{Im}\left(A_h\right)\right]\bar{h} = 0 \tag{2.9}$$

$$\left[-I_\alpha\omega^2 + I_\alpha\omega_\alpha{}^2 - \mathrm{Re}\left(B_\alpha\right)\right]\bar{\alpha} + i\left[\omega C_\alpha - \mathrm{Im}\left(B_\alpha\right)\right]\bar{\alpha} = 0 \tag{2.10}$$

If the blade vibrates in a vacuum, there is only structural damping C_h and C_α. In flow, the blade vibration itself generates additional aerodamping. By examining the imaginary parts of Equations (2.9) and (2.10), the equivalent aerodamping coefficient can be written as,

$$C_h^{aero} = -\frac{\mathrm{Im}(A_h)}{\omega} \tag{2.11}$$

$$C_\alpha^{aero} = -\frac{\mathrm{Im}(B_\alpha)}{\omega} \tag{2.12}$$

A positive aerodamping stabilizes the blade vibration and a negative aerodamping destabilizes the blade vibration, which is the same convention as structural damping. Since the aerodamping C_h^{aero} and C_α^{aero} are proportional to the negative of $\mathrm{Im}(A_h)$ and $\mathrm{Im}(B_\alpha)$, without structural damping a positive $\mathrm{Im}(A_h)$ and $\mathrm{Im}(B_\alpha)$ indicate a unstable case in the flutter analysis.

2.2 Unsteady Aerodynamics

Neglecting the flow viscosity, the flow field in axial/centrifugal compressor can be described by the Euler equations:

$$\frac{\partial \rho}{\partial t} + \vec{U} \cdot \nabla \rho + \rho \nabla \cdot \vec{U} = 0 \tag{2.13}$$

$$\frac{\partial \vec{U}}{\partial t} + \vec{U} \cdot \nabla \vec{U} = -\frac{\nabla p}{\rho} \tag{2.14}$$

The unsteady flow is assumed to be a small perturbation to the mean flow.

$$\begin{aligned} \vec{U} &= \vec{U}_0 + \vec{u} \\ p &= p_0 + p' \\ \rho &= \rho_0 + \rho' \end{aligned} \tag{2.15}$$

where $\vec{U}_0$, p_0 and ρ_0 are the steady mean velocity, pressure and density. $\vec{u}$, p' and ρ' are the corresponding unsteady perturbation quantities.

For perfect gas undergoing an isentropic process,

$$\frac{\partial p}{\partial \rho} = a_0^{\,2} \tag{2.16}$$

where a_0 is the sound speed.

The linearized Euler equations are obtained by substituting Equation (2.15) into Equations (2.13) and (2.14). The mean flow is described by Equations (2.17) and (2.18),

$$\vec{U}_0 \cdot \nabla \rho_0 + \rho_0 \nabla \cdot \vec{U}_0 = 0 \tag{2.17}$$

$$\vec{U}_0 \cdot \nabla \vec{U}_0 = -\frac{\nabla p_0}{\rho_0} \tag{2.18}$$

And the small perturbation unsteady flow is described by Equations (2.19) and (2.20),

$$\frac{D_0}{Dt}\left(\frac{p'}{\rho_0 a_0^{\,2}}\right) + \frac{1}{\rho_0}\nabla \cdot \left(\rho_0 \vec{u}\right) = 0 \tag{2.19}$$

$$\frac{D_0 \vec{u}}{Dt} + \vec{u} \cdot \nabla \vec{U}_0 = -\nabla\left(\frac{p'}{\rho_0}\right) \tag{2.20}$$

where $\frac{D_0}{Dt} \equiv \frac{\partial}{\partial t} + \vec{U}_0 \cdot \nabla$ is the convective material derivative.

2.2.1 Axial compressor

In an axial compressor, the hub to tip radius ratio is usually large enough that the annular flow field can be considered as a two dimensional flow in the axial and tangential directions. With the flat plate cascade model of the blade row, the mean flow is uniform. The linearized Euler Equations (2.19) and (2.20) about a uniform mean flow in axial and tangential directions are:

$$\frac{\partial \rho'}{\partial t} + U_x \frac{\partial \rho'}{\partial x} + U_y \frac{\partial \rho'}{\partial y} + \rho_0 \left(\frac{\partial u_x}{\partial x} + \frac{\partial u_y}{\partial y}\right) = 0 \tag{2.21}$$

$$\frac{\partial u_x}{\partial t} + U_x \frac{\partial u_x}{\partial x} + U_y \frac{\partial u_x}{\partial y} + \frac{1}{\rho_0}\frac{\partial p'}{\partial x} = 0 \tag{2.22}$$

$$\frac{\partial u_y}{\partial t} + U_x \frac{\partial u_y}{\partial x} + U_y \frac{\partial u_y}{\partial y} + \frac{1}{\rho_0}\frac{\partial p'}{\partial y} = 0 \tag{2.23}$$

where U_x and U_y are uniform mean flow velocity in the axial and tangential directions. u_x and u_y are the corresponding unsteady perturbation velocities. ρ_0 is mean flow density. ρ' and p' are unsteady perturbation density and pressure. Since the mean flow is uniform, these equations are linear with constant coefficients.

The unsteady perturbation quantities are assumed to be harmonic in time and space:

$$\begin{aligned} p' &= \overline{p} e^{i(\omega t+\alpha x+\beta y)} \\ u_x' &= \overline{u_x} e^{i(\omega t+\alpha x+\beta y)} \\ u_y' &= \overline{u_y} e^{i(\omega t+\alpha x+\beta y)} \end{aligned} \tag{2.24}$$

where $\overline{p}$, $\overline{u_x}$ are $\overline{u_y}$ are the complex perturbation amplitudes. α and β are the axial and tangential wave number, respectively. ω is the frequency.

Substituting Equation (2.24) into the Equations (2.21) to (2.23) yields:

$$\begin{bmatrix} \left(\omega+U_x\alpha+U_y\beta\right) & a_0{}^2\alpha\rho_0 & a_0{}^2\beta\rho_0 \\ \alpha/\rho_0 & \omega+U_x\alpha+U_y\beta & 0 \\ \beta/\rho_0 & 0 & \omega+U_x\alpha+U_y\beta \end{bmatrix} \begin{bmatrix} \overline{p} \\ \overline{u_x} \\ \overline{u_y} \end{bmatrix} = 0 \tag{2.25}$$

This set of equations must be indeterminate to have a nontrivial solution. Thus the determinate of the coefficients matrix must be zero,

$$\left(\omega+U_x\alpha+U_y\beta\right)\left[\left(\omega+U_x\alpha+U_y\beta\right)^2 - a_0{}^2\left(\alpha^2+\beta^2\right)\right] = 0 \tag{2.26}$$

The characteristic equation $\left(\omega+U_x\alpha+U_y\beta\right)=0$ corresponds to a vorticity wave. Its axial wave number is,

$$\alpha = -\frac{\omega+U_y\beta}{U_x} \tag{2.27}$$

Substituting Equation (2.27) into Equation (2.25) and solving the system of equations, yields:

$$\overline{p} = 0 \tag{2.28}$$

$$\overline{u_x} = -\frac{\beta}{\alpha}\overline{u_y} \tag{2.29}$$

The perturbation vorticity in the flow ζ is given by

$$\zeta = \frac{\partial u_y}{\partial x} - \frac{\partial u_x}{\partial y} = \overline{\zeta} e^{i(\omega t + \alpha x + \beta y)} \tag{2.30}$$

$$\overline{\zeta} = i\alpha \overline{u_y} - i\beta \overline{u_x} \tag{2.31}$$

The vorticity wave is convected with the mean flow with no associated pressure perturbation.

The other characteristic equation $\left[\left(\omega + U_x\alpha + U_y\beta\right)^2 - a_0{}^2\left(\alpha^2 + \beta^2\right)\right] = 0$ corresponds to pressure waves. Its axial wave numbers are

$$\alpha = \frac{U_x\left(\omega + U_y\beta\right) \pm a_0\sqrt{\left(\omega + U_y\beta\right)^2 - \left(a_0{}^2 - U_x{}^2\right)\beta^2}}{a_0{}^2 - U_x{}^2} \tag{2.32}$$

where the plus sign corresponds to an upstream going pressure wave and the minus sign corresponds to a downstream going pressure wave.

When $\left(\omega + U_y\beta\right)^2 - \left(a_0{}^2 - U_x{}^2\right)\beta^2 > 0$, the radical is real. The unsteady pressure wave propagates at a constant amplitude. This behavior is referred to as superresonant or cut-on. When $\left(\omega + U_y\beta\right)^2 - \left(a_0{}^2 - U_x{}^2\right)\beta^2 < 0$, the radical is a complex number. The unsteady pressure wave propagates with exponential decay. This behavior is referred to as subresonant or cut-off. When $\left(\omega + U_y\beta\right)^2 - \left(a_0{}^2 - U_x{}^2\right)\beta^2 = 0$, the radical is zero. There is only one real axial wave number. This division point between cut-on and cut-off wave is called the acoustic resonance point. Examining the radical reveals that generally waves with high frequency ω, or low tangential wave number β are more likely to be cut-on.

Substituting Equation (2.32) into Equation (2.25) and solving the system of equations, yields:

$$\overline{p} = -\frac{\rho_0\left(\omega + U_x\alpha + U_y\beta\right)}{\alpha}\overline{u_y} \tag{2.33}$$

$$\overline{u_x} = \frac{\alpha}{\beta}\overline{u_y} \tag{2.34}$$

the perturbation vorticity,

$$\overline{\zeta} = i\alpha \overline{u_y} - i\beta \overline{u_x} = 0 \tag{2.35}$$

The pressure wave is propagating at the speed of sound with no associated vorticity perturbation.

2.2.2 Centrifugal Compressor

In a centrifugal compressor, the vaneless space between the impeller and the vaned diffuser is usually in the shape of a thin annulus. The flow field can be considered as a two dimensional flow in the radial and circumferential directions. Due to the change of the cross-section area in the radial direction, the mean flow is non-uniform.

2.2.2.1 Mean Flow Field

In a 2D cylindrical coordinate system and assuming the mean flow is axisymmetric, i.e. $\frac{\partial}{\partial\theta}=0$, the mean flow continuity Equation (2.17) and momentum Equation (2.18) are,

$$\frac{\rho_0}{r}U_{r0}+U_{r0}\frac{\partial\rho_0}{\partial r}+\rho_0\frac{\partial U_{r0}}{\partial r}=0 \tag{2.36}$$

$$U_{r0}\frac{\partial U_{r0}}{\partial r}-\frac{U_{\theta0}^2}{r}=-\frac{1}{\rho_0}\frac{\partial p_0}{\partial r} \tag{2.37}$$

$$\frac{\partial U_{\theta0}}{\partial r}=-\frac{U_{\theta0}}{r} \tag{2.38}$$

Integrating Equation (2.38) yields the mean flow circumferential velocity,

$$U_{\theta0}=\frac{c_2}{r} \tag{2.39}$$

where c_2 is a constant.

Equation (2.38) is valid for a compressible flow and implies that the mean flow is irrotational since

$$\nabla\times\vec{U}_0=\frac{1}{r}\left(U_{\theta0}+r\frac{\partial U_{\theta0}}{\partial r}-\frac{\partial U_{r0}}{\partial\theta}\right)\hat{e}_z=0 \tag{2.40}$$

For a low speed centrifugal compressor, two additional assumptions can be made. First, the mean flow density is assumed to be nearly constant in the vaneless space, i.e.

$\frac{\partial \rho_0}{\partial r} = 0$. Second, the square of the mean flow Mach number is negligible. These two assumption are valid for a centrifugal compressor with low impeller exit Mach number and small vaneless space.

With these assumptions, Equation (2.36) becomes,

$$\frac{U_{r0}}{r} + \frac{\partial U_{r0}}{\partial r} = 0 \tag{2.41}$$

Integrating Equation (2.41) yields the mean flow radial velocity

$$U_{r0} = \frac{c_1}{r} \tag{2.42}$$

where c_1 is a constant.

Substituting Equations (2.39) and (2.42) intro Equation (2.37) gives

$$\frac{\partial p_0}{\partial r} = \rho_0 \left(\frac{{c_1}^2}{r^3} + \frac{{c_2}^2}{r^3} \right) \tag{2.43}$$

Integrating Equation (2.43) yields the mean flow pressure,

$$p_0 = -\frac{\rho_0}{2r^2}\left({c_1}^2 + {c_2}^2 \right) + c_3 \tag{2.44}$$

where c_3 is a constant.

2.2.2.2 Unsteady Flow Field

The linearized 2D Euler equations, Equations (2.19) and (2.20), are the governing equations for the unsteady flow field. As shown by Goldstein [32], when the mean flow is irrotational (Equation (2.40)), the pressure waves and vorticity wave, i.e. the impeller wake, are uncoupled. Therefore, use Goldstein's splitting method $\vec{u} = \vec{u}_a + \vec{u}_v$ where $\vec{u}_a$ is the potential part related to the acoustic pressure wave and $\vec{u}_v$ is the vortical part related to the vorticity wave. Substituting $\vec{u} = \vec{u}_a + \vec{u}_v$ into Equations (2.19) and (2.20), uncouples the pressure wave and the vorticity wave. For the pressure wave $\vec{u}_v = 0$ and for the vorticity wave $p' = 0$.

The pressure wave governing equations are,

$$\frac{D_0}{Dt}\left(\frac{p'}{\rho_0 {a_0}^2}\right)+\frac{1}{\rho_0}\nabla\cdot\left(\rho_0\vec{u}_a\right)=0 \tag{2.45}$$

$$\frac{D_0\vec{u}_a}{Dt}+\vec{u}_a\cdot\nabla\vec{U}_0=-\nabla\left(\frac{p'}{\rho_0}\right) \tag{2.46}$$

The vorticity wave governing equations are,

$$\frac{D_0}{Dt}\left(\frac{p'}{\rho_0 {a_0}^2}\right)+\frac{1}{\rho_0}\nabla\cdot\left(\rho_0\vec{u}_a\right)=-\frac{1}{\rho_0}\nabla\cdot\left(\rho_0\vec{u}_v\right) \tag{2.47}$$

$$\frac{D_0\vec{u}_v}{Dt}+\vec{u}_v\cdot\nabla\vec{U}_0=0 \tag{2.48}$$

where p' in Equation (2.47) is the induced pressure fluctuation caused by the vorticity wave which acts as a source term on the right hand side of Equation (2.47) [32-33]. Since the vorticity wave is convected with mean flow, its induced pressure fluctuation is also convected with the mean flow which is different from the acoustic pressure wave p' in Equation (2.45).

These equations can be written in terms of the potential perturbation φ,

The pressure wave governing equations become,

$$\frac{D_0}{Dt}\left(\frac{1}{{a_0}^2}\frac{D_0\varphi}{Dt}\right)-\frac{1}{\rho_0}\nabla\cdot\left(\rho_0\nabla\varphi\right)=0 \tag{2.49}$$

$$p'=-\rho_0\frac{D_0\varphi}{Dt} \tag{2.50}$$

The vorticity wave governing equations become,

$$\frac{D_0}{Dt}\left(\frac{1}{{a_0}^2}\frac{D_0\varphi}{Dt}\right)-\frac{1}{\rho_0}\nabla\cdot\left(\rho_0\nabla\varphi\right)=\frac{1}{\rho_0}\nabla\cdot\left(\rho_0\vec{u}_v\right) \tag{2.51}$$

$$\frac{D_0\vec{u}_v}{Dt}+\vec{u}_v\cdot\nabla\vec{U}_0=0 \tag{2.52}$$

To reduce the complexity of the problem and change the PDE to an ODE, the unsteady perturbations are assumed to be harmonic in time and in the circumferential direction,

$$q=\overline{q}(r)\,\mathrm{e}^{i(\omega t+k_\theta\theta)} \tag{2.53}$$

where q is a perturbation property, i.e. φ , p' , u_{ra} , $u_{\theta a}$, u_{rv} , $u_{\theta v}$.

In addition, under the low Mach number assumption made before, the mean flow velocities are $U_{r0}=\frac{c_1}{r}$ and $U_{\theta 0}=\frac{c_2}{r}$ as shown in Equations (2.42) and (2.39). Thus, the pressure wave equation (2.49) becomes,

$$\frac{\partial^2\varphi}{\partial r^2}+\left(\frac{1}{r}-\frac{2c_1 i\omega}{r{a_0}^2}\right)\frac{\partial\varphi}{\partial r}+\left(\frac{\omega^2}{{a_0}^2}+\frac{2c_2\omega k_\theta}{r^2{a_0}^2}-\frac{{k_\theta}^2}{r^2}\right)\varphi=0 \tag{2.54}$$

Equation (2.54) is a second order ODE which can be transferred to a Bessel equation by change of variable. Similar to the derivation by Roger [34], the solution is a combination of Hankel functions of the first and second kinds.

$$\varphi=Ar^{\frac{c_1\omega i}{{a_0}^2}}H_\nu^{(1)}\left(\frac{\omega}{a_0}r\right)+Br^{\frac{c_1\omega i}{{a_0}^2}}H_\nu^{(2)}\left(\frac{\omega}{a_0}r\right) \tag{2.55}$$

where A, B are constants and the order $\nu=\sqrt{{k_\theta}^2-\frac{2c_2\omega k_\theta}{{a_0}^2}-\frac{{c_1}^2\omega^2}{{a_0}^4}}$

and the corresponding velocity and pressure perturbations for pressure wave are:

$$\vec{u}_a=\nabla\varphi\text{, thus } u_{ra}=\frac{\partial\varphi}{\partial r} \text{ and } u_{\theta a}=\frac{1}{r}\frac{\partial\varphi}{\partial\theta}=\frac{ik_\theta}{r}\varphi \tag{2.56}$$

$$p'=-\rho_0\frac{D_0\varphi}{Dt}=-\rho_0\left(i\omega\varphi+\frac{c_1}{r}\frac{\partial\varphi}{\partial r}+\frac{c_2}{r^2}ik_\theta\varphi\right) \tag{2.57}$$

With the same assumptions, the vorticity wave momentum Equation (2.52) becomes,

$$\frac{\partial u_{\theta v}}{\partial r}+\left(\frac{i\omega}{c_1}r+\frac{\frac{c_2}{c_1}ik_\theta+1}{r}\right)u_{\theta v}=0 \tag{2.58}$$

$$\frac{\partial u_{rv}}{\partial r}+\left(\frac{i\omega}{c_1}r+\frac{\frac{c_2}{c_1}ik_\theta-1}{r}\right)u_{rv}=2\frac{c_2}{c_1}\frac{u_{\theta v}}{r} \tag{2.59}$$

Both Equations (2.58) and (2.59) are first order ODEs. Their solutions are

$$u_{\theta v}=De^{-\frac{i\omega}{2c_1}r^2-\frac{c_2ik_\theta}{c_1}\ln r}\frac{1}{r} \tag{2.60}$$

$$u_{rv} = e^{-\frac{i\omega}{2c_1}r^2 - \frac{c_2 i k_\theta}{c_1}\ln r}\left(Er - \frac{c_2}{c_1}D\frac{1}{r}\right) \tag{2.61}$$

where E,D are constants

In order to satisfy the vorticity wave continuity Equation (2.51), there is an induced pressure fluctuation caused by the purely convected vorticity wave [32-33]. Under the low Mach number and constant mean flow density assumption, Equation (2.51) becomes,

$$\frac{\partial^2\varphi_v}{\partial r^2} + \left(\frac{1}{r} - \frac{2c_1 i\omega}{r{a_0}^2}\right)\frac{\partial\varphi_v}{\partial r} + \left(\frac{\omega^2}{{a_0}^2} + \frac{2c_2\omega k_\theta}{r^2{a_0}^2} - \frac{{k_\theta}^2}{r^2}\right)\varphi_v = -\left(\frac{u_{rv}}{r} + \frac{\partial u_{rv}}{\partial r} + \frac{ik_\theta}{r}u_{\theta v}\right) \tag{2.62}$$

The homogenous solution is the same as Equation (2.55) for the pressure wave. For the vorticity wave, the homogenous solution should be zero.

Substituting Equations (2.60) and (2.61) into Equation (2.62), the particular solution gives the potential perturbation of the induced pressure fluctuation,

$$\begin{aligned}\varphi_v = {} & \frac{\pi}{2}r^{\frac{c_1\omega i}{{a_0}^2}}J_\nu\left(\frac{\omega}{a_0}r\right)\int_1^r Y_\nu\left(\frac{\omega}{a_0}\xi\right)e^{-\frac{i\omega}{2c_1}\xi^2}\xi^{-\frac{c_2 i k_\theta}{c_1}-\frac{c_1\omega i}{{a_0}^2}}\left(g_1\xi^3 + g_2\xi + g_3\frac{1}{\xi}\right)d\xi \\ & -\frac{\pi}{2}r^{\frac{c_1\omega i}{{a_0}^2}}Y_\nu\left(\frac{\omega}{a_0}r\right)\int_1^r J_\nu\left(\frac{\omega}{a_0}\xi\right)e^{-\frac{i\omega}{2c_1}\xi^2}\xi^{-\frac{c_2 i k_\theta}{c_1}-\frac{c_1\omega i}{{a_0}^2}}\left(g_1\xi^3 + g_2\xi + g_3\frac{1}{\xi}\right)d\xi\end{aligned} \tag{2.63}$$

where J_ν and Y_ν are the Bessel functions of the first and second kind with order $\nu = \sqrt{{k_\theta}^2 - \frac{2c_2\omega k_\theta}{{a_0}^2} - \frac{{c_1}^2\omega^2}{{a_0}^4}}$. g_1 , g_2 and g_3 are the complex constants defined by,

$$\begin{aligned} g_1 &= -\frac{i\omega}{c_1}E \\ g_2 &= \frac{c_2 i\omega}{{c_1}^2}D + \left(2 - \frac{c_2 k_\theta}{c_1}i\right)E \\ g_3 &= \left(\frac{{c_2}^2 k_\theta}{{c_1}^2}i + k_\theta i\right)D \end{aligned} \tag{2.64}$$

2.3 Uniformly Spaced Flat Plate Cascade Model

Based on the unsteady waves solutions derived in Section 2.2, a flat plate cascade model [11] can be constructed to quantify the response of interaction between unsteady waves and a blade row. Although flow turning is the main purpose of a blade row, a flat plate cascade provides a simple and fast analytical solution which still maintains the essential kinematics of the problem. Compared to the prediction of non-linear Euler analysis, experiments conducted in GE Aircraft Engines shows that the classic flat plate cascade model is able to do a comparable good perdition of the unsteady loading on compressor blades due to wake excitation at normal loading conditions [35].

The vorticity wave and pressure waves are independent solutions of the linearized Euler equations. These waves propagate through the flow field independently without interacting with each other. Only at a boundary such as solid blade surface, can they interact and exchange energy. The analysis in this section follows the classic flat plate cascade model LINSUB [11]. LINSUB is a 2D linearized frequency method for calculating the interaction between unsteady flows and an isolated flat plate cascade in an inviscid compressible flow during an isentropic process. As shown in Figure 2.2, LINSUB models the blade row by a row of discrete bound vortices. The whole unsteady flow may be considered as being due to bound vortices which replace the blades and their associated unsteady waves. The problem is to find the bound vortex distributions which give the correct induced velocity distributions along the blades that cancels the excitation upwash velocity so that the blade surface boundary condition is satisfied. Once these bound vortices are determined, the unsteady lift, unsteady moment and out-going pressure waves and vorticity wave can be calculated.

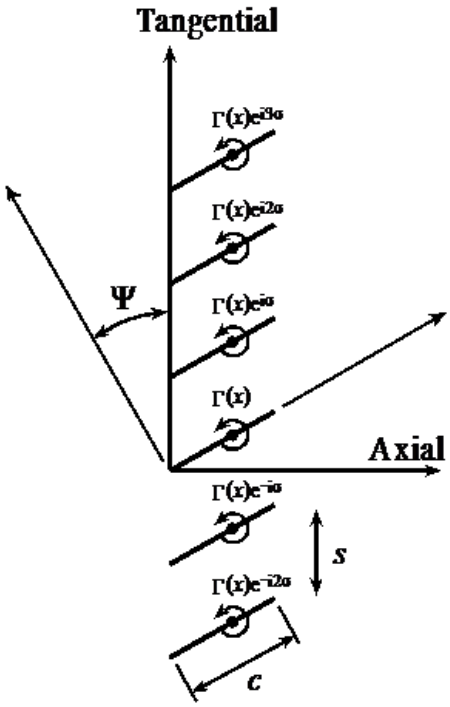

Figure 2.2. Blade row modeled as a row of discrete bound vortices [11].

As shown in Figure 2.2, for a uniformly spaced blade row, at a specific chordwise location the bound vortex strength is constant from one blade to the next except for a shift in phase equal to the interblade phase angle σ. The discrete bound vortices on blades in the tangential direction can be expressed mathematically as

$$\gamma(y) = \bar{\gamma}(y)e^{i\omega t} = \sum_{j=0}^{B-1} \Gamma e^{ij\sigma}\delta(y - js)e^{i\omega t} \tag{2.65}$$

where $\delta(z)$ is the delta function defined as zero except at $z=1$ where its value is 1. B is the number of blades in the blade row. s is the tangential spacing between two adjacent blades. j is the blade index.

Physically, $\gamma(y)$ is a periodic function with period Bs. Represent this periodic function by a complex Fourier series,

$$\bar{\gamma}(y) = \sum_{r=-\infty}^{+\infty} a_r e^{\left(i\frac{2\pi ry}{Bs}\right)} \tag{2.66}$$

The Fourier coefficient a_r can be calculated as,

$$a_r = \frac{1}{Bs}\int_0^{Bs} \overline{\gamma}(y) e^{\left(-i\frac{2\pi ry}{Bs}\right)} dy \tag{2.67}$$

Substitute Equation (2.65) for $\overline{\gamma}(y)$ intro Equation (2.67) and note that the integral is non-zero only when $y = js$

$$a_r = \frac{\Gamma}{Bs}\sum_{j=0}^{B-1} e^{ij\sigma} e^{\left(-i\frac{2\pi rj}{B}\right)} \tag{2.68}$$

For an excitation at ND nodal diameter, the interblade phase angle is

$$\sigma = \frac{2\pi ND}{B} \tag{2.69}$$

Substitute Equation (2.69) into Equation (2.68)

$$a_r = \frac{\Gamma}{Bs}\sum_{j=0}^{B-1} e^{\left(i\frac{2\pi(ND-r)j}{B}\right)} \tag{2.70}$$

Use the math identity $\sum_{j=0}^{B-1} z^j = \frac{1-z^B}{1-z}$ with $z = e^{\left(i\frac{2\pi(ND-r)j}{B}\right)}$, to get

$$a_r = \begin{cases} \frac{0}{0} & \text{if } r = ND - nB \quad \text{where n is any integer} \\ 0 & \text{otherwise} \end{cases}$$

To find an expression for a_r when $r = ND - nB$ begin with Equation (2.70)

$$a_r = \frac{\Gamma}{Bs}\sum_{j=0}^{B-1} e^{(i2\pi nj)} = \frac{\Gamma}{s} \tag{2.71}$$

Thus,

$$a_r = \begin{cases} \frac{\Gamma}{s} & \text{if } r = ND - nB \quad \text{where n is any integer} \\ 0 & \text{otherwise} \end{cases}$$

Substituting a_r into Equation (2.66), the discrete bound vortices are represented as a series of continuous cascade waves with the same amplitude $\frac{\Gamma}{s}$

$$\bar{\gamma}(y) = \sum_{n=-\infty}^{+\infty} \frac{\Gamma}{s} e^{\left(i\frac{\sigma-2\pi n}{s}y\right)} \tag{2.72}$$

The corresponding tangential wave number and nodal diameter for the n^{th} cascade waves are

$$\beta_n = \frac{\sigma - 2\pi n}{s} = \frac{2\pi(ND - nB)}{Bs} \tag{2.73}$$

$$ND_n = ND - nB \tag{2.74}$$

The derivation above shows that at a specific chord location z , a blade row can be modeled as a row of discrete bound vortices of strength Γ with a constant phase angle shift from one blade to its adjacent one. The row of discrete bound vortices is equivalent to a series of cascade waves of the same amplitude Γ / s but different tangential wave number as given in Equation (2.73). When $n = 0$, the cascade wave has nodal diameter equal to the excitation nodal diameter ND. This cascade wave is known as the fundamental mode. When $n \neq 0$ the cascade waves have nodal diameter $ND - nB$ and are known as higher order scattering modes.

Take a blade row with 4 uniformly spaced blades as an example. Assume the blade row is excited by an unsteady wave with nodal diameter $ND = 2$. Figure 2.3 shows the strength of the corresponding row of discrete bound vorticities and the equivalent cascade waves, among which the fundamental mode $ND = 2$ and its associated scattering modes with $n = \pm 1$ are plotted.

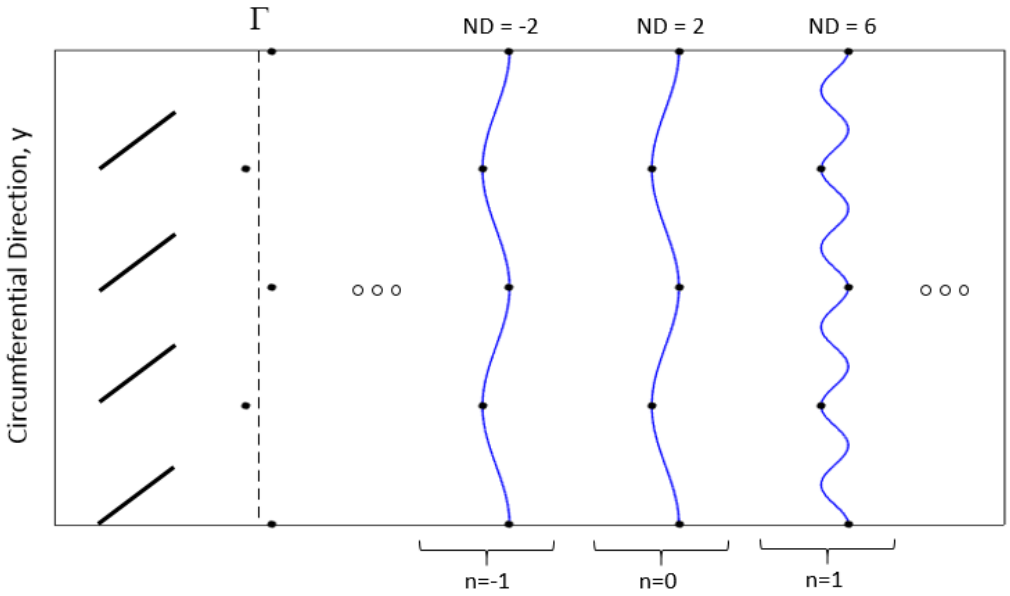

Figure 2.3. Schematic of a blade row modeled by a row of discrete bound vortices and cascade waves.

Since cascade waves of the fundamental mode and its associated scattering modes have the same strength, and the phase shift from blade to blade is only different by an integer multiple of 2π, they are commonly treated together as a single group. In the rest of this section, "fundamental harmonic mode" is used to refer the cascade waves of the fundamental mode and its associated higher order scattering modes.

In order to obtain an accurate unsteady loading along the chord, each blade is discretized into a finite number of panels. There are one vortex point and one control point on each panel. A vortex point is point where the bound vortex is located, and a control point is a point where the excitation upwash velocity is specified. The discrete bound vortices at the same chordwise position over the entire blade row are equivalent to a series of cascade waves. The cascade waves create pressure and vorticity waves traveling upstream and downstream and cause induced velocity at the control points on the entire blade row. The induced velocity at the control point j caused by the cascade waves at vortex point k for the first blade can be expressed as $K_{jk}\Gamma_k$, where K_{jk} is the kernel function representing the effect of the row of bound vortices at panel k on the control point j of the first blade.

Thus for a blade row which is discretized into np panels along the chord, and the bound vortex on each panel of the first blade are $\Gamma_1, \Gamma_2, \cdots \Gamma_{np}$. The total induced velocity at control point j of the first blade is

$$u_{induced}{}^{j} = \sum_{k=1}^{np} K_{jk}\Gamma_k \tag{2.75}$$

At the control points of every blade, the total induced velocity $u_{induced}$ must cancel the upwash velocity u_{upwash} due to either an internal blade vibration and/or an external excitation wave in order to satisfy the blade surface boundary condition. Following Equation (2.75), the boundary condition at control point j of the first blade can be expressed as

$$u_{upwash}{}^{j} = -u_{induced}{}^{j} = -\sum_{k=1}^{np} K_{jk}\Gamma_k \tag{2.76}$$

The boundary conditions at all control points of the first blade can be expressed in the matrix form

$$\begin{bmatrix} K_{11} & K_{12} & \cdots & K_{1(np)} \\ K_{21} & K_{22} & \cdots & K_{2(np)} \\ \vdots & \vdots & \ddots & \vdots \\ K_{(np)1} & K_{(np)2} & \cdots & K_{(np)(np)} \end{bmatrix} \begin{bmatrix} \Gamma_1 \\ \Gamma_2 \\ \vdots \\ \Gamma_{np} \end{bmatrix} = - \begin{bmatrix} u_{upwash}{}^{1} \\ u_{upwash}{}^{2} \\ \vdots \\ u_{upwash}{}^{np} \end{bmatrix} \tag{2.77}$$

The governing equation of the boundary conditions on other blades can be reduced to the one on the first blade, Equation (2.77). Consider the boundary conditions on blade m. The induced velocity at control point j of blade m caused by cascade waves at vortex point k is $K_{jk}e^{i(m-1)\sigma}\Gamma_k$, where σ is the interblade phase angle of the fundamental mode. Although the kernel function represents the summation of the effect of all cascade waves, the kernel function has the same interblade phase angle as the cascade wave of the fundamental mode. In Equation (2.73), the cascade waves interblade phase angles are $\sigma - 2\pi n$ where n can be any integer. Thus if the induced velocity on the first blade is $K_{jk}\Gamma_k$, the induced velocity on blade m is $K_{jk}e^{i(m-1)(\sigma-2\pi n)}\Gamma_k$, which can be simplified to $K_{jk}e^{i(m-1)\sigma}\Gamma_k$. Similarly, for the excitation with interblade phase angle σ, if

the upwash velocities on the first blade is $\left[u_{upwash}{}^{1} \quad u_{upwash}{}^{2} \quad \cdots \quad u_{upwash}{}^{np} \right]^T$, the upwash velocity on the m^{th} blade is $\left[u_{upwash}{}^{1} e^{i(m-1)\sigma} \quad u_{upwash}{}^{2} e^{i(m-1)\sigma} \quad \cdots \quad u_{upwash}{}^{np} e^{i(m-1)\sigma} \right]^T$. Thus, the boundary conditions for all control points on blade m can be expressed in the matrix form,

$$\begin{bmatrix} K_{11}e^{i(m-1)\sigma} & K_{12}e^{i(m-1)\sigma} & \cdots & K_{1(np)}e^{i(m-1)\sigma} \\ K_{21}e^{i(m-1)\sigma} & K_{22}e^{i(m-1)\sigma} & \cdots & K_{2(np)}e^{i(m-1)\sigma} \\ \vdots & \vdots & \ddots & \vdots \\ K_{(np)1}e^{i(m-1)\sigma} & K_{(np)2}e^{i(m-1)\sigma} & \cdots & K_{(np)(np)}e^{i(m-1)\sigma} \end{bmatrix} \begin{bmatrix} \Gamma_1 \\ \Gamma_2 \\ \vdots \\ \Gamma_{np} \end{bmatrix} = - \begin{bmatrix} u_{upwash}{}^{1} e^{i(m-1)\sigma} \\ u_{upwash}{}^{2} e^{i(m-1)\sigma} \\ \vdots \\ u_{upwash}{}^{np} e^{i(m-1)\sigma} \end{bmatrix} \tag{2.78}$$

This is the same as Equation (2.77) after dividing both sides by the same phase shift from the first blade to the m^{th} blade $e^{i(m-1)\sigma}$.

In a compact form, Equation (2.77) can be written as

$$[K]_{np\times np}[\Gamma]_{np\times 1} = [U]_{np\times 1} \tag{2.79}$$

where $[K]_{np\times np}$, $[\Gamma]_{np\times 1}$ and $[U]_{np\times 1}$ are the kernel matrix , bound vortices vector and upwash velocity vector, respectively.

Once the bound vortices is found, the pressure difference across the blade can be calculated using Kutta-Joukowski theorem,

$$\Delta p = p_{-}^{'} - p_{+}^{'} = -\frac{\rho_0 U_z}{c}\Gamma \tag{2.80}$$

where c is the chord length, and U_z is the chordwise main flow velocity.

The response unsteady lift, moment, outgoing pressure waves and vorticity wave can all be calculated by different integration functions of the bound vortices along the blade. This can be summarized in the following post-processing formulation,

$$[X]_{5\times np}[\Gamma]_{np\times 1}=[C]_{5\times 1} \tag{2.81}$$

where $[X]_{5\times np}$ performs the summation of the contribution from all the bound vortices $[\Gamma]_{np\times 1}$ to give the final output unsteady aerodynamic influence coefficients $[C]_{5\times 1}$. The five rows are for five different responses, i.e. unsteady lift, moment, vorticity wave, upstream going pressure wave and downstream going pressure wave. These unsteady aerodynamic influence coefficients are used to quantify the unsteady response of a blade row to internal or external excitations.

2.4 Generalized Uniformly Spaced Flat Plate Cascade Model

Considering the example in Figure 2.3, a uniformly spaced blade row with 4 blades can be represented by a row of discrete bound vortices of strength Γ with a constant phase shift from one blade to its adjacent one. The row of discrete bound vortices is equivalent to a series of cascade waves of the same strength Γ / s. The fundamental mode has the same nodal diameter as the excitation. The higher order scattering mode has nodal diameter $ND-4n$, where n can be any integer.

If for some reason Blade 2 is missing, the blade spacing is not a constant any more. The amplitudes of the bound vortices on the remaining blades are not the same due to the breakdown of symmetry. In order to work in the same theoretical framework of the uniformly spaced blade row, the missing Blade 2 is retained as an imaginary blade which just indicates the position but is not physically present. Since the fluid at the position of the imaginary blade cannot sustain a stable unsteady pressure difference, the bound vortices at the imaginary Blade 2 must have zero strength.

Thus by a finer discretization in the tangential direction, a non-uniformly spaced blade row can be transformed into a generalized uniformly spaced blade row with both real and imaginary blades. For a generalized uniformly spaced blade row with N blades (real blades + imaginary blades), the bound vorticities on each blade usually have

different amplitudes and phases. Using discrete Fourier representation, the bound vorticity on the m^{th} blade, Γ^m can be expressed as

$$\Gamma^m = \sum_{k=0}^{N-1} b_k e^{\left(i\frac{2\pi k(m-1)}{N}\right)} \tag{2.82}$$

The bound vortex on each blade is the summation of the bound vortex of N fundamental harmonic modes. The strength of each mode is b_k and the nodal diameter and interblade phase angle of each mode are $ND_k = k$ and $\sigma_k = \frac{2\pi k}{N}$ where $k = 0,1,2,\cdots N-1$

In the example of the generalized uniformly spaced blade row with 4 blades, the bound vortices on each blade can be expressed as the summation of 4 fundamental harmonic modes with nodal diameter equal to 0,1,2,3

$$\begin{bmatrix}\Gamma^1\\ \Gamma^2\\ \Gamma^3\\ \Gamma^4\end{bmatrix} = b_1\begin{bmatrix} e^{\left(i\frac{2\pi(0)}{4}0\right)}\\ e^{\left(i\frac{2\pi(0)}{4}1\right)}\\ e^{\left(i\frac{2\pi(0)}{4}2\right)}\\ e^{\left(i\frac{2\pi(0)}{4}3\right)}\end{bmatrix} + b_2\begin{bmatrix} e^{\left(i\frac{2\pi(1)}{4}0\right)}\\ e^{\left(i\frac{2\pi(1)}{4}1\right)}\\ e^{\left(i\frac{2\pi(1)}{4}2\right)}\\ e^{\left(i\frac{2\pi(1)}{4}3\right)}\end{bmatrix} + b_3\begin{bmatrix} e^{\left(i\frac{2\pi(2)}{4}0\right)}\\ e^{\left(i\frac{2\pi(2)}{4}1\right)}\\ e^{\left(i\frac{2\pi(2)}{4}2\right)}\\ e^{\left(i\frac{2\pi(2)}{4}3\right)}\end{bmatrix} + b_4\begin{bmatrix} e^{\left(i\frac{2\pi(3)}{4}0\right)}\\ e^{\left(i\frac{2\pi(3)}{4}1\right)}\\ e^{\left(i\frac{2\pi(3)}{4}2\right)}\\ e^{\left(i\frac{2\pi(3)}{4}3\right)}\end{bmatrix} \tag{2.83}$$

Each fundamental harmonic mode contains both the fundamental mode and its associated higher order scattering modes. Figure 2.4 shows the cascade wave representation of the generalized uniformly spaced blade row with 4 blades, under an excitation with $ND = 2$. Compared to the normal uniformly spaced blade row in Figure 2.3, all possible fundamental harmonic modes are present.

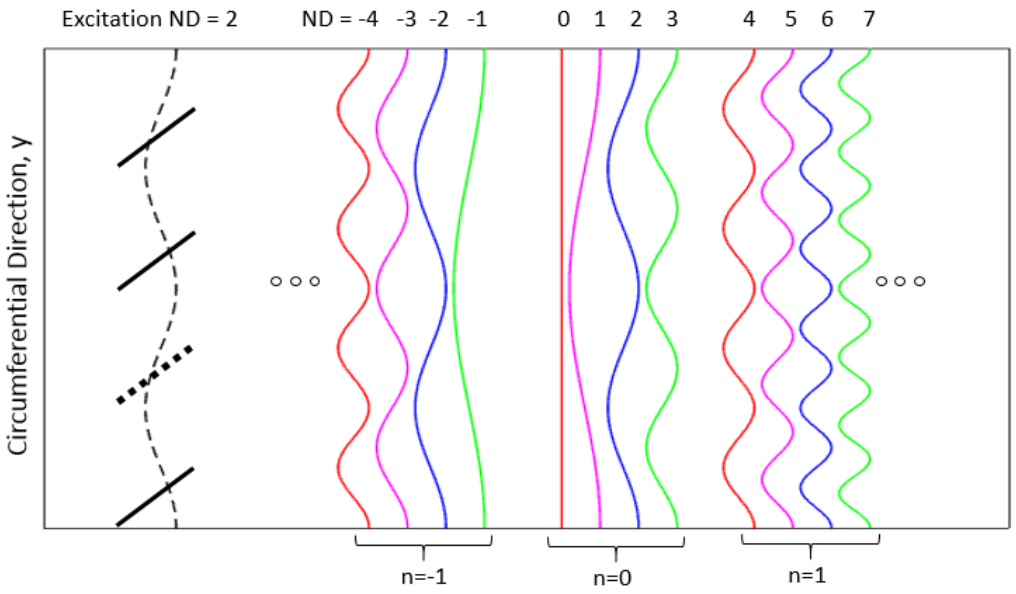

Figure 2.4. Schematic of generalized uniformly spaced blade row with blade 2 missing modeled by a series of cascade waves of all possible fundamental harmonic modes.

For the case of a normal uniformly spaced blade row, the bound vortices on each blade $\left[\Gamma^1 \quad \Gamma^2 \quad \Gamma^3 \quad \Gamma^4\right]^T = \left[\Gamma \quad \Gamma e^{i\sigma} \quad \Gamma e^{i2\sigma} \quad \Gamma e^{i3\sigma}\right]^T$. If the excitation nodal diameter is 2, the interblade phase angle $\sigma = \frac{2\pi(2)}{4}$. Thus, Equation (2.83) gives $b_3 = \Gamma$ and $b_1 = b_2 = b_4 = 0$. In other words, for a normal uniformly spaced blade row, the bound vortices can be represented by a single fundamental harmonic mode with the nodal diameter equal to the excitation nodal diameter as shown in Figure 2.3.

For the case of generalized uniformly spaced blade row with Blade 2 missing, the bound vortex on imaginary blade $\Gamma^2 = 0$ and the bound vortex on real blades Γ^1, Γ^3 and Γ^4 are complex values with different amplitudes. This set of bound vorticity need to be represented by all 4 fundamental harmonic modes. Due to the linearity of the governing equations, each mode can be treated independently and summed together to give the total response. Thus, the blade row with blade 2 missing, can be considered as a superposition of 4 normal uniformly spaced blade rows, each of which is represented by the cascade waves of one fundamental harmonic mode. If the strength of the each fundamental harmonic mode is found, the total effect is the summation of the effect of all modes.

2.4.1 Governing Matrix

To represent a generalized uniformly spaced blade row with N blades (real blades + possible imaginary blades), all N fundamental harmonic modes need to be included. N equations are required to solve for the strengths of the N fundamental harmonic modes. Each real blade and each imaginary blade provides an independent equation.

On each real blade, the blade surface boundary condition needs to be satisfied, i.e. the total induced velocity is equal to the upwash velocity due to excitation. If the blade chord is discretized into np panels, the induced velocity on a real blade m by mode j, $\left[V\right]_{np\times 1}^{m,\mathrm{j}}$ can be expressed as

$$\left[V\right]_{np\times 1}^{m,\mathrm{j}} = \left[K\right]_{np\times np}^{j} e^{\left(i\sigma_j(m-1)\right)} \left[B\right]_{np\times 1}^{j} \tag{2.84}$$

where $\left[K\right]_{np\times np}^{j}$ is the kernel matrix of mode j for the first blade, the interblade phase angle for mode j is $\sigma_j = \dfrac{2\pi\left(j-1\right)}{N}$, and $\left[B\right]_{np\times 1}^{j}$ is the mode strength vector of mode j on each panel of the first blade.

The total induced velocity on real blade m $\left[V\right]_{np\times 1}^{m}$ is equal to the summation of the induced velocity caused by all modes, thus

$$\left[V\right]_{np\times 1}^{m} = \sum_{j=1}^{N} \left[K\right]_{np\times np}^{j} e^{\left(i\sigma_j(m-1)\right)} \left[B\right]_{np\times 1}^{j} \tag{2.85}$$

If the excitation interblade blade phase angle is σ_{ex} , the upwash velocity on real Blade m $\left[U\right]_{np\times 1}^{m}$ is,

$$\left[U\right]_{np\times 1}^{m} = \left[U\right]_{np\times 1} e^{\left(i\sigma_{ex}(m-1)\right)} \tag{2.86}$$

where $\left[U\right]_{np\times 1}$ is the upwash velocity on each panel of the first blade.

Finally, the blade surface boundary condition on real blade m can be written as,

$$\sum_{j=1}^{N} \left[K\right]_{np\times np}^{j} e^{\left(i\sigma_j(m-1)\right)} \left[B\right]_{np\times 1}^{j} = -\left[U\right]_{np\times 1} e^{\left(i\sigma_{ex}(m-1)\right)} \tag{2.87}$$

On an imaginary blade, both the induced velocity and upwash velocity are not zero. However, since there is no solid surface, both the unsteady velocity perturbations propagate through the imaginary blade independently. The governing equation on the imaginary blade comes from fact that bound vortex cannot exist in the fluid without a solid surface. Thus, on each imaginary blade, the strength of the bound vortex has to be zero.

The contribution of mode j to the bound vortex on imaginary blade n is

$$\left[\Gamma\right]_{np\times 1}^{\mathrm{n,j}} = \left[I\right]_{np\times np} e^{\left(i\sigma_j(n-1)\right)} \left[B\right]_{np\times 1}^{j} \tag{2.88}$$

The total bound vortex on imaginary blade n is equal to the summation of the contribution of all fundamental harmonic modes. The total bound vortex on imaginary blade is zero, thus

$$\sum_{j=1}^{N} \left[I\right]_{np\times np} e^{\left(i\sigma_j(n-1)\right)} \left[B\right]_{np\times 1}^{j} = \left[0\right]_{np\times 1} \tag{2.89}$$

The governing equation for real blades and imaginary blades can be put together to form a linear system of equations, the solution of which is the strength of each fundamental mode. Consider the case of a generalized uniformly spaced blade row with Blade 2 missing. The resulting linear system of equations has the following form:

$$\begin{bmatrix} \left[K\right]_{np\times np}^{1} & \left[K\right]_{np\times np}^{2} & \left[K\right]_{np\times np}^{3} & \left[K\right]_{np\times np}^{4} \\ \left[I\right]_{np\times np} e^{(i1\sigma_1)} & \left[I\right]_{np\times np} e^{(i1\sigma_2)} & \left[I\right]_{np\times np} e^{(i1\sigma_3)} & \left[I\right]_{np\times np} e^{(i1\sigma_4)} \\ \left[K\right]_{np\times np}^{1} e^{(i2\sigma_1)} & \left[K\right]_{np\times np}^{2} e^{(i2\sigma_2)} & \left[K\right]_{np\times np}^{3} e^{(i2\sigma_3)} & \left[K\right]_{np\times np}^{4} e^{(i2\sigma_4)} \\ \left[K\right]_{np\times np}^{1} e^{(i3\sigma_1)} & \left[K\right]_{np\times np}^{2} e^{(i3\sigma_2)} & \left[K\right]_{np\times np}^{3} e^{(i3\sigma_3)} & \left[K\right]_{np\times np}^{4} e^{(i3\sigma_4)} \end{bmatrix} \begin{bmatrix} \left[B\right]_{np\times 1}^{1} \\ \left[B\right]_{np\times 1}^{2} \\ \left[B\right]_{np\times 1}^{3} \\ \left[B\right]_{np\times 1}^{4} \end{bmatrix} = -\begin{bmatrix} \left[U\right]_{np\times 1} \\ \left[0\right]_{np\times 1} \\ \left[U\right]_{np\times 1} e^{(i2\sigma_{ex})} \\ \left[U\right]_{np\times 1} e^{(i3\sigma_{ex})} \end{bmatrix} \tag{2.90}$$

where kernel matrix of mode j, $\left[K\right]_{np\times np}^{j}$ and upwash velocity vector $\left[U\right]_{np\times 1}$ are calculated in the same way as the normal uniformly spaced blade row discussed before.

For a generalized uniform blade row with N total blades (real + imaginary), if blade m is a real blade and blade n is an imaginary blade, the whole matrix system of the governing equations has the following form.

$$\begin{bmatrix} \cdots & \cdots & \cdots & \cdots & \cdots \\ [K]^1_{np\times np} e^{(i(m-1)\sigma_1)} & [K]^2_{np\times np} e^{(i(m-1)\sigma_2)} & [K]^3_{np\times np} e^{(i(m-1)\sigma_3)} & \cdots & [K]^N_{np\times np} e^{(i(m-1)\sigma_N)} \\ \cdots & \cdots & \cdots & \cdots & \cdots \\ [I]_{np\times np} e^{(i(n-1)\sigma_1)} & [I]_{np\times np} e^{(i(n-1)\sigma_2)} & [I]_{np\times np} e^{(i(n-1)\sigma_3)} & \cdots & [I]_{np\times np} e^{(i(n-1)\sigma_N)} \\ \cdots & \cdots & \cdots & \cdots & \cdots \end{bmatrix} \begin{bmatrix} [B]^1_{np\times 1} \\ [B]^2_{np\times 1} \\ [B]^3_{np\times 1} \\ \vdots \\ [B]^N_{np\times 1} \end{bmatrix} = -\begin{bmatrix} \cdots \\ [U]_{np\times 1} e^{(i(m-1)\sigma_{ex})} \\ \cdots \\ [0]_{np\times 1} \\ \cdots \end{bmatrix}$$

(2.91)

2.5 Multistage Interactions

Blade rows are coupled together aerodynamically by the unsteady pressure and vorticity waves in the flow field. Hall and Sikowaski [12-13] used spinning modes to represent the coupling unsteady waves and model the multistage interactions. The multistage interactions model developed in this study closely follows Hall and Sikowaski's method and formulation [12-13].

Before going into the model details, the physical processes of multistage interaction need to be understood first. Consider the forced response analysis of a rotor excited by the wake of an upstream stator as an example (Figure 2.5). The rotor blade row with B_2 blades is embedded between the upstream stator with B_1 blades and downstream stator with B_3 blades. In the rotor reference frame, the wake from stator1 impinges on the rotor blade with frequency ω_0 and nodal diameter n_0 (step (1)). The Fourier transformation of the stator1 wake in the circumferential direction contains modes with an infinite number of nodal diameters. Due to the linearity of the model, each mode can be treated independently. The final result is the summation of the effect of all modes. For the stator1 wake, the primary mode has nodal diameter $n_0 = B_1$. In the rotor reference frame, the primary mode has frequency $\omega_0 = n_0\Omega$.

Impinging on the rotor blade row, the stator 1 wake produces an unsteady aerodynamic loading on the rotor. In addition, both upstream going pressure waves (step (2)) and downstream going pressure waves and vorticity waves (step (2')) are generated. The upstream going pressure wave travels upstream and interacts with stator1 (step(3)). The downstream going pressure waves and vorticity waves travel downstream and interact with stator2 (step (3')). The upstream going pressure wave travels upstream and

impings on stator1, produces an unsteady aerodynamic loading on stator1, and generates both upstream going pressure waves (step (3u)) and downstream going pressure waves and vorticity waves (step (4)), which impinge on the rotor (step (5)). Similarly, the downstream going pressure wave and vorticity waves in step (3') impinging on stator2 produce an unsteady aerodynamic loading on stator2 and generate both downstream going pressure waves and vorticity waves (step (3'd)) and upstream going pressure waves (step(4')), which travel upstream and impinge on rotor again(step(5')).

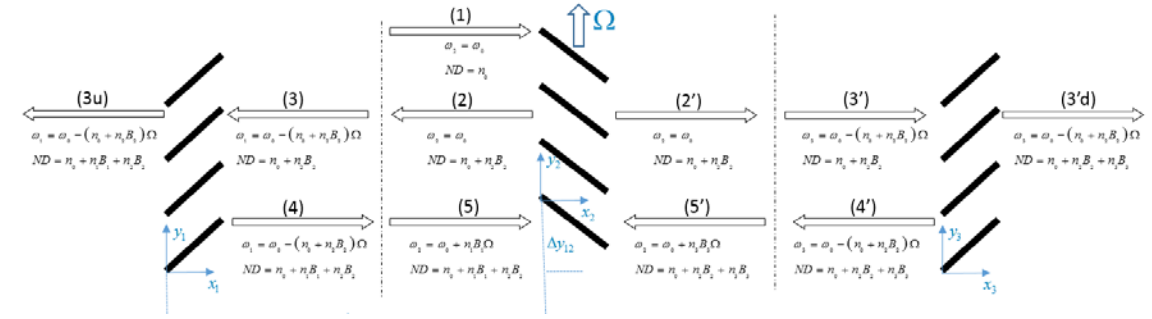

(a)

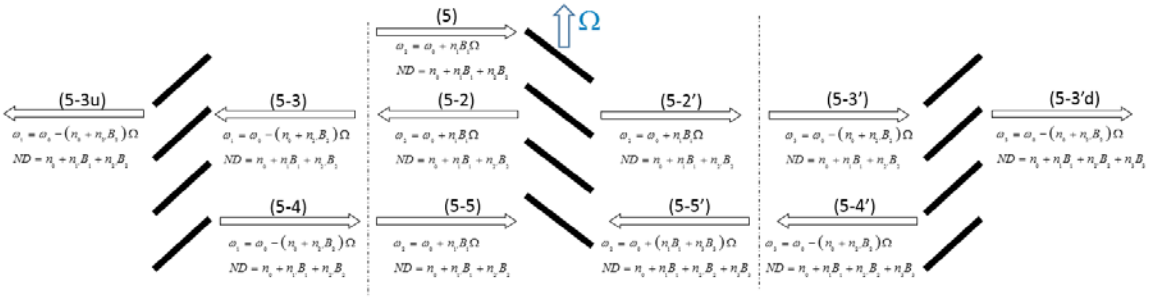

(b)

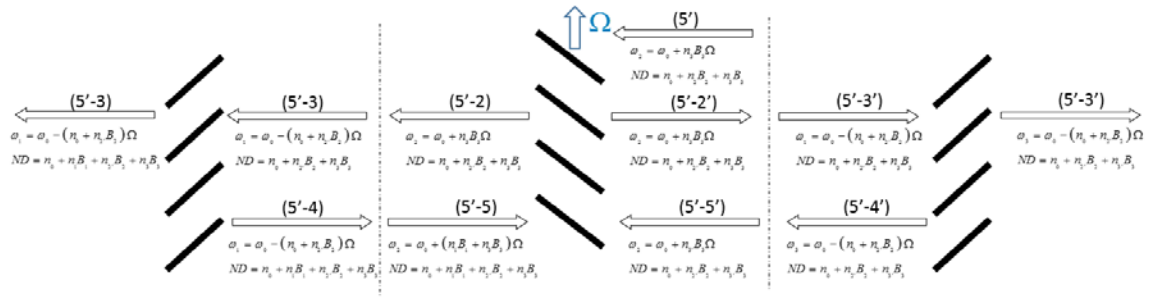

(c)

Figure 2.5. The multistage interaction physical process of stator 1 wake impinging on the rotor with scattering and frequency shifting effect. a) initial excitation by stator1 wake b) secondary excitation by the reflection waves from stator1 c) secondary excitation by the reflection waves from stator2.

The whole process will repeat again with the new excitations on the rotor, which are the upstream going pressure wave in step(5') and the downstream going pressure wave and vorticity wave in step(5) as illustrated in Figure 2.5(b) and Figure 2.5(c). Note the frequency and nodal diameter changes during the process. This is due the scattering effect of each blade row and the frequency shifting effect in different reference frames. Both the scattering effect and frequency shifting effect will be discussed in detail later. This process is repeated many times and eventually a steady state is achieved where the unsteady aerodynamics around each blade row is steady (i.e. the strength of each mode is no longer changing.)

The blade rows are coupled together by the unsteady waves in between. When an unsteady wave impinges on a blade row, it will be scattered into an infinite number of the unsteady waves with the same frequency but different tangential wave numbers. When an unsteady wave travels from one blade row to another, its frequency is shifted when viewed in the reference frame of the new blade row. Both scattering and frequency shifting are discussed in detail in the following sections.

2.5.1 Scattering

The scattering effect is rooted in the fact that the finite number of blades is discretely distributed in the circumferential direction while the coupling fluid in between is continuous. Consider an excitation with interblade phase angle and frequency (σ_0, ω_0) impinging on a blade row having B blades. The initial excitation can be both external excitations (upstream going pressure waves and downstream going pressure waves and vorticity waves) and internal excitations (blade vibrations). The unsteady upwash velocity due to the initial excitation on each blade is $\overline{v_u} e^{i(\omega_0 t + m\sigma_0)}$, where m is the m^{th} blade. In order to balance the unsteady upwash velocity caused by the excitation, bound vortices are generated on each blade. The set of discrete bound vortices can be represented by a series of cascade waves as discussed in Section 2.3. Each cascade wave contains upstream going pressure waves and downstream going pressure waves and vorticity waves. Since the boundary condition only needs to be met at the control points

of each blade, the outgoing waves have the same frequency ω_0 but an infinite set of interblade phase angles $\sigma_0 + n2\pi$. The additional integer multiple of 2π won't change the phase information at each blade location since $\exp(\sigma_0 + n2\pi) = \exp(\sigma_0)$. In other words, adding $n2\pi$ changes the phase information of continuous wave properties (e.g. unsteady pressure, unsteady velocity) between the blades, but doesn't change the phase information of the discrete properties (e.g. unsteady loading, upwash velocity etc.) on each blade . Thus the scattering on the blade row due to excitation with interblade phase angle and frequency (σ_0, ω_0) can be expressed as

$$\overline{v_u} e^{i(\omega_0 t + m\sigma_0)} \rightarrow \overline{q} e^{i(\omega_0 t + m(\sigma_0 + n2\pi))}$$

where $\overline{q}$ represents the three outgoing waves, n is an integer of any value, m is the m^{th} blade.

Nodal diameter ND is related to interblade phase angle σ by

$\sigma = \dfrac{ND2\pi}{B}$ where B is blade number in the blade row (2.92)

Assume the initial interblade phase angle σ_0 corresponds to nodal diameter n_0. After scattering, the outgoing waves have interblade phase angle $\sigma_0 + n2\pi$ which corresponds to nodal diameter $n_0 + nB$, where n can take any integer value. The initial excitation mode and its scattering modes have the same frequency ω_0 and an infinite set of nodal diameters $n_0 + nB$. They are considered a "scatter group".

The reverse of the process is also true. When the infinite set of modes in the same scatter group interact with a blade row, they can all generate a single output.

$$\overline{v_u} e^{i(\omega_0 t + m(\sigma_0 + n2\pi))} \rightarrow \overline{q} e^{i(\omega_0 t + m\sigma_0)}$$

2.5.2 Frequency Shifting

Frequency shifting, also known as the Doppler Effect, is rooted in the relative motion between each row. For example, one unsteady wave with frequency ω_0, axial wave number α and tangential wave number β in the first blade row can be expressed as

$$q(x_1, y_1, t) = \bar{q} e^{i(\omega_0 t + \alpha x_1 + \beta y_1)} \tag{2.93}$$

As shown in Figure 2.5(a), in the reference frame of second blade row, the first blade row coordinate becomes

$$x_1 = x_2 + \Delta x_{12} \ , \ y_1 = y_2 + \Delta y_{12} + R\Omega t \tag{2.94}$$

where Ω is the angular rotational speed of the second blade row. Substituting Equation (2.94) to Equation (2.93), the unsteady wave in the second blade row can be expressed as

$$q(x_2, y_2, t) = \bar{q} e^{i((\omega_0 + \beta R\Omega)t + \alpha(x_2 + \Delta x_{12}) + \beta(y_2 + \Delta y_{12}))} \tag{2.95}$$

Thus, the frequency of the unsteady wave has shifted from ω_0 to $\omega_0 + \beta R\Omega$ in the second blade row. The tangential wave number β is related to the nodal diameter ND as $\beta = \frac{ND}{R}$. Thus if the unsteady wave has nodal diameter n_0, the frequency of the unsteady wave in the second blade row has shifted from ω_0 to $\omega_0 + n_0\Omega$.

2.5.3 Spinning Mode

Based on the cascade wave discussion in the previous section, a single cascade wave is referred to as a spinning mode which is characterized by a unique set of (ω, ND). A detailed description of multistage interactions in terms of the spinning modes is given here in order to illustrate how the nodal diameter and frequency changes due to the scattering and frequency shifting effect in each blade row as shown in the Figure 2.5.

The initial excitation from the stator1 wake has frequency ω_0 and nodal diameter n_0 in the reference frame of the second blade row (Figure 2.5(a), step1). A constant radius R

is assumed when the 3D annular flow field has been 'unwrapped' into a 2D sheet, so $y = R\theta$. The initial excitation unsteady wave can be expressed in (x_2, θ_2) as

$$q(x_2, \theta_2, t) = \bar{q} e^{i(\omega_0 t + \alpha x_2 + n_0 \theta_2)} \tag{2.96}$$

It interacts with the second blade row and generates an infinite set of scattering modes with the same frequency ω_0 and but different scattered nodal diameter $n_0 + n_2 B_2$ where n_2 can be any integer. (Figure 2.5(a), step2 and step2'). Thus, after interacting with the second blade row , the initial excitation spinning mode (ω_0, n_0) becomes an infinite set of spinning modes $(\omega_0, n_0 + n_2 B_2)$. The upstream going pressure wave travels upstream towards the first blade row. When viewed in the reference frame of the first blade row, these spinning modes have the same nodal diameter $n_0 + n_2 B_2$. But due to the Doppler Effect, their frequency has shifted to $\omega_0 - (n_0 + n_2 B_2)\Omega$. (Figure 2.5(a), step3)

$$q(x_1, \theta_1, t) = \bar{q} e^{i\left[(\omega_0 - (n_0 + n_2 B_2)\Omega)t + \alpha(x_1 - \Delta x_{12}) + (n_0 + n_2 B_2)(\theta_1 - \Delta y_{12}/R)\right]} \tag{2.97}$$

When the upstream going pressure wave impinges on the first blade row, it is scattered to spinning mode $(\omega_0 - (n_0 + n_2 B_2)\Omega \ , \ n_0 + n_1 B_1 + n_2 B_2)$. After interaction, the outgoing waves are upstream going pressure waves (Figure 2.5(a), step 3u) and downstream going pressure waves and vorticity waves (Figure 2.5(a), step 4). When viewed in the reference frame of the second blade row, these spinning modes has the same nodal diameter $n_0 + n_1 B_1 + n_2 B_2$ but their frequency have shifted to $\omega_0 + n_1 B_1 \Omega$ (Figure 2.59(a), step5). These reflected waves from the first blade row become new excitation on the second blade row. Similarly, for the second blade row and third blade row interaction, the waves go through step 2', step 3', step4' and step5' and become the new excitation on the second blade row due to the reflection from the third blade row. With the reflected new excitation, the whole process repeats again as shown in Figure 2.5(b) and Figure 2.5(c).

After the steady state has been reached, the nodal diameter ND and frequency in each blade row are:

$$ND = n_0 + n_1 B_1 + n_2 B_2 + n_3 B_3 \tag{2.98}$$

$$\begin{aligned} \omega_1 &= \omega_3 = \omega_0 - \left(n_0 + n_2 B_2\right)\Omega \\ \omega_2 &= \omega_0 + \left(n_1 B_1 + n_3 B_3\right)\Omega \end{aligned} \tag{2.99}$$

where the scattering index in each blade row n_1 , n_2 and n_3 can be any integer.

In general, for a three blade row environment, each blade row has B_1, B_2 and B_3 blades, the angular rotational speed of the first and third blade row is Ω_1 and the angular rotational speed of the second blade row is Ω_2. If the initial excitation has frequency and nodal diameter $\left(\omega_0, n_0\right)$, the general formula for the nodal diameter *ND* in each blade row is the same

$$ND = n_0 + n_1 B_1 + n_2 B_2 + n_3 B_3 \tag{2.100}$$

If the initial excitation is in the first and third row, the general formula for frequency ω in each row is:

$$\begin{aligned} \omega_1 &= \omega_3 = \omega_0 + \left(n_2 B_2\right)\left(\Omega_1 - \Omega_2\right) \\ \omega_2 &= \omega_0 + \left(n_0 + n_1 B_1 + n_3 B_3\right)\left(\Omega_2 - \Omega_1\right) \end{aligned} \tag{2.101}$$

If the initial excitation is in the second row, the general formula for frequency ω in each row is:

$$\begin{aligned} \omega_1 &= \omega_3 = \omega_0 + \left(n_0 + n_2 B_2\right)\left(\Omega_1 - \Omega_2\right) \\ \omega_2 &= \omega_0 + \left(n_1 B_1 + n_3 B_3\right)\left(\Omega_2 - \Omega_1\right) \end{aligned} \tag{2.102}$$

Note that for a given initial excitation ω_0, n_0 and angular rotational speed Ω_1, Ω_2, the frequency and nodal diameter of each spinning mode in each blade row is specified by a set of scattering indices $\left(n_1, n_2, n_3\right)$

2.5.4 Governing Matrix

As derived in Section 2.2, for an isentropic process in a 2D inviscid compressible flow field under the small perturbation assumption, there are three unsteady waves upstream going pressure wave, downstream going pressure wave, and vorticity wave. In the multistage interaction analysis, each spinning mode contains all 3 unsteady waves. The objective of a multistage interaction analysis is to get the strength of all 3 unsteady waves for each spinning mode at every blade row after applying the initial excitation. With this information, the unsteady loading on each blade row and the strength of the outgoing pressure waves can be calculated for each spinning mode.

During the modelling, the multistage interaction problem can be divided into two basic domains: blade row and the inter-blade fluid region. Each domain can be modelled by a matrix mathematically. These matrices are then assembled into a system with correct non-reflection boundary conditions and specified input excitations. By solving the system, all the unsteady pressure and vorticity waves can be obtained.

The blade row domain is modeled as a transmission/reflection matrix. As shown in Figure 2.6, when incoming excitation waves reach a blade row they are reflected from and transmitted through the blade row. The airfoil row is represented by a matrix $[W]$ which contains nine reflection/transmission coefficients that relate the incoming pressure and vorticity waves to the outgoing pressure and vorticity waves. These reflection and transmission coefficients are calculated using the two dimensional linearized compressible flow flat plate cascade model LINSUB discussed in Section 2.3. Considering the scattering effect, the incoming waves $\left[P_R^+, P_L^-, \zeta_L\right]_r$ of mode r are reflected, transmitted and scattered into the outgoing waves $\left[P_L^+, P_R^-, \zeta_R\right]_q$ of mode q. As discussed before, an incoming unsteady wave of mode r with a single nodal diameter can be scattered into a series of outgoing unsteady waves of mode $q = -\infty \; to + \infty$ with different nodal diameters, and a series of incoming unsteady waves of mode $r = -\infty \; to + \infty$ with different nodal diameters can be combined into one outgoing

pressure wave of mode q with a single nodal diameter. Thus, the reflection, transmission and scattering at an airfoil row are modeled in the following system of equations,

$$\begin{bmatrix} P_L^+ \\ P_R^- \\ \zeta_R \end{bmatrix}_q = \sum_{r=-\infty}^{\infty} \begin{bmatrix} w_{11} & w_{12} & w_{13} \\ w_{21} & w_{22} & w_{23} \\ w_{31} & w_{32} & w_{33} \end{bmatrix}_{qr} \begin{bmatrix} P_R^+ \\ P_L^- \\ \zeta_L \end{bmatrix}_r + \begin{bmatrix} b_1 \\ b_2 \\ b_3 \end{bmatrix}_q \tag{2.103}$$

The vector $\begin{bmatrix} b_1 & b_2 & b_3 \end{bmatrix}$ are the additional outgoing waves $\begin{bmatrix} P_L^+ & P_R^- & \zeta_R \end{bmatrix}_q$ of mode q. This term is used to specify the initial excitation as the model input.

Figure 2.6. Schematic of the transmitted and reflected unsteady wave (red) generated by the impinging unsteady waves (blue) and blade row interaction.

In addition, the outgoing waves from a blade row travel upstream/downstream to excite the neighboring rows as shown in Figure 2.7. The two neighboring rows are coupled by the unsteady waves in-between the rows. Each inter-row region can be represented by a diagonal matrix of axial wave numbers α and tangential wave number β. The upstream going pressure wave axial wave number α_1, downstream going pressure wave axial wave number α_2 and downstream going vorticity wave axial wave number α_3 are functions of excitation frequency, tangential wave number and steady flow properties. Thus, the axial wave number is different from mode to mode. But the axial wave numbers stay the same regardless of the blade row reference frame. The exact expressions of these axial wave numbers are derived in Section 2.2.1. The axial and tangential offsets between two rows are denoted by Δx and Δy. The wave transmission in the inter-row space for a single spinning mode q is modeled by the following equation systems,

$$\begin{bmatrix} P_{L,2}^{+} \\ P_{L,2}^{-} \\ \zeta_{L,2} \end{bmatrix}_q = \begin{bmatrix} e^{i(\alpha_{1,q}\Delta x+\beta_q\Delta y)} & 0 & 0 \\ 0 & e^{i(\alpha_{2,q}\Delta x+\beta_q\Delta y)} & 0 \\ 0 & 0 & e^{i(\alpha_{3,q}\Delta x+\beta_q\Delta y)} \end{bmatrix} \begin{bmatrix} P_{R,1}^{+} \\ P_{R,1}^{-} \\ \zeta_{R,1} \end{bmatrix}_q \tag{2.104}$$

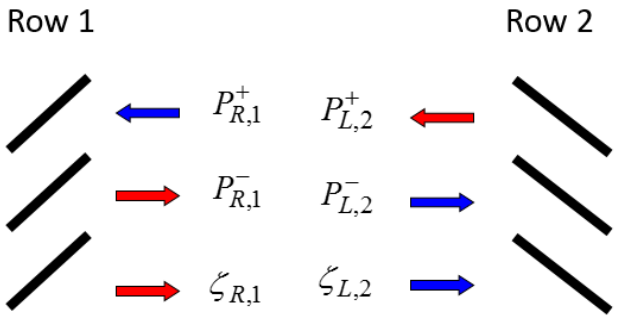

Figure 2.7. Schematic of unsteady waves travels between two neighboring blade rows.

Finally, non-reflective boundaries at the first blade row inlet and at the last blade row outlet are assumed. In this way, the whole system is represented by a large matrix which contains the reflection/transmission matrix for each row, transmission matrix for each inter row spacing and boundary conditions. By solving the system, all the strengths of the unsteady pressure and vorticity waves for each spinning mode at each blade row can be calculated. The effect of spinning modes with the same frequency need to be added together to get the total unsteady loading on the blade row at the specific frequency.

2.6 Rotor Blade Optimization Based on Lifting Line Theory

The foundation of the Lifting line theory for propeller blade optimization has been well studied and documented. At normal operating conditions, the air flow through a wind turbine is incompressible. It is very similar to marine propellers except cavitation of no concern. Most of the Lifting line theory part in this study follows the extensive marine propeller design research work of Kerwin [27] and later the work of Epps [28].

2.6.1 Flow Field and Lifting Line Theory

A rotor (propeller or turbine) generally operates in a very complicated flow field due to the interaction between the rotor and the surrounding flow. This interaction generates a lot of vorticity and turbulence in flow. To simplify the problem, it is traditionally assumed that the total velocity field around the rotor is a linear superposition of the inflow velocity in the absence of the rotor, and the induced velocity caused by the rotor.

Similar to the airplane wing, the rotor blades can be modelled using the Lifting line method to predict the forces on the rotor. Taking the marine propeller as an example, Figure 2.8 shows that a propeller blade can be represented by a lifting line with a radial distribution of the bound circulation Γ and the free shedding vortex sheet γ. Note that most of wind turbine blades have a much higher aspect ratio than the marine propeller blade, and thus are better suited for the Lifting line model. Assuming the free shedding vortex sheets are convected at a constant radius, the strength of the free shedding vortex γ and bound circulation Γ are related by,

$$\gamma(r) = -\frac{d\Gamma}{dr} \tag{2.105}$$

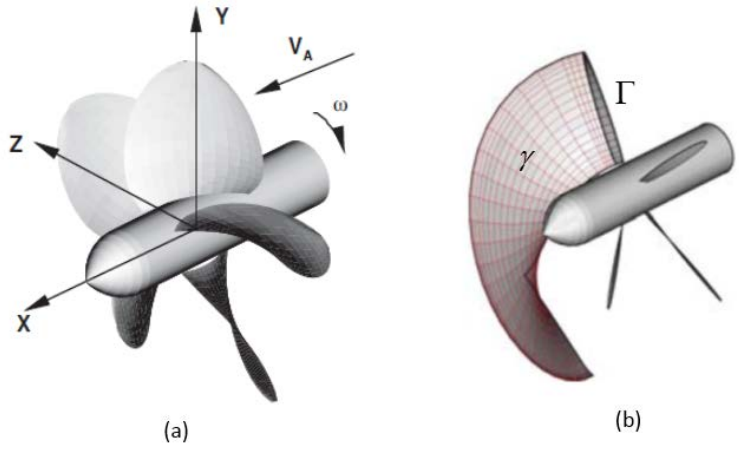

Figure 2.8 Lifting line representation of a propeller blade [27].

At a particular propeller blade section, the velocity and force diagram is shown in Figure 2.9. V_a and V_t are the axial and tangential inflow velocities. u_a^* and u_t^* are the axial and tangential induced velocities. ω is the angular rotation velocity. V^* and V_0 are the total velocity and total velocity without induced velocity. β_i and β are the total flow angle and total flow angle without induced velocities. $\beta_i - \beta$ is analogous to the induced angle in the wing Lifting Line theory. e_a and e_t are the propeller moving directions. The opposite directions of e_a and e_t are chosen as the positive velocity directions.

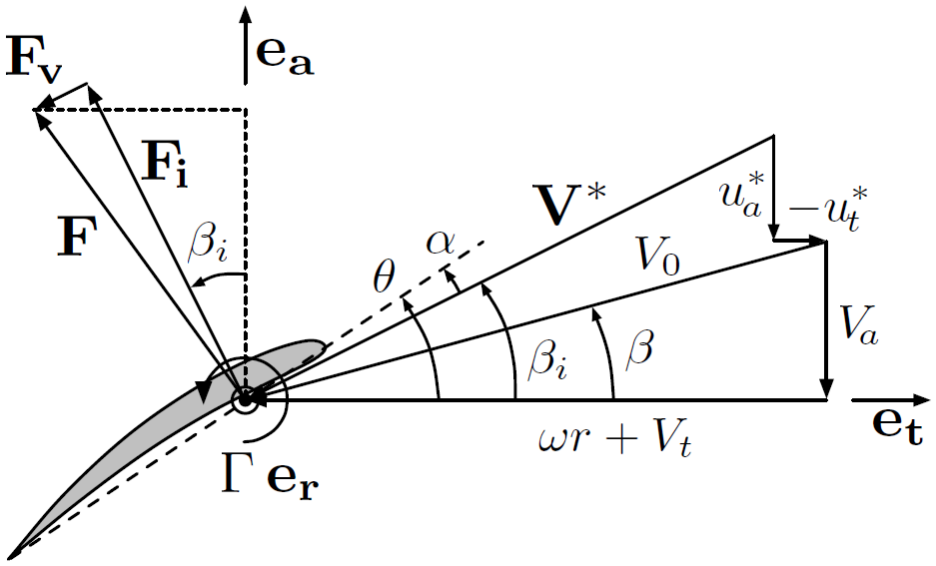

Figure 2.9. Velocity and force diagram at a particular propeller blade section [28].

F_i, F_v and F are the inviscid lifting force, viscous drag force and total force, respectively. The inviscid lifting force F_i can be calculated using the Kutta-Joukowski theorem.

$$F_i = \rho V^* \Gamma \tag{2.106}$$

The viscous drag F_v can be calculated based on the blade section chord length c and the 2D sectional drag coefficient C_D

$$F_v = \frac{1}{2}\rho\left(V^*\right)^2 C_D c \tag{2.107}$$

Integrating over the blade span and summing the effect of all blades, the total thrust T and torque Q are

$$T = Z\int_{r_h}^{R}\left[F_i\cos\beta_i - F_v\sin\beta_i\right]dr \tag{2.108}$$

$$Q = Z\int_{r_h}^{R}\left[F_i\sin\beta_i + F_v\cos\beta_i\right]rdr \tag{2.109}$$

where Z is the number of blades, r_h and R are the hub and tip radius of the blades. The power required by the propeller P is

$$P = Q\omega \tag{2.110}$$

The useful power produced by propeller is TV_f, where V_f is the propeller moving velocity or the free stream velocity in the rotor reference frame. The efficiency of a propeller η is defined as the ratio of the useful power produced by the propeller and the power required to drive the propeller.

$$\eta = \frac{TV_f}{Q\omega} \tag{2.111}$$

Physically, a propeller absorbs power from an engine and accelerates the flow to generate thrust. A horizontal-axis turbine works in the opposite way by decelerating the flow and absorbing power from the flow to generate power. In the Lifting-line model, a horizontal-axis turbine is equivalent to a propeller with a negative bound circulation. The corresponding induced velocities, thrust, torque and power are also the negative of the propeller values. The velocity and force diagram at a particular turbine blade section is shown in Figure 2.10. Note that for both propeller and turbine, the induced velocities reduce the angle of attack and thus undermine the blade sectional performance.

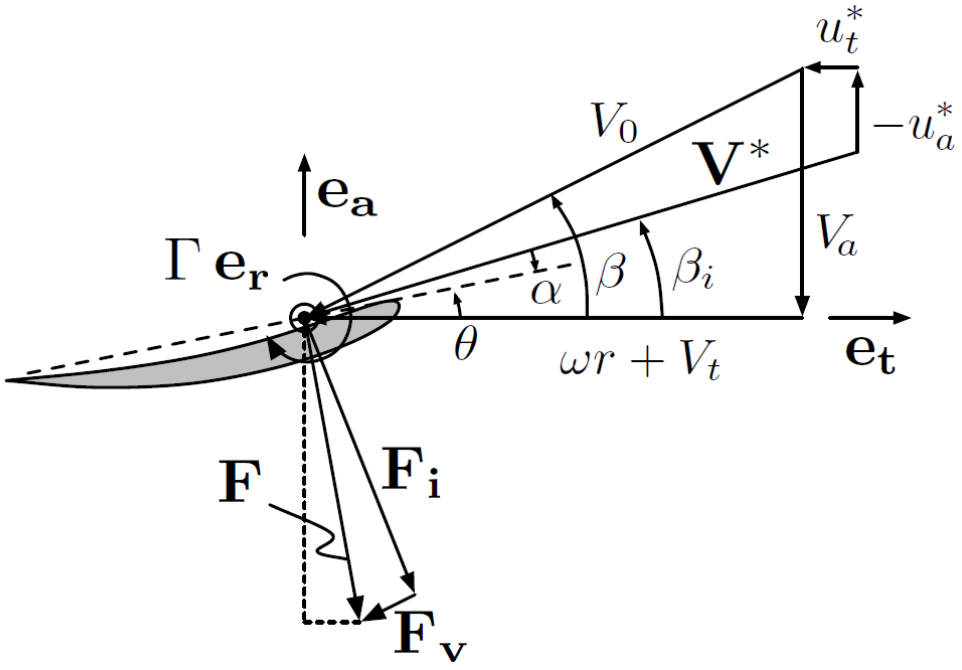

Figure 2.10. Velocity and force diagram at a particular blade section of a turbine [28].

For both propeller (Figure 2.9) and turbine (Figure 2.10), the total velocity V^* and the total flow angle β_i can written as,

$$V^* = \sqrt{\left(V_a + u_a^*\right)^2 + \left(\omega r + V_t + u_t^*\right)^2} \tag{2.112}$$

$$\beta_i = \tan^{-1}\left[\frac{V_a + u_a^*}{\omega r + V_t + u_t^*}\right] \tag{2.113}$$

Nondimensionalized by the free flow velocity in the rotor reference frame V_f, the thrust coefficient C_T, torque coefficient C_Q and power coefficient C_P are defined as,

$$C_T = \frac{T}{\frac{1}{2}\rho {V_f}^2 \left(\pi R^2\right)} \tag{2.114}$$

$$C_Q = \frac{Q}{\frac{1}{2}\rho {V_f}^2 \left(\pi R^3\right)} \tag{2.115}$$

$$C_P = \frac{Q\omega}{\frac{1}{2}\rho {V_f}^3 \left(\pi R^2\right)} = \frac{C_Q \pi}{J} = C_Q \lambda \tag{2.116}$$

where J and λ are two important nondimensionalized quantities that describe the rotation speed and the free flow velocity ratio. The advance coefficient J commonly used in propeller literature is defined as

$$J = \frac{V_f}{2Rn} \tag{2.117}$$

where n is the rotation speed in rev per second, and $n = \frac{\omega}{2\pi}$

The tip speed ratio λ commonly used in wind turbine literature is defined as

$$\lambda = \frac{\omega R}{V_f} \tag{2.118}$$

2.6.2 Induced Velocity by Helical Vortices

In the Lifting line model, the rotor blades are represented by lifting lines with bound circulation and the shed vortex wake. For straight radial lifting lines, the bound circulation doesn't induce any velocity along the same lifting line. For a rotor with uniform blade to blade angular spacing, the induced velocity on one lifting line caused by the bound circulations on the other lifting lines are cancelled because of symmetry. Thus the total induced velocities by bound circulation Γ is zero. The induced velocities are caused by the shedding vortex γ only. The induced velocities at r_c can be expressed as

$$u_a^*(r_c) = \int_{r_h}^{R} \gamma(r_v)\,\bar{u}_a(r_c, r_v)\,dr_v \tag{2.119}$$

$$u_t^*(r_c) = \int_{r_h}^{R} \gamma(r_v)\,\bar{u}_t(r_c, r_v)\,dr_v \tag{2.120}$$

where the influence functions $\bar{u}_a(r_c, r_v)$ and $\bar{u}_t(r_c, r_v)$ are defined as the axial and tangential induced velocities at r_c caused by a unit-strength constant-radius constant-pitch helical vortex wake which is shed from r_v. In general, $\bar{u}_a(r_c, r_v)$ and $\bar{u}_t(r_c, r_v)$ can be calculated numerically with some effort using the Biot-Savart law. Fortunately, for a constant-radius constant-pitch helical vortex wake with pitch angle β_w, a closed form highly accurate analytical approximation was developed by Wrench [36].

For $r_c < r_v$:

$$\bar{u}_a\left(r_c, r_v\right) = \frac{Z}{4\pi r_c}\left(y - 2Zyy_0F_1\right) \tag{2.121}$$

$$\bar{u}_t\left(r_c, r_v\right) = \frac{Z^2}{2\pi r_c} y_0F_1 \tag{2.122}$$

For $r_c > r_v$:

$$\bar{u}_a\left(r_c, r_v\right) = -\frac{Z^2}{2\pi r_c} yy_0F_2 \tag{2.123}$$

$$\bar{u}_t\left(r_c, r_v\right) = \frac{Z}{4\pi r_c}\left(1 + 2Zy_0F_2\right) \tag{2.124}$$

Where

$$F_1 \approx \frac{-1}{2Zy_0}\left(\frac{1+{y_0}^2}{1+y^2}\right)^{0.25}\left\{\frac{U}{1-U} + \frac{1}{24Z}\left[\frac{9{y_0}^2+2}{\left(1+{y_0}^2\right)^{1.5}} + \frac{3y^2-2}{\left(1+y^2\right)^{1.5}}\right]\ln\left|1+\frac{U}{1-U}\right|\right\}$$

$$F_2 \approx \frac{1}{2Zy_0}\left(\frac{1+{y_0}^2}{1+y^2}\right)^{0.25}\left\{\frac{1}{U-1} - \frac{1}{24Z}\left[\frac{9{y_0}^2+2}{\left(1+{y_0}^2\right)^{1.5}} + \frac{3y^2-2}{\left(1+y^2\right)^{1.5}}\right]\ln\left|1+\frac{1}{U-1}\right|\right\}$$

$$U = \left\{\frac{y_0\left(\sqrt{1+y^2}-1\right)}{y\left(\sqrt{1+{y_0}^2}-1\right)}\exp\left(\sqrt{1+y^2}-\sqrt{1+{y_0}^2}\right)\right\}^Z$$

$$y = \frac{r_c}{r_v \tan\beta_w}$$

$$y_0 = \frac{1}{\tan\beta_w}$$

In the limit of an infinite number of blades which resembles the actuator disk case, the influence functions are reduced to

For $r_c < r_v$:

$$\bar{u}_a\left(r_c, r_v\right) = \frac{Z}{4\pi r_v \tan\beta_w} \tag{2.125}$$

$$\bar{u}_t\left(r_c, r_v\right) = 0 \tag{2.126}$$

For $r_c > r_v$:

$$\bar{u}_a\left(r_c, r_v\right) = 0 \tag{2.127}$$

$$\bar{u}_t\left(r_c, r_v\right) = \frac{Z}{4\pi r_c} \tag{2.128}$$

Note that the equations for influence functions $\bar{u}_a\left(r_c, r_v\right)$ and $\bar{u}_t\left(r_c, r_v\right)$ in Kerwin's paper [27] contain three typos. The current equations are checked with Kerwin's PVL codes [37] and Epps's OpenProp codes [38].

2.6.3 Blade Discretization

For numerical calculation using the Lifting Line model, each blade is discretized into M panels extending from blade hub r_h to the blade tip R. Each panel can be modelled as a horseshoe element consisting of a bound circulation of strength Γ and two free shedding vortex filament of strength $\pm\Gamma$. The bound circulation of the m^{th} panel Γ(m) is placed at the control point r_c(m), the two free shedding vortex filament of strength Γ(m) and $-\Gamma$(m) are shed from the vortex point r_v(m+1) and r_v(m), respectively

Since the induced velocities are caused by the free shedding vortex only, the induced velocities at the control point of the n^{th} panel can be calculated using the discretized version of Equations (2.119) and (2.120).

$$u_a^*\left(r_c(n)\right) = \sum_{m=1}^{M} \Gamma\left(m\right) \cdot \bar{u}_a^*\left(n, m\right) \tag{2.129}$$

$$u_t^*\left(r_c(n)\right) = \sum_{m=1}^{M} \Gamma\left(m\right) \cdot \bar{u}_t^*\left(n, m\right) \tag{2.130}$$

where $\bar{u}_a^*$ and $\bar{u}_t^*$ are the horseshoe influence functions

$$\bar{u}_a^*\left(n, m\right) = \bar{u}_a\left(r_c\left(n\right), r_v\left(m+1\right)\right) - \bar{u}_a\left(r_c\left(n\right), r_v\left(m\right)\right) \tag{2.131}$$

$$\bar{u}_t^*\left(n, m\right) = \bar{u}_t\left(r_c\left(n\right), r_v\left(m+1\right)\right) - \bar{u}_t\left(r_c\left(n\right), r_v\left(m\right)\right) \tag{2.132}$$

As shown in Equation (2.121) to Equation (2.128) the influence functions $\bar{u}_a$ and $\bar{u}_t$ are functions of helical wake pitch angle β_w. Under a moderately loaded rotor assumption, the helical wake pitch is aligned with the total velocity at the blade, i.e. the helical wake pitch angle β_w is equal to the total flow angle β_i. Using Epps's wake model [28], each horseshoe element panel is assumed to form a single piece of helical wake with constant pitch and constant radius, although helical wakes from different panels may have different helical pitches. On the m^{th} panel, the helical pitch is $r_c(m)\tan\beta_i(m)$ at the control point. The tangent of the helical wake pitch angle $\tan\beta_w$ is equal to $\frac{r_c(m)\tan\beta_i(m)}{r_v(m)}$ at vortex point $r_v(m)$ and equal to $\frac{r_c(m)\tan\beta_i(m)}{r_v(m+1)}$ at vortex point $r_v(m+1)$ as shown in Figure 2.11.

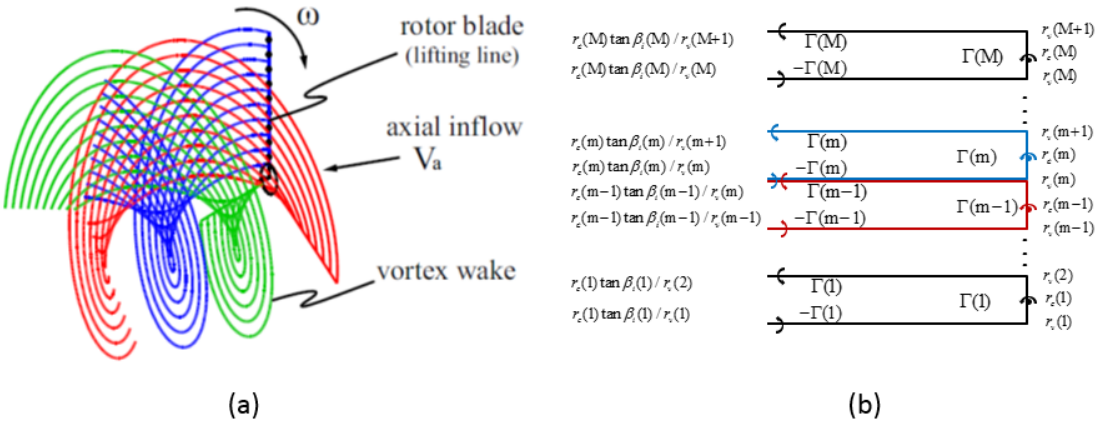

Figure 2.11. Discretized lifting line model of rotor (a) and the detailed wake model (b) [28].

To increase computational efficiency, cosine spacing is used for placing the vortex and control points. The radius of the lower vortex point of the m^{th} panel $r_v(m)$ and radius of the control point of n^{th} panel $r_c(n)$ are

$$r_v(m) = r_h + h\left[1-\cos\left(2(m-1)\delta\right)\right] \tag{2.133}$$

$$r_c(n) = r_h + h\left[1-\cos\left(2(n-1)\delta\right)\right] \tag{2.134}$$

where $h = \frac{R-r_h}{2}$ and $\delta = \frac{\pi}{2M}$

2.6.4 Hub Model

In addtion to the rotor blade, the rotor hub can also be modelled in the Lifting line framework. The hub is treated as an infinitely long cylindar. Under the same potential flow assumption in the Lifting line theory, the flow field around the hub can be calculated using the method of image vortex. To satisfy the boundary condition that the total normal velocity on the hub surface is zero, an image vortex with opposite strength is placed within the hub circle at raidus r_i on the same radial line of the real vortex. For a rotor with hub radius r_h, the image vortex of the real vortex at radius r is placed at

$$r_i = \frac{r_h^{\,2}}{r} \tag{2.135}$$

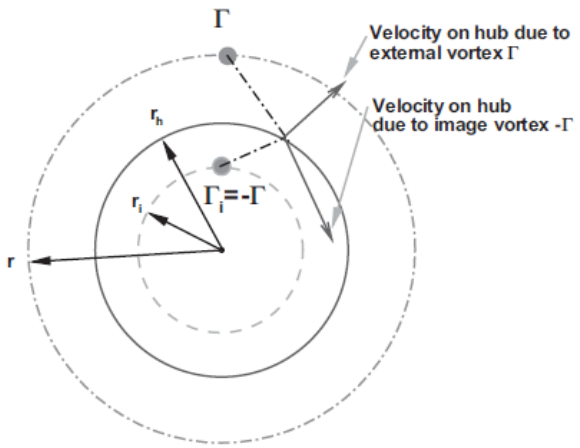

Figure 2.12. Schematic of the hub image vortex [27].

Thus, the induced velocity caused by the hub image vortex at control point of n^{th} panel $r_c(n)$ are

$$u^*_{a\_hub}\left(r_c(n)\right)=\sum_{m=1}^{M}\Gamma(m)\cdot\bar{u}_{a\_hub}{}^*(n,m) \tag{2.136}$$

$$u^*_{t\_hub}\left(r_c(n)\right)=\sum_{m=1}^{M}\Gamma(m)\cdot\bar{u}_{t\_hub}{}^*(n,m) \tag{2.137}$$

where $\bar{u}^*_{a\_hub}$ and $\bar{u}^*_{t\_hub}$ are the corresponding hub horseshoe influence functions

$$\bar{u}^*_{a\_hub}(n,m)=\bar{u}_a\left(r_c(n),\frac{r_h{}^2}{r_v(m)}\right)-\bar{u}_a\left(r_c(n),\frac{r_h{}^2}{r_v(m+1)}\right) \tag{2.138}$$

$$\bar{u}^*_{t\_hub}(n,m)=\bar{u}_a\left(r_c(n),\frac{r_h{}^2}{r_v(m)}\right)-\bar{u}_a\left(r_c(n),\frac{r_h{}^2}{r_v(m+1)}\right) \tag{2.139}$$

And $\tan\beta_w$ for the hub image vortex of the two free shedding vortices at the m^{th} panel are equal to $\frac{r_c(m)\tan\beta_i(m)}{r_h{}^2/r_v(m)}$ and $\frac{r_c(m)\tan\beta_i(m)}{r_h{}^2/r_v(m+1)}$. The total induced velocities at the control point of the n^{th} panel $r_c(n)$ are the sum of the effect of the real vortex calculated in Equations (2.129), (2.130) and the effect of the hub image vortex calculated in Equations (2.136), (2.137).

Besides causing additional induced velocities, the hub vortex can also cause additional drag due to the low pressure region created when the concentrated hub vortex sheds into the flow. Using the classical Rankine vortex model, it can be shown that the drag force F_{hub} is approximately

$$F_{hub}=\frac{\rho}{16\pi}\left(\ln\frac{r_h}{r_0}+3\right)\left(Z\Gamma_0\right)^2 \tag{2.140}$$

where r_0 is the hub vortex core radius and Γ_0 is the bound vorticity at the hub surface [39]

2.6.5 Optimum Circulation Distribution for a Propeller

For a specific inflow condition, blade number and rotor diameter, an optimum propeller is the one that delivers the desired thrust while requires minimum torque from the engine. To design an optimum propeller is to find the optimum loading (i.e. bound circulation) distribution such that the thrust coefficient C_T is equal to the desired value while the torque coefficient C_Q is minimized.

2.6.5.1 PVL Method

This constrained optimization problem was first solved by Betz [23] for uniform inflow and later extended by Lerbs [31] to allow for non-uniform inflow. Their approach is based on a physical variational principle that if the propeller is truly optimum, the incremental efficiency $\eta^* = \dfrac{\delta T V_f}{\delta Q \omega}$ associated with an increment loading $\delta\Gamma$ anywhere along the blade stays the same. This physical based statement about the optimum propeller has been validated mathematically using calculus of variations [40]. Assuming there is no tangential inflow velocity, by applying Munk's theorem to the far downstream, the incremental trust δT and incremental torque δQ due to an incremental loading $\delta\Gamma(r)$ are :

$$\delta T = \rho\left[\omega r + 2u_t^*(r)\right]\delta\Gamma(r) \tag{2.141}$$

$$\delta Q = \rho\left[V_a(r) + 2u_a^*(r)\right]\delta\Gamma(r)\, r \tag{2.142}$$

For an optimum propeller, the incremental efficiency η^* is a constant

$$\eta^* = \frac{\delta T V_f}{\delta Q \omega} = \frac{\omega r + 2u_t^*}{V_a + 2u_a^*}\cdot\frac{V_f}{\omega r} = \text{constant} \tag{2.143}$$

Assume the induced velocities $u_a^*(r) \ll V_a(r)$ and $u_t^*(r) \ll \omega r$,

$$\eta^* \approx \frac{\omega r + 2u_t^* + \left(u_t^*\right)^2/(\omega r)}{V_a + 2u_a^* + \left(u_a^*\right)^2/V_a}\cdot\frac{V_f}{\omega r} = \left[\frac{\omega r + u_t^*}{V_a + u_a^*}\right]^2\left[\frac{V_a}{\omega r}\right]^2\cdot\frac{V_f}{V_a} = \frac{\tan^2\beta(r)}{\tan^2\beta_i(r)}\cdot\frac{V_f}{V_a(r)} = \text{constant}$$

Thus, $\frac{\tan\beta(r)}{\tan\beta_i(r)} = \text{constant}\sqrt{\frac{V_a(r)}{V_f}}$ (2.144)

Equation (2.144) is the 'Lerbs Criterion' [31] for the optimum propeller. If the axial inflow velocity is uniform and equal to the free flow velocity in the propeller reference frame i.e. $V_a(r) = V_f$, the 'Lerbs Criterion' reduces to the well-known 'Betz condition' for the optimum propeller.

$$\frac{\tan\beta(r)}{\tan\beta_i(r)} = \text{constant} \quad (2.145)$$

Assuming there is no tangential inflow velocity, $\tan\beta(r) = \frac{V_a}{\omega r}$. 'Betz condition' [23] can be rewritten as

$\frac{V_a/\omega r}{\tan\beta_i} = \text{constant}$. For an uniform inflow velocity V_a and fixed rotational speed ω,

$$\tan\beta_i r = \text{constant} \quad (2.146)$$

The helical vortex wake has a pitch of $\tan\beta_w r$. Under a moderately loaded rotor assumption, the helical wake pitch angle β_w is equal to β_i. Thus the 'Betz condition' indicates that an optimum propeller forms a constant pitch helical wake. It can be shown that the total induced velocity caused by a constant pitch helical wake is perpendicular to the total velocity V^* [27].

The vortex lattice lifting line method code PVL developed by Kerwin [27, 37] is based on 'Lerbs Criterion' to find the optimum blade loading. The constant in the Lerbs criterion Equation (2.144) is a function of the desired thrust coefficient. If the constant is known, $\tan\beta_i(r)$ can calculated based on $\tan\beta(r)$ by Equation (2.144).

From the velocity diagram (Figure 2.9), assuming there is no tangential inflow velocity $V_t = 0$

$$\tan\beta_i = \frac{V_a + u_a^*}{\omega r + u_t^*} \quad (2.147)$$

Through some algebraic manipulation, it can be rewritten as

$$u_a^* - u_t^* \tan\beta_i = V_a\left(\frac{\tan\beta_i}{\tan\beta} - 1\right) \tag{2.148}$$

In the discrete form,

$$\sum_{m=1}^{M}\left[\bar{u}_a^*(n,m) - \bar{u}_t^*(n,m)\tan\beta_i(n)\right]\Gamma(m) = V_a(n)\left(\frac{\tan\beta_i(n)}{\tan\beta(n)} - 1\right) \quad n = 1,\ldots M \tag{2.149}$$

Using Equation (2.149), the bound circulation distribution $\Gamma(r)$ can be calculated based on $\tan\beta_i(r)$. After knowing $\Gamma(r)$, the thrust coefficient C_T is calculated using Equations (2.108) and (2.114). The calculated C_T is then compared with the desired C_T. The constant in Lerbs criterion is updated iteratively until the calculated C_T matches the desired C_T. The corresponding $\Gamma(r)$ is the optimum bound circulation distribution.

2.6.5.2 Lagrange Multiplier Method

Besides the classical Lerbs criterion, the optimum propeller blade loading distribution can also be found by using the Lagrange Multiplier method. Coney [41] implemented the Lagrange Multiplier method and developed the code PLL which later became the industry standard for preliminary marine propeller design. Epps [28] improved the code and rewrote it in Matlab that is available to the public as an open source code Openprop [38].

The Lagrange Multiplier method is a well-known constrained optimization method. In order to minimize the Torque Q under the constrain that the thrust is equal to the specified value $T = T_s$, the Lagrange function H with Lagrange multiplier λ_1 is defined as

$$H = Q + \lambda_1(T - T_s) \tag{2.150}$$

Both torque Q and thrust T are integral functions of the bound circulation $\Gamma(r)$. After discretizing the blade into M panels, the Lagrange function H is a function of $M+1$ variables, i.e. $\Gamma(1)$ to $\Gamma(M)$ and λ_1. The optimized result with constraint is achieved when

$$\frac{\partial H}{\partial \lambda_1} = 0,\ \frac{\partial H}{\partial \Gamma(i)} = 0 \qquad i = 1, 2, \cdots M \tag{2.151}$$

This is a non-linear equation system with M+1 equations and M+1 variables, which can be solved interactively. Both Torque Q and thrust T are functions of the induced velocity u_a^* and u_t^* which in turn depends on $\Gamma(r)$. In the Epps' Lagrange Multiplier method implementation, based on Equations (2.129) and (2.130), it is assumed that

$$\frac{\partial u_a^*}{\partial \Gamma(i)} = \bar{u}_a^*(m,i) \tag{2.152}$$

$$\frac{\partial u_t^*}{\partial \Gamma(i)} = \bar{u}_t^*(m,i) \tag{2.153}$$

However, this is only an approximation since both $\bar{u}_a^*(m,i)$ and $\bar{u}_t^*(m,i)$ are functions of $\tan\beta_w(i)$ which in turn is a function of $\Gamma(i)$.

2.6.5.3 Interior Point Method

The Interior Point methods is known for solving linear and nonlinear convex optimization problems with constraints. It is more flexible and robust than the classical Lagrange multiplier method. The typical procedure of implementing the Interior Point method is: 1) reduce the equality and inequality constraints into standard form by introducing slack variables; 2) replace the inequality constraints with logarithmic barrier terms in the objective function; 3) incorporate the equality constraints into the objective function using Lagrange multipliers; 4) apply Newton's method to compute search directions; and 5) Solve the system iteratively.

Instead of writing the Interior Point algorithm from scratch, a Matlab internal function fmincon is used. fmincon provides a collection of four different optimization algorithms (including Interior-point, Trust-region-reflective, SQP and Active-set method) in order to solve the general constrained nonlinear optimization problem in the format of

$$\text{Find } \min_x f(x) \text{ such that } \begin{cases} c(x) \le 0 \\ c_{eq}(x) = 0 \\ A \cdot x \le b \\ A_{eq} \cdot x = beq \\ lb \le x \le ub \end{cases}$$

where nonlinear functions $c(x)$ and $c_{eq}(x)$ are used for setting nonlinear constraints, matrices A and A_{eq} are used for setting linear constrains. And lb and ub are the upper and lower bound of the optimization variable x .

fmincon with the Interior Point method is used in this study for both propeller optimization and horizontal-axis turbine optimization which will be discussed later. The same as the Lagrange multiplier methods, the rotor blade is first discretized into M panels. However, instead of using bound circulation $\Gamma(i)$, $\tan\beta_i(i)$ is used as the optimization variable. This is because $\tan\beta_i$ is closely related to $\tan\beta$ and thus it is much easier to specify a reasonable initial guess, and lower and upper bound.

For propeller optimization, the initial guess of $\tan\beta_i$ is set to be $\tan\beta / \eta_{ac}$. η_{ac} is the propeller efficiency estimated using Actuator Disk theory [27] and it is equal to

$$\eta_{ac} = \frac{V_A}{V_A + u_a^*} = \frac{2}{1+\sqrt{1+C_T}} \tag{2.154}$$

The lower bound of $\tan\beta_i$ is set to $\tan\beta$ since the induced velocity always increases the angle of attack (Figure 2.9). The upper bound of $\tan\beta_i$ is set to be $5\tan\beta$ which is equivalent to an efficiency of 0.2 estimated using actuator disk theory. Most of the propeller operates far above this efficiency. However, if extra features are included (e.g. hub model), the lower bound may need to be decreased to ensure the interior point method is able to converge to the optimized value.

The objective function is C_Q and the equality constraint is C_T . During each iteration, the circulation distribution $\Gamma(i)$ is first calculated based on the value of $\tan\beta_i(i)$ by solving Equation (2.149). The C_Q and C_T are calculated based on the circulation distribution $\Gamma(i)$ using the discrete form of Equations (2.108) and (2.109).

2.6.6 Optimum Circulation Distribution for Horizontal-axis Turbine

Compared to a propeller, an optimum horizontal-axis turbine is the one, which generates maximum torque with no requirement on the thrust. To design an optimum turbine is to find the optimum loading (i.e. bound circulation) distribution such that the magnitude of torque coefficient C_Q is maximized. As discussed previously, a horizontal-axis turbine is the same as a propeller in the Lifting line frame work except that the bound circulation and thus the corresponding induced velocities, thrust, torque, power, and thrust, torque, power coefficients are all negative using the sign convention for propellers. Thus to maximize the magnitude of C_Q is to minimize the value of C_Q since C_Q is negative for a turbine.

2.6.6.1 Actuator Disk Models

The simplest model of a horizontal-axis turbine is an actuator disk. As shown in Figure 2.13, the actuator disk slows the flow from the far upstream axial velocity V_1 to the far down stream axial velocity V_3. The decrease of the kinetic energy is considered to be extracted by the turbine.

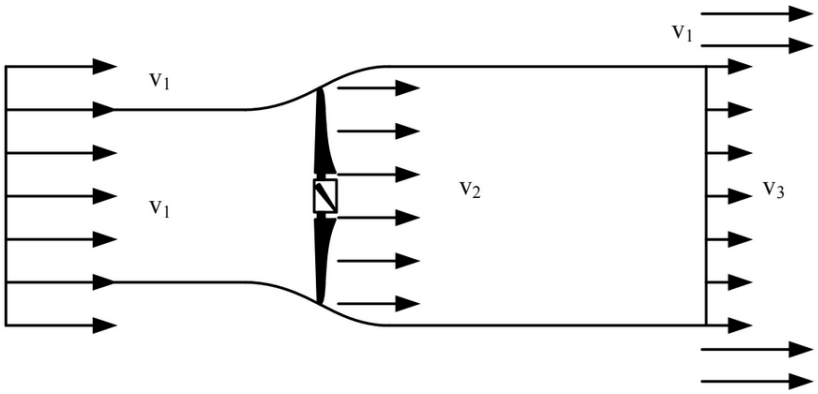

Figure 2.13. 1D Actuator Disc model for horizontal-axis turbine [42].

Betz [22] showed that when the velocity at the actuator disk V_2 is equal to $\frac{2}{3}V_1$ (which is equivalent to $u_a^* = -\frac{1}{3}V_a$ in Figure 2.10), maximum power is extracted. The

maximum $C_P = \frac{16}{27}$ is known as the Betz Limit, and the corresponding thrust coefficient is $C_T = \frac{8}{9}$. The Betz limit is the maximum theoretical power coefficient that can be achieved. In practice, there are three major losses that lead to a lower power coefficient than the Betz limit. They are 1) the loss due to wake rotation 2) tip losses associated with a finite number of blade and 3) the loss due to viscous drag.

The loss due to wake rotation can be modelled using a rotating actuator disk. Schmitz [30] considered this wake rotation and showed that when the total flow angle at the rotor plane is equal to 2/3 of the flow angle far upstream of the rotor plane (i.e. $\beta_i = \frac{2}{3}\beta$ in Figure 2.10), the output power is maximized. The maximum power coefficient can be calculated as

$$C_P = \int_0^1 4\lambda \left(\frac{r}{R}\right)^2 \frac{\sin^3\left(\frac{2}{3}\beta\right)}{\sin^2(\beta)} d\left(\frac{r}{R}\right) \qquad (2.155)$$

Betz's actuator disk model of the horizontal-axis turbine is an asymptotic analysis for a turbine with an infinite number of blades and infinite tip speed ratio. Schmitz's rotating actuator disk model of the horizontal-axis turbine is an asymptotic analysis for a turbine with an infinite number of blades but a finite tip speed ratio.

The Lifting line method is a much more realistic model than the actuator models. Both wake rotation and tip loss are automatically included in the formulation. The viscous drag force can be accounted for easily by using Equation (2.107). Unfortunately, the current wind turbine preliminary design still relies on the Blade Element Momentum (BEM) method that uses a rotating actuator disk model for the flow field analysis and blade element theory for the blade loading calculation. Blade element theory assumes there is no aerodynamic interaction between blade elements. Lifting Line method takes account of the aerodynamic interaction between blade elements automatically. In addition, the extra features like hub model can be incorporated into the lifting line model easily.

2.6.6.2 PVL Method

As discussed in the propeller section, Lerbs criterion has been validated using the Calculus of Variations method to give an optimized circulation distribution $\Gamma(r)$ that minimizes C_Q for a specific thrust coefficient C_T. By sweeping through all possible thrust coefficients C_T from -1 to 0 and comparing the minimized C_Q for each C_T, the overall minimum C_Q can be found. Thus the original PVL code for propeller design can be used directly without any modification for turbine design by specifying a range of negative C_T from -1 to 0 and searching for the overall minimum C_Q.

2.6.6.3 Lagrange Multiplier Method

Several studies [28, 43] have been conducted to find optimum turbine designs by simply setting the Lagrange multiplier λ_1 equal to 0 in order to get rid of the thrust constraint. However, the results are far from the values given by the Actuator Disk models because the approximation of the partial derivative in Equations (2.152) and (2.153) become poorer and invalid for the turbine optimization. Based on analysis of the General Momentum Theory that requires the induced velocity to be perpendicular to the total velocity, Epps [28] partially solved the turbine problem by enforcing the same perpendicularity requirement in the Lifting Line model regardless of the number of blades. As discussed by Epps, this 'hard-wired' implementation only works for uniform inflow.

2.6.6.4 Interior Point Method

Unlike the Lagrange Multiplier method with the approximation of partial derivatives, the Interior Point method can be used for the turbine optimization simply by specifying a no thrust constraint. The same as propeller optimization, each blade is first discretized into M panels. The optimization variables are $\tan\beta_i(i)$. The initial guess of $\tan\beta_i(i)$ is chosen to be $\tan\left(\frac{2}{3}\beta(i)\right)$ based on the estimation of the General Momentum

theory. The upper bound of $\tan\beta_i(i)$ is set to $\tan\beta(i)$ since the induced velocity always increases the angle of attack (Figure 2.10). The lower bound is set to be zero. However, if extra features are included (e.g. hub model), the upper bound may need to be increased to ensure the interior point method is able to converge to the optimized value.

CHAPTER 3. GENERALIZED UNIFORMLY SPACED FLAT PLATE CASCADE MODEL RESULTS

In this chapter, validations and case studies for the generalized uniformly spaced flat plate cascade model developed in Section 2.4 are presented. The pre-processing and post-processing procedure for using the model are given in Section 3.1. The Purdue transonic compressor introduced in Section 3.2 is used as the baseline geometry and flow condition for the validation and case studies in Section 3.3. Three different aerodynamic mistuning patterns are investigated in detail to study their effect on the forced response, aeroacoustics and flutter of a non-uniformly spaced blade row.

3.1 Pre-processing and Post-processing

To use the generalized uniformly spaced flat plate cascade model, some pre-processing and post-processing steps are needed. First, the non-uniformly spaced blade row with B blades needs to be transformed to a generalized uniformly spaced blade row with N blades by finer discretization in the tangential direction. During this process, $N-B$ imaginary blades are added. The case of the generalized uniformly spaced blade row with Blade 2 missing (discussed in Section 2.4) is one example that a non-uniformly spaced blade row with 3 blades is transformed to a generalized uniformly spaced blade row with 4 total blades where Blade 2 is an imaginary blade. The real blade and imaginary blade index need to be specified as input with the convention that the first blade is always a real blade.

In addition, two inputs to the normal uniformly spaced flat plate cascade model LINSUB, space to chord ratio and excitation interblade phase angle need to be changed accordingly by using the total number of the blades N. The rest of the model inputs, such as stager angle, Mach number, and reduced frequency stay the same.

The direct solution of the generalized uniformly spaced model is the strength of each fundamental harmonic mode. Depending on the applications, the direct solution needs to be post-processed in different ways.

For a forced response analysis, the unsteady loading distribution on each real blade is the quantity of interest. Because of the linearity of the model, the contribution of each fundamental harmonic mode can be calculated independently. The total unsteady loading distribution is the summation of the contribution of all fundamental harmonic modes.

For a flutter analysis, the unsteady loading and aerodamping due to blade vibration at all possible interblade phase angles are the quantities of interest. The unsteady loading and aerodamping are generally different from blade to blade due to non-uniform spacing. As in the forced response analysis, the contribution of each fundamental harmonic mode is calculated independently first, and then summed together to obtain the total unsteady loading and aerodamping on each blade. However, the total aerodamping calculated in this way is referenced to the phase of vibration of the first blade. To check the stability of each blade, the phase of aerodamping on a certain blade needs to be corrected so that it refers to the phase of vibration of the specific blade.

For an acoustic analysis, only the propagating (cut-on) pressure waves are considered. Each fundamental harmonic mode contains the cascade waves of the fundamental mode and higher scattering modes. Depending on the tangential wave number of the cascade waves, some of the associated pressure waves are cut-on and some are cut-off. The cut-on pressure waves are selected and their strength can be calculated based on the strength of the corresponding mode.

3.2 Purdue Transonic Compressor

The Purdue Transonic Compressor is a 1.5 stage axial compressor which represents the front stages of high-pressure compressor in an advanced aircraft engine. At the design operation condition, the rotation speed is 20000rpm, the mass flow rate is 9.57 lbm/s and the maximum pressure ratio is 1.38. The compressor consists of an inlet guide vane (IGV) with 20 vanes, an integrally bladed rotor (IBR) with 18 blades, and a

downstream stator of 20 vanes. The compressor stage has a tip diameter of 12 inches and a constant hub-to-tip ratio of 2/3. The rotor blades have a Controlled Diffusion Airfoil (CDA) shape with a chord length of 1.8 inches to 2.0 inches from hub-to-tip. The IGV and stator vanes also have a CDA shape but have a constant chord length of 1.75 inches. Both IGV and stator vanes feature variable stagger angles and adjustable axial spacing.

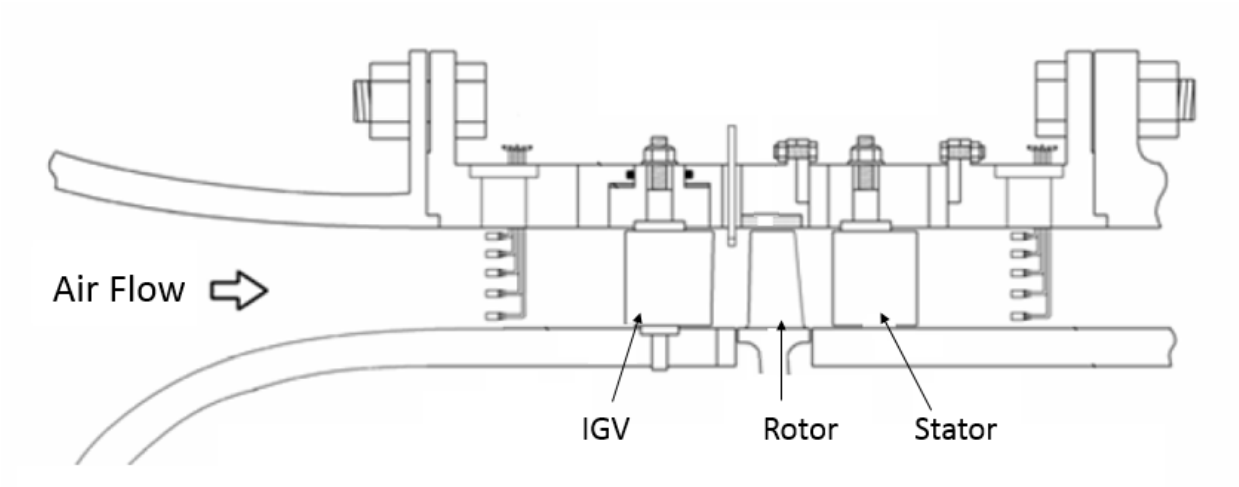

Figure 3.1. Purdue Transonic Compressor cross section.

An ANSYS finite element analysis was performed to predict the IBR's natural frequencies for different vibration modes [44]. The Campbell diagram for the rotor is shown in Figure 3.2. The resonant crossing indicates that at 17,000 rpm the wakes of the IGV excite the rotor at its 2nd bending natural frequency. In addition, at the design speed of 20,000 rpm the predicted natural frequency of the first torsion mode is around 3074Hz.

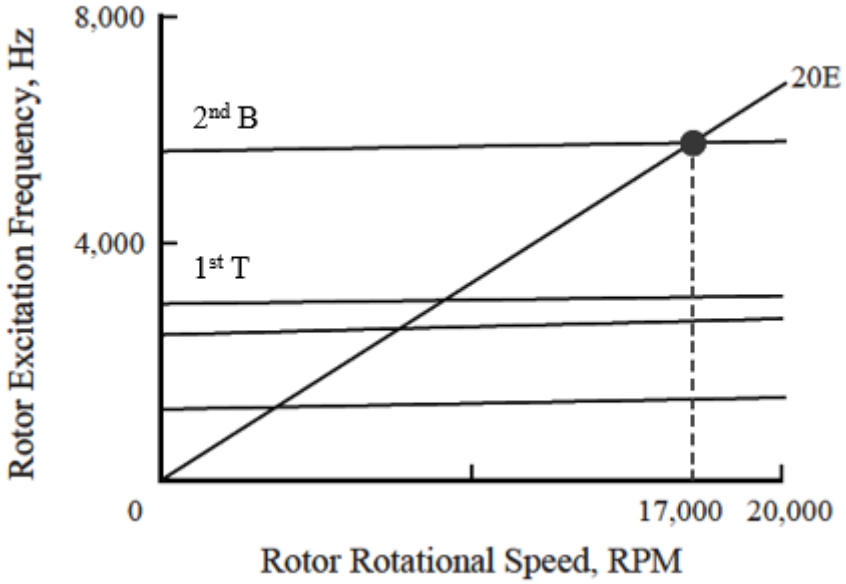

Figure 3.2. Rotor Campbell diagram [16].

3.3 Validation and Case Studies

The geometry and flow condition of the Purdue Transonic Compressor rotor is used as the baseline configuration in this study. Three different aerodynamically mistuned configurations were investigated using the generalized uniformly spaced flat plate cascade model in order to study the effect of different non-uniformly spaced patterns on the forced response, flutter and acoustic behavior of the rotor.

The studies are performed at 90% span of the rotor, which corresponds to a radius of 5.8 inches. At this spanwise location, the stagger of the IGV is approximately 0^o, while the stagger of the rotor is approximately 64^o. The axial distance between IGV and rotor is 0.78 inches. The transient operation condition at 17000rpm is used for the forced response analysis and corresponding acoustic analysis on the rotor. The design operation condition at 20000rpm is used for the flutter analysis on rotor with the first torsion mode. In order to comply with the flat plate cascade model, the geometry and flow field of in IGV-rotor stage was modified slightly. The modified geometry and flow field used as the input for the model are listed in Table 3.1.

Table 3.1. The modified geometry and flow conditions of Purdue transonic compressor IGV-rotor stage.

Purdue transonic compressor		
	IGV	Rotor
Blade number	20	18
Chord(in)	1.75	2
Radius(in)	5.8	5.8
Stagger angle (degree)	0.1	71.0
Chordwise velocity (in/s)	3564 / 4192.9	10929.6 /12858
Mach number	0.268 / 0.315	0.822 / 0.966
Rotation speed (rad/s)	0	-1780.24 / -2094.4
Inter-row spacing (in)	0.781	----------

In Table 3.1, the first chordwise velocity and Mach number correspond to the lower rotational speed, 1780.24rad/s which is the 17000rpm transient operating condition used for the forced response analysis. The second chordwise velocity and Mach number correspond to the higher rotational speed, 2094.4 rad/s which is the 20000rpm design operating condition used for the flutter analysis.

The three different aerodynamic mistuned configurations used in the analysis are the rotor blade with alternating spacing, with sinusoidal spacing and with one blade missing. Unwrapping the rotor at 90% span into a 2D flat plate cascade, the rotor blade positions in the tangential direction are shown in Figure 3.3 for the aerodynamic tuned (uniform spacing) and the three aerodynamic mistuned configurations.

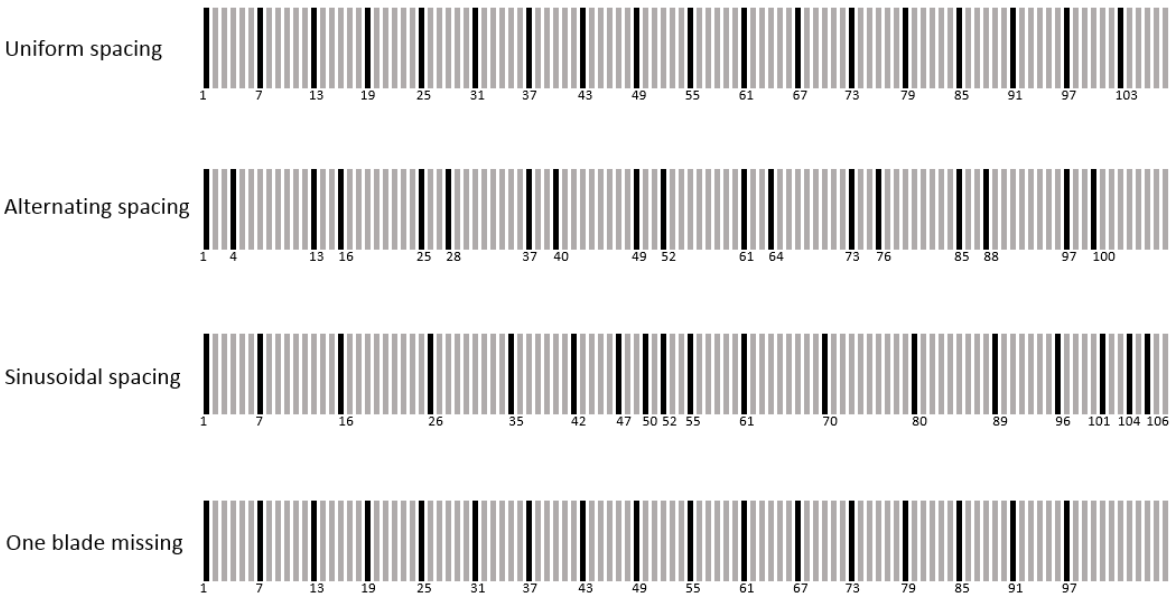

Figure 3.3. Real blades positions of different rotor blade row configurations in the generalized uniformly spaced cascade with 108 total blades.

In order to use the generalized uniformly spaced cascade model, the rotor blade row is discretized into 108 total blades. With the convention that the first blade is always a real blade, the uniformly spaced blade row has real blades at blade index [1 7 13 19 25 31 37 43 49 55 61 67 73 79 85 91 97 103]. The alternating spacing blade row has a blade spacing ratio of 1:3, and thus the real blades are at blade index [1 4 13 16 25 28 37 40 49 52 61 64 73 76 85 88 97 100]. The sinusoidal spacing blade row has an average blade spacing of 6 and 2 cycles of sinusoidal wave with amplitude of 4. Rounded to the 108 discretized total blade positions, the real blades of the sinusoidal spacing blade row are at blade index [1 7 16 26 35 42 47 50 52 55 61 70 80 89 96 101 104 106]. The blade row with blade 18 missing has real blades at blade index [1 7 13 19 25 31 37 43 49 55 61 67 73 79 85 91 97].

In addition, a systematic parametric study is conducted to show the effect of the excitation nodal diameter, Mach number and reduced frequency on the unsteady aerodynamic response of the blade row with different non-uniform spacing patterns.

3.3.1 Validation

Since the generalized uniformly spaced flat plate cascade model(Generalized LINSUB) is developed in the same theoretical frame work as the normal uniformly spaced flat plate cascade model LINSUB, the first validation is to compare the results from the two models for the baseline configuration of the Purdue transonic compressor rotor (Table 3.1). The unsteady loading on rotor due to both internal excitation and external excitation are calculated and compared. The surface Δp distributions caused by the blade bending vibration and IGV wake excitation are shown in Figure 3.4 and Figure 3.5, respectively.

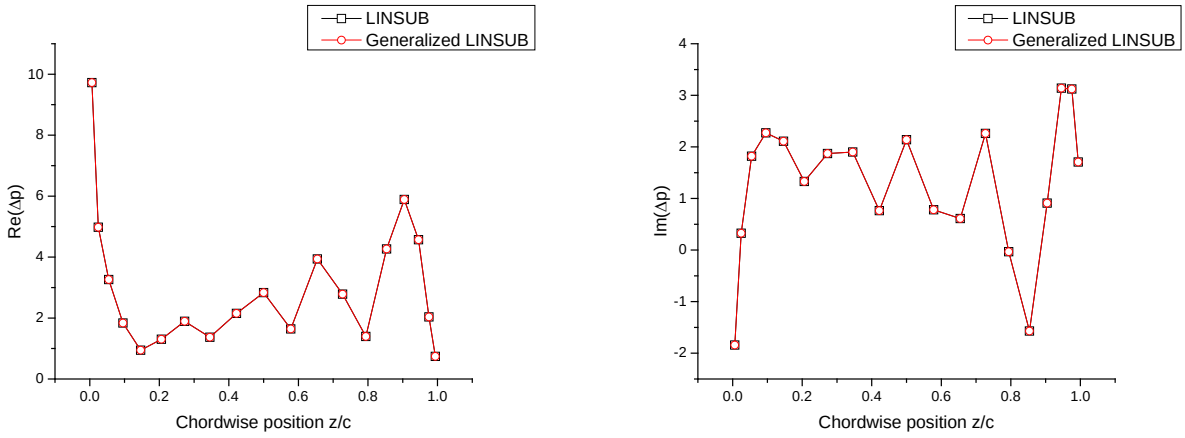

Figure 3.4 Comparison of the surface Δp distributions caused by blade bending vibration

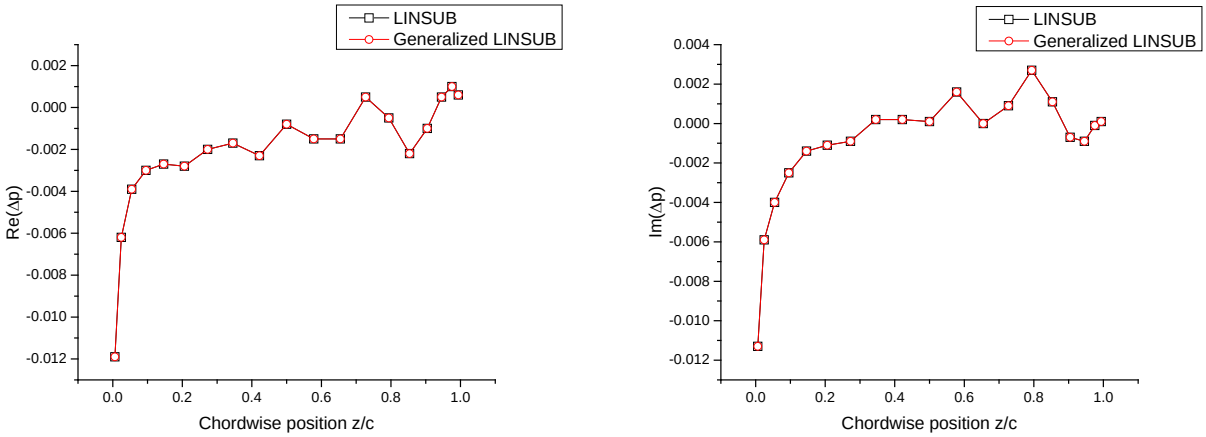

Figure 3.5. Comparison of the surface Δp distributions caused by IGV wake excitation.

The excellent agreement between the results by the two models shows that the generalized uniformly spaced flat plat cascade model (Generalized LINSUB) can be reduced to the normal uniformly spaced flat plate cascade models LINSUB successfully. The second validation is to compare the unsteady loading on the alternating spacing blade row calculated by Generalized LINSUB and Scott Sawyer's Detuned Cascade model [4]. Scott Sawyer's Detuned Cascade model combines two normal uniformly spaced cascade models in order to calculate the unsteady aerodynamic performance of a detuned cascade. It treats the two adjacent blades as a single symmetry group, and thus its application is limited to the blade row with alternating spacing only. Depending on the spacing to the adjacent blades, the blades in the cascade with alternating spacing can be categorized into two different types. The surface Δp distribution on type A blade and type B blade caused by blade bending vibration are shown in Figure 3.6 and Figure 3.7, respectively. Due to the limitation of Scott Sawyer's Detuned Cascade model, only ten vortex points are specified along the blade.

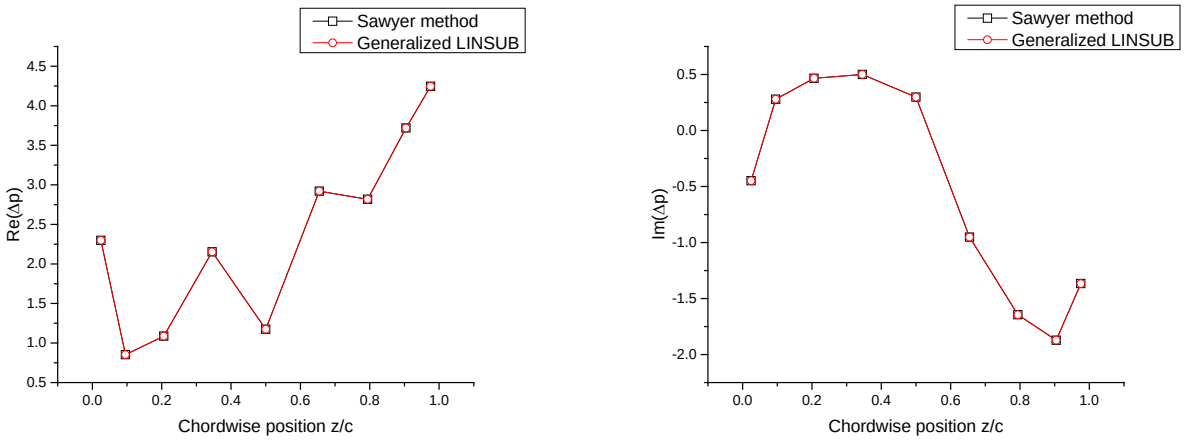

Figure 3.6. Comparison of the surface Δp distribution on type A blades caused by blade bending vibration.

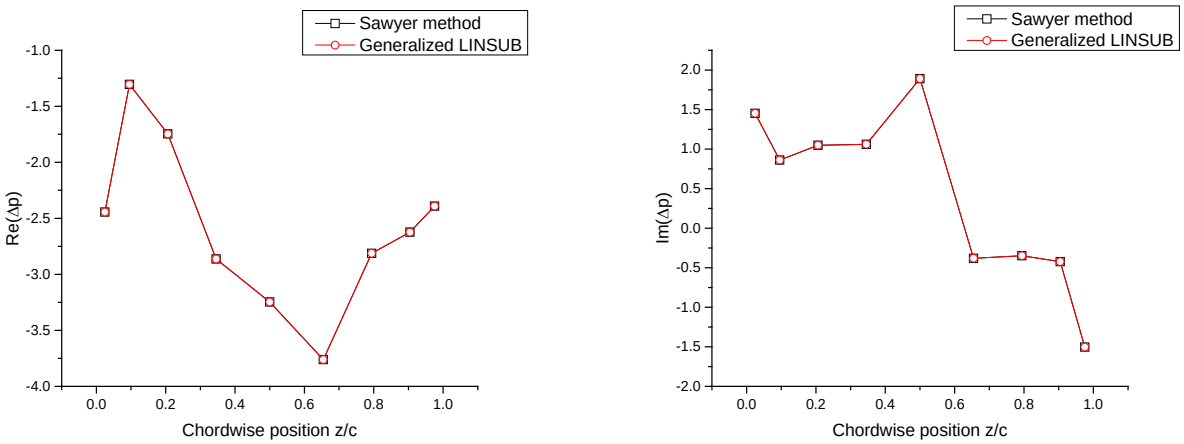

Figure 3.7. Comparison of the surface Δp distribution on type B blades caused by blade bending vibration.

The excellent agreement of these results provides an additional validation for the generalized uniformly spaced flat plate cascade model developed in this study.

3.3.2 Forced Response Analysis

At 17000rpm, the wake of IGV excites the second bending mode of the rotor. The nodal diameter of the excitation is $ND = 20$ the reduced frequency is $k = 6.5$ and Mach number along the rotor blade is $Ma = 0.82$. Using the generalized uniformly spaced flat plate cascade model, the surface Δp distribution on each blade is calculated for the three non-uniform spacing patterns and compared with the surface Δp distribution for the uniformly spaced blade row.

Figure 3.8 shows the comparison between the blade row with alternating spacing and the blade row with uniform spacing. The blades of an alternating spacing blade row can be categorized into two types. Figure 3.8 shows the blade row with alternating spacing has two types of surface Δp distribution. Both of them are different from the result of uniformly spaced blade row.

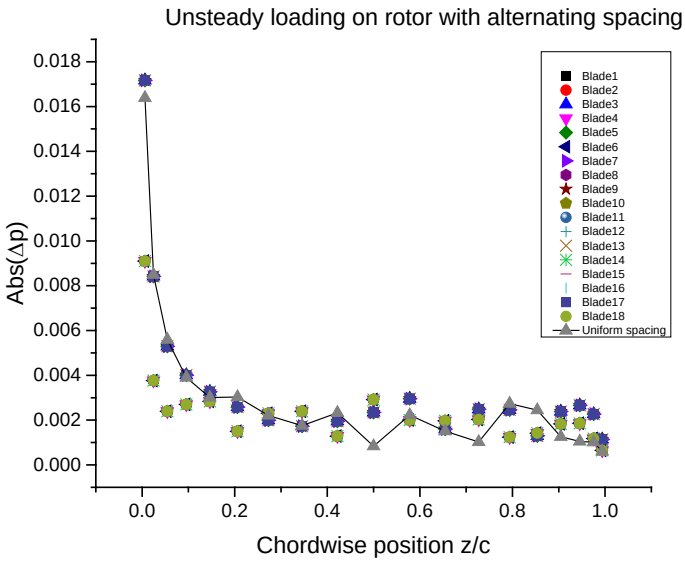

Figure 3.8. Comparison of the surface Δp distribution on each blade of the blade row with alternating spacing and the blade row with uniform spacing.

Figure 3.9 shows the comparison between the blade row with sinusoidal spacing and the blade row with uniform spacing. Since the spacing follows a sinusoidal wave with two cycles in the circumferential direction, the surface Δp distribution should also contain two periods. As expected, there are $18/2=9$ different types of surface Δp distribution shown in Figure 3.9. The variation of surface Δp distribution on the blades of a sinusoidal spacing blade row are larger than that of the alternating spacing blade row.

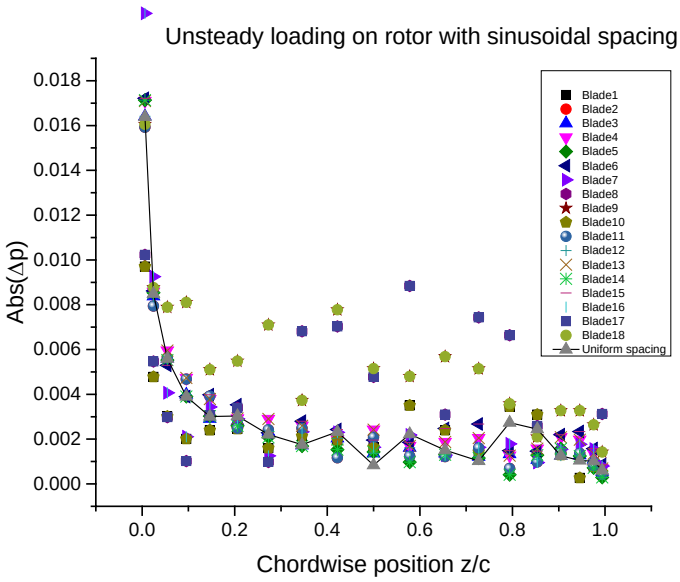

Figure 3.9. Comparison of the surface Δp distribution on each blade of the blade row with sinusoidal spacing and the blade row with uniform spacing.

Figure 3.10 shows the comparison between the blade row with one blade missing and the blade row with uniform spacing. Although there is only one blade missing, the symmetry of the whole blade row is broken. The unsteady loadings on the each blade are all different from one another. However, since there is only one blade missing, the unsteady loading on most of the blades are close to the value from the uniformly spaced blade row.

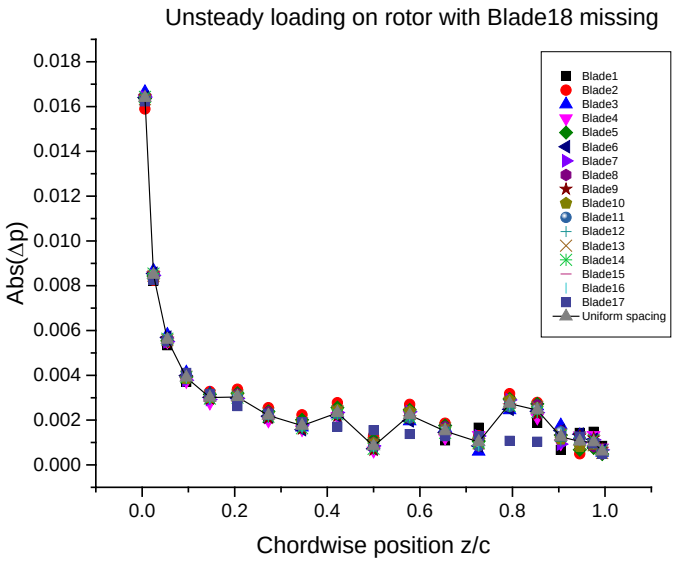

Figure 3.10. Comparison of the surface Δp distribution on each blade of the blade row with one blade missing and blade row with uniform spacing.

Next, the average and standard deviation of surface Δp distribution are analyzed for the three non-uniformly spaced blade rows at different excitation nodal diameter, different Mach number and different reduced frequency. The results are compared with that from the uniformly spaced blade row in order to study the advantage and disadvantage of these non-uniformly spaced blade rows' unsteady aerodynamic behavior at different excitation and flow conditions.

3.3.2.1 Effect of Excitation Nodal Diameter

The blade surface Δp distributions due to wake excitation at three different nodal diameters $ND = 1, 10, 20$ for the blade row with alternating spacing, the blade row with sinusoidal spacing and the blade row with one blade missing are shown in Figure 3.11, Figure 3.12 and Figure 3.13. From Figure 3.11, the average unsteady loading on the blade row with alternating spacing is generally higher than the value on the blade row with uniform spacing for the first 80% of the chord length but not for the remaining 20% of the chord length. Similar behavior can be observed in the blade row with sinusoidal

spacing as shown in Figure 3.12. The standard deviation is higher on the blade row with sinusoidal spacing than the blade row with alternating spacing. From Figure 3.13, the average unsteady loading on the blade row with one blade missing is very close to the value on the uniformly spaced blade row. The corresponding standard derivation is also smaller than the value on the blade row with alternating spacing and the blade row with sinusoidal spacing. Regarding the effect of excitation nodal diameter on the unsteady loading on the non-uniformly spaced blade rows, the results shows the general trend that the higher the excitation nodal diameter, the lower the average unsteady loading and smaller the standard deviation.

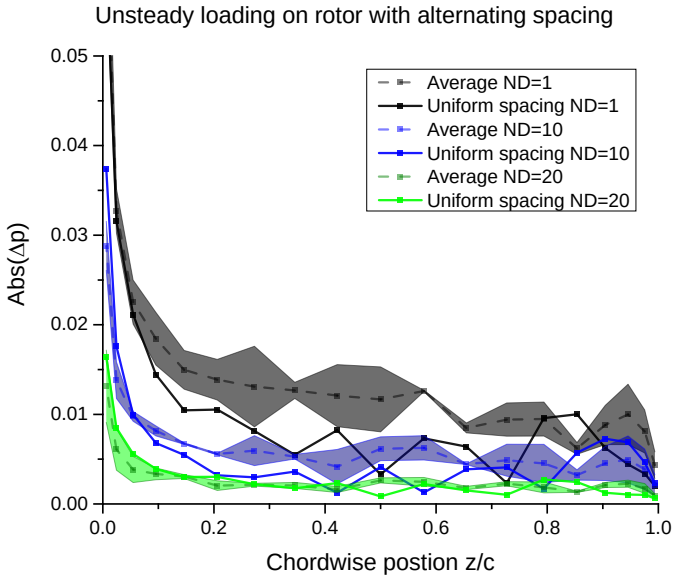

Figure 3.11. Comparison of the average and standard deviation of surface Δp distribution for blade row with alternating spacing and blade row with uniform spacing at different excitation nodal diameters.

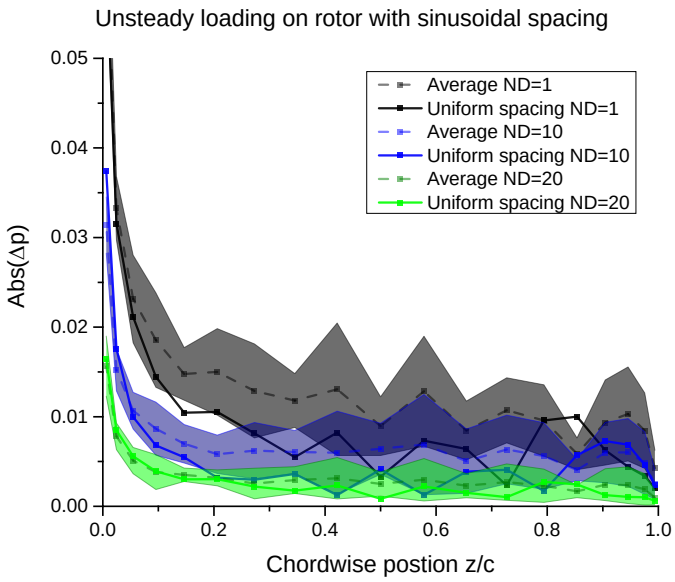

Figure 3.12. Comparison of the average and standard deviation of surface Δp distribution for blade row with sinusoidal spacing and blade row with uniform spacing at different excitation nodal diameters.

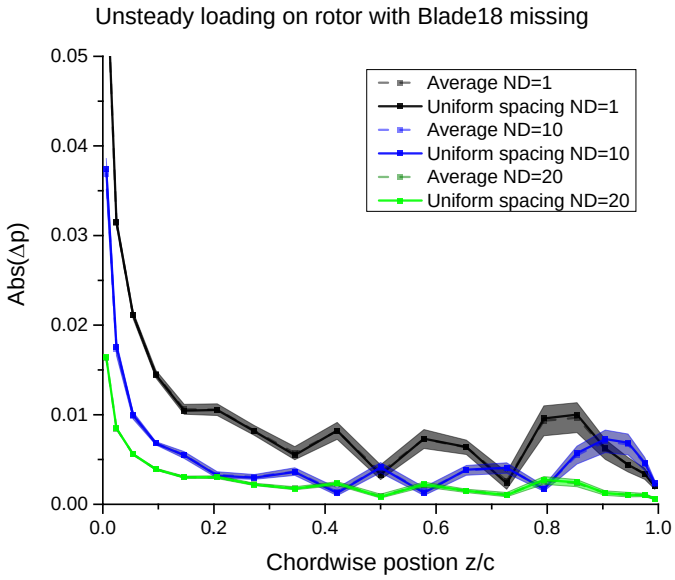

Figure 3.13. Comparison of the average and standard deviation of surface Δp distribution for blade row with one blade missing and blade row with uniform spacing at different excitation nodal diameters.

3.3.2.2 Effect of Mach Number

The blade surface Δp distributions due to wake excitation at three different Mach numbers $Ma = 0.1, 0.5, 0.82$ are shown in Figure 3.14 for the blade row with alternating spacing, in Figure 3.15 for the blade row with sinusoidal spacing and in Figure 3.16 for the blade row with one blade missing. These figures show that the average unsteady loading on non-uniformly spaced blade rows are generally higher than uniformly spaced blade row on most of the blade. The unsteady loading standard deviation on the blade row with sinusoidal spacing is higher than the other two types of non-uniformly spaced blade rows. From Figure 3.16, the average unsteady loading on the blade row with one blade missing is very close to the value on the uniformly spaced blade row. The corresponding standard derivation is also smaller than the value on the blade row with alternating spacing and the blade row with sinusoidal spacing. There is no clear trend on how the Mach number affects the unsteady loading on the non-uniformly spaced blade rows. However, on the blade rows with alternating spacing and sinusoidal spacing, the highest average unsteady loading occurs at a medium Mach number.

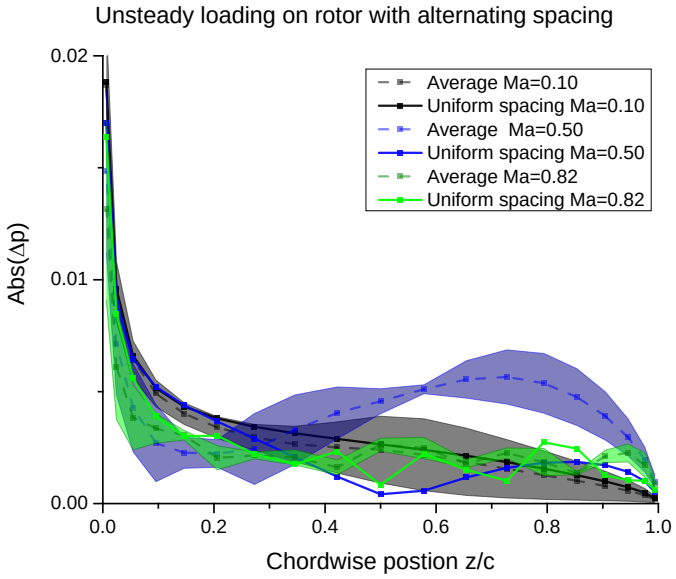

Figure 3.14. Comparison of the average and standard deviation of surface Δp distribution for blade row with alternating spacing and blade row with uniform spacing at different Mach numbers.

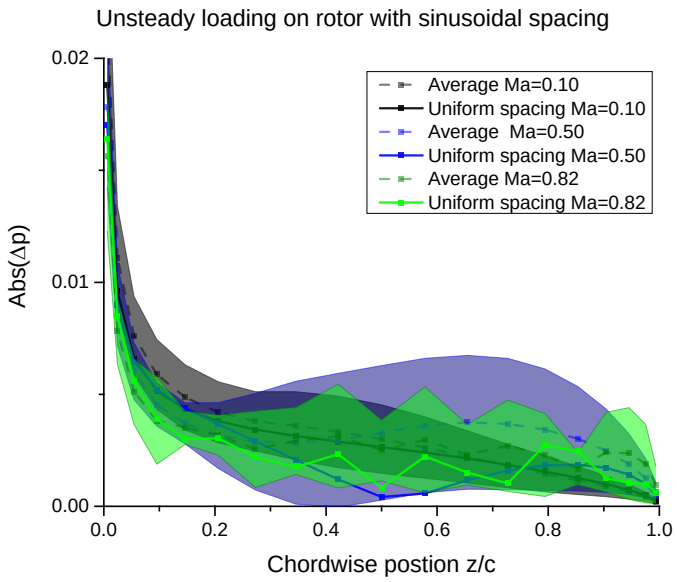

Figure 3.15. Comparison of the average and standard deviation of surface Δp distribution for blade row with sinusoidal spacing and blade row with uniform spacing at different Mach numbers.

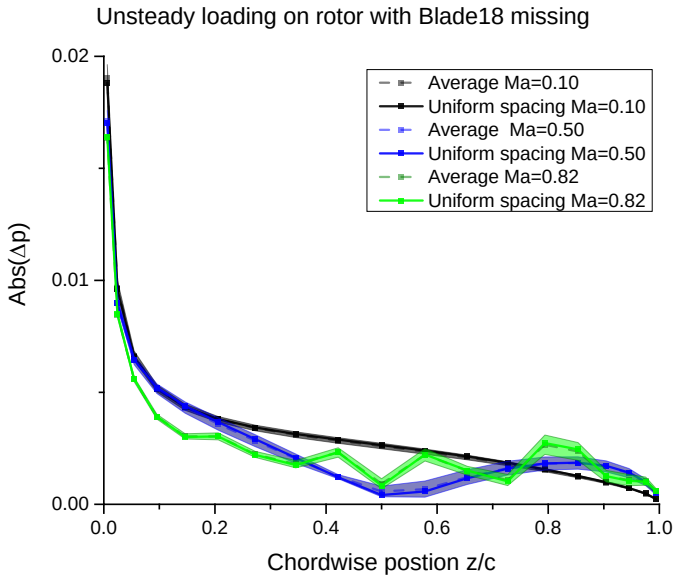

Figure 3.16. Comparison of the average and standard deviation of surface Δp distribution for blade row with one blade missing and blade row with uniform spacing at different Mach numbers.

3.3.2.3 Effect of Reduced Frequency

The effect of reduced frequency on the surface Δp distributions on the non-uniformly spaced blade rows are shown in Figure 3.17, Figure 3.18 and Figure 3.19. Generally, the average unsteady loading on the non-uniformly spaced blade rows are higher than the value on uniformly spaced blade row. The average unsteady loading on the blade row with one blade missing is very close to the value on the uniformly spaced blade row. The unsteady loading standard deviations are the highest on the blade row with sinusoidal spacing and are the lowest on the blade row with one blade missing. Regarding the effect of reduced frequency on the unsteady loading on the non-uniformly spaced blade rows, the general trend is that the higher the reduced frequency, the lower the average unsteady loading and the smaller the standard deviation.

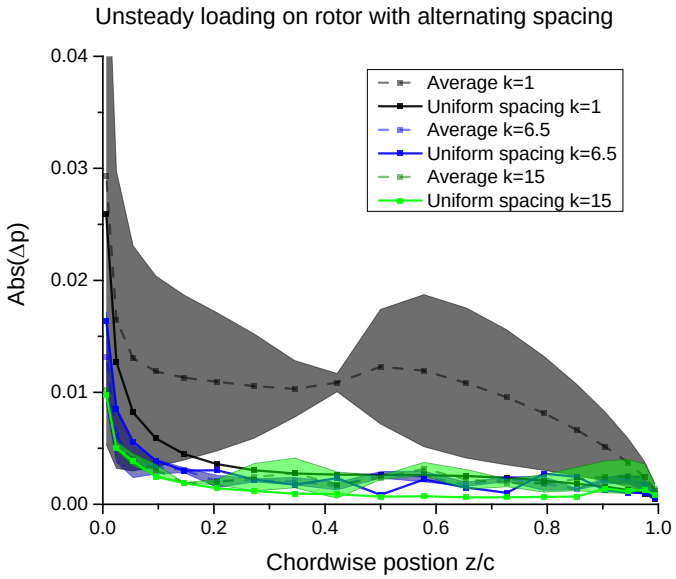

Figure 3.17. Comparison of the average and standard deviation of surface Δp distribution for blade row with alternating spacing and blade row with uniform spacing at different reduced frequencies.

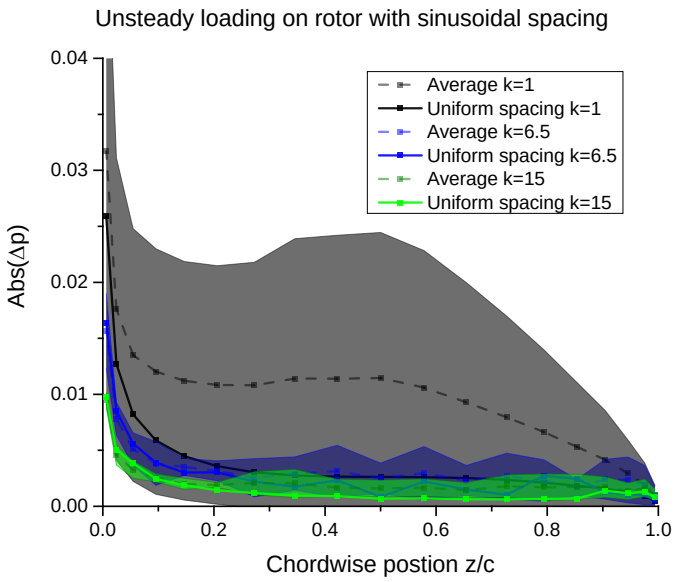

Figure 3.18. Comparison of the average and standard deviation of surface Δp distribution for blade row with sinusoidal spacing and blade row with uniform spacing at different reduced frequencies.

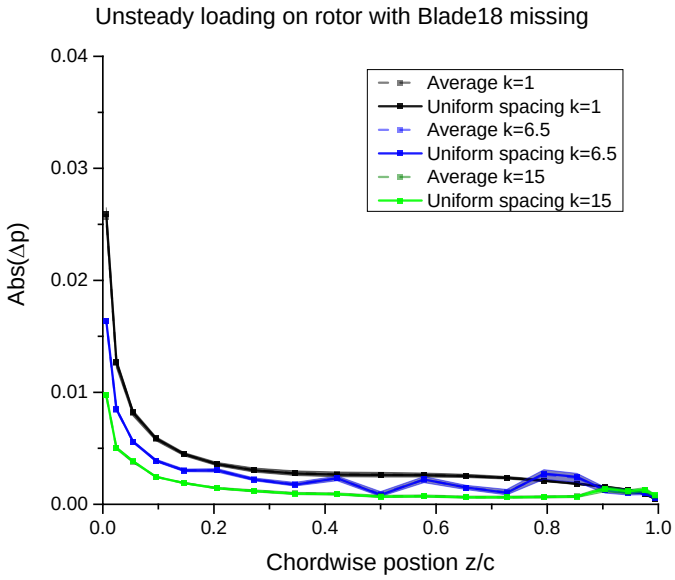

Figure 3.19. Comparison of the average and standard deviation of surface Δp distribution for blade row with one blade missing and blade row with uniform spacing at different reduced frequencies.

3.3.3 Aeroacoustics Analysis

The aeroacoustics analysis is done at the transient operation condition of 17000rpm, the same as the forced response analysis. The propagating pressure waves caused by the IGV wake and rotor interaction are calculated using the generalized uniformly spaced flat plate cascade model. The IGV wake excitation has nodal diameter $ND = 20$. The excitation frequency in the rotor reference frame is $\omega_0 = 20 \times 17000\,\text{rpm}$ =5667Hz.

For a uniformly spaced blade row, the output pressure waves have the same frequency as the excitation frequency, and a series of nodal diameters due to the scattering effect of the blade row. As derived in Equation (2.74), the output pressure wave nodal diameter $ND = ND_{ex} - nB$, where B is the blade number and n can be any integer. For a non-uniformly spaced blade row, the output pressure waves have all possible nodal diameters due to the breakdown of the symmetry. By examining the axial wave number, the output pressure waves with ND=-8 to +83 are the propagating modes. The output pressure waves have the same frequency as the excitation frequency in the rotor reference frame. However due to the Doppler shifting effect, from Equation (2.102) the frequency in the stationary reference frame is $\omega_s = \omega_0 - ND\Omega$, where Ω is the rotor rotational speed.

The upstream going pressure wave and downstream going pressure wave amplitude of the propagating modes for the different non-uniformly spaced blade rows and at different excitation nodal diameters are plotted with the results from the uniformly spaced blade row in order to analyze the acoustic behavior of the non-uniformly spaced blade rows under the excitation of different nodal diameters. For the baseline condition, the IGV wake excitation has $ND = 20$. The corresponding spectrum of the propagating upstream going pressure wave and downstream going pressure wave are shown in Figure 3.20. The spectrum of the propagating pressure waves to a wake excitation with $ND = 10$ and $ND = 1$ are shown in Figure 3.21 and Figure 3.22. As expected, the acoustic energy spreads out over more frequency components for the non-uniformly spaced blade row than the uniformly spaced blade row. As shown in Figure 3.3, the uniformly spaced blade

row has a symmetry group of 1 blade. The blade row with alternating spacing has a symmetry group of 2 blades. The blade row with sinusoidal spacing has symmetry group of 9 blades since it contains two periods. The symmetry is totally broken down for the blade row with one blade missing. In general, the blade with fewer symmetry groups has less symmetry, and thus contains more fundamental harmonic modes and has more frequency components.

In addition, the blade row with one blade missing has a similar spectrum as the blade row with uniform spacing, except there are many very weak scattered modes. This is because all the remaining blades of the blade row with one blade missing are at the same position as the uniformly spaced blade row. The blade row with sinusoidal spacing has the largest spacing variation and thus the acoustic energy spreads more uniformly over the spectrum. Thus the non-uniformly spaced blade row with larger spacing variation tends to generate a more broadband-like noise than the typical discrete tone noise generated by the uniformly spaced rotor row and wake interaction. Comparing Figure 3.20, Figure 3.21 and Figure 3.22, it also shows that in general the higher wake excitation nodal diameter ND, the lower the strength of the output pressure wave over the spectrum.

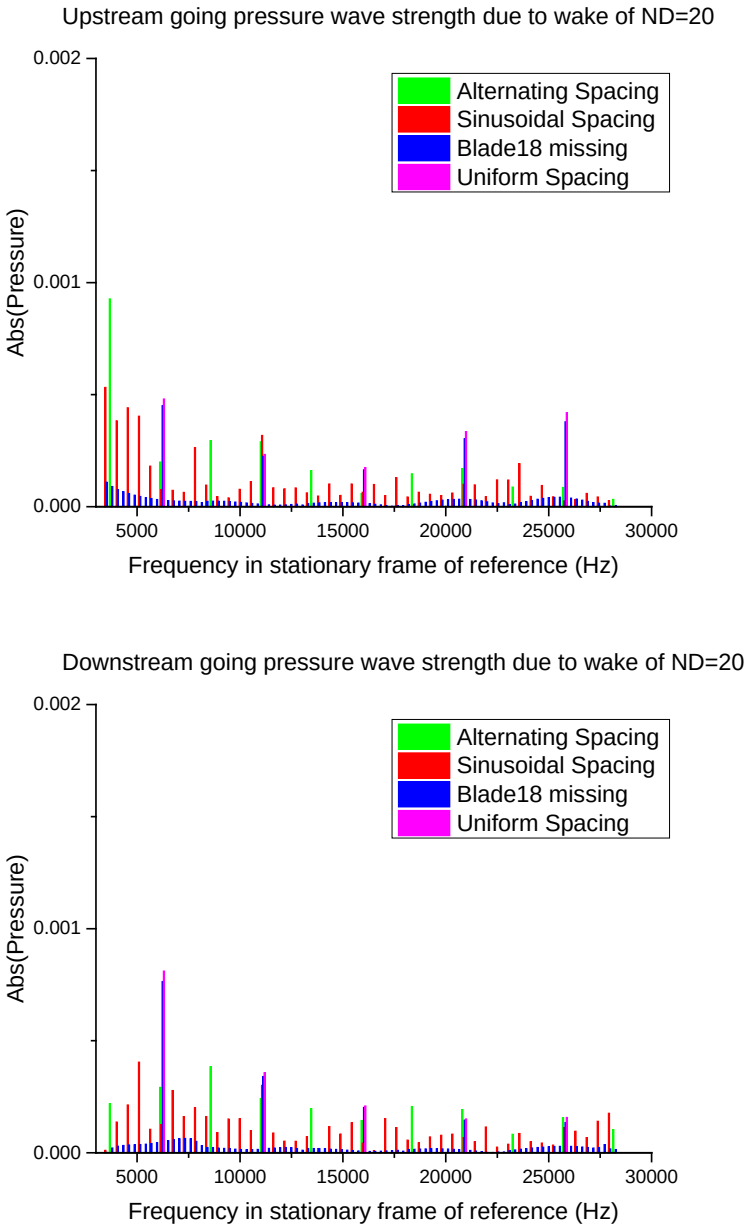

Figure 3.20. The propagating upstream going pressure wave and downstream going pressure wave spectrum due to wake of ND=20.

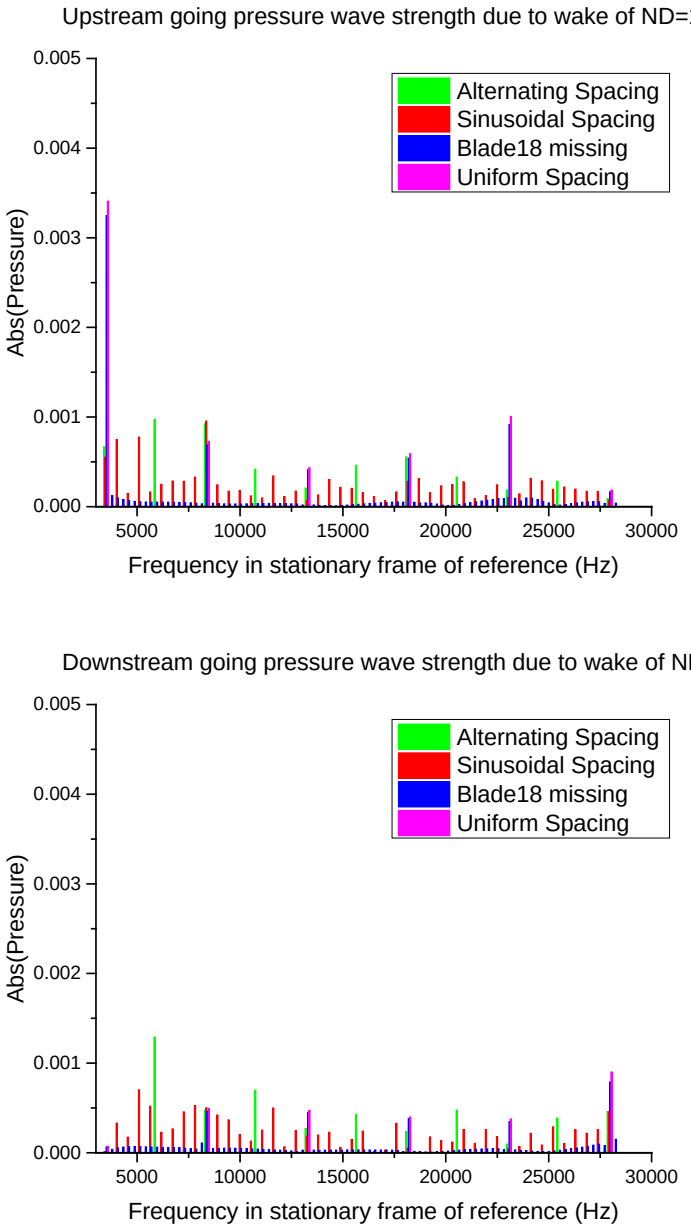

Figure 3.21. The propagating upstream going pressure wave and downstream going pressure wave spectrum due to wake of ND=10.

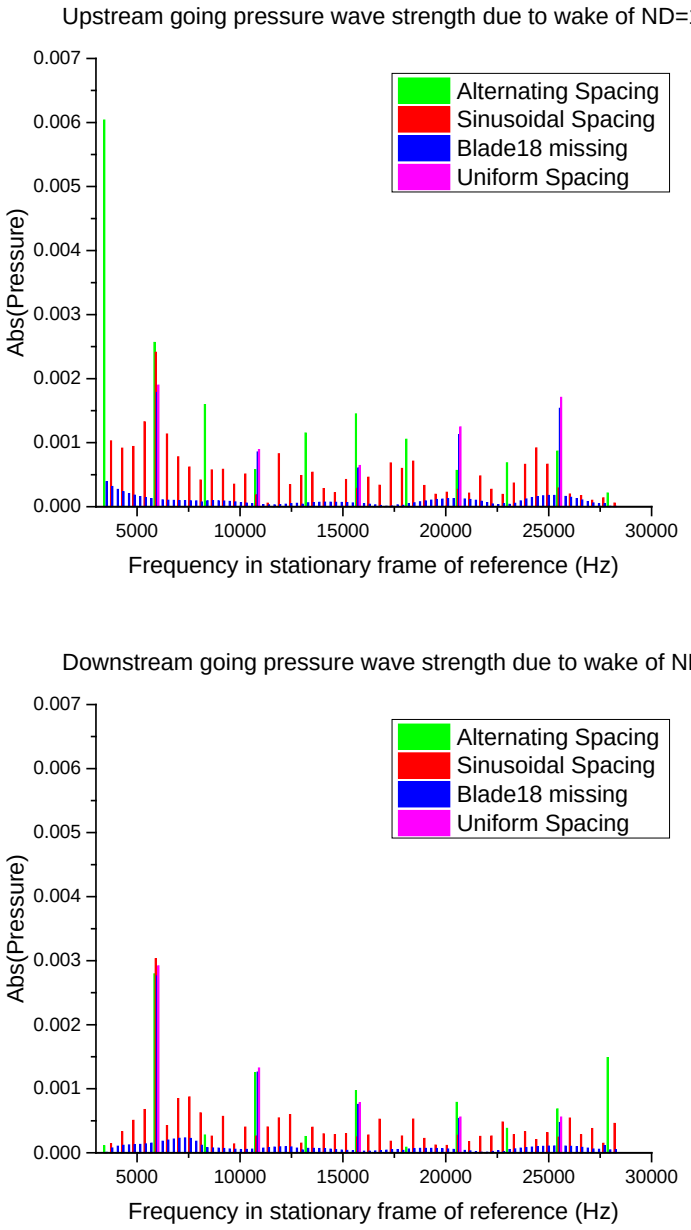

Figure 3.22. The propagating upstream going pressure wave and downstream going pressure wave spectrum due to wake of ND=1.

3.3.4 Flutter Analysis

The flutter analysis is done for the first torsion mode (3074Hz) of the rotor blade at the operating condition. The design rotational speed is 20000rpm. The reduced frequency $k = 3.0$ and Mach number along the blade $Ma = 0.966$.

The unsteady moment due to blade torsional vibration $\mathrm{Abs}(B_\alpha)$ and $\mathrm{Im}(B_\alpha)$ on each blade are calculated for the non-uniformly spaced blade rows at all possible interblade phase angles. As shown in Equation (2.12), the aerodamping for a torsional vibration mode C_α^{aero} is equal to $-\frac{\mathrm{Im}(B_\alpha)}{\omega}$. Thus a positive $\mathrm{Im}(B_\alpha)$ indicates a negative aerodamping which leads to a possible unstable condition. When calculating $\mathrm{Im}(B_\alpha)$, the phase of unsteady moment on the blade other than the first blade needs to be shifted so that it refers to the phase of excitation on the specific blade. In this way, the aerodamping is calculated in the correct context in order to indicate possible flutter unstable conditions for each blade.

The unsteady moment $\mathrm{Abs}(B_\alpha)$ and $\mathrm{Im}(B_\alpha)$ on each blade of the blade row with alternating spacing is shown in Figure 3.23. The blade row with alternating spacing has a symmetry group of 2 blades, and thus there are two different unsteady loading patterns. Compared with the uniformly spaced blade row, one type of the blades (Blade 2,4,6,8,10,12,14,16,18) has lower unsteady loading and lower aerodamping at almost all interblade phase angles. The other type of blades (Blade 1,3,5,7,9,11,13,15,17) has higher unsteady loading and higher aerodamping at interblade phase angle from 0 degree to 120 degrees, but lower unsteady loading and lower aerodamping for the other interblade phase angles.

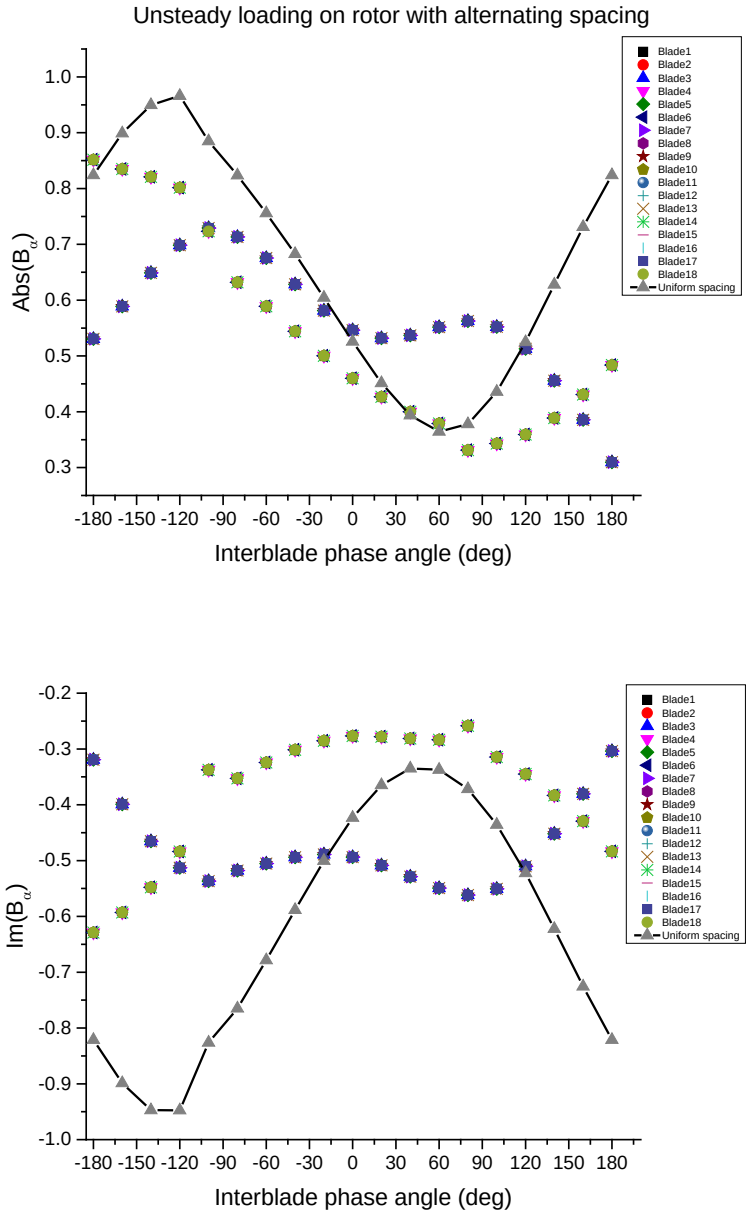

Figure 3.23. The unsteady moment $\mathrm{Abs}\left(B_\alpha\right)$ and $\mathrm{Im}\left(B_\alpha\right)$ on each blade of the blade row with alternating spacing.

The unsteady moment $\mathrm{Abs}\left(B_\alpha\right)$ and $\mathrm{Im}\left(B_\alpha\right)$ on each blade of the blade row with one blade missing is shown in Figure 3.24. The results are very similar to the values on blades of the uniformly spaced blade row, except the immediate adjacent blades to the missing blade 18, i.e. Blade 1 and Blade 17. Blade 1 has the most significant difference

from the value on the blade of a uniformly spaced blade row. It has higher unsteady loading and higher aerodamping at the interblade phase angle from 0 degree to 120 degrees, and lower unsteady loading and lower aerodamping at the rest of interblade phase angles.

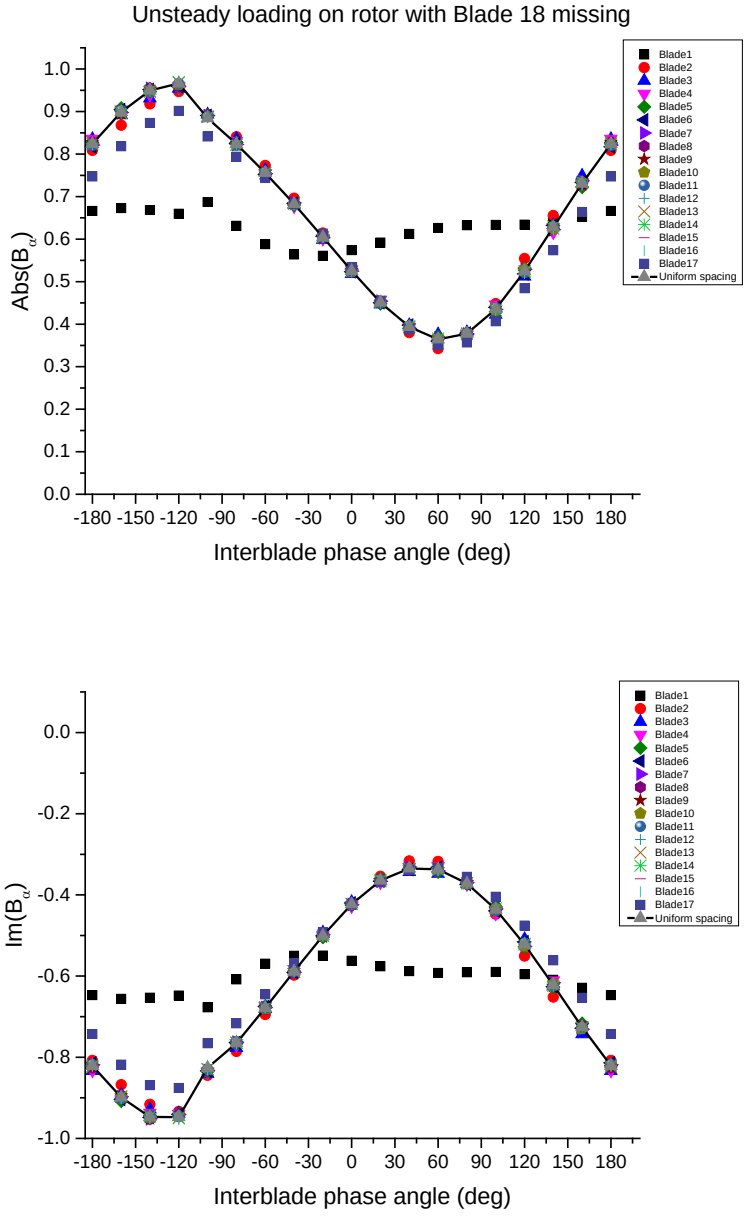

Figure 3.24. The unsteady moment $\mathrm{Abs}\left(B_\alpha\right)$ and $\mathrm{Im}\left(B_\alpha\right)$ on each blade of the blade row with one blade missing.

The unsteady moment $\mathrm{Abs}(B_\alpha)$ and $\mathrm{Im}(B_\alpha)$ on each blade of the blade row with sinusoidal spacing is shown in Figure 3.25. The blade row with sinusoidal spacing has a symmetry group of 9 blades, and thus there are nine different unsteady loading patterns. The unsteady moment and aerodamping variation from blade to blade are larger than the other two non-uniformly spaced blade rows.

In general, most blades have lower unsteady loading and lower aerodamping for most of the interblade phases, except that Blade 4, 5, 6 and Blade 13, 14, 15 have higher unsteady loading and higher aerodamping at interblade phase angles from 0 degree to 120 degree. The feature of higher unsteady loading and higher aerodamping at interblade phase angles from 0 degree to 120 degrees also occurs on Blade 1,3,5,7,9,11,13,15,17 of the blade row with alternating spacing and Blade 1 of the blade row with blade 18 missing. Examining the positions of these blades in Figure 3.3 shows that they all have the common feature that the blade on their left is farther away from them than the blade on their right.

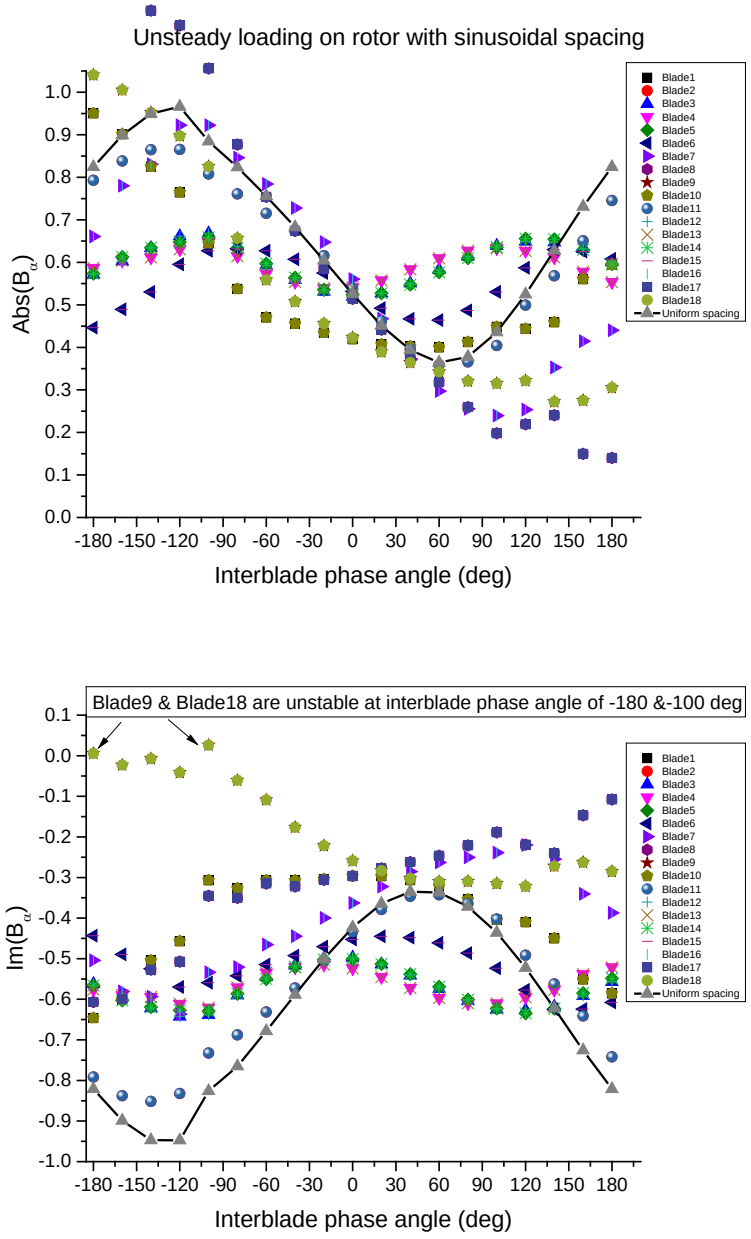

Figure 3.25. The unsteady moment $\mathrm{Abs}\left(B_\alpha\right)$ and $\mathrm{Im}\left(B_\alpha\right)$ on each blade of the blade row with sinusoidal spacing.

In addition, Figure 3.25 shows that Blade 9 and 18 have positive $\mathrm{Im}\left(B_\alpha\right)$ and thus negative aerodamping and thus are unstable at the interblade phase angles of -180 and -100 deg. A parametric study with varying Mach number ($Ma = 0.1, 0.5, 0.966$) and

varying reduced frequency ($k = 1.0, 3.0, 15$) shows two more unstable cases. As shown in Figure 3.26, Blade1,3,5,7,9,11,13,15,17 of the blade row with alternating spacing are unstable at an interblade phase angle of 180 degrees when $Ma = 0.966$ and $k = 1.0$. As shown in Figure 3.27, when $Ma = 0.1$ and $k = 3.0$, for a blade row with sinusoidal spacing, Blade 7 and Blade 16 are unstable at interblade phase angles of 60, 80 and 100 degrees, Blade 8 and Blade 17 are unstable at interblade phase angles of 140 and 160 degrees, and Blade 9 and Blade 18 are unstable at interblade phase angles of 160 and 180 degrees.

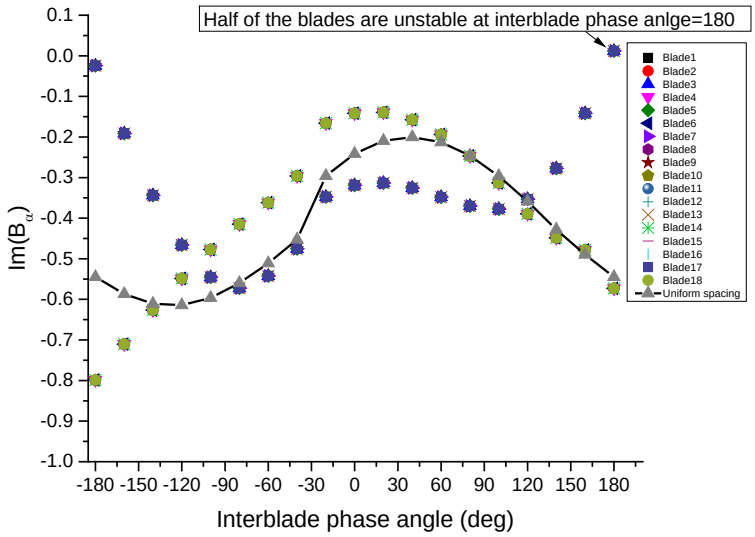

Figure 3.26. $\mathrm{Im}(B_\alpha)$ on each blade of the blade row with alternating spacing when $Ma = 0.966$ and $k = 1.0$.

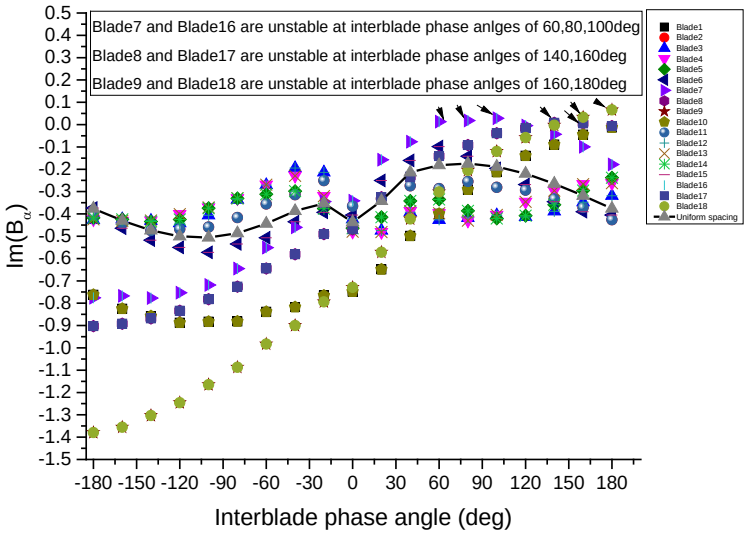

Figure 3.27 $\mathrm{Im}\left(B_\alpha\right)$ on each blade of the blade row with sinusoidal spacing when $Ma = 0.1$ and $k = 3.0$

Next, parametric studies at three different Mach numbers ($Ma = 0.1, 0.5, 0.966$) and three different reduced frequencies ($k = 1.0, 3.0, 15$) are conducted to examine their effect on the flutter for non-uniformly spaced blade rows. The average and standard deviation of the unsteady moment and aerodamping on each blade of non-uniformly spaced blade rows are plotted against the results from the uniformly spaced blade row.

3.3.4.1 Effect of Mach Number

The effect of Mach number is shown in Figure 3.28, Figure 3.29 and Figure 3.30 for the three non-uniformly spaced blade rows. In general, at medium Mach numbers the average of the unsteady loading is higher than, and the standard deviation of the unsteady loading is larger than, the corresponding values at low and high Mach numbers. At medium Mach number the average of the aerodamping is higher than, and the standard deviation of the aerodamping is larger than, the corresponding values at low and high Mach number. For the blade rows with alternating spacing and sinusoidal spacing, the average unsteady loading and the average aerodamping can be significantly different

from the values on the uniformly spaced blade row at most of the interblade phase angles. The blade row with sinusoidal spacing has the largest standard deviation of the unsteady loading and aerodamping. The blade row with one blade missing has the smallest standard deviation of the unsteady loading and aerodamping.

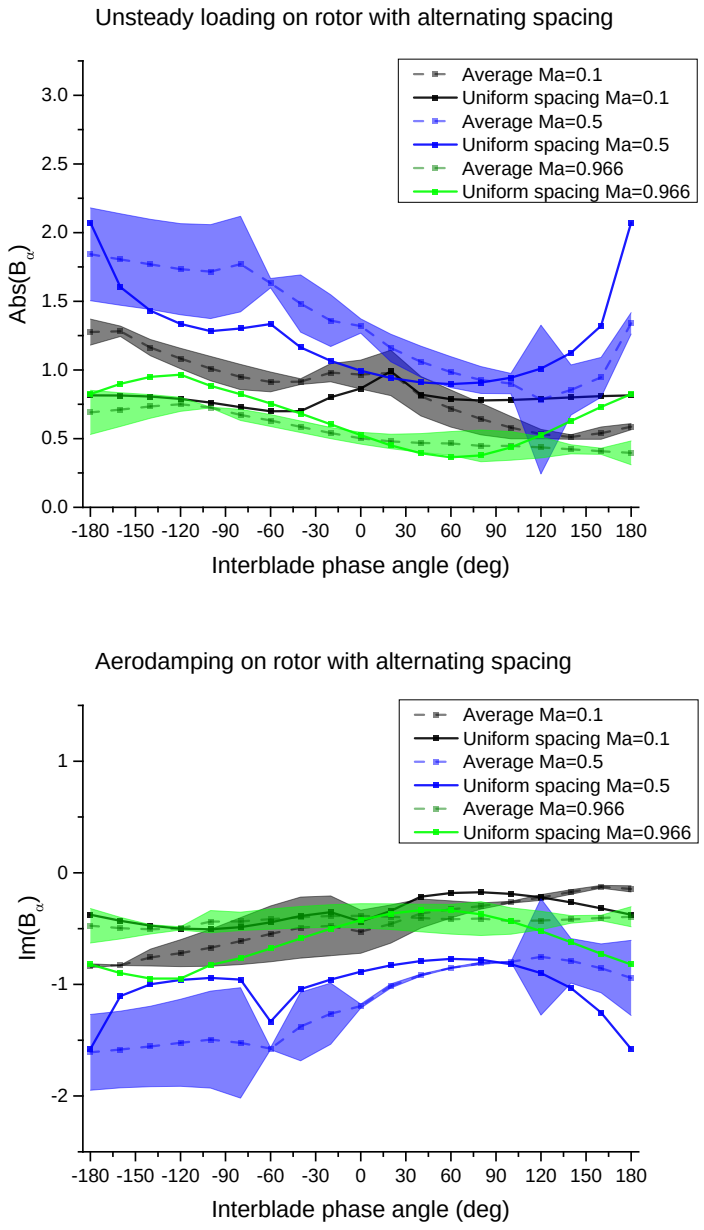

Figure 3.28. The average and standard deviation of $\mathrm{Abs}\left(B_\alpha\right)$ and $\mathrm{Im}\left(B_\alpha\right)$ on the blade row with alternating spacing at different Mach numbers.

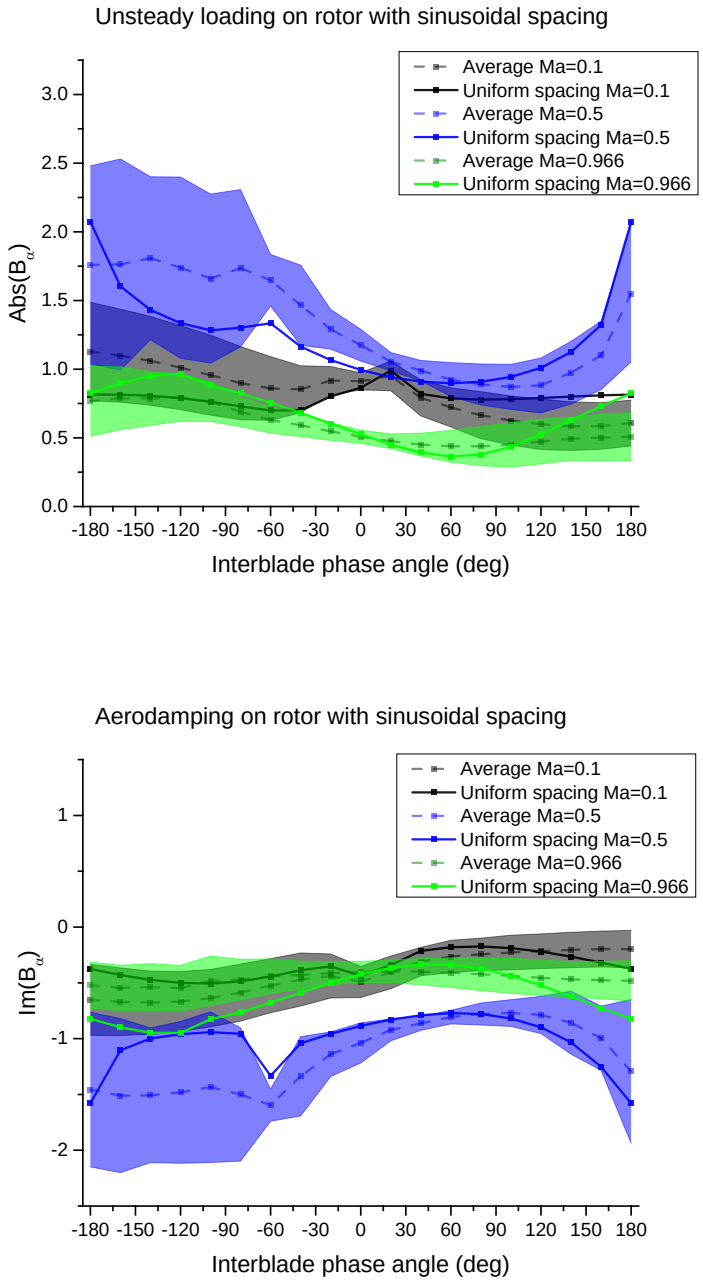

Figure 3.29. The average and standard deviation of $\mathrm{Abs}\left(B_\alpha\right)$ and $\mathrm{Im}\left(B_\alpha\right)$ on the blade row with sinusoidal spacing at different Mach numbers.

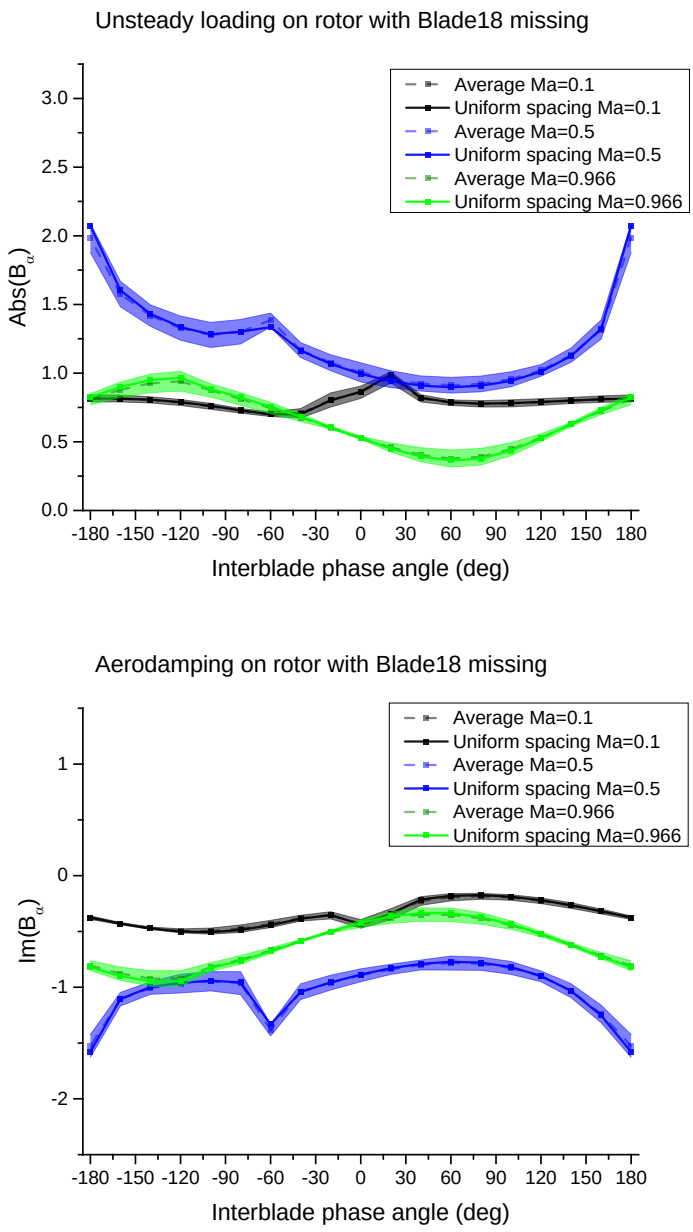

Figure 3.30. The average and standard deviation of $\mathrm{Abs}\left(B_\alpha\right)$ and $\mathrm{Im}\left(B_\alpha\right)$ on the blade row with one blade missing at different Mach numbers.

3.3.4.2 Effect of Reduced Frequency

The effect of reduced frequency is shown in Figure 3.31, Figure 3.32 and Figure 3.33 for the three non-uniformly spaced blade rows. In general, the higher the reduced frequency, the larger the average unsteady loading and the average of the aerodamping. The standard deviation of the unsteady loading and aerodamping also increase with the reduced frequency. Similar to the results at different Mach numbers, for the blade rows with alternating spacing and sinusoidal spacing, the average unsteady loading and average aerodamping can be significantly different from the values on the uniformly spaced blade row at most of the interblade phase angles. The blade row with sinusoidal spacing has the largest standard deviation for the unsteady loading and aerodamping. The blade row with one blade missing has the smallest standard deviation for the unsteady loading and aerodamping.

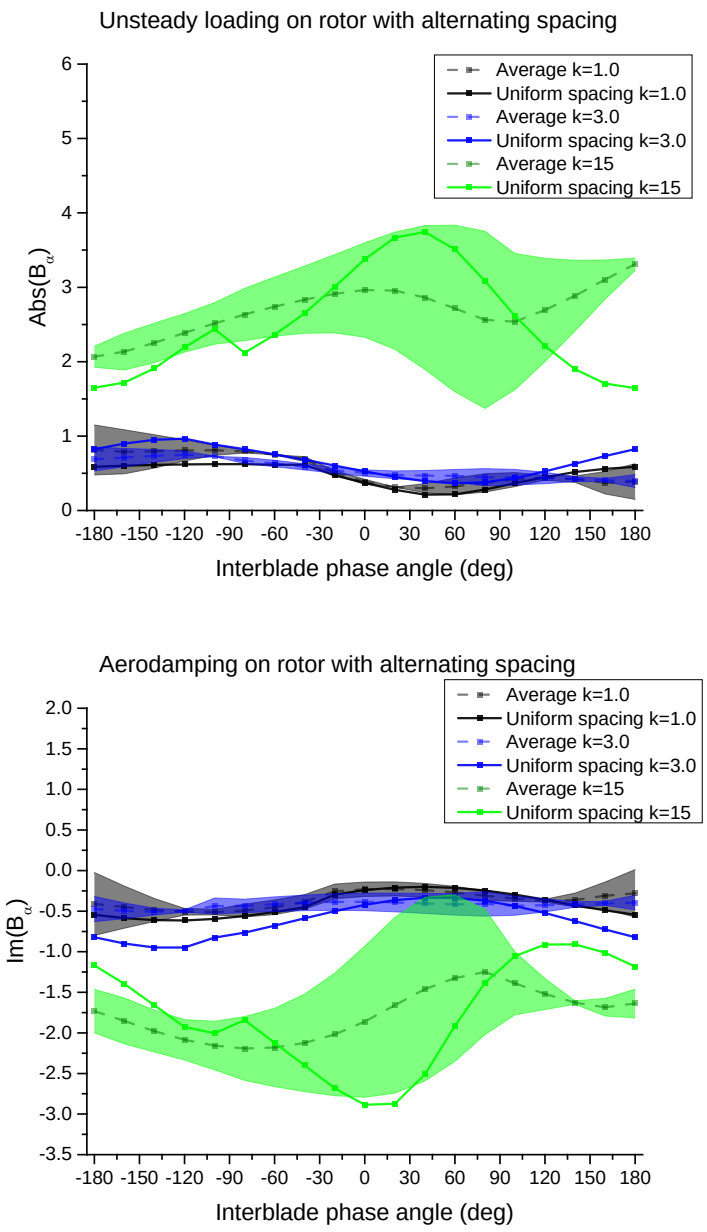

Figure 3.31. The average and standard deviation of $\mathrm{Abs}\left(B_\alpha\right)$ and $\mathrm{Im}\left(B_\alpha\right)$ on the blade row with alternating spacing at different reduced frequency.

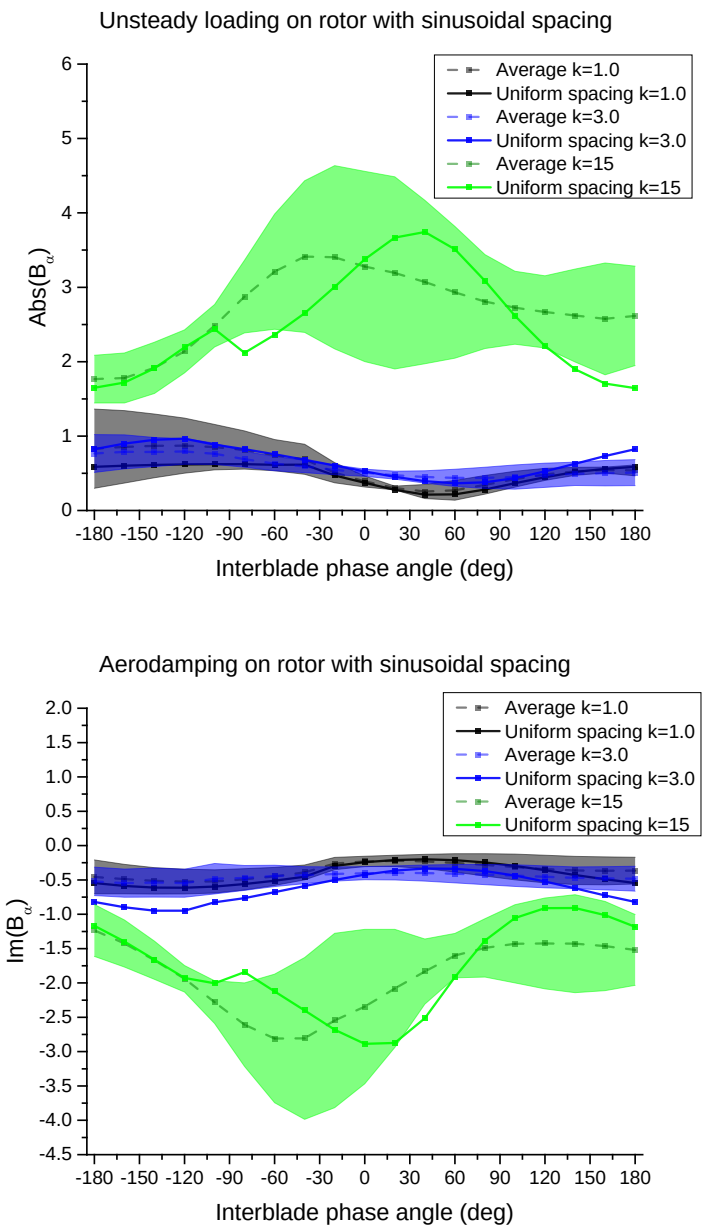

Figure 3.32. The average and standard deviation of $\mathrm{Abs}\left(B_\alpha\right)$ and $\mathrm{Im}\left(B_\alpha\right)$ on the blade row with sinusoidal spacing at different reduced frequency.

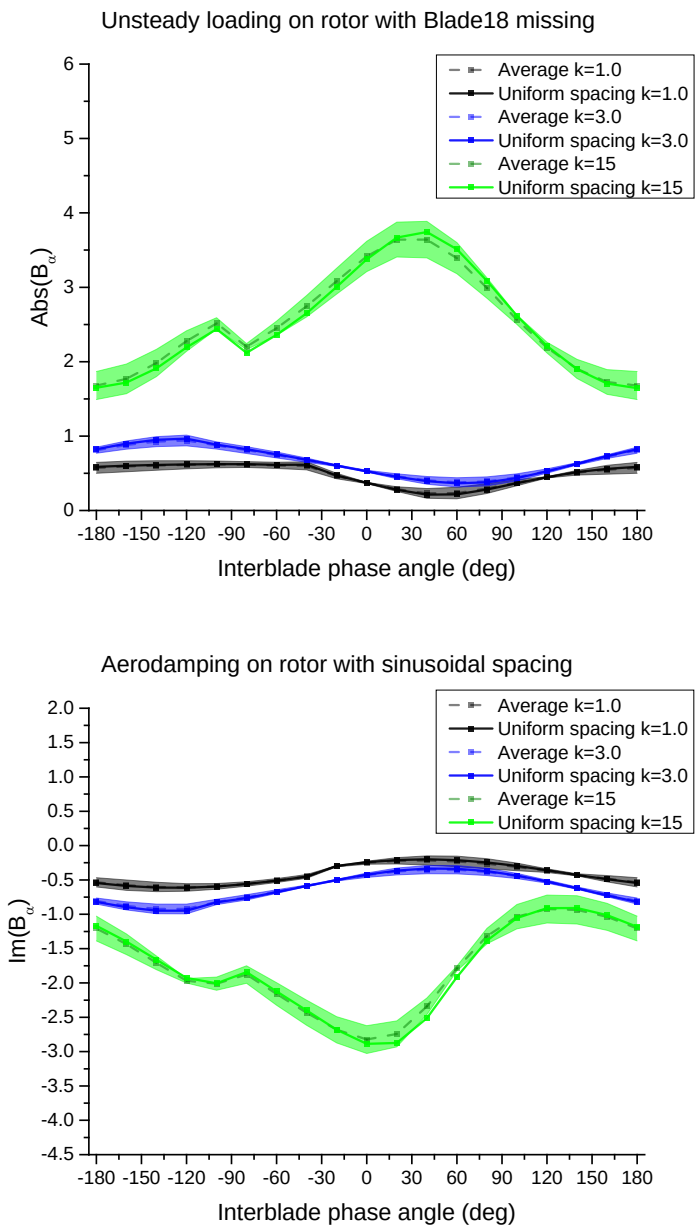

Figure 3.33. The average and standard deviation of $\mathrm{Abs}\left(B_\alpha\right)$ and $\mathrm{Im}\left(B_\alpha\right)$ on the blade row with one blade missing at different reduced frequency.

3.4 Summary

In this chapter, the generalized uniformly spaced flat plate cascade model is first validated by the uniformly spaced flat plate cascade model LINSUB and Sawyer's Detuned Cascade model. Case studies based on the geometry and flow condition of the Purdue Transonic Compressor rotor are then conducted to study the effect of different aerodynamic mistuning configurations on the forced response, flutter and acoustic behavior of the rotor at different excitation nodal diameters, Mach number and reduced frequency. The three different non-uniformly spaced patterns used in the analysis are the rotor blade with alternating spacing, with sinusoidal spacing and with one blade missing. Forced response analysis shows that the unsteady loading on the rotor due to the excitation of the IGV wake is different from blade-to-blade for a non-uniformly spaced blade row. The average unsteady loading on the three non-uniformly spaced blade rows are generally higher than the value on the blade row with uniform spacing over most of the blade chord and for most of the flow conditions. The standard deviation of the unsteady loading is the highest for the blade row with sinusoidal spacing, and is the lowest for the blade row with one blade missing. Parametric study shows that the higher the excitation nodal diameter and the higher the reduced frequency, the lower the average unsteady loading and smaller the standard deviation of the unsteady loading on the aerodynamically mistuned blade row. There is no clear trend on how the Mach number affects the unsteady loading on the aerodynamically mistuned blade row.

Acoustic analysis shows that the acoustic energy of the propagating pressure waves generated on the rotor due to the excitation of the IGV wake spread out over more frequency components for the non-uniformly spaced blade row than the uniformly spaced blade row. The spectrum comparison among the blade rows with different aerodynamically mistuned patterns shows that the non-uniformly spaced blade row with larger spacing variation tends to generate a more broadband-like noise than the typical discrete tone noise generated by the uniformly spaced rotor row. Parametric study shows that in general the higher the wake excitation nodal diameter ND, the lower the strength of the output pressure wave over the spectrum.

Flutter analysis shows that blades on a non-uniformly spaced blade row experience different unsteady loading and aerodamping from the blades on a uniformly spaced blade row. Some blades with a non-uniformly spaced blade row may become unstable at certain interblade phase angles and under certain operating conditions when the corresponding uniformly spaced blade row has no flutter problem. The average unsteady loading and the average aerodamping of a non-uniformly spaced blade row can be significantly different from the values on the uniformly spaced blade row at most of the interblade phase angles. The blade row with sinusoidal spacing has the largest standard deviation of the unsteady loading and aerodamping. Parametric study shows that a higher reduced frequency leads a larger average and standard deviation of unsteady loading and aerodamping, while there is no clear trend on the effect of Mach number.

CHAPTER 4. MULTISTAGE INTERACTION MODEL RESULTS

In this chapter, validations and case studies for the multistage interaction model developed in Section 2.5 are presented. The pre-processing and post-processing procedure to use the multistage interaction model are given first in Section 4.1 and Section 4.2. The validation is then conducted for both forced response analysis and flutter analysis in a multistage environment by comparing with the results from Hall & Silkowski's work in Section 4.3. Based on the geometry and flow conditions of the Purdue 3-Stage Research Compressor introduced in Section 4.4, a series of case studies are done in Section 4.5 to investigate the multistage interaction effect (by varying inter-row spacing and vane clocking positions) on the forced response, flutter and aeroacoustic behavior of the embedded rotor row.

4.1 Pre-processing

Besides the geometry and flow condition of each blade row, initial excitations and involved spinning modes need to be given as inputs to the multistage interaction model. Due to the scattering effect, a single mode initial excitation is scattered into an infinite set of spinning modes at each blade row. Involving an infinite set of spinning modes is certainly not feasible for a numerical study. Thus important modes need to be specified in the input in order to be included in the multistage analysis.

As discussed in Section 2.5.3, a spinning mode is characterized by its unique frequency and nodal diameter, which are in turn determined by the group of scattering indices (n_1, n_2, n_3). The initial excitation mode is the fundamental spinning mode, which corresponds to scattering indices $(0, 0, 0)$. When choosing the scattering indices, the fundamental mode should always be included and then the modes with lower nodal

diameter should be chosen first, since the lower the nodal diameter, the more likely the mode is cut-on. In addition, the set of modes should also be chosen to ensure the connectivity of each mode to the fundamental mode. Usually a "symmetric" set of scattering indices is recommended. For example, one can start with $n = -1, 0, 1$ for each blade row which gives $3 \times 3 \times 3 = 27$ different (n_1, n_2, n_3) spinning modes for a three blade rows system. Then the scattering indices is increased to $n = -2, -1, 0, 1, 2$ which gives $5 \times 5 \times 5 = 125$ different (n_1, n_2, n_3) spinning modes. The range of the scattering indices should be increased until the convergence is achieved, i.e. when including the additional modes does not change the strengths of current modes significantly.

The initial excitation is specified in the vector $[b]$ in Equation (2.103) or specified as an incoming unsteady wave boundary condition from far upstream or far downstream. If the initial excitation is the upstream going pressure wave, its strength b_1 should be specified in the blade row downstream of the excited blade row. If the initial excitation is the downstream going pressure wave or vorticity wave, its strength b_2, b_3 should be specified in the blade row upstream of the excited blade row. If the initial excitation is the upstream going pressure wave from the far downstream or downstream going pressure wave and vorticity wave from far upstream, their strength should be specified at the last blade row or the first blade row respectively as an incoming unsteady wave boundary condition. If the initial excitation is due to blade vibration itself, the strength of the all three outgoing unsteady waves due to the blade vibration should be calculated first and then specified in the excited blade row.

4.2 Post-processing

The direct solution of the multistage analysis model is the strength of the unsteady pressure and vorticity waves for each spinning mode at each blade row. Depending on the applications, the direct solution needs to be post-processed in different ways.

For a forced repose analysis, an external excitation is specified to excite a certain vibration mode of a blade row of interest. The total unsteady loading on the blade row at

the initial excitation frequency is the desired result. For each spinning mode at the initial excitation frequency, the three incoming wave strengths on the blade row is first extracted from the direct solution $\left[P^+, P^-, \zeta\right]$. The incoming waves strength multiplying the unsteady aerodynamic influence coefficient $\left[A_u \quad A_d \quad A_G\right]$ and $\left[B_u \quad B_d \quad B_G\right]$ gives the unsteady lift and unsteady moment respectively. The summation of the unsteady loading from the three incoming waves gives the total unsteady loading for the spinning mode $(A_u P^+ + A_d P^- + A_G \zeta)$, $(B_u P^+ + B_d P^- + B_G \zeta)$. The summation of the unsteady loading from all the spinning modes having the initial excitation frequency is the desired total unsteady loading on the blade row at the natural frequency of the vibration mode. $\sum (A_u P^+ + A_d P^- + A_G \zeta)_q$, $\sum (B_u P^+ + B_d P^- + B_G \zeta)_q$.

With the total unsteady loading, the vibration amplitude can be calculated based on the structural dynamics model in Section 2.1. Take the torsional vibration as an example. Neglecting structural damping, and since the excitation frequency is equal to the natural frequency of the blade row $\omega = \omega_\alpha$, Equation (2.8) becomes

$$\bar{\alpha} = -\frac{B_G \bar{\zeta} + B_u \overline{P^+} + B_d \overline{P^-}}{B_\alpha} \tag{4.1}$$

Considering multi-blade row interaction, the secondary excitation waves with the frequency equal to the resonant frequency $(i = 1 \text{ to } n)$ should also be included, so the final blade vibration angle is

$$\bar{\alpha} = -\frac{\sum_{i=1}^{n} \left(B_{G,i} \bar{\zeta}_i + B_{u,i} \overline{P^+}_i + B_{d,i} \overline{P^-}_i \right)}{\sum_{i=1}^{n} B_{\alpha,i}} \tag{4.2}$$

For a flutter analysis, the internal excitation due to the blade vibration itself is specified at the blade row of interest. For axial compressor blades, the flutter frequency is usually very close to the natural frequency of a certain blade vibration mode. Similar to forced response, the total unsteady loading on the vibrating blade row from all the spinning modes which have the same frequency as the internal excitation frequency is the desired result. The total unsteady loading needs to be calculated at all possible interblade

phase angle of the blade row of interest. If the aerodamping derived from the total unsteady loading is negative, the blade row is prone to flutter.

For an acoustic analysis, only the propagating (cut-on) pressure waves are considered. Since the direct solution of the multistage model is the result after the “steady state” has been reached, the strength of the upstream going pressure wave from the first blade row and the strength of the downstream going pressure wave from the last blade row of the cut-on spinning modes are the desired results. If the first blade row or the last blade row is not a stator row, the frequency of the outing pressure waves needs to be shifted to a stationary reference frame.

4.3 Validation

The validation of the multistage interactions model developed in this study is done by comparing the results of the two case studies in Hall & Silkowski’s work [12]. The first case study is a forced response analysis with two blade rows. The second case study is a flutter analysis with three blade rows.

4.3.1 Validation Case 1: Forced Response Analysis with Two Blade Rows

This case study is based on configuration A in Hall & Silkowski’s work [12]. It is a rotor/stator two blade row combination. The upstream rotor generates a wake and then interacts with the downstream stator. The stage geometry and operating conditions are shown in the Table 4.1.

Table 4.1. Blade row parameters for Configuration A.

Validation case configuration A		
	Rotor	**Stator**
Blade numbers	38	50
Chord	1.00	0.57
Radius	4.54	4.54
Stagger angle (degree)	-60	0
Chordwise velocity	1	0.5
Mach number	0.6 to 0.9	0.3 to 0.45
Rotation speed (rad/s)	0.1909	----------
Inter-row spacing	1.5	----------

Totally nine modes are considered during the rotor-stator interaction process. The modes are $(n_1, n_2) = (0, -1), (0, 0), (0, 1), (0, 2), (-1, -2), (-1, -1), (-1, 0), (-1, 1), (-1, 2)$. The resulting unsteady lift on the stator at the first and second blade passing frequencies 1BPF 2BPF, and unsteady lift on rotor at the first and second vane passing frequencies 1VPF 2VPF at different rotor relative Mach numbers are shown in Figure 4.1 and Figure 4.2. The current results are in a very good agreement with Hall & Silkowski's results except for a small difference in the unsteady lift on the rotor at 2VPF at high Mach number. This is probably due to the round-off errors because the unsteady lift on rotor at 2VPF due to reflected pressure wave is very small (the numerical value is around 1e-5 as shown in the Figure 4.2.

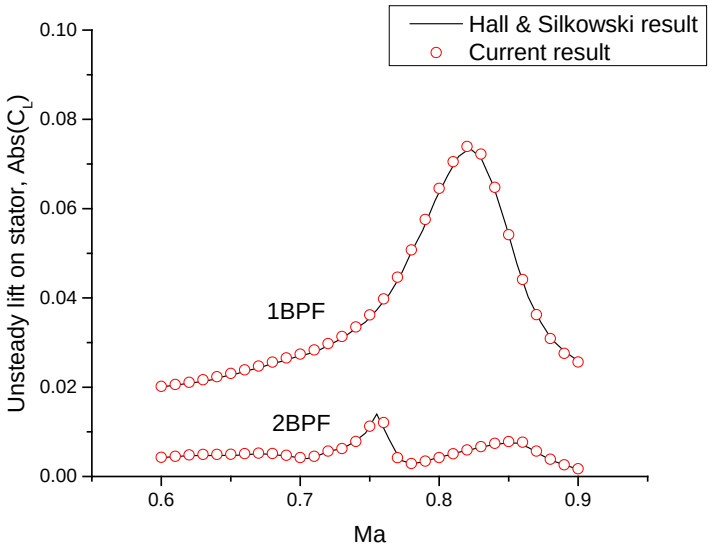

Figure 4.1. Comparison of the unsteady lift on stator for Configuration A.

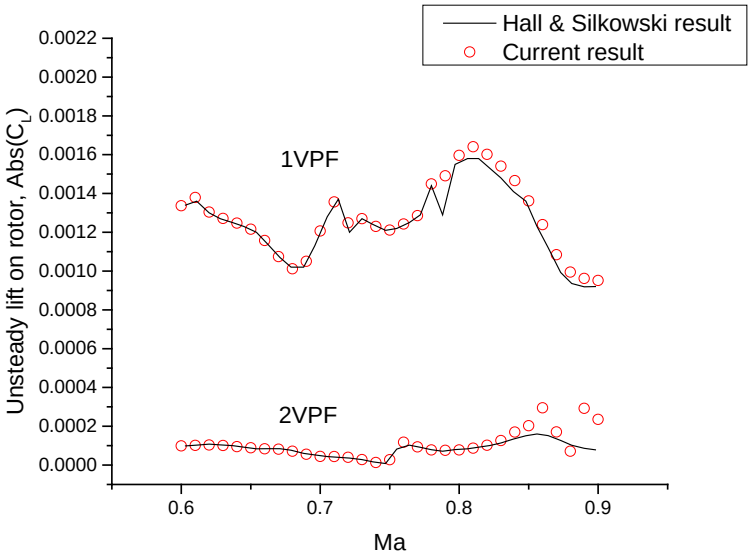

Figure 4.2. Comparison of the unsteady lift on rotor for Configuration A.

4.3.2 Validation Case 2: Flutter Analysis with Three Blade Rows

This case study is based on configuration B in Hall & Silkowski's work [12]. It is a stator/rotor/stator three blade row combination. The rotor is vibrating with a bending motion. It generates pressure waves and a vorticity wave which interact with the surrounding stators. The stage geometry and operating conditions are given in Table 4.2. Note that the sign difference from the rotation speed in Table 2 of Hall & Silkowski's work is due to a different convention. In this work, the positive rotation direction is defined as the same as the positive y direction as shown in Figure 2.5.

Table 4.2. Blade row parameters for Configuration B.

Validation case configuration B			
	Stator1	**Rotor**	**Stator2**
Blade numbers	72	72	72
Chord	1.00	1.00	1.00
Radius	8.59	8.59	8.59
Stagger angle (degree)	45	-45	45
Chordwise velocity	1.0	1.0	1.0
Mach number	0.7	0.7	0.7
Rotation speed (rad/s)	0	0.1645	0
Inter-row spacing	0.2	0.2	----------
Excitation frequency (rad/s)	----------	1.0	----------
Excitation phase angle (degree)	----------	-180 to 180	----------

Totally nine modes are considered during the stator-rotor-stator interaction process. The modes are $(n_1, n_2) = (-1, -1), (-1, 0), (-1, 1), (0, -1), (0, 0), (0, 1), (1, -1), (1, 0), (1, 1)$. For this flutter analysis, the real and imaginary parts of the resulting unsteady lifts on the rotor at all possible inter-blade phase angles are shown in Figure 4.3 and Figure 4.4. The current results are in a very good agreement with Hall& Silkowski's results except for a small difference in the imaginary part of the unsteady lift on the rotor around inter-blade phase angle 140 degrees. This is may be due to round-off errors too.

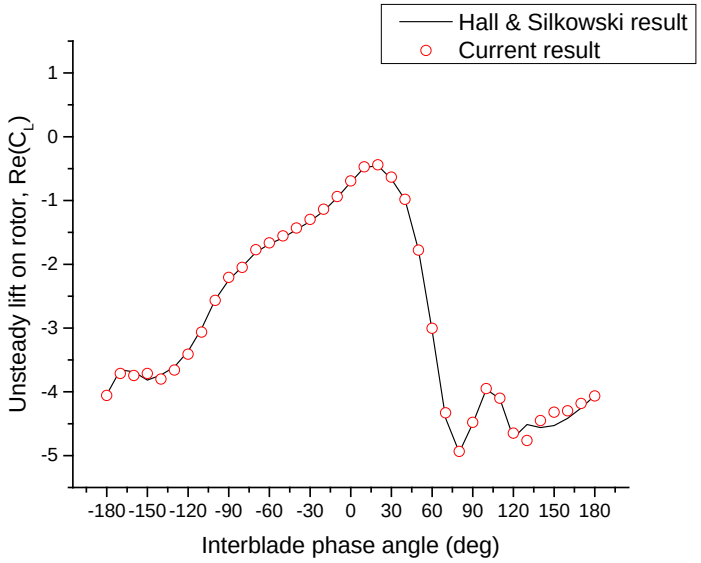

Figure 4.3. Comparison of the real part of the unsteady lift on rotor for Configuration B.

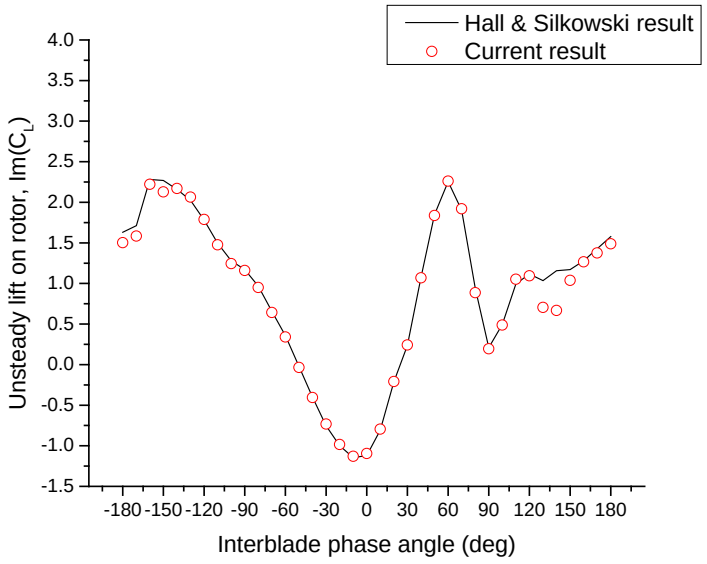

Figure 4.4. Comparison of the imaginary part of the unsteady lift on rotor for Configuration B.

4.4 Purdue 3-Stage Research Compressor

The Purdue 3-Stage Research Compressor is a highly loaded axial compressor aerodynamically representative of the aft stages of a Rolls-Royce high pressure compressor [44]. The compressor consists of an inlet guide vane, three integrally bladed rotors (IBRs) and three stator rows (Figure 4.5). The design speed is 5000rpm at which is the corrected mass flow rate is around 20lbm/s. The mean diffusion factors are from 0.433 to 0.464. The design overall pressure ratio is 1.31. The hub and tip diameter are 20 inches and 24 inches, respectively. The detailed blade row information is listed in Table 4.3

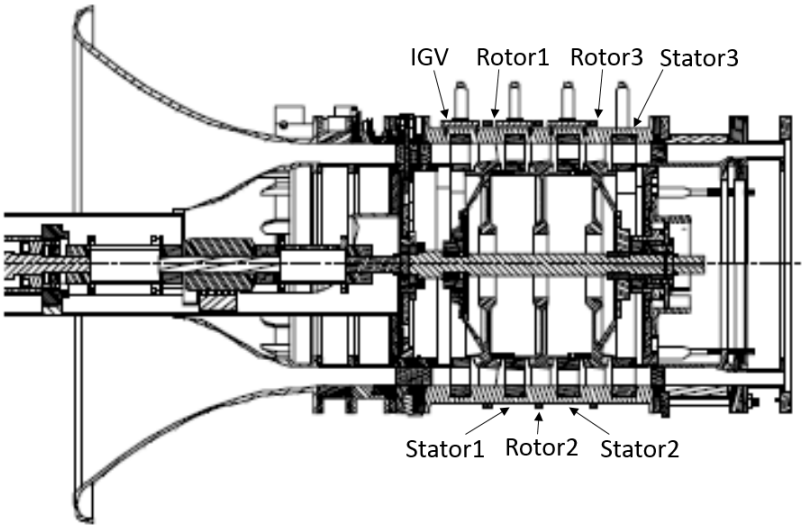

Figure 4.5. Purdue 3-Stage Research Compressor cross section.

Table 4.3. Purdue 3-Stage Research Compressor detailed blade row information.

Stage	**Hub Stagger (degree)**	**Tip Stagger (degree)**	**Hub Chord (inch)**	**Tip Chord (inch)**	**Number of blades**	**Blade airfoil type**
IGV	8.2	9.0	2.00	2.00	44	DCA
Rotor 1	32.6	47.8	2.46	2.81	36	DCA
Stator 1	25.6	24.0	2.11	2.11	44	NACA 65 series
Rotor 2	35.4	49.8	2.60	2.96	33	DCA
Stator 2	26.1	24.6	2.22	2.22	44	NACA 65 series
Rotor 3	38.2	51.8	2.75	3.13	30	DCA
Stator 3	19.7	18.1	2.35	2.35	50	NACA 65 series

An ANSSYS finite element analysis was performed to predict Rotor2's mode shapes and corresponding natural frequencies [44]. The Campbell diagram for Rotor2 is shown in Figure 4.6. The primary excitation on Rotor2 is the wake from Stator1 and the potential field from both Stator1 and Stator2. The resonant condition closest to the design operation speed is the first torsion mode intercepting 44E line at approximately 3700rpm. The ANSYS analysis also shows that the first torsion mode is blade dominated and the natural frequency approximately stays the same over all possible nodal diameters.

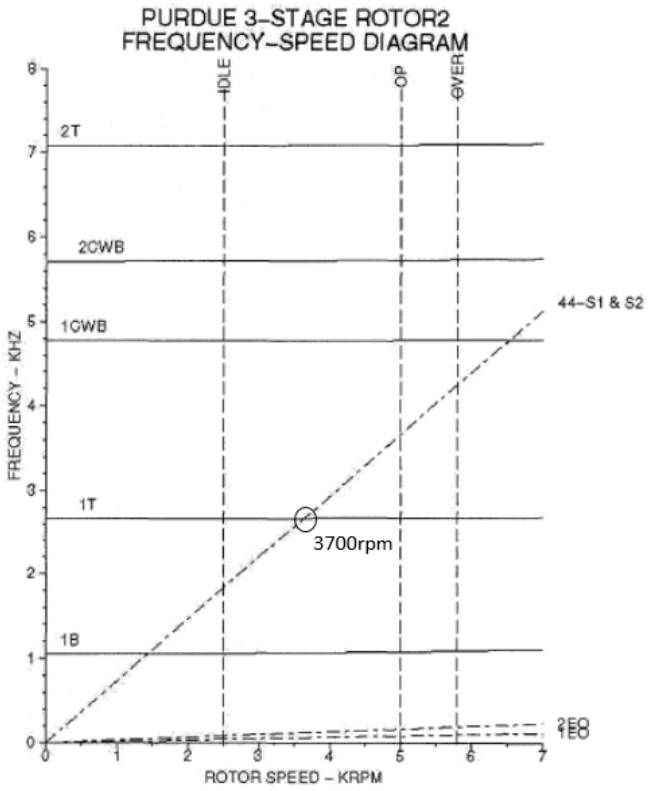

Figure 4.6. Rotor2 Campbell diagram [44].

The vane clocking experiments were performed on Stator1, Rotor2 and Stator2 at the design loading operating condition [16]. The resonant vibration amplitude of the first torsion mode of Rotor2 was measured by an Agilis Non-intrusive Stress Measurement System (NSMS) at different clocking configurations defined by the Stator1 percent vane passage (vp) location minus the Stator2 percentage vp position. Six clocking configurations were tested in this study. They are 0%, 15%, 32%, 49%, 66% and 83% of

vp and denoted as CL-1, CL-2, CL-3, CL-4, CL-5 and CL-6, respectively (Figure 4.7). During the clocking, both stator1 and IGV relative position and stator2 and stator3 relative position were kept fixed. The NSMS data were collected during a constant transient through the resonance at 3700RPM at a sweep rate of 4.5 RPM/s.

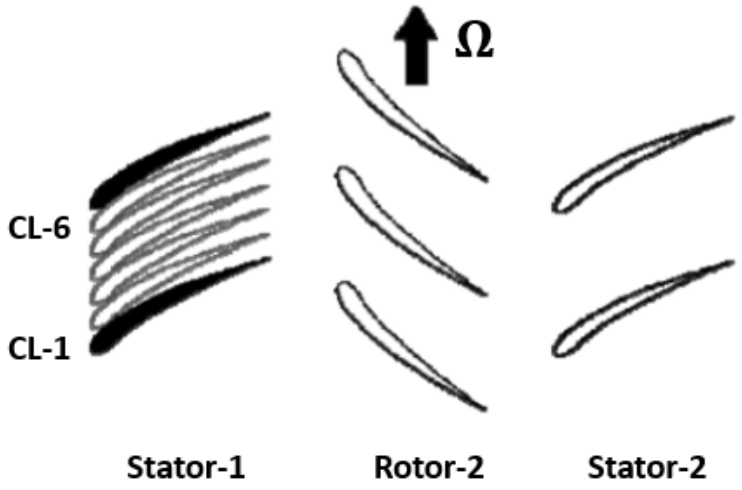

Figure 4.7. Schematics of vane clocking configurations [16].

4.5 Case Studies

Based on Purdue 3-Stage Research Compressor's geometry and operating condition, case studies using the multistage interaction model are conducted on the stator1-rotor2-stator2 of Purdue 3-Stage Research Compressor at 4 inter-row axial spacings and 6 vane clocking positions. The effect of axial spacing (i.e. Δx) and vane clocking (i.e. Δy) on the forced response and flutter of the rotor, and acoustic behavior due to multi blade row interactions were analyzed systematically in the following sections. This study explores the potential of varying inter-row axial spacing and vane clocking as passive techniques to reduce the aeromechanic and aeroacoustics problems in a multistage environment.

The transient operating condition at 3700rpm is used for the forced response analysis and corresponding acoustic analysis on the rotor. The design operating condition at 5000rpm is used for the rotor flutter analysis. The first torsion mode is the structural

mode of interest. The geometry and flow field in stator1-rotor2-stator2 was modified a little in order to accommodate the flat plate cascade model uses in the multistage interaction analysis. The modified geometry and flow condition is listed in Table 4.4

Table 4.4. The modified geometry and flow conditions of Purdue 3-Stage Research Compressor used in multistage interaction analysis.

Purdue 3 stage compressor			
	Stator1	**Rotor2**	**Stator2**
Blade numbers	44	33	44
Chord(in)	2.11	2.96	2.22
Radius(in)	12	12	12
Stagger angle (degree)	-24.3	49.8	-24.3
Chordwise velocity (in/s)	3120 / 4216	4406 / 5954	3120 / 4216
Mach number	0.2331 / 0.3150	0.3292 / 0.4449	0.2331 / 0.3150
Rotation speed (rad/s)	0	-387.46/-523.60	0
Inter-row spacing (in)	0.65 (0.2, 1.3, 10)	0.65 (0.2, 1.3, 10)	----------
Vane clocking (% of vane passage gap)	0%, 15%, 32%, 49%, 66%, 83%	----------	0

The first chordwise velocity and Mach number corresponds to the lower rotational speed, 387.46rad/s which is the 3700rpm transient operating condition used for forced response analysis. The second chordwise velocity and Mach number corresponds to the higher rotational speed, 523.60 rad/s which is the 5000rpm design operating condition used for flutter analysis.

In the following case studies, the 4 inter-row spacings used are 0.2in, 0.65in, 1.3in and 10in measured from the upstream blade row trailing edge to the downstream blade row leading edge. The inter-row spacing of 0.65in is the standard configuration used in Purdue 3-Stage Research Compressor. The extra-long inter-row spacing of 10in is used to compare the results from the multistage analysis with the one from the single blade row model LINSUB.

4.5.1 Mode Convergence Study

To determine how many spinning modes are needed to represent the unsteady waves in Purdue 3-Stage Research Compressor, a convergence study was conducted to calculate the unsteady moment on Rotor2 due to both external excitations from Stator1 and Stator2 and internal excitation due to the torsional vibration itself. Since Stator1 and Stator2 have the same geometry and similar flow fields, Stator2 can be considered as a repeated blade row of Stator1. Thus each spinning mode has the same properties in Stator1 and Stator2. A pair of scattering indexes from Stator1 and Rotor2 (n1, n2) is sufficient to specify a spinning mode.

With one mode ($n_1 = 0$, $n_2 = 0$), 9 modes ($n_1 = -1 \sim 1$, $n_2 = -1 \sim 1$), 25 modes ($n_1 = -2 \sim 2$, $n_2 = -2 \sim 2$) and 49 modes ($n_1 = -3 \sim 3$, $n_2 = -3 \sim 3$), the unsteady moment on Rotor2 due to a unit strength Stator1 wake, due to a unit strength pressure wave from Stator1 (i.e. Stator1 potential field), due to a unit strength pressure wave from Stator2 (i.e. Stator2 potential field) and a unit rotor blade torsional vibration amplitude C_{m_G}, C_{m_d}, C_{m_u} and C_{m_α} are calculated using the multistage interaction model at standard inter-row spacing with no vane clocking. All the excitations have nodal diameter $ND = -44$ and frequency $\omega = 17048\, rad/s$ (i.e. the resonant point at the interception of the 1T and 44E lines at 3700rpm on the rotor Campbell diagram Figure 4.6). Both the real part and imaginary part of these unsteady moment on Rotor2 are shown in Figure 4.8.

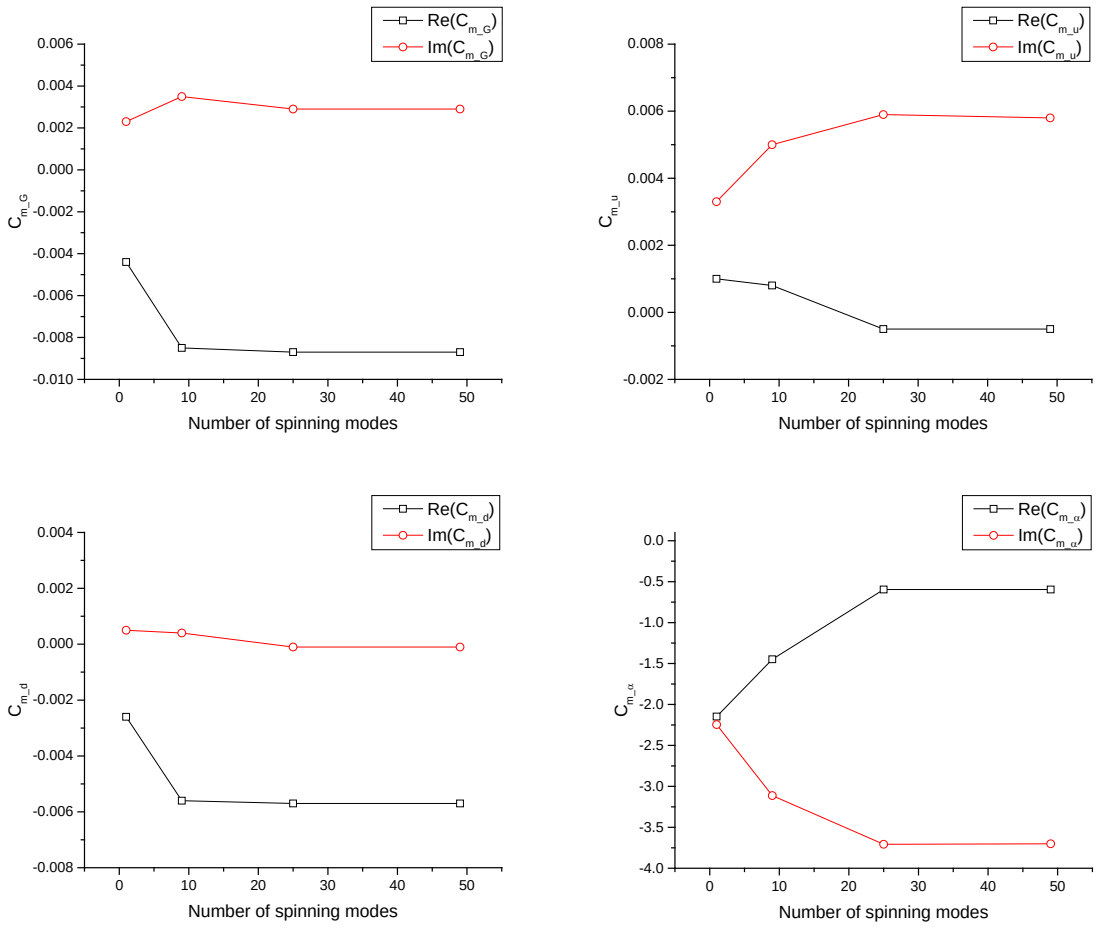

Figure 4.8. Convergence study of the unsteady moment on Rotor2 due to different excitations using different number of spinning modes.

From Figure 4.8, the unsteady moment calculated using 25 modes and 49 modes are very close. Thus it can be concluded that 25 spinning modes ($n_1 = -2 \sim 2$, $n_2 = -2 \sim 2$) are enough to represent the major unsteady waves for the multistage interaction analysis for the Purdue 3-Stage Research Compressor's geometry and operating conditions. The detailed properties of the 25 spinning modes are listed in the Table 4.5

Table 4.5. Detailed properties of the 25 spinning modes.

Mode #	n_1	n_2	ND	ω_1 (rad/s)	ω_2 (rad/s)	Upstream going pressure wave axial wave number
1	-2	-2	-198	-25573	51144	-0.0729 -16.8820i
2	-2	-1	-165	-12786	51144	0.0809 -14.0661i
3	-2	0	-132	0	51144	0.2348 -11.2026i
4	-2	1	-99	12786	51144	0.3886 - 8.2422i
5	-2	2	-66	25572	51144	0.5425 - 5.0160i
6	-1	-2	-154	-25573	34096	-0.1512 -13.1138i
7	-1	-1	-121	-12786	34096	0.0027 -10.3189i
8	-1	0	-88	0	34096	0.1565 - 7.4684i
9	-1	1	-55	12786	34096	0.3104 - 4.4571i
10	-1	2	-22	25572	34096	1.5842 + 0.0000i
11	0	-2	-110	-25573	17048	-0.2294 - 9.3184i
12	0	-1	-77	-12786	17048	-0.0756 - 6.5569i
13	0	0	-44	0	17048	0.0783 - 3.7342i
14	0	1	-11	12786	17048	0.7921 + 0.0000i
15	0	2	22	25572	17048	0.3859 - 0.4687i
16	1	-2	-66	-25573	0	-0.3077 - 5.4389i
17	1	-1	-33	-12786	0	-0.1539 - 2.7195i
18	1	0	0	0	0	-0.0000 + 0.0000i
19	1	1	33	12786	0	0.1538 - 2.7195i
20	1	2	66	25572	0	0.3077 - 5.4390i
21	2	-2	-22	-25573	-17048	-0.3860 - 0.4686i
22	2	-1	11	-12786	-17048	-0.7921 + 0.0000i
23	2	0	44	0	-17048	-0.0783 - 3.7342i
24	2	1	77	12786	-17048	0.0756 - 6.5569i
25	2	2	110	25572	-17048	0.2294 - 9.3184i

From Table 4.5, Modes 11,12,13,14,15 have the same excitation frequency as the initial excitation on the Rotor 2. Thus the summation of these modes' unsteady loading are used for the forced response and flutter analyses. By examining the axial wave number of the pressure waves, it can be seen that Modes 10, 14 and 22 are the propagating modes. Their strengths are calculated for the acoustic analysis.

4.5.2 Forced Response Analysis

At 3700rpm the wake from Stator1 and potential fields of Stator1 and Stator2 excite the first torsion mode of the rotor. Due to the linearity of the model, different excitations can be treated independently. The total unsteady loading is the sum of the results from each excitation. In the Rotor2 reference frame, these excitations have nodal diameter $ND = -44$ and frequency $\omega = 17048\,\text{rad/s}$. They are the primary excitation mode corresponding to mode 13.

4.5.2.1 Unsteady Loading

The unsteady moment on the rotor due to a unit strength Stator1 wake C_{m_G} at 4 different inter-row spacings and 6 different vane clocking positions is shown in Figure 4.9. The results from the multistage model are normalized by the result from the single isolated row model LINSUB in order to show the effect of the multistage interactions.

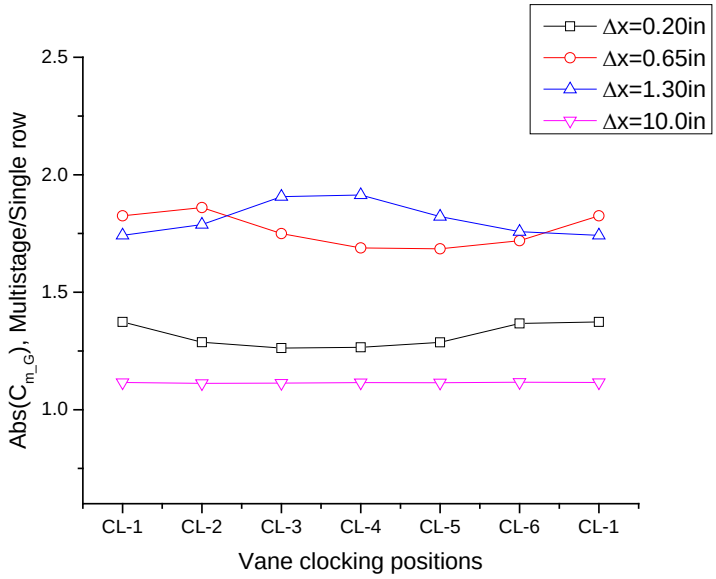

Figure 4.9. Normalized Rotor2 unsteady moment due to Stator1 wake at different inter-row axial spacings and different vane clocking positions.

Note first that the unsteady moment on the rotor considering the multistage effect is higher than the one from the single row analysis. When the inter-row spacing is 1.3in, the ratio is close to 2 at the third and fourth vane clocking position. Even with the extra-long inter-row spacing of 10in, the ratio is still larger than one (close to 1.1). The additional unsteady moment with the extra-long inter-row spacing comes from the cut-on secondary excitation modes (mode 10, 14, 22) whose amplitudes do not decay as they propagate in the inter-row space. Especially mode 14 has the same frequency as the primary excitation mode 13, and thus contributes to the unsteady moment on the rotor directly.

Secondly, even with a single primary excitation (Stator1 wake in this case), the unsteady moment on the rotor still varies with vane clocking position. The maximum variation (defined as (max-min)/average) at different vane clocking positions is 8.5%, 10%, 9.4%, and 0.4% with inter-row spacing of 0.2in, 0.65in,1.3in and 10in, respectively. The variation of unsteady loading on the rotor due to a single excitation fundamentally results from the multistage interaction with the blade row scattering effect. If there is no multistage interaction, the vane clocking of Stator1 only changes the phase of the Stator1 wake impinging on Rotor2. The amplitude of the wake excitation on rotor2 stays the same, and thus the resulting unsteady moment on rotors stays the same. In addition, blade row scattering also plays an important role. If only the primary excitation mode is retained in the multistage model (i.e. ignore the scattering effect), a single primary excitation will NOT cause variation of unsteady moment amplitude on Roror2 at different vane clocking position. This can be seen in Figure 4.10.

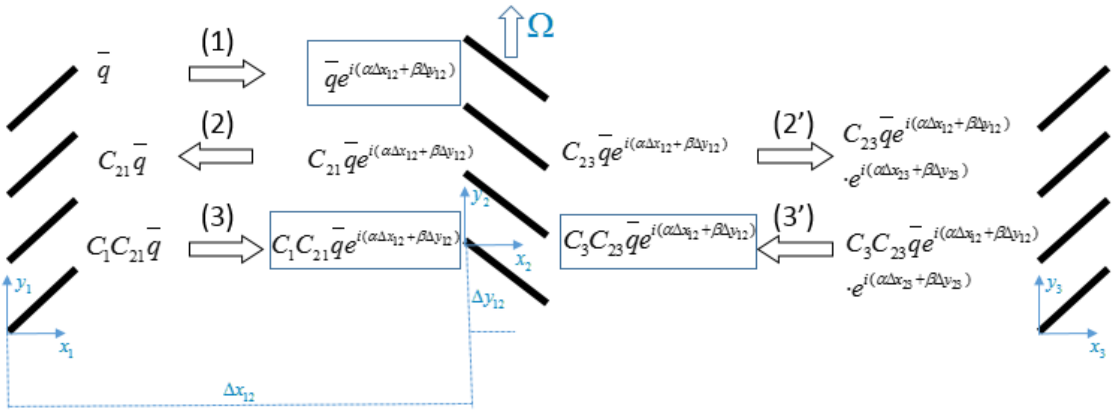

Figure 4.10. Schematic of the vane clocking effect on rotor unsteady loading with only one primary excitation and no scatting effect.

A single primary excitation from Stator1 of strength $\bar{q}$ travels downstream to Rotor2 and becomes $\bar{q}e^{i(\alpha\Delta x_{12}+\beta\Delta y_{12})}$ (Figure 4.10, step 1) The interaction with the rotor generates an upstream going wave of strength $C_{21}\bar{q}e^{i(\alpha\Delta x_{12}+\beta\Delta y_{12})}$ and downstream going wave of strength $C_{23}\bar{q}e^{i(\alpha\Delta x_{12}+\beta\Delta y_{12})}$. The upstream going wave travels to Stator1 and becomes $C_{21}\bar{q}$ (step 2). Reflected from Stator1, the strength changes to $C_1C_{21}\bar{q}$ which again travels downstream and becomes a secondary excitation on the rotor of strength $C_1C_{21}\bar{q}e^{i(\alpha\Delta x_{12}+\beta\Delta y_{12})}$ (step 3). Similarly the downstream going wave from the rotor is reflected back from Stator 2 and becomes a secondary excitation on the rotor of strength $C_3C_{23}\bar{q}e^{i(\alpha\Delta x_{12}+\beta\Delta y_{12})}$ (step 2', 3'). Thus after the "steady state" has been reached, the total excitation on Rotor2 after the multistage interactions is the single primary excitation and two additional secondary excitations $\bar{q}e^{i(\alpha\Delta x_{12}+\beta\Delta y_{12})}+C_1C_{21}\bar{q}e^{i(\alpha\Delta x_{12}+\beta\Delta y_{12})}+C_3C_{23}\bar{q}e^{i(\alpha\Delta x_{12}+\beta\Delta y_{12})}$. The vane clocking done on Stator1 changes the relative circumferential position between Stator1 and Rotor2, i.e. Δy_{12}. This changes the phase of the total excitation on rotor2, but the amplitude $\left|\bar{q}+C_1C_{21}\bar{q}+C_3C_{23}\bar{q}\right|$ stays the same.

Thus the variation of the unsteady loading on rotor2 due to a single primary excitation is the total effect of the primary excitation mode and the additional scattered modes which couples the three blade rows. Due to different axial and tangential wave numbers of each mode, the phase of each mode's effect on Rotor 2 are different. The constructive and destructive summation of all modes causes the variation with vane clocking positions.

Besides the variation of the unsteady loading, the inter-row axial spacing also affects the average of the unsteady loading on rotor2 at different vane clocking positions. The average values are 1.31, 1.75, 1.82 and 1.11 with inter-row spacing of 0.2in, 0.65in,1.3in and 10in respectively. Since different modes have different axial wave numbers, different inter-row axial spacing changes the inter-row coupling behavior differently. Note that the smaller inter-row spacing does mean a stronger inter-row coupling, but does not necessarily lead to a lower average or variation of the unsteady loading on the rotor at different vane clocking positions. This is because of the complicated constructive and destructive addition of unsteady waves of the spinning modes. At the extra-large inter-row spacing of 10in, the inter-row coupling becomes much weaker, and thus both the average and variation of the loading become smaller, although it is still different from the result from the single blade row analysis because of the cut-on spinning modes.

The other two primary excitations on the rotor are the potential fields from Stator1 and Stator2. The unsteady moment on Rotor2 due to a unit strength pressure wave from Stator1 (i.e. Stator1 potential field) C_{m_d} and due to a unit strength pressure wave from Stator2 (i.e. Stator2 potential field) C_{m_u} at different inter-row spacings and vane clocking positions are shown in Figure 4.11 and Figure 4.12.

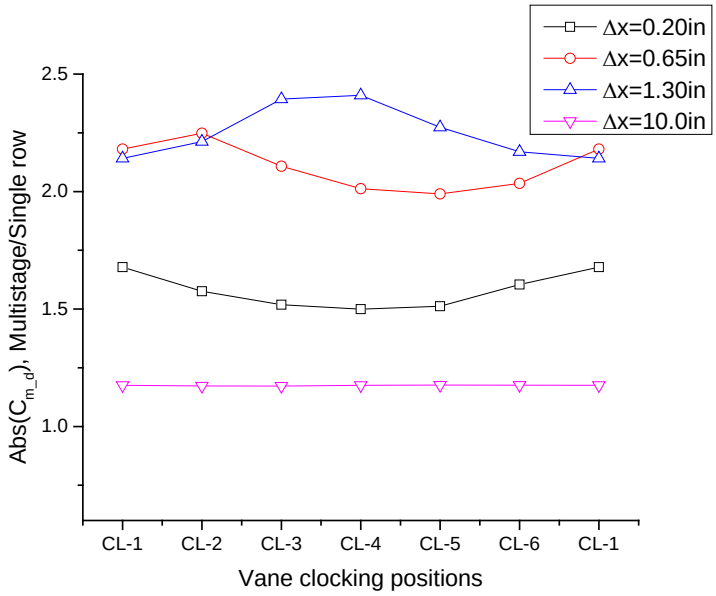

Figure 4.11. Normalized Rotor2 unsteady moment due to Stator1 potential filed at different inter-row axial spacings and different vane clocking positions.

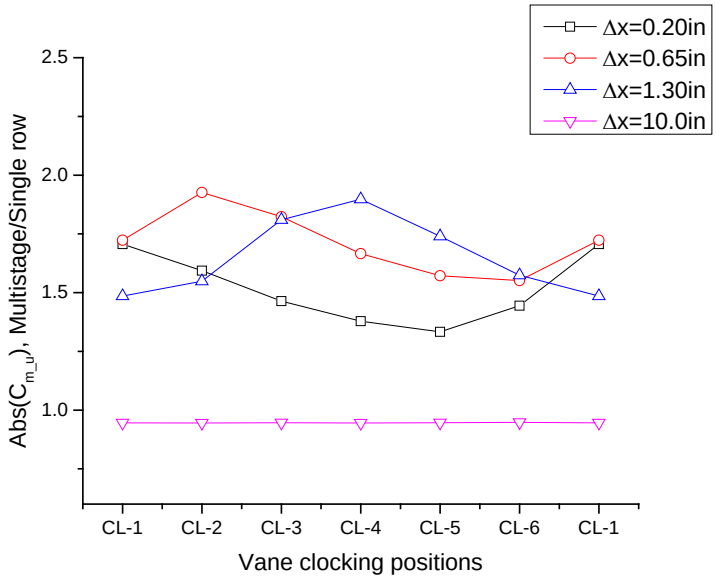

Figure 4.12. Normalized Rotor2 unsteady moment due to Stator2 potential filed at different inter-row axial spacings and different vane clocking positions.

A similar discussion as the Stator1 wake excitation on Rotor2 can be applied to the Rotor2 unsteady moment due to excitations from the Stator1 and Stator2 potential fields. First, the unsteady moment on the rotor from the multistage analysis is

significantly different from the single row analysis. The amplitude of the unsteady moment considering the multistage interaction is generally higher and up to more than twice the amplitude from the single row analysis. Secondly, the unsteady moment on the rotor changes with vane clocking position and the maximum variation (defined as (max-min)/mean) is up to 25.1% and 12.3% for excitations from the stator2 potential field and stator1 potential fields, respectively. Thirdly, the inter-row axial spacing plays an additional role affecting both the average and variation of the unsteady loadings on rotors at different vane clocking positions. When inter-row axial spacing becomes much larger than the chord length, the inter-row coupling effect becomes weak and the results from the multistage analysis approach the results from the single blade row analysis.

Besides the three external excitations discussed above, the vibration of the blade also generates unsteady loading on itself. This quantity is needed to calculate the resonant vibration amplitude of Rotor2 blade under external excitations. The unsteady moment loading on Rotor2 due to a unit rotor blade torsional vibration amplitude C_{m_α} at different inter-row axial spacings and vane clocking positions is shown in Figure 4.13. Both inter-row axial spacing and vane clocking position affects the unsteady moment on Rotor2 similarly to external excitations.

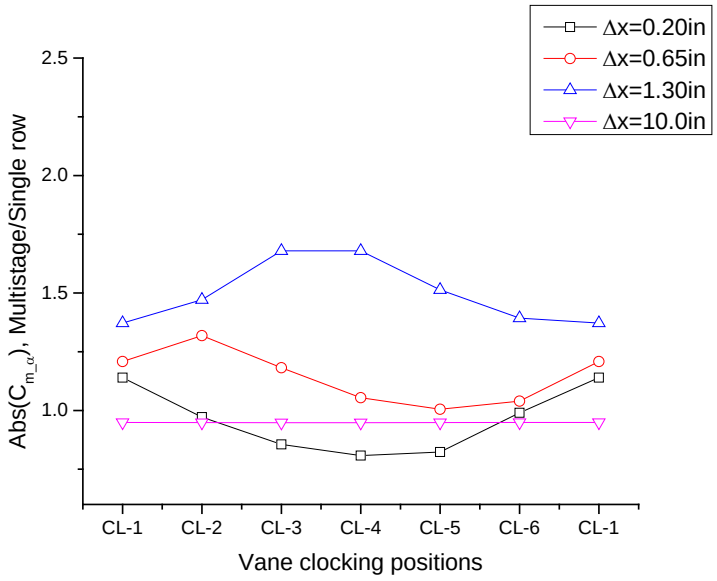

Figure 4.13. Normalized Rotor2 unsteady moment due to the torsional vibration of Rotor2 blade itself at different inter-row axial spacings and different vane clocking positions.

A summary of the normalized unsteady moment on Rotor2 at different inter-row axial spacings and vane clocking positions under both external excitations and internal excitations is give in Table 4.6.

Table 4.6. The average and variation of the normalized unsteady moment on Rotor2 at different inter-row axial spacings and vane clocking positions.

	Normalized unsteady moment (multistage/single row) on Rotor2 at different vane clocking positons							
Excitation	**Stator1 wake**		**Stator1 potential field**		**Stator2 potential field**		**Rotor 2 blade torsional vibration**	
Axial spacing (inch)	**Average**	**(Max-Min) /Average**	**Average**	**(Max-Min) /Average**	**Average**	**(Max-Min) /Average**	**Average**	**(Max-Min) /Average**
$\Delta x = 0.20$	1.31	8.50%	1.56	11.50%	1.49	25.10%	0.93	35.60%
$\Delta x = 0.65$	1.75	10.00%	2.1	12.30%	1.71	21.90%	1.13	27.60%
$\Delta x = 1.30$	1.82	9.40%	2.27	11.80%	1.68	24.60%	1.52	20.30%
$\Delta x = 10.0$	1.11	0.40%	1.17	0.40%	0.95	0.30%	0.95	0.10%

4.5.2.2 Resonant Vibration Amplitude

As derived earlier using a simple structural dynamic model in Section 2.1, the resonant torsional vibration amplitude due to a single external excitation can be calculated using Equation (4.2)

$$\bar{\alpha} = -\frac{\sum_{i=1}^{n}\left(B_{G,i}\bar{\zeta}_i + B_{u,i}\overline{P^+}_i + B_{d,i}\overline{P^-}_i\right)}{\sum_{i=1}^{n}B_{\alpha,i}} \qquad (4.2)$$

For the case studies here with 25 spinning modes (Table 4.5), modes 11 to 15 have the same excitation frequency as the primary excitation frequency. Thus the summation sign in the equation is for mode 11 to mode 15. The numerator $\sum_{i=1}^{n}\left(B_{G,i}\bar{\zeta}_i + B_{u,i}\overline{P^+}_i + B_{d,i}\overline{P^-}_i\right)$ is the total unsteady moment due to external excitation. The denominator ($\sum_{i=1}^{n}B_{\alpha,i}$) is the total unsteady moment due to blade torsional vibration. No matter what the external excitation is, the denominator $\sum_{i=1}^{n}B_{\alpha,i}$ stays the same.

The normalized resonant vibration amplitude(multistage/singe row) at different vane clocking positions and different inter-row spacings due to each external excitation alone are shown in Figure 4.14, Figure 4.15 and Figure 4.16.

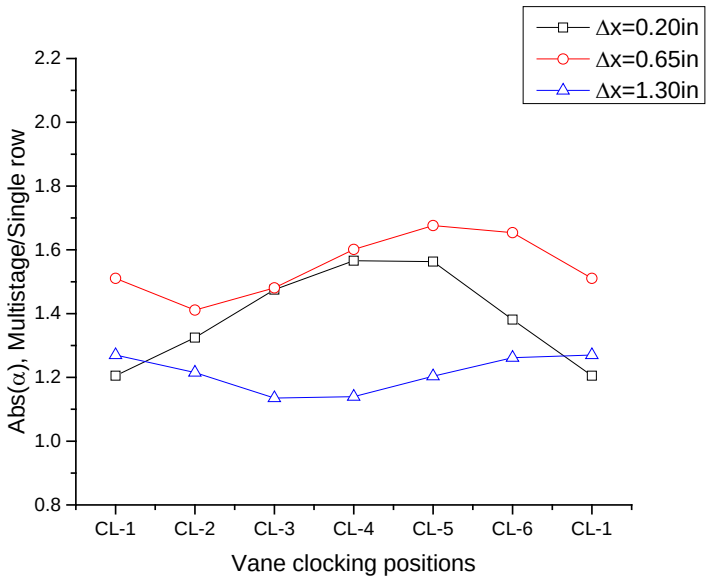

Figure 4.14. Normalized Rotor2 blade resonant vibration amplitude due to Stator1 wake at different inter-row axial spacings and different vane clocking positions.

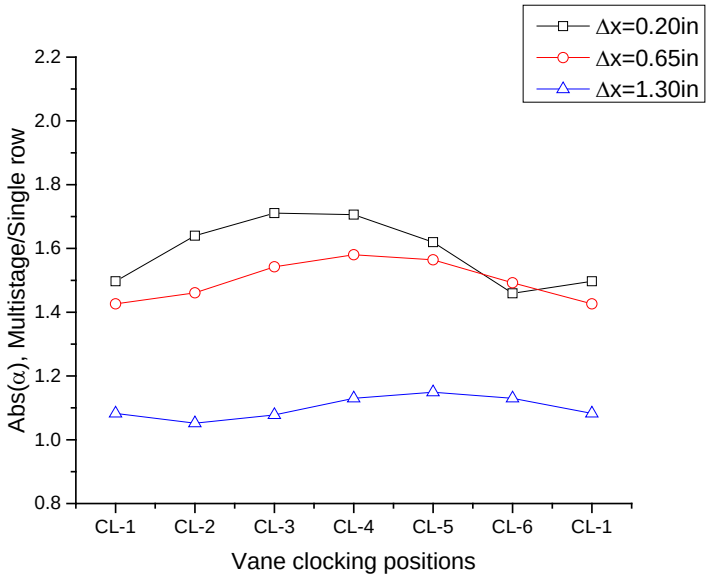

Figure 4.15. Normalized Rotor2 blade resonant vibration amplitude due to Stator2 potential field at different inter-row axial spacings and different vane clocking positions.

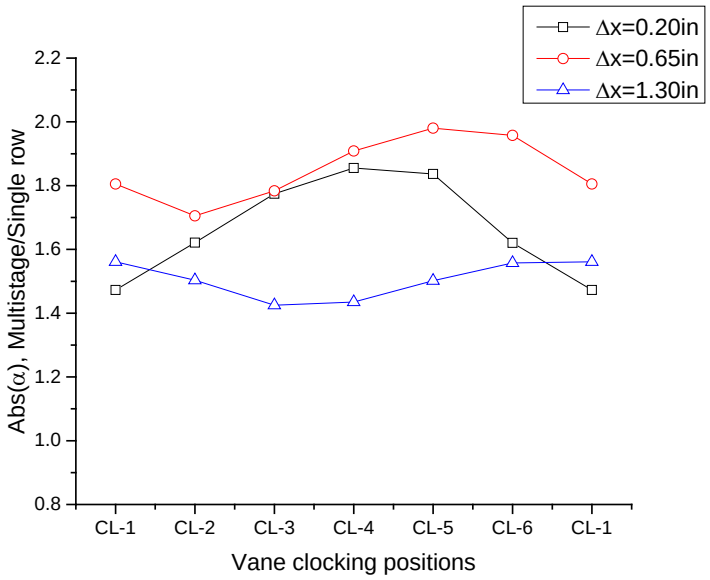

Figure 4.16. Normalized Rotor2 resonant vibration amplitude due to Stator1 potential field at different inter-row axial spacings and different vane clocking positions.

The resonant vibration amplitude calculated including multistage interaction effects is generally larger and up to more than twice the amplitude from the single row analysis. Both inter-row axial spacing and vane clocking position affect the resonant vibration amplitude significantly.

In real life applications, all three external excitations occur at the same time. If the non-dimensional strength of the three external excitations are c_1, c_2 and c_3, due to the linearity of the model, the total vibration angle is the summation of the results of all external excitations. Thus,

$$\bar{\alpha} = -\frac{c_1 C_{m\_\mathrm{u}} + c_2 C_{m\_\mathrm{d}} + c_3 C_{m\_G}}{C_{m\_\alpha}} \tag{4.3}$$

To compare with the experimental results [16], the resonant vibration amplitude is normalized again with the amplitude at vane clocking position 1 (i.e. no vane clocking). At the normal axial spacing $\Delta x = 0.65\,\mathrm{in}$ the normalized resonant vibration angle due to each and all external excitations are compared with the experiment results in Figure 4.17. By trial and error, when the relative strength of the Stator1 wake, potential field and

Stator 2 potential filed ratio vo : pdn : pup=1: 0.2 : 0.4 (the ratio can be complex number), the results closely match the experimental results.

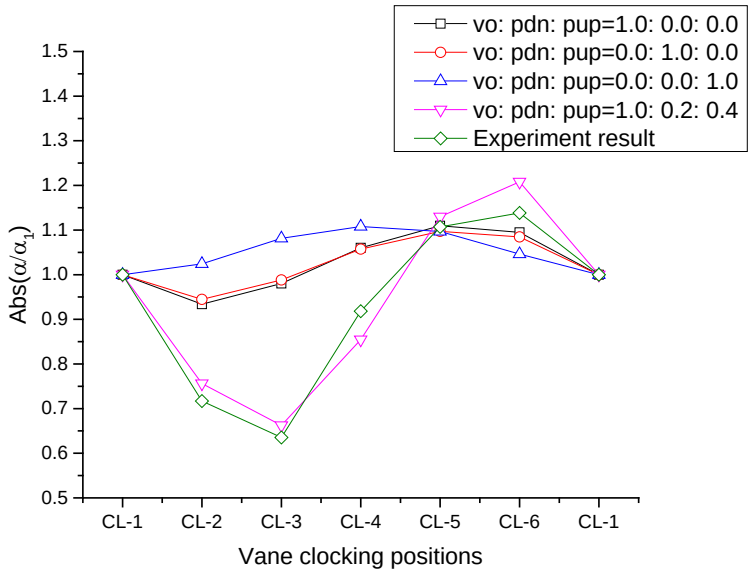

Figure 4.17. Comparison of normalized resonant vibration amplitude at different vane clocking positions with the experimental results.

Note that when considering the total effect of all three external excitations, the vane clocking changes the relative phase between the excitations from Stator1 (wake and downstream going pressure wave) and the excitation from Stator2, as shown in Figure 4.18. Thus the variation of the total effect at different vane clocking positions are more noticeable than considering only one external excitation.

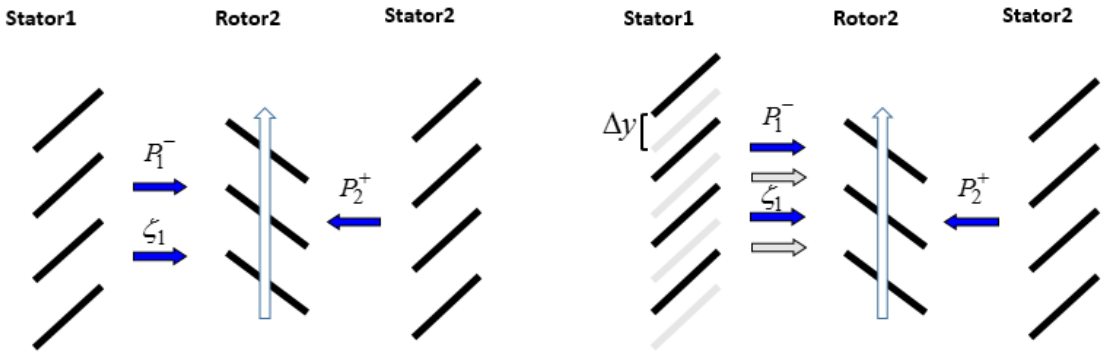

Figure 4.18. Schematic of the excitations relative phase change due to vane clocking.

4.5.3 Flutter Analysis

The flutter analysis of the first torsion mode of Rotor2 is done at the 5000rpm operating condition. Results at different inter-row axial spacings and vane clocking positions are compared with the single blade row analysis in order to examine the effect of the multistage interactions. The unsteady moments on Rotor2 due to Rotor2 blades torsional vibration at all possible interblade phase angles at different inter-row axial spacings and at different vane clocking positions are shown in Figure 4.19 and Figure 4.20, respectively.

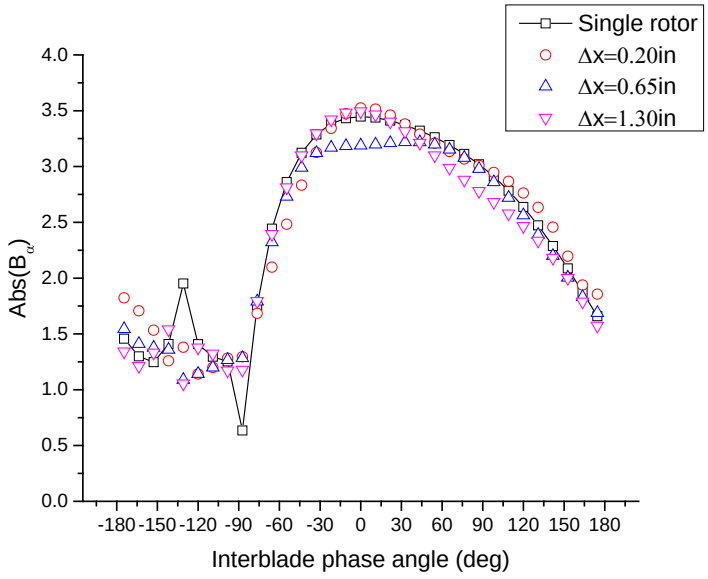

Figure 4.19. Rotor2 unsteady moment due to the torsional vibration of Rotor2 blade at different inter-row axial spacings.

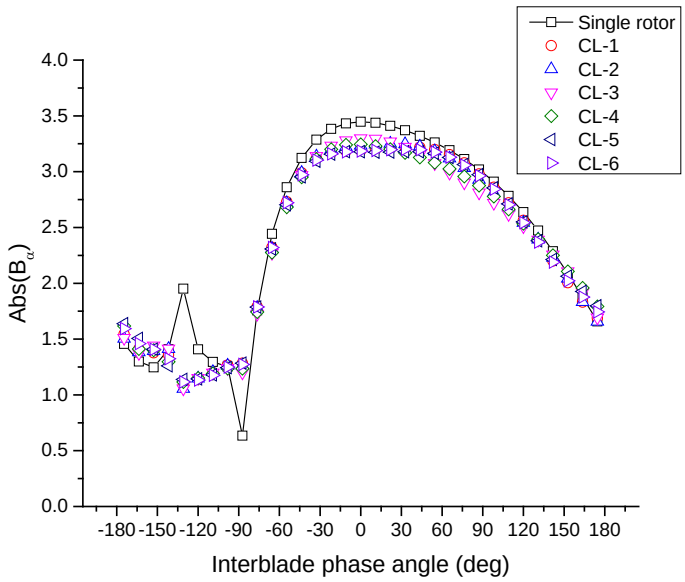

Figure 4.20. Rotor2 unsteady moment due to the torsional vibration of Rotor2 blade at different vane clocking positions.

Firstly, the results using the multistage analysis are clearly different from the results from the single blade row analysis even for the interblade phase angles at which the primary mode is cut-off. The primary mode is cut-on when interblade phase angle is from -180 to -129 degrees and cut-off at other angles. Although a cut-on primary mode provides more coupling between blades rows, the vorticity wave in a cut-off primary mode is always 'cut-on'. In addition, if the inter-row spacing is small enough, the cut-off pressure waves can still interact with neighboring blade rows.

Secondly, the unsteady moment on the rotor changes with inter-row axial spacing and vane clocking positions. In the current case study with the Purdue 3-Stage Research Compressor geometry and flow field, the axial spacing plays a more noticeable role in affecting unsteady moment on the rotor over most of the interblade phase angles than dose vane clocking.

A more important parameter for flutter analysis is aerodamping since a negative aerodamping indicates an unstable condition where flutter will occur. As discussed in Section 2.1, for a torsional vibration mode the aerodamping is proportional to $-\mathrm{Im}\left(B_\alpha\right)$.

Thus a positive $\mathrm{Im}(B_\alpha)$ indicates a negative aerodamping which leads to a possible unstable condition. $\mathrm{Im}(B_\alpha)$ at different inter-row axial spacings and vane clocking positions over all possible inter blade phase angles is shown in Figure 4.21 and Figure 4.22. As expected, all $\mathrm{Im}(B_\alpha)$ values are negative which indicates a stable condition. No first torsion mode flutter will occur on Rotor2 of the Purdue 3-Stage Research Compressor at the design operating condition.

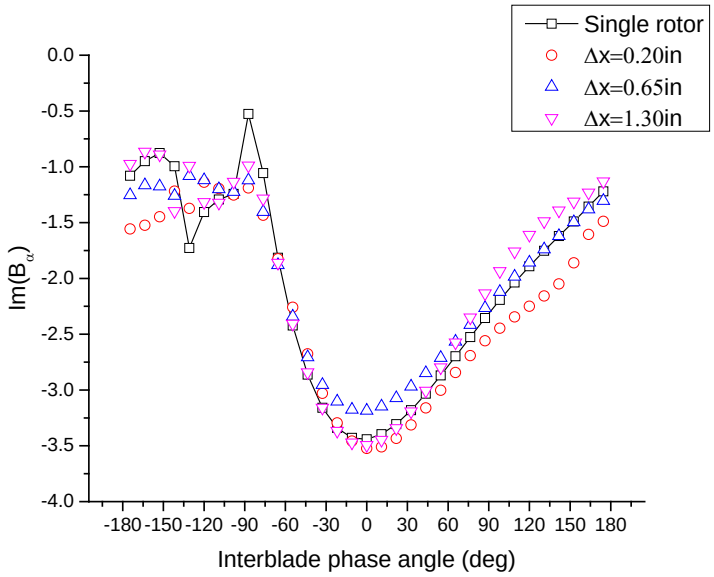

Figure 4.21. $\mathrm{Im}(B_\alpha)$ of Rotor2 first torsion mode at different inter-row axial spacings.

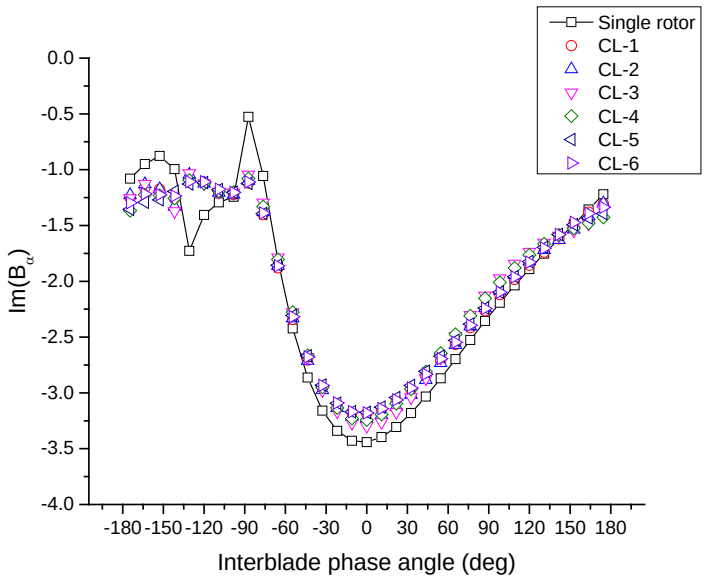

Figure 4.22. $\mathrm{Im}\left(B_\alpha\right)$ of Rotor2 first torsion mode at different vane clocking positions.

Similar to the multistage interaction effects on the unsteady moment on Rotor 2 due to rotor blade torsional vibration, the aerodamping considering multistage interaction is markedly different from that without multistage effects. At a reduced inter-row spacing $\Delta x = 0.2\,\mathrm{in}$, the multistage interaction makes aerodamping generally larger than the single row analysis. At standard inter-row axial spacing $\Delta x = 0.65\,\mathrm{in}$, multistage interaction reduces the aerodamping over most of the interblade phase angles, although Figure 4.22 shows vane clocking provides some control over how much the aerodamping changes.

4.5.4 Aeroacoustics Analysis

Since the stator potential field is always decaying, the acoustic analysis is done for the wake interaction with the rotor at different inter-row axial spacings and vane clocking positions. Just as in the forced response analysis, the transient operating condition at 3700rpm is used in the acoustic analysis. Both upstream going pressure wave and downstream going pressure waves of the propagating modes are analyzed. As shown in Table 4.5, the propagating modes are mode 10, 14, and 22.

The scattering index Graduate School Exit Questionnaire for mode 14, mode 10 and mode 22 are $(0, 1)$, $(-1, 2)$ and $(2, -1)$ respectively. Mode 14 is the first scattering mode from Rotor 2 and it is the only propagating mode which a single isolated rotor row can produce. It has frequency ω =2035Hz with $ND = -11$ in the reference frame of the stator. Mode 10 and mode 22 contain the scattering modes on both the stator and rotor, thus they do not exist in the single rotor row analysis. In the stator reference frame, mode 10 has frequency ω =4070Hz with ND=-22 and mode 22 has frequency ω =-2035Hz with ND=11.

The upstream going pressure wave and downstream going pressure wave of mode 14 at different inter-row axial spacing and vane clocking positions are shown in Figure 4.23 and Figure 4.24 together with the results from the single row analysis. It can be seen that both the upstream going pressure wave and the downstream going pressure wave in a multistage environment has higher amplitude than the results from wake and single rotor row interaction. Since vane clocking is done on Stator1, the upstream going pressure wave interacts with Stator1 and has larger amplitude variation at different vane clocking positions than the downstream going pressure wave. In addition, the inter row axial spacing affects the amplitude of the pressure waves significantly.

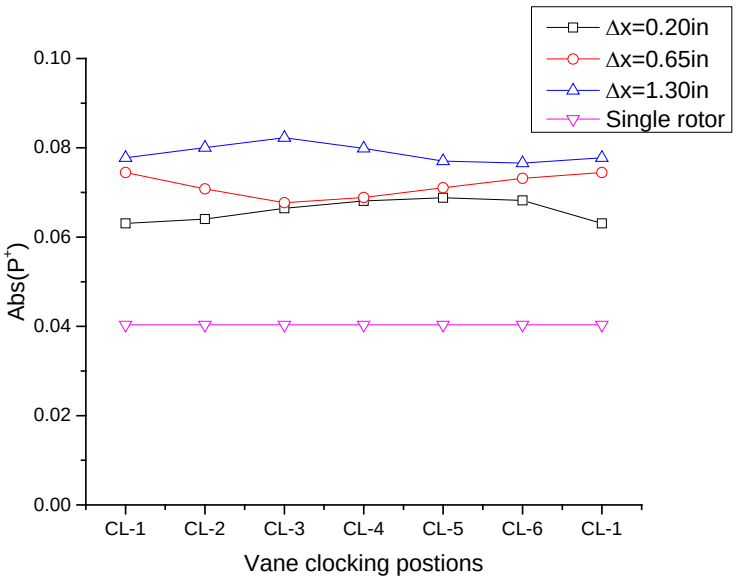

Figure 4.23. Upstream going pressure wave of mode 14 due to Stator1 wake and Rotor2 interaction at different inter-row axial spacings and vane clocking positions.

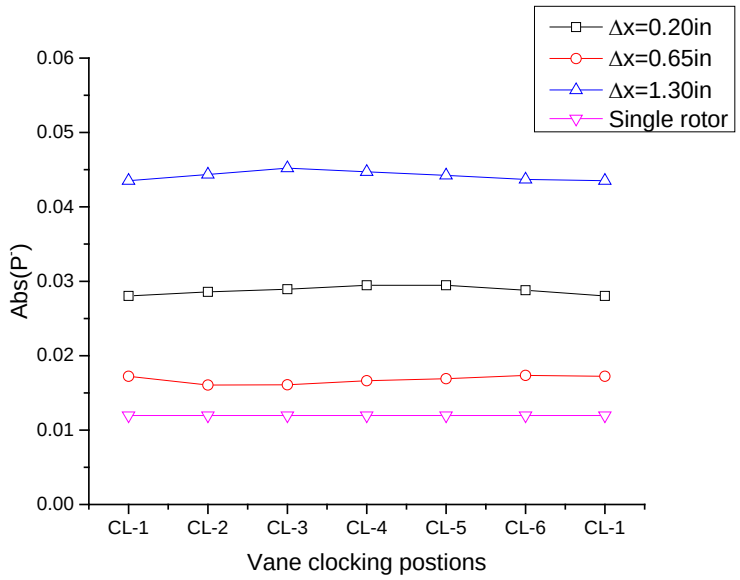

Figure 4.24. Downstream going pressure wave of mode 14 due to Stator1 wake and Rotor2 interaction at different inter-row axial spacings and vane clocking positions.

The upstream going pressure wave and downstream going pressure wave of mode 10 and mode 22 at different inter-row spacings and vane clocking positions are shown in Figure 4.25, Figure 4.26 and Figure 4.27, Fig 4.28. Since both mode 10 and mode 22 involve scattering from stator row, they can't be analyzed using the single blade row model. The pressure wave amplitudes in mode 10 and mode 22 are much smaller than the one in mode 14 due to additional scattering at the stator row. Similar to mode 14, both inter-row spacing and vane clocking can affects the pressure wave amplitude significantly.

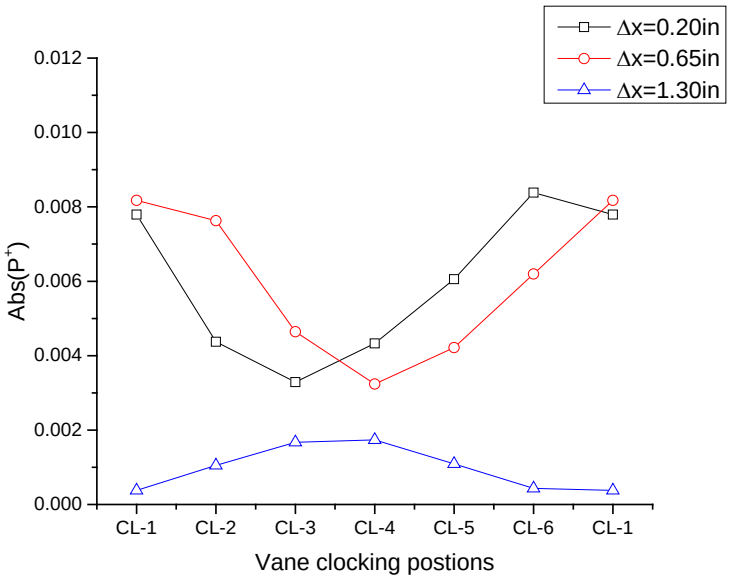

Figure 4.25. Upstream going pressure wave of mode 10 due to Stator1 wake and Rotor2 interaction at different inter-row axial spacings and vane clocking positions.

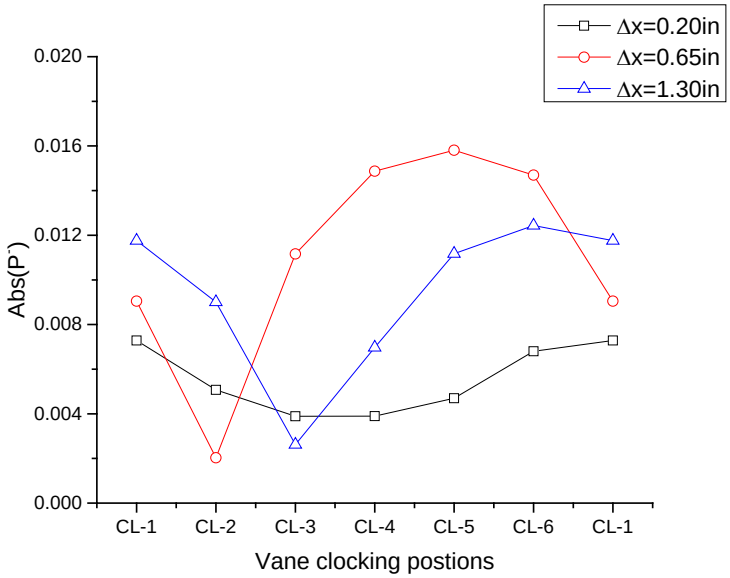

Figure 4.26. Downstream going pressure wave of mode 10 due to Stator1 wake and Rotor2 interaction at different inter-row axial spacings and vane clocking positions.

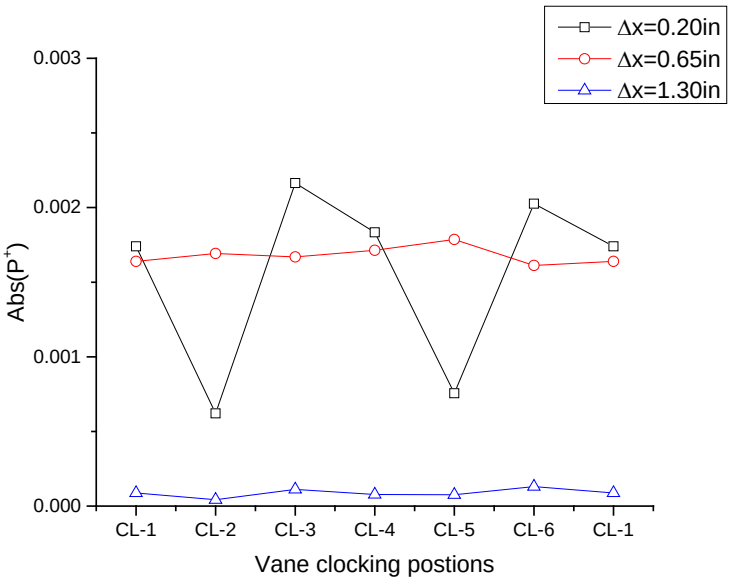

Figure 4.27. Upstream going pressure wave of mode 22 due to Stator1 wake and Rotor2 interaction at different inter-row axial spacings and vane clocking positions.

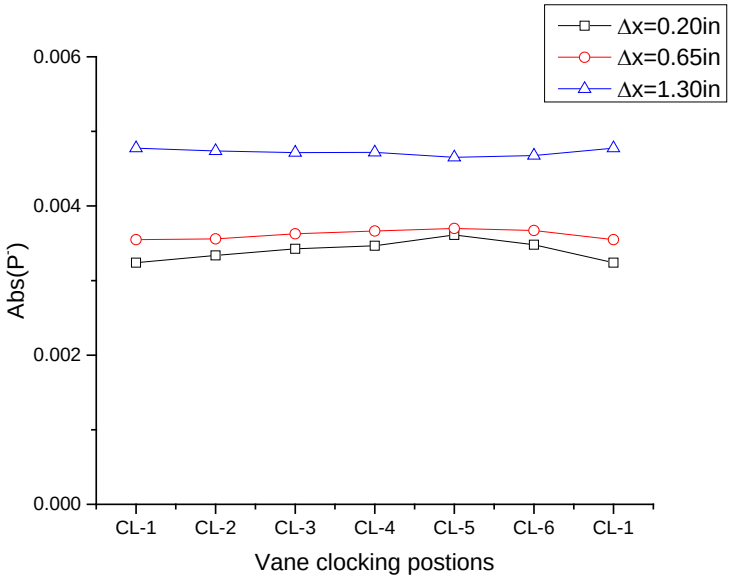

Figure 4.28. Downstream going pressure wave of mode 22 due to Stator1 wake and Rotor2 interaction at different inter-row axial spacings and vane clocking positions.

4.6 Summary

In this chapter, the multistage interaction model is first validated with the Hall & Silkowski's work for both forced response analysis and flutter analysis. Case studies based the geometry and flow condition of the Purdue 3-Stage Research Compressor are then conducted to investigate the multistage interaction effect on the forced response, flutter and aeroacoustic behavior of the embedded rotor. Parametric studies with different inter-row axial spacings and vane clocking positions are performed to explore their potential to work as passive control techniques to reduce the aeromechanic and aeroacoustic problems of the rotor in multistage environments.

Forced response analysis shows that the unsteady moment and resonant vibration amplitude of the rotor due to external excitation from the adjacent stator is significantly different from (generally higher and up to twice) the values from the single row analysis. The variation of the unsteady loading and resonant vibration amplitude at different vane clocking positions and different inter-row axial spacings fundamentally result from the multistage interaction with the blade row scattering effect. The blade rows are coupled together by the spinning modes which have different axial and tangential wave numbers. The constructive and destructive summation of all modes causes the variations. By trial and error, excitations with a certain relative strength ratio give the resonant vibration amplitudes that closely match the experimental result at different vane clocking positions. Flutter analysis shows that multistage interaction markedly affects the unsteady loading and aerodamping of the rotors at most of the interblade phase angles. The single blade row flutter analysis may give misleading results. Through controlling the inter-row spacing and vane clocking, the multistage effect can be altered in a favorable way to reduce unsteady loading and increase the aerodamping of the rotor.

Acoustic analysis shows that multistage interaction amplifies the existing pressure waves in the single blade row analysis. In addition, propagating pressure waves which do not exist in a single blade row analysis are generated due to the multistage interactions. Both inter-row spacing and vane clocking can affect the amplitude of propagating pressure waves significantly.

CHAPTER 5. NON-UNIFORMLY SPACED BLADE ROW IN MULTISTAGE ENVIRONMENT

In the chapter, the non-uniformly spaced cascade model and multistage interaction model are combined together to analyze the effect of a non-uniformly spaced IGV on the flutter stability of the downstream rotor. Non-uniformly spaced IGV has been used in real gas turbines to reduce the forced repose problem of rotor vibration. However, it can also affect the rotor stability in two aspects. First, due to the multistage interactions, the reflected waves from the IGV provide secondary excitation to the rotor. Second, compared with a uniformly spaced IGV, the reflected waves from a non-uniformly spaced IGV have a much larger set of modes as discussed in Section 2.4. These additional unsteady waves can substantially change the unsteady loading and aerodynamic damping of the downstream rotor. Based on the Purdue Transonic Compressor geometry and flow conditions, validation is done first to show that the multistage interaction model has been successfully extended to include blades row with non-uniform spacing. Case studies with two commonly used non-uniformly spaced IGV configurations (Half-half and Sinusoidal spacing) are conducted to investigate their effect on the unsteady loading and aerodamping of the downstream rotor.

5.1 Validation and Case Studies

The Purdue Transonic Compressor geometry and flow conditions introduced in Section 3.2 are used as the baseline configuration in this study. To simplify the problem, only the IGV and rotor row are retained in the multistage interaction analysis. The flutter analysis is done at the operating speed of 20000rpm for the 1st torsion mode (3074Hz) of the rotor blade.

The most commonly used non-uniformly spaced IGV/stator are in the ‘Half-half’ configuration [7] which features uniformly spaced vanes in a half circle and a different number of uniformly spaced vanes in the other half circle. Another popular non-uniformly spaced IGV/stator features blade spacing in a sinusoidal wave [6]. Both non-uniformly spaced IGV configurations are studied and compared with uniformly spaced IGV in terms of the influence on the flutter stability of the rotor. The Purdue Transonic Compressor IGV has 20 vanes. In order to use the generalized uniformly spaced cascade model, the IGV row is discretized into 120 total blades. As shown in Figure 5.1, the uniform spacing IGV row has real blades at blade index [1 7 13 19 25 31 37 43 49 55 61 67 73 79 85 91 97 103 109 115]. The Half-half spacing IGV row has real blades at blade index [1 6 11 16 21 26 31 36 41 46 51 56 61 69 77 85 93 101 109 117]. The sinusoidal spacing IGV row has real blades at blade index [1 8 16 24 33 42 51 59 67 74 80 85 89 93 96 99 102 106 110 115].

A mode convergence study shows that nine symmetrical modes with scattering index $n_1 = -1 \sim 1$ and $n_2 = -1 \sim 1$ is sufficient to model the uniformly spaced IGV and rotor interactions. For the rotor flutter analysis, the lowest internal excitation nodal diameter is -9 (corresponding interblade phase angle is $-9(2\pi)/18 = -180\,\text{deg}$) and highest internal excitation nodal diameter is 9 (corresponding interblade phase angle is $9(2\pi)/18 = 180\,\text{deg}$). If the excitation nodal diameter is -9, the nodal dimeters of the nine modes are [-47 -29 -11 -27 -9 9 -7 11 29]. If the excitation nodal diameter is 9, the nodal dimeters of the nine modes are [-29 -11 7 -9 9 27 11 29 47]. Since 120 total blades are used in the generalized uniformly spaced cascade model, at least 120 modes are needed to model the non-uniformly spaced IGV. Thus, modes with nodal diameters from -60 to 59 are used in this study to model both the non-uniformly spaced IGV and multistage interaction effects properly.

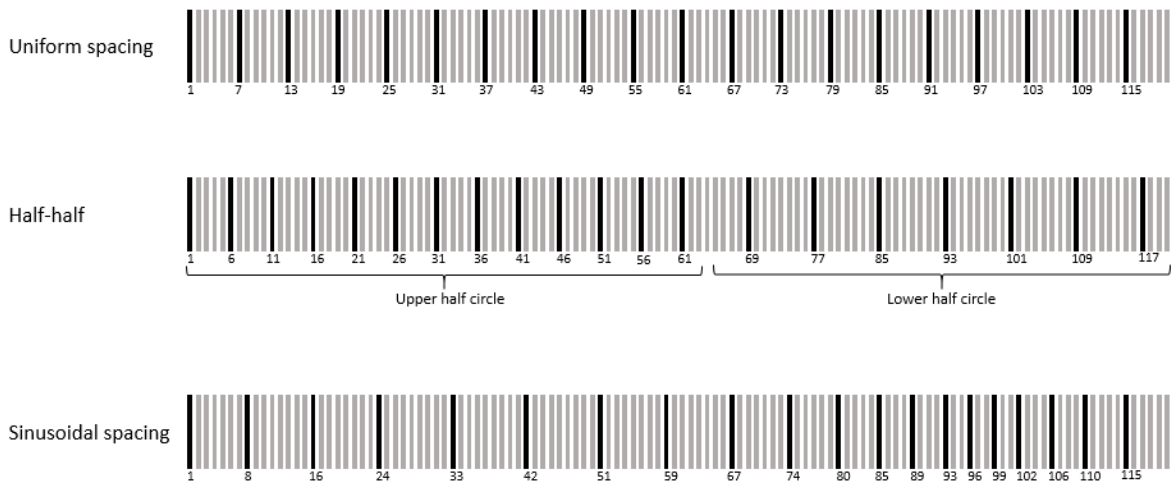

Figure 5.1. Real blades positions of different IGV row configurations in the generalized uniformly spaced cascade with 120 total blades.

5.1.1 Validation

Both the non-uniformly spaced cascade model and the multistage interaction model have been validated individually in the previous sections. This study involves the extension of the multistage interaction model such that each blade row is allowed to have non-uniform spacing. Since there is no similar model existing to the author's knowledge, the validation is done to check whether the new model can be reduced to the multistage interaction model with uniformly spaced blade rows. The IGV is modeled using the generalized uniformly spaced cascade model with 120 total blades. The real blade of uniformly spaced IGV is shown in Figure 5.1. The unsteady moment $\mathrm{Abs}\left(B_\alpha\right)$ and $\mathrm{Im}\left(B_\alpha\right)$ (which is proportional to the negative of aerodamping) on rotor are calculated using the multistage interaction model with uniformly spaced blade rows (Multistage uniform) and the new model of multistage interaction with generalized uniformly spaced blade rows (Generalized tuned). The comparison of the results is shown in Figure 5.2. The excellent agreement between the results of the two models shows that the multistage interaction model has been successfully extended to include blades row with non-uniform spacing.

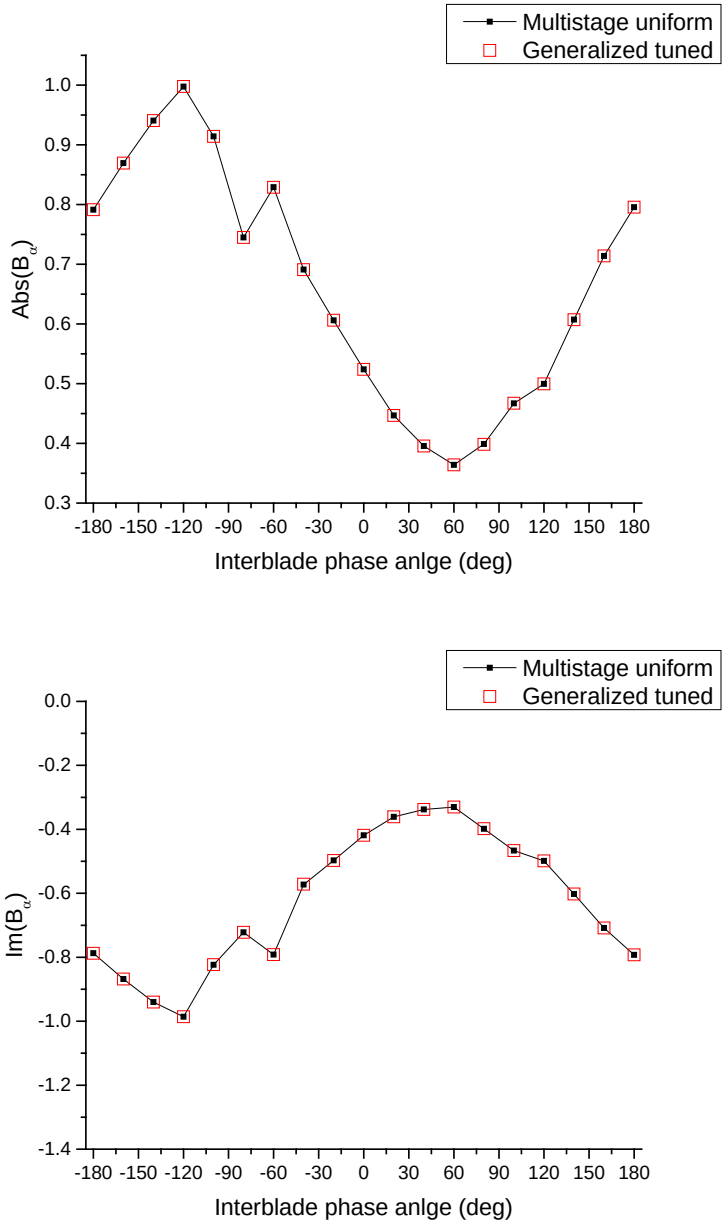

Figure 5.2. Unsteady moment $\mathrm{Abs}\left(B_\alpha\right)$ and $\mathrm{Im}\left(B_\alpha\right)$ on rotor due to the torsional vibration of rotor blade.

5.1.2 Flutter Analysis

First, the unsteady moment $\mathrm{Abs}\left(B_\alpha\right)$ and $\mathrm{Im}\left(B_\alpha\right)$ on the rotor from uniformly spaced IGV-rotor interaction is compared with the results from single rotor analysis in

Figure 5.3. The comparison shows there are noticeable differences for interblade phase angles from -180 to -60 degrees and from 90 to 180 degrees

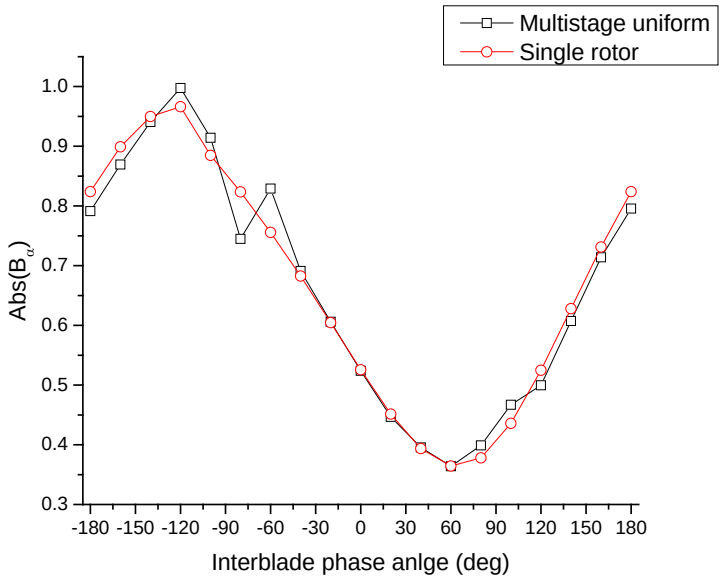

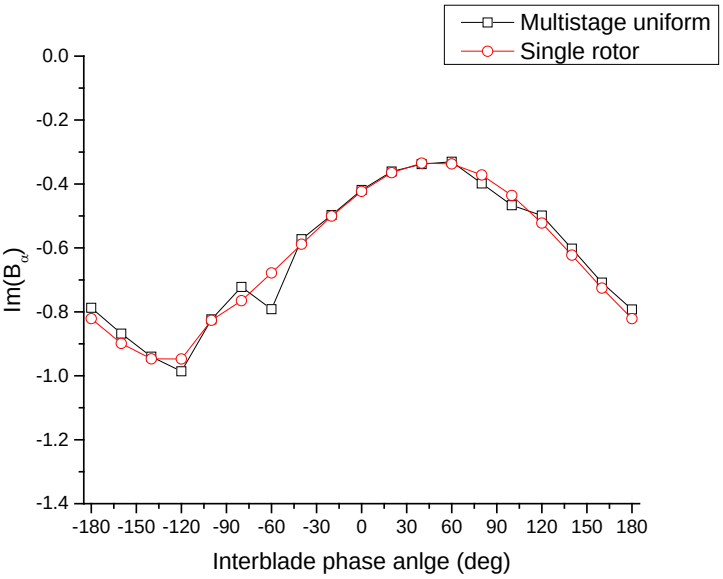

Figure 5.3. Unsteady moment $\mathrm{Abs}\left(B_\alpha\right)$ and $\mathrm{Im}\left(B_\alpha\right)$ on rotor based on uniformly spaced IGV-rotor interaction analysis and single rotor analysis.

Secondly, the unsteady moment $\mathrm{Abs}(B_\alpha)$ and $\mathrm{Im}(B_\alpha)$ on the rotor due to uniform spacing IGV-rotor interaction, half-half spacing IGV-rotor interaction and sinusoidal spacing IGV-rotor interaction are compared in Figure 5.4 and Figure 5.5. Both figures show that the results from non-uniformly spaced IGV-rotor interactions are different from the uniformly spaced IGV-rotor interactions, especially at the interblade phase angles from -180 to -60 degrees. The difference is due to the additional unsteady waves generated from upstream going pressure wave from rotor and non-uniformly spaced IGV interaction. When the axial spacing is reduced from the standard value $\Delta x = 0.78\,\mathrm{in}$ to a reduced spacing $\Delta x = 0.10\,\mathrm{in}$, the difference between the results from non-uniformly spaced IGV and uniformly spaced IGV becomes larger. This is due to fact that the additional unsteady waves generated on non-uniformly spaced IGV are relatively weak and most of them are cut-off. The reduced axial spacing enhances the effect of these additional cut-off modes during IGV-rotor interaction. From Figure 5.4 and Figure 5.5, compared with the uniformly spaced IGV, both half-half spacing IGV and sinusoidal spacing IGV at the reduced axial spacing cause a larger unsteady moment and high aerodamping at most interblade phase angles of the rotor flutter analysis.

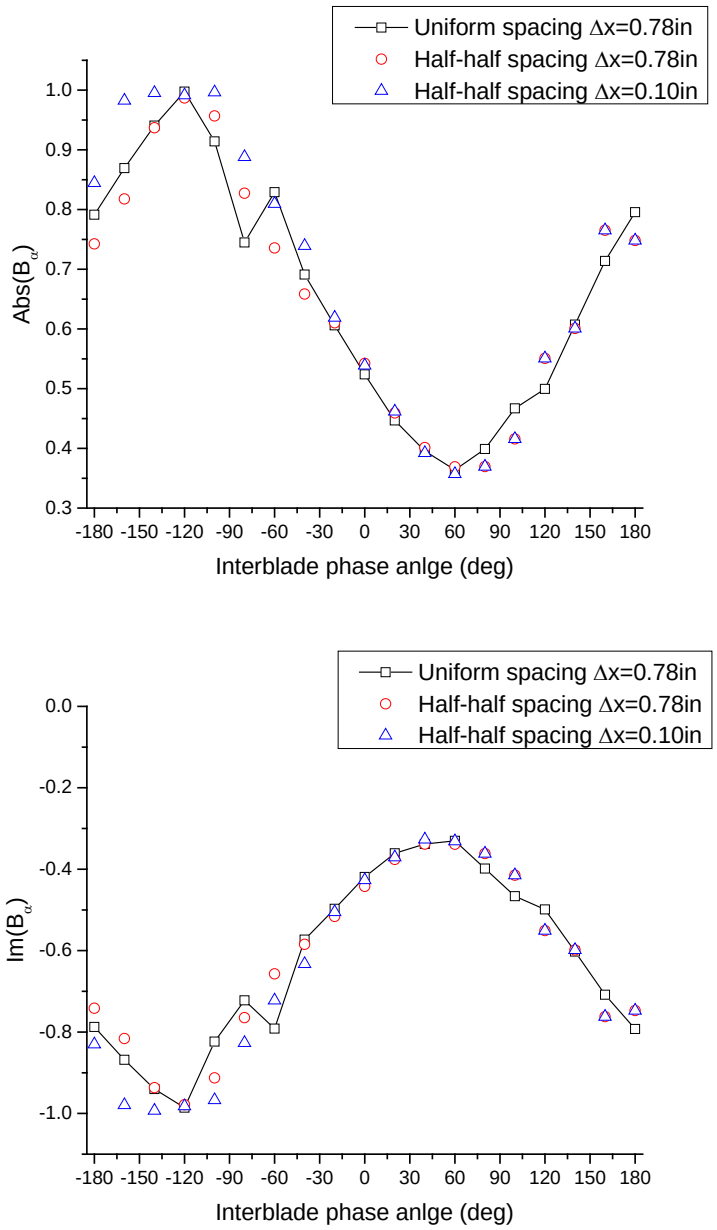

Figure 5.4. Unsteady moment $\mathrm{Abs}\left(B_\alpha\right)$ and $\mathrm{Im}\left(B_\alpha\right)$ on rotor for uniform spacing IGV-rotor interaction and half-half spacing IGV-rotor interaction.

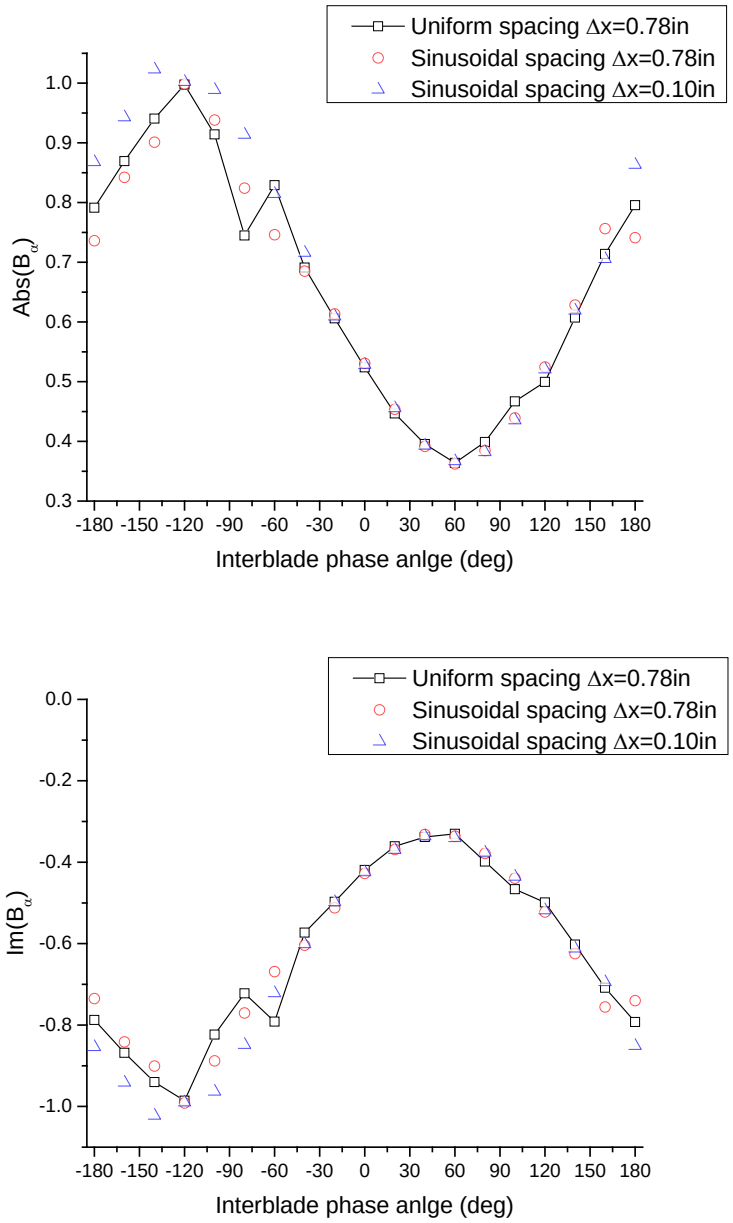

Figure 5.5. Unsteady moment $\mathrm{Abs}\left(B_\alpha\right)$ and $\mathrm{Im}\left(B_\alpha\right)$ on rotor for uniform spacing IGV-rotor interaction and sinusoidal spacing IGV-rotor interaction.

Lastly, Figure 5.6 shows the unsteady moment $\mathrm{Abs}\left(B_\alpha\right)$ and $\mathrm{Im}\left(B_\alpha\right)$ on rotor based the IGV-rotor interaction analysis with all different configurations of IGV, with the

single rotor analysis also shown. It shows both the effects of multistage interaction and non-uniformly spaced IGV cause the difference from the results of the single row analysis.

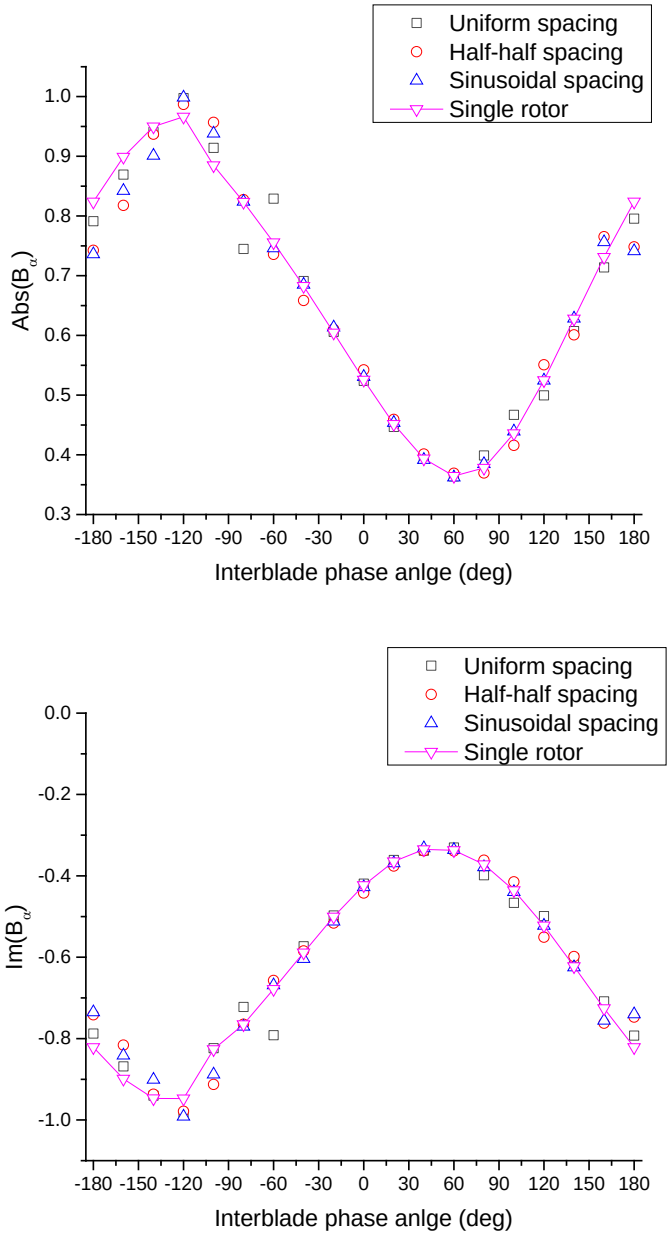

Figure 5.6. Unsteady moment $\mathrm{Abs}\left(B_\alpha\right)$ and $\mathrm{Im}\left(B_\alpha\right)$ on rotor based IGV-rotor interaction analysis of different IGV configurations and single rotor analysis.

5.2 Summary

In this chapter, the non-uniformly spaced cascade model and multistage interaction model are combined together to study the non-uniform spaced IGV's effect on the downstream rotor flutter stability based on the Purdue Transonic Compressor's geometry and flow conditions. The validation is done by showing that the new combined model can be reduced to the multistage interaction model with uniformly spaced blade row. Two non-uniformly spaced IGV configurations studied are the IGVs with Half-half spacing and with Sinusoidal spacing.

Case studies show that the unsteady loading and aerodamping on rotor due to rotor blade vibration are noticeably different between the results with non-uniformly spaced IGV and uniformly spaced IGV. When the inter-row spacing is reduced, the difference becomes larger because additional unsteady waves generated by the non-uniformly spaced IGV are relatively weak and most of them are cut-off. The reduced axial spacing enhances the effect of these additional cut-off modes during IGV-rotor interaction. Case studies show that both the effects of multistage interaction and non-uniformly spaced IGV make the classic flutter analysis of a single rotor inaccurate at certain interblade phase angles.

CHAPTER 6. RADIAL UNSTEADY WAVE PROPAGATION IN CENTRIFUGAL COMPRESSOR

To analyze the aeromechanic risk of the impeller due to impeller-diffuser vane interaction, three major physical processes as shown in Figure 6.1 have to be understood: (1) the impeller wake travels downstream, (2) the wake interacts with the diffuser vane and generates the pressure waves, (3) the pressure wave travels upstream and excites the impeller. This study focuses on modeling process 1 and 3, i.e. developing an analytical solution for the wake and pressure wave propagation in the vaneless space with a mean swirling flow. These wave propagation properties are also fundamental to the linearized modeling of the unsteady aerodynamics in radial cascades, process 2.

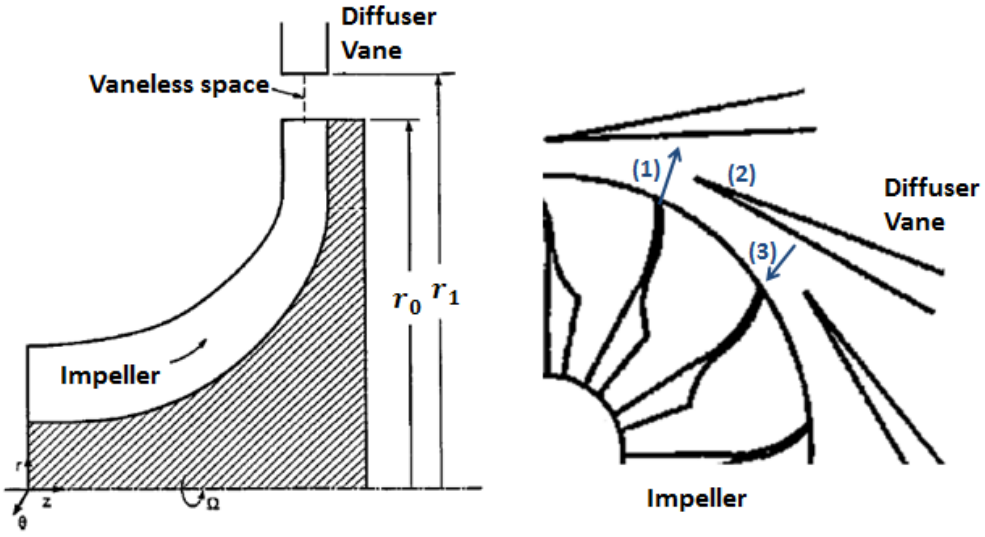

Figure 6.1. Schematic of a centrifugal compressor [21].

The analytical solution for the propagation of unsteady pressure and vorticity waves in the vaneless space of a low speed centrifugal compressor have been derived in Section 2.2.2. Purdue Low Speed Centrifugal Compressor described in Section 6.1 is used as the baseline geometry and flow conditions for the following case studies in Section 6.2. Parametric studies with different impeller blade number and different back sweep angle are conducted to investigate their effect on the impeller wake and pressure wave propagation in the vaneless space.

6.1 Purdue Low Speed Centrifugal Compressor

The geometry and flow condition of the Purdue Low-Speed Centrifugal Research Compressor [20] is used as the baseline configuration in this study. It operates at 1790rpm. The impeller consists of 23 blades, and the vaned diffuser has 30 vanes. The impeller exit radius and diffuser vane leading edge radius are 0.366m and 0.404m, respectively. With a flow coefficient of 0.3, the impeller exit absolute flow angle α is 55.5 degrees, and the relative flow angle β is -62.0 degrees. At the impeller exit, the absolute mean flow radial velocity U_{r0} is 20.6m/s, and the absolute mean flow circumferential velocity $U_{\theta 0}$ is 29.9m/s. This flow condition satisfies the low Mach number assumptions made in Section 2.2.2. A schematic of the flow field at impeller exit is shown in Figure 6.2.

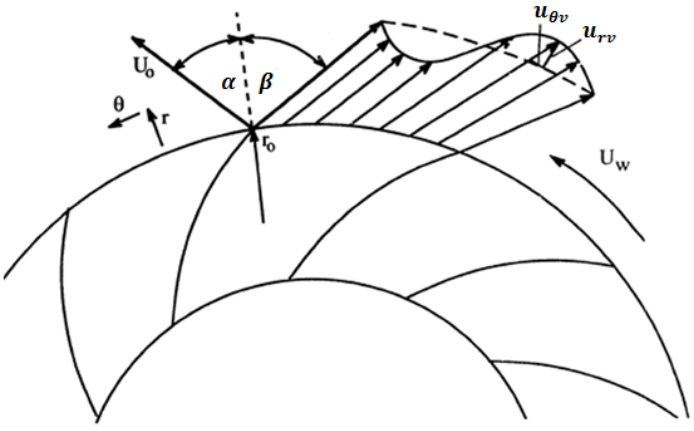

Figure 6.2. Schematic of the flow field at impeller exit [20].

6.2 Case Studies

Based on the analytical solutions derived in Section 2.2.2, the effect of impeller blade number (affecting the circumferential wave number k_θ) and back sweep angle (affecting the relative flow angle β) on the impeller wake (vorticity wave) and pressure wave propagation in the vaneless space are studied.

6.2.1 Vorticity Wave Propagation

Case studies with three different circumferential wave numbers k_θ and three different relative flow angles β are analyzed to investigate their effect on the impeller wake propagation downstream. Case 1 is the baseline case with 23 blades and β =-62.0 degrees. In Case 2 and Case 3, the number of blades is changed to 18 and 28, respectively, with the relative flow angle β unchanged. In Case 4 and Case 5, the relative flow angles is changed to β =-52.0 degrees and β =-72.0 degrees, respectively, with the number of blades unchanged. Note that in case 4 and case 5, due to the reduced back sweep angle, the mean flow field is also changed. At the impeller exit, the absolute mean flow velocities at β =-52.0 degrees and β =-72.0 degrees are approximately 1.22 and 0.74 times of the mean flow velocities in the baseline case.

The unsteady radial or circumferential velocity at impeller exit needs to be specified to calculate the wake propagation downstream. Here it is assumed that the unsteady radial and circumferential velocities are in phase and their amplitude ratio is the same as the mean flow relative radial and circumferential velocity ratio, i.e. $u_{\theta v} = u_{rv} \tan\beta$ at the impeller exit (Figure 6.2).

The change of the unsteady circumferential and radial velocities with radius is shown in Figure 6.3 and 6.4, with each normalized by their corresponding value at the impeller exit. As shown in Figure 6.3, the amplitude of the unsteady circumferential velocity $u_{\theta v}$ decreases at the same rate for all cases. The radial wavelength reduces with increasing number of blades ($\propto k_\theta$) and increasing of the back sweep angle ($\propto -\beta$). These effects can also be seen from Equation (2.60). The amplitude of $u_{\theta v}$ is proportional

to 1/r. The equivalent radial wave number can be written as $k_r = -\frac{i\omega}{2c_1} r - \frac{c_2 i k_\theta}{c_1} \frac{\ln r}{r}$. Increasing k_θ and ω by increasing the blade number, and reducing the mean flow radial velocity constant c_1 by increasing back sweep angle, both cause an increase of the radial wave number k_r and thus the decrease of the radial wavelength. Note the equivalent radial wavenumber k_r itself is also a function of radius r.

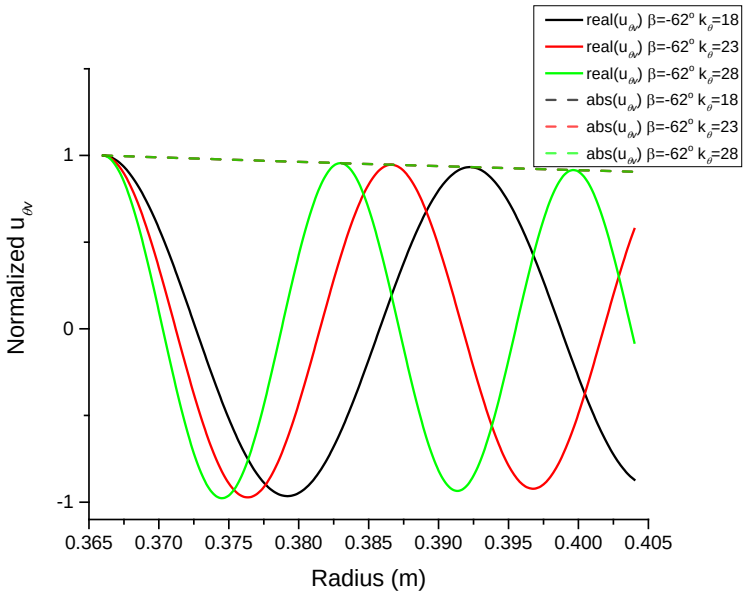

(a)

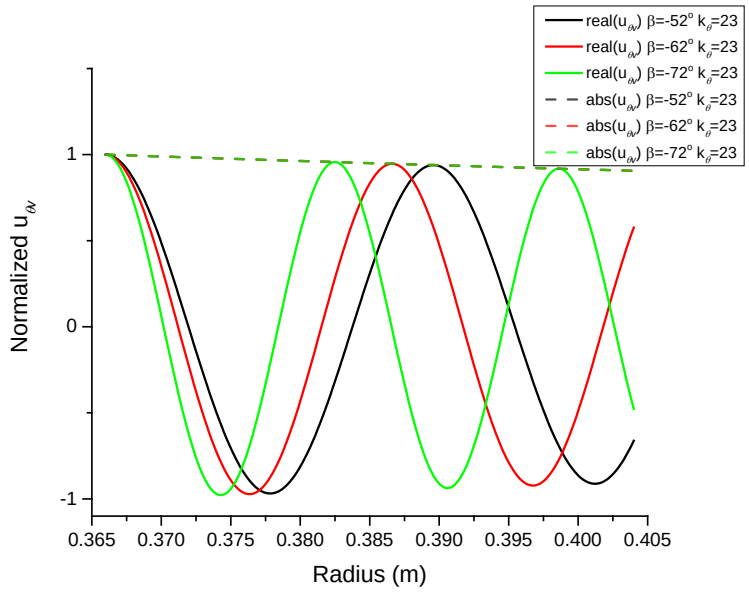

(b)

Figure 6.3. Normalized unsteady circumferential velocity profile (a) at different circumferential wave number k_θ and (b) at different relative flow angle β.

As shown in Figure 6.4, changing the number of blades ($\propto k_\theta$) does not affect the amplitude of the unsteady radial velocity decay rate. However, increasing back sweep angle ($\propto -\beta$) causes the amplitude of the unsteady radial velocity to decay at a higher rate. Regarding the radial wavelength, the same trends are seen as those observed in the unsteady circumferential velocity: Increasing the number of blades and increasing the back sweep angle reduce the wavelength in the radial direction. From Equation 2.61, the equivalent radial wavenumber Graduate School Exit Questionnaire is the same as that for the unsteady circumferential velocity. Physically, both the unsteady radial and circumferential velocities are from the same vorticity wave, and thus must have the same wave number. The amplitude of the unsteady radial velocity u_{rv} is proportional to $\left| Er - \frac{c_2}{c_1} D \frac{1}{r} \right|$. The change in the decay rate with β is due to the assumption that the initial unsteady velocities at the impeller exit are related by the relative flow angle β, $u_{\theta v} = u_{rv} \tan \beta$. Increasing the back sweep angle causes a relatively larger $u_{\theta v}$ and smaller u_{rv}. This causes the change of constants E and D and thus the change in the amplitude decay rate.

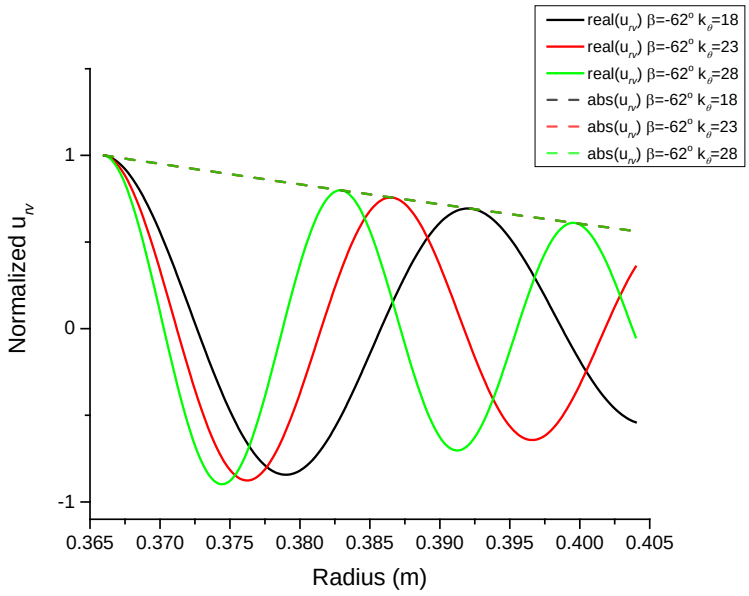

(a)

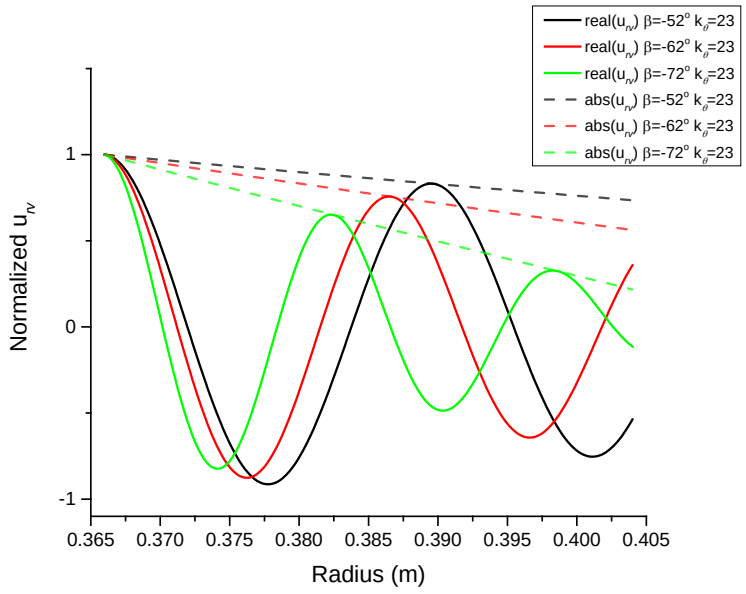

(b)

Figure 6.4. Normalized unsteady radial velocity profile (a) at different circumferential wave number k_θ and (b) at different relative flow angle β.

Note that the unsteady circumferential velocity $u_{\theta v}$ and unsteady radial velocity u_{rv} change in different ways over radius, with $|u_{\theta v}| \propto \frac{1}{r}$ and $|u_{rv}| \propto \left| Er - \frac{c_2}{c_1} D \frac{1}{r} \right|$. This causes distortion of the wake profile as the impeller wake travels downstream. With the inviscid flow assumption in this study, $|u_{rv}| \propto r$ as radius gets larger. This may be contrary to the experimental observation that the impeller wake almost always decays due to turbulent mixing and viscous effects. However, in a similar study of vorticity waves in an inviscid axial annular swirling flow, Golubev and Atassi [33] found a similar linear growth of the unsteady axial velocity as it travels downstream. In fact, the divergent behavior of the unsteady wave in swirling flow is well studied in the area of centrifugal instability [45]. In a two dimensional inviscid flow with only a circumferential mean velocity $U_{\theta 0}$, an axisymmetric disturbance, i.e. $k_\theta = 0$, will become unstable when $\frac{\partial (rU_{\theta 0})}{\partial r} < 0$, which is known as Rayleigh's criterion. In this study, $\frac{\partial (rU_{\theta 0})}{\partial r} = 0$ is on the edge of Rayleigh's criterion. However, with a radial mean flow and non-axisymmetric disturbance, the flow field in this study is more complicated. There is no existing stability criterion for the flow field. Note that the model in this research is a linearized model based on small perturbation theory in inviscid flow. In actual compressors, either viscous dissipation or nonlinear effects will mitigate the growth the vorticity amplitude in the radial direction.

6.2.2 Pressure Wave Propagation

Five case studies are conducted to investigate the effect of the circumferential wavenumber k_θ and the relative flow angle β on the pressure wave propagation upstream from the vaned diffuser due to the impeller wake - diffuser vane interaction. At the design rotation speed Ω of 1790rpm, the wakes of the impeller (23 blades) excite the diffuser vane (30 vanes) at frequency $\omega = \Omega NB = 686 Hz$. Just like the scattering effect in an axial compressor discussed in Section 2.5.1, the diffuser vane generates pressure waves at the same frequency ω , but different circumferential wavenumbers

$$k_\theta = NB + nNV \tag{6.1}$$

where NB and NV are the number of blades and vanes, respectively, and the scattering index n can be any integer.

With the scattering index n equal to 0, -1 and 1, the resulting circumferential wave numbers k_θ are 23, -7 and 53 in Cases 1,2 and 3, respectively. The relative flow angle β in case1, 2 and 3 are equal to the baseline β of -62.0 degrees. In Case 4 and 5, the relative flow angle β is changed to -52 degrees and -72 degrees, respectively with the baseline k_θ of 23. Figure 6.5 shows the variation of the pressure wave amplitudes (in log scale as commonly used for acoustic study) as they propagate from the diffuser vane leading edge to the impeller trailing edge, with the pressure wave amplitudes normalized by their corresponding values at the diffuser vane leading edge. It can be seen that as the pressure waves propagate inwardly, their amplitudes increase for all cases due to space contraction and thus the increase of the acoustic energy density. Larger circumferential wave numbers lead to a higher amplitude growth rate. In addition, the change of relative flow angle and its corresponding change of mean flow velocity have a negligible effect on the change of the pressure wave amplitude growth rate.

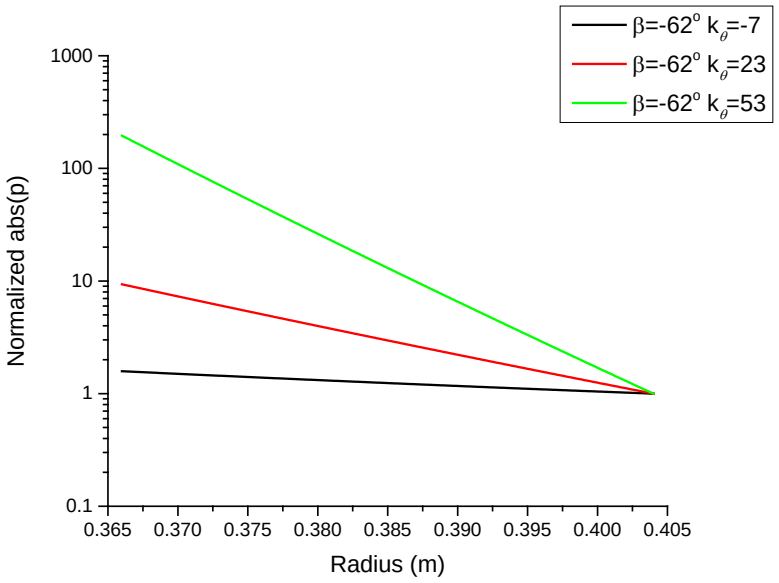

(a)

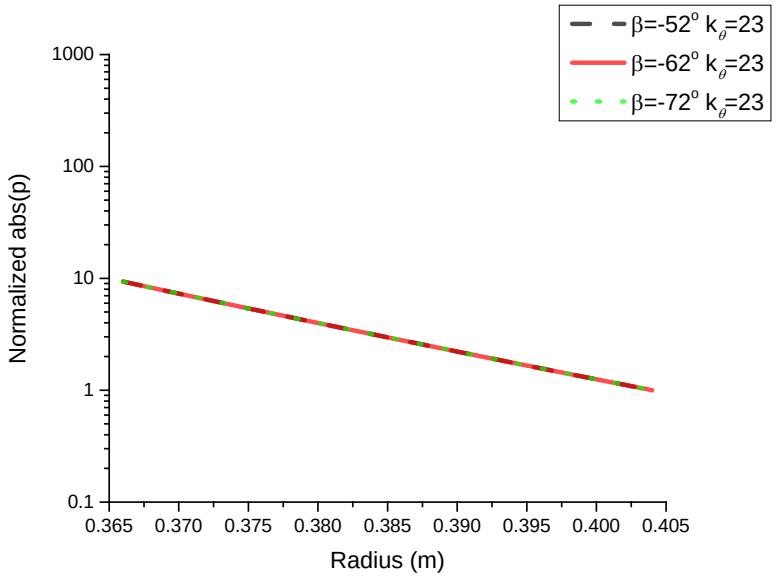

(b)

Figure 6.5. Normalized unsteady pressure amplitude profile (a) at different circumferential wave number k_θ and (b) at different relative flow angle β.

Note that the circumferential wave number has a significant effect on the radial pressure wave growth rate. The larger the circumferential wave number, the higher the growth rate. This is opposite the trend for axial compressors. Smith [11] modeled the pressure wave in an axial compressor as the pressure wave travelling in a thin axial annular duct. The axial wave numbers derived in Equation (2.32) shows that the larger the circumferential wavenumber, the more likely the pressure wave will be cut-off and will decay faster in the axial direction. Thus higher order scattering modes tend to be neglected in acoustics and aeromechanics analyses in axial compressors. This study shows that the higher order scattering pressure waves may be an important excitation source to the impeller as their amplitude growth is much faster than the lower order modes as they travel inwardly.

6.3 Summary

In this chapter, the propagation of the impeller wake and pressure wave in the vaneless space is investigated through parametric studies with different impeller blade number (affecting the circumferential wave number k_θ) and back sweep angle (affecting the relative flow angle β).

For vorticity wave propagation, results show that the unsteady circumferential velocity $u_{\theta v}$ and unsteady radial velocity u_{rv} change in different ways over radius. This causes distortion of the wake profile as the impeller wake travels downstream. Increasing the number of blades and increasing the back sweep angle reduce the wavelength of the unsteady circumferential velocity $u_{\theta v}$ and unsteady radial velocity u_{rv} of the impeller wake.

For pressure wave propagation, results show that the amplitude of the pressure waves always increase as they propagate inwardly, due to space contraction and thus the increase of the acoustic energy density. The relative flow angle and its corresponding mean flow velocity have a negligible effect on the pressure wave amplitude growth rate. On the other hand, the circumferential wave number has a significant effect on the radial pressure wave growth rate. Opposite to the trend in axial compressors, the larger the circumferential wave number, the higher the pressure wave growth rate.

CHAPTER 7. UNIFIED PROPELLER AND HORIZONTAL-AXIS TURBINE OPTIMIZATION

The Lifting line theory and different rotor blade optimization methods have been discussed in Section 2.6. A unified propeller and horizontal-axis turbine preliminary design code based on the Lifting line model of the rotor and using the Interior point method for optimization is developed in this study. The code is called Optimized Rotor with Lifting Line model, or OptRotor. Discussion in Section 2.6 also shows that the classical PVL code for propeller design can be used for horizontal-axis turbine design by sweeping through all possible C_T (-1 to 0) to find the minimum overall C_Q. This new implementation of the PVL is called PVL for turbine, or PVLt.

The cases studies in this chapter aim to provide a thorough validation for OptRotor and PVLt by comparing their results with the results from the classical PVL code [37] and also the OpenProp [38] code that is based a Lifting line model using the Lagrange multiplier method for optimization. The feature and capability of each code are compared in Table 7.1.

Table 7.1. Comparison of the feature and capability of different codes.

	General Momentum Theory (GMT)	**PVL**	**OpenProp**	**OptRotor**
Model	Rotating Actuator Disk	Lifting line	Lifting line	Lifting line
Optimization Method	First Derivative Test	Calculus of Variations	Lagrange Multiplier	Interior Point
Wake rotation loss model	Yes	Yes	Yes	Yes
Tip loss model	No	Yes	Yes	Yes
Propeller design	Possible	Yes	Yes	Yes
Horizontal-axis turbine design	Yes	Yes, with the new implementation PVLt	Yes	Yes
Hub model	No	Yes	Yes	Yes
Non-uniform inflow	No	Yes	Yes for propeller No for turbine	Yes
Extra design constrains	No	Possible	Possible	Yes
Computation time	seconds	seconds	<1 minute	<1 minute

The OptRotor code is first used for the propeller design case studies with uniform inflow and also with non-uniform inflow. The results are validated with the results from PVL and OpenProp in Section 7.1.

Horizontal-axis turbine optimization validation and case studies is done in Section 7.2. PVLt and OptRotor are validated with General Momentum Theory first in case study1 and case study2. Case study3 with uniform inflow and hub model is then conducted using PVLt, OptRotor and OpenProp. Since OpenProp cannot handle turbine optimization with non-uniform inflow, Case study4 with non-uniform inflow and Case study5 with non-uniform inflow and hub image are conducted using PVLt and OptRotor. The results from different codes are compared for validation and also for finding out the advantage and limitation of each code. Finally, a more complicated and realistic case study6 with structural consideration is conducted to show the capability of the OptRotor code.

7.1 Validation and Case Studies for Propeller Design

The propeller case studies are based on the example in Kerwin's paper [27] Table 4.3. It is a propeller with 5 blades, $Z = 5$. The desired thrust coefficient is 1, $C_T = 1$. The blade hub starts at $r_h = 0.2R$. No hub model is included. The viscous drag is neglected.

The first case study has a uniform inflow $V_a / V_f = 1$ and $V_t / V_f = 0$. The optimized circulation distribution Γ using the codes PVL, OpenProp and OptRotor at three different advance coefficients, $J = 0.1$, $J = 0.8$ and $J = 1.5$ are shown in Figure 7.1. The corresponding total flow angles β_i are shown in Figure 7.2. At $J = 0.1$ and $J = 0.8$, the results from three codes are almost identical. At a higher advance coefficient $J = 1.5$, OpenProp favors a slightly higher loading Γ and thus a slightly higher total flow angle β_i on the outer region of the blade than PVL, while the results from OptRotor are in between. The overall performance parameters C_Q , C_P and η predicted by PVL, OpenProp and OptRotor are very close as shown in Table 7.2.

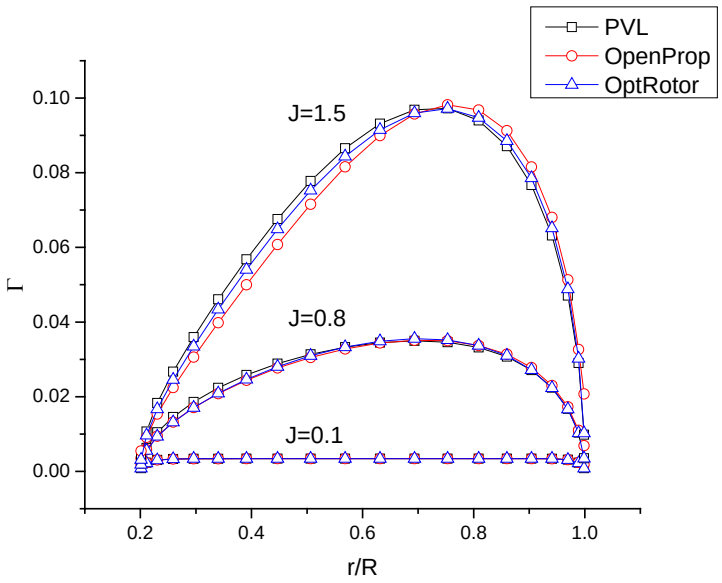

Figure 7.1. Optimized circulation distributions by different codes at different advance coefficients for propeller case study1.

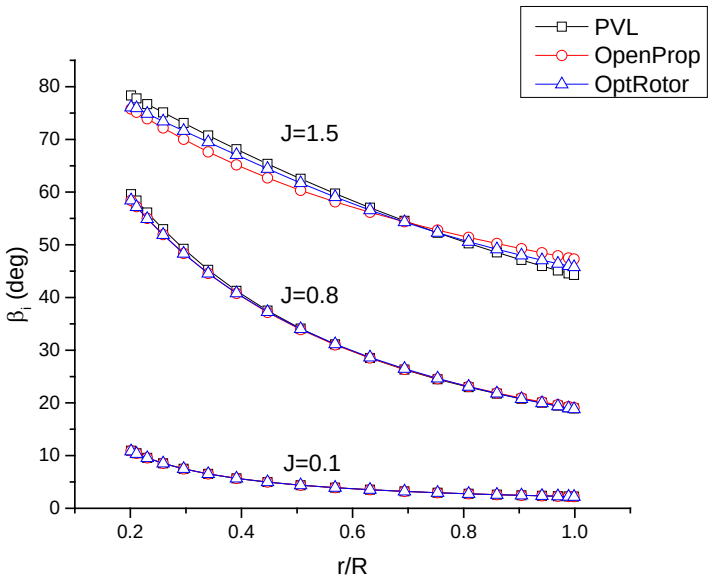

Figure 7.2. Total flow angle β_i by different codes at different advance coefficients for propeller case study1.

Table 7.2. Comparison of C_Q, C_P and η by different codes at different advance coefficients for propeller case study1.

	$J=0.1$			$J=0.8$			$J=1.5$		
	PVL	OpenProp	OptRotor	PVL	OpenProp	OptRotor	PVL	OpenProp	OptRotor
C_Q	0.039	0.039	0.039	0.343	0.343	0.343	0.974	0.976	0.972
C_P	1.221	1.221	1.221	1.347	1.347	1.347	2.040	2.045	2.036
η	0.819	0.819	0.819	0.742	0.742	0.742	0.490	0.489	0.491

The second case study has a non-uniform inflow. Following the Kerwin's example, the inflow velocity is V_a / V_f = [0.7197 0.7430 0.7626 0.7946 0.8203 0.8420 0.8607 0.8773 0.8922 0.8991 0.9057] at radial position r / R = [0.20 0.25 0.30 0.40 0.50 0.60 0.70 0.80 0.90 0.95 1.00] and $V_t / V_f = 0$ at all radial positions. The optimized circulation distribution Γ using code PVL, OpenProp and OptRotor at three different advance coefficients, $J = 0.1$, $J = 0.8$ and $J = 1.5$ are shown in Figure 7.3. The corresponding total flow angle β_i are shown in Figure 7.4. The overall performance

parameters C_Q, C_P and η are listed in Table 7.3. Similar to the first case study, the results from code PVL, OpenProp and OptRotor are almost identical, except that OpenProp favors a slightly higher loading Γ and thus a slightly higher total flow angle β_i on the outer region of the blade than PVL at high advance coefficient $J = 1.5$.

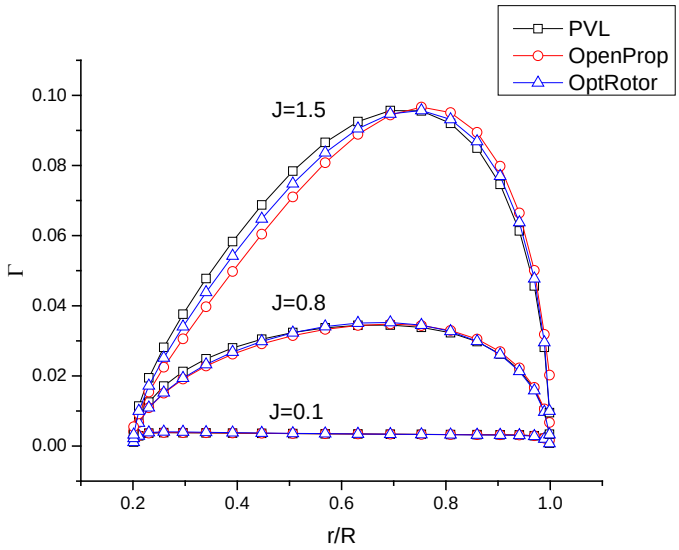

Figure 7.3. Optimized circulation distributions by different codes at different advance coefficients for propeller case study2.

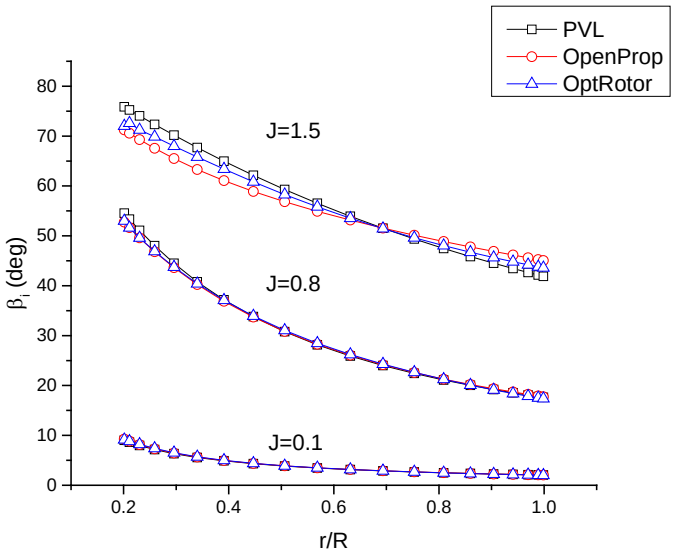

Figure 7.4. Total flow angle β_i by different codes at different advance coefficients for propeller case study2.

Table 7.3. Comparison of C_Q, C_P and η by different codes at different advance coefficients for propeller case study2.

	$J=0.1$			$J=0.8$			$J=1.5$		
	PVL	OpenProp	OptRotor	PVL	OpenProp	OptRotor	PVL	OpenProp	OptRotor
C_Q	0.035	0.035	0.035	0.308	0.309	0.309	0.873	0.879	0.875
C_P	1.090	1.096	1.096	1.209	1.215	1.215	1.828	1.841	1.832
η	0.783	0.778	0.778	0.705	0.702	0.702	0.466	0.463	0.465

These two cases studies provide a validation for the newly developed OptRotor code. The close match with the other existing propeller codes PVL an OpenProp shows that both the Lifting line model and Interior point optimization method have been correctly implemented in the code.

7.2 Validation and Case Studies for Horizontal-axis Turbine Design

The first two case studies aim to validate the PVLt code with the analytical solution from the Betz's Actuator Disk model and from the Schmitz's Rotating Actuator Disk model (i.e. General Momentum theory). Betz's Actuator Disk model is a limiting case for an infinite number of blades and infinite tip speed ratio. One-hundred blades and a tip speed ratio of 100 are specified in PVLt to resemble Betz's Actuator Disc model. Schmitz's Rotating Actuator Disk model is a limiting case for an infinite number of blades. One-hundred blades and a tip speed ratio of 6 are specified in PVLt in order to compare with the results from Schmitz's Rotating Actuator Disk model.

In both case studies, a very small hub radius $r_h = 0.005R$ without hub model is used since there is no hub in both Actuator Disk models. The viscous drag is also neglected. By sweeping C_T from -1 to 0, the corresponding minimized C_P calculated by PVLt is plotted in Figure 7.5. The minimum C_P (i.e. maximum magnitude of C_P) is -0.59 occurring at $C_T = -0.89$ for the case $Z = 100$ and $\lambda = 100$. This result is the same as the 'Betz limit' $C_P = 16/27$ and the corresponding $C_T = 8/9$. The minimum C_P is -0.57 occurring at $C_T = -0.88$ for the case $Z = 100$ and $\lambda = 6$. This result is very close to the Schmitz's result $C_P = 0.5759$ calculated using Equation (2.155) and the corresponding

$C_T = 0.8847$. Note that since the propeller convention is used in all the codes in this study, the PVLt's results are all negative.

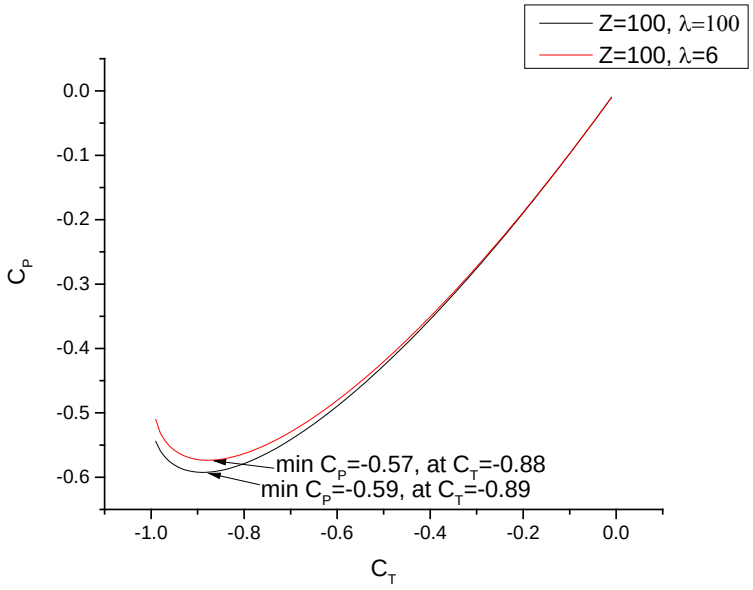

Figure 7.5. Minimized C_P for C_T from -1 to 0 by PVLt code.

In order to do a detailed comparison, the second case study ($Z = 100$, $r_h = 0.005R$,no hub model, no viscous drag and uniform inflow $V_a / V_f = 1$ and $V_t / V_f = 0$) with tip speed ratio $\lambda = 1, 2, \cdots 10$ are conducted again with OpenProp and OptRotor. In Figure 7.6, the maximum magnitude of C_P predicted by PVLt, OpenProp and OptRotor are plotted against the analytical solution calculated from Equation (2.155) by the General Momentum Theory. It can be seen that the results from all three codes match the General Momentum Theory perfectly, except that at the low tip speed ratio $\lambda = 1$, C_P predicted by PVLt is slightly lower than the value predicted by the General Momentum Theory. The difference is due to the poor assumption that the induced velocity $u_t^* \ll \omega r$ at the low tip speed ratio.

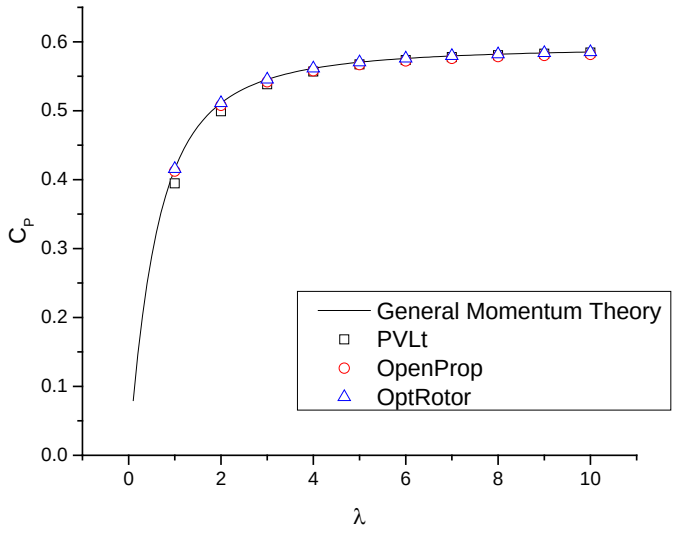

Figure 7.6. C_P predicted by PVLt, OpenProp and OptRotor compared with General Momentum Theory.

At a commonly used tip speed ratio $\lambda = 6$, the optimized circulation distribution Γ using code PVLt, OpenProp, OptRotor and General Momentum Theory (GMT) are shown in Figure 7.7. The corresponding the total flow angle β_i and induced velocity u_a^* and u_t^* are shown in Figures 7.8, 7.9 and 7.10. The comparison shows that the results from both OpenProp and OptRotor match the results from General Momentum Theory perfectly. This serves as a validation for the newly developed OptRotor on horizontal-axis turbine designs. PVLt results are different from the General Momentum Theory in the inner region of the blade ($r < 0.3R$). This difference is due to the poor assumption that the induced velocity $u_t^* \ll \omega r$ at small radius made when deriving the 'Lerbs criterion' in Equation (2.144).

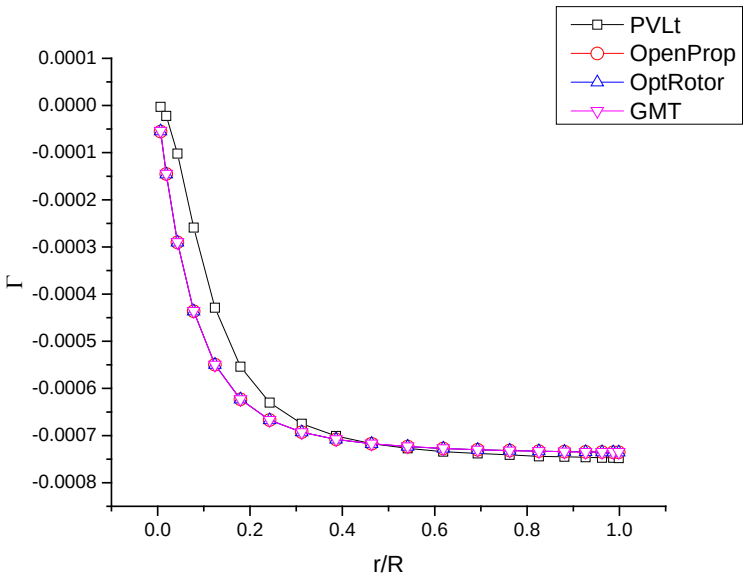

Figure 7.7. Optimized circulation distributions Γ given by PVLt, OpenProp, OptRotor and general momentum theory (GMT) for turbine case study2.

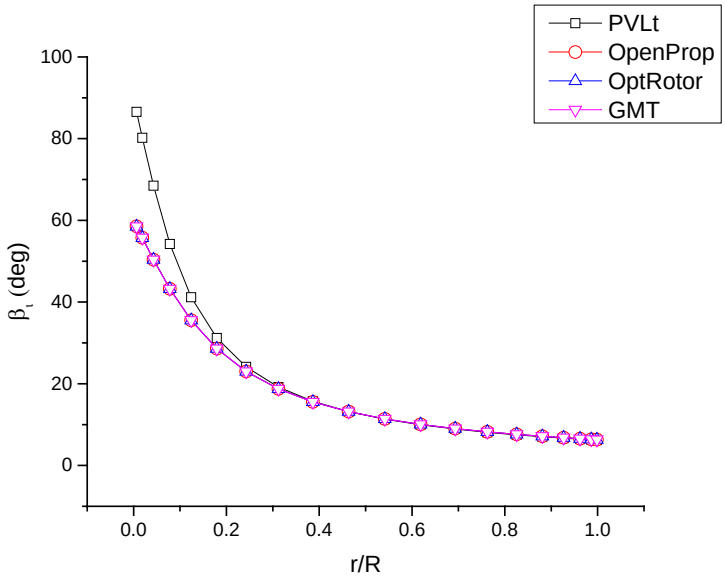

Figure 7.8. Total flow angle β_i given by PVLt, OpenProp, OptRotor and general momentum theory (GMT) for turbine case study2.

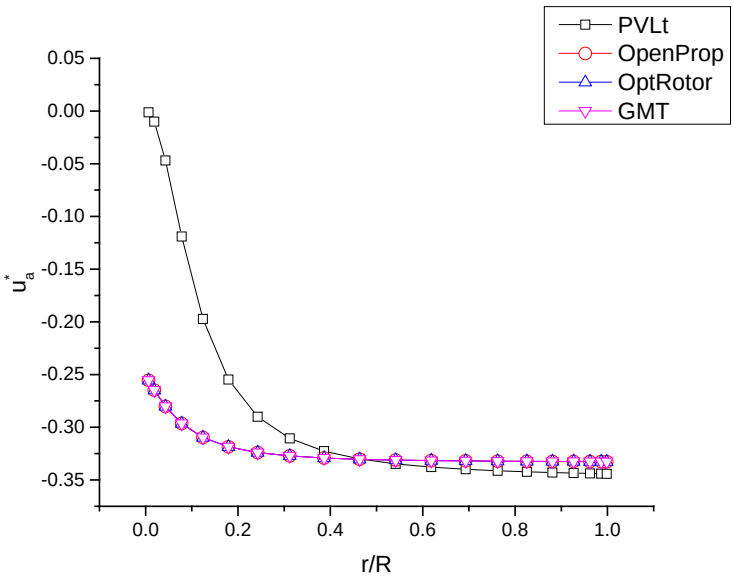

Figure 7.9. Axial induced velocity u_a^* given by PVLt, OpenProp, OptRotor and general momentum theory (GMT) for turbine case study2.

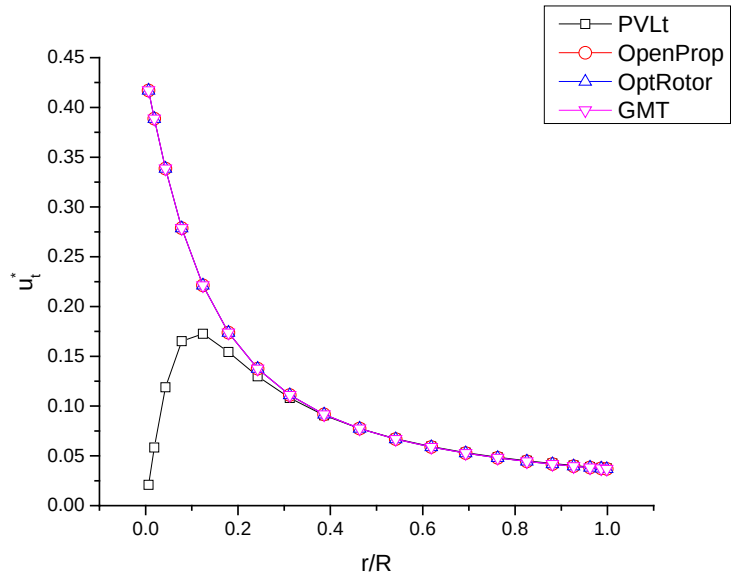

Figure 7.10. Tangential induced velocity u_t^* given by PVLt, OpenProp, OptRotor and general momentum theory (GMT) for turbine case study2.

The first two case studies considered 100 blades for validation with Actuator Disk models. The third case study is a more realistic case with 3 blades $Z=3$, a rub $r_h=0.1R$ and under uniform inflow $V_a/V_f=1$ and $V_t/V_f=0$. The hub is modelled using the vortex image method discussed before. The viscous drag is neglected. The optimized circulation distribution Γ using code PVLt, OpenProp and OptRotor at three tip speed ratios $\lambda=4$, $\lambda=6$ and $\lambda=10$ are shown in Figure 7.11. The corresponding total flow angles β_i are shown in Figure 7.12. Note that there is a non-zero strength bound circulation at the hub surface due to the hub model. The results from the three codes are very close to each other at $\lambda=6$ and $\lambda=10$. At low tip speed ratio $\lambda=4$, PVLt favors a lower loading (magnitude) and thus a higher β_i than OpenProp at the inner region of the blade. The results from OptRotor are in between. The overall performance parameters C_Q, C_P predicted by PVLt, OpenProp and OptRotor are very close as shown in Table 7.4. This case study serves an additional validation of OptRotor and PVLt for turbine optimization with hub model under uniform inflow conditions.

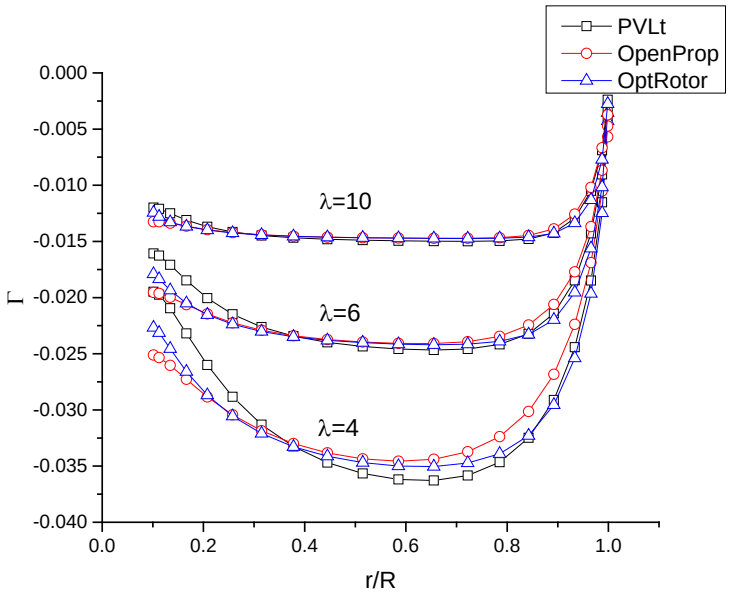

Figure 7.11. Optimized circulation distributions by different codes at different tip speed ratio for turbine case study3.

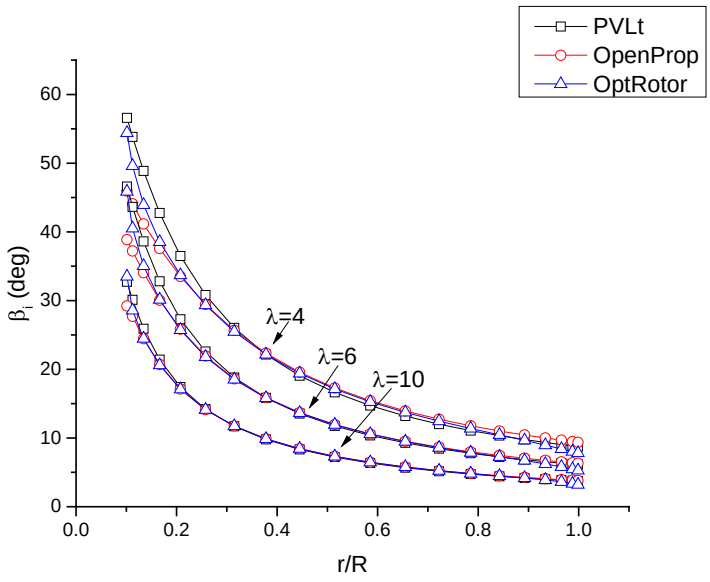

Figure 7.12. Total flow angle β_i by different codes at different tip speed ratio for turbine case study3.

Table 7.4. Comparison of C_Q and C_P by different codes at different tip speed ratio for turbine case study3.

	$\lambda = 4$			$\lambda = 6$			$\lambda = 10$		
	PVLt	OpenProp	OptRotor	PVLt	OpenProp	OptRotor	PVLt	OpenProp	OptRotor
C_Q	-0.118	-0.119	-0.119	-0.086	-0.086	-0.086	-0.055	-0.055	-0.055
C_P	-0.473	-0.477	-0.475	-0.514	-0.516	-0.514	-0.545	-0.546	-0.546

OpenProp works only for uniform incoming flow. The newly developed code OptRotor and new implementation of the PVL code, PVLt have no such restrictions. The inflow velocity for large wind turbines is inherently non-uniform due to the atmospheric boundary layer. The fourth case study is for a turbine with 3 blades $Z = 3$, a rub $r_h = 0.1R$ but without hub model, under a non-uniform inflow $V_a/V_f = 1 - 0.1\left(r/R\right)^2$ and $V_t/V_f = 0$. Viscous drag is neglected. The optimized circulation distribution Γ using code PVLt and OptRotor at three tip speed ratios $\lambda = 4$, $\lambda = 6$ and $\lambda = 10$ are shown in Figure 7.13. The corresponding total flow angles β_i are shown in Figure 7.14. It can be seen that OptRotor favors a higher loading and thus lower β_i in the inner region of the blade. The

difference between the results from OptRotor and PVLt is larger as the tip speed ratio decreases. This is because of the assumption that the induced velocity $u_t^* \ll \omega r$ used in PVLt Equation (2.144) is getting poorer at smaller radii and lower tip speed ratios. This assumption in PVLt also leads to a lower C_Q and C_P than the turbine optimized using OptRotor as seen in Table 7.5. Although there is no existing code for turbine optimization under a non-uniform inflow for validation, the close match of the results from codes PVLt and OptRoror shows the capability of both codes to optimize turbine design with non-uniform inflow. OptRotor gives a little better result than PVLt as suggested by its higher C_P value.

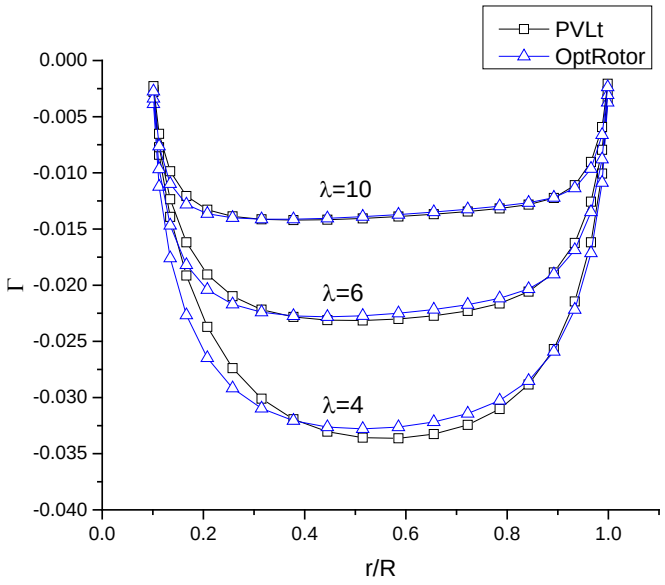

Figure 7.13. Optimized circulation distributions by different codes at different tip speed ratio for turbine case study4.

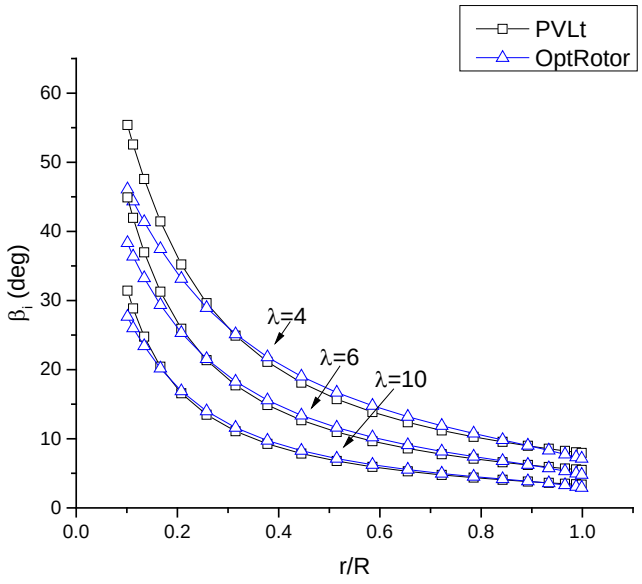

Figure 7.14. Total flow angle β_i by different codes at different tip speed ratio for turbine case study4.

Table 7.5. Comparison of C_Q and C_P by different codes at different tip speed ratio for turbine case study4.

	$\lambda = 4$		$\lambda = 6$		$\lambda = 10$	
	PVLt	OptRotor	PVLt	OptRotor	PVLt	OptRotor
C_Q	-0.101	-0.104	-0.072	-0.075	-0.046	-0.047
C_P	-0.402	-0.414	-0.434	-0.447	-0.458	-0.472

The fifth case is the same as the fourth case except a hub model is included. The optimized circulation distribution Γ using code PVLt and OptRotor at three tip speed ratios $\lambda = 4$, $\lambda = 6$ and $\lambda = 10$ are shown in Figure 7.15. The corresponding total flow angles β_i are shown in Figure 7.16. The overall performance parameters C_Q , C_P are listed in Table 7.6. Similar to the trends seen in the fourth case study, the results from both codes are very close except PVLt favors a lower loading (magnitude) and thus a higher β_i in the inner region of the blade. C_Q , C_P of the turbine optimized by PVLt is a bit lower than the turbine optimized by OptRotor. The close match of the results from codes PVLt and OptRoror shows the capability of both codes to optimize turbine design with

both non-uniform inflow and hub model. OptRotor gives a little better load distributions which leads to a higher C_P value than PVLt's result.

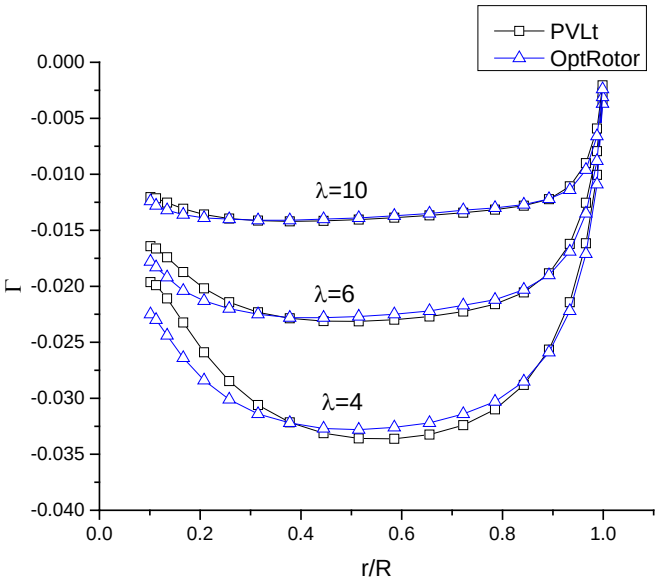

Figure 7.15. Optimized circulation distributions by different codes at different tip speed ratio for turbine case study5.

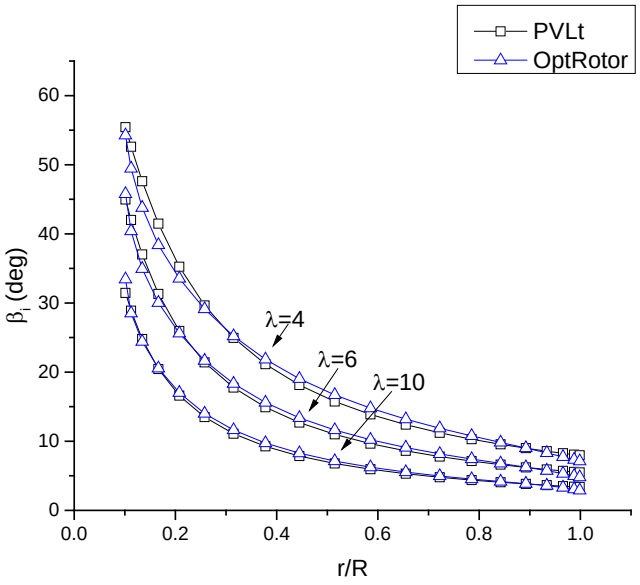

Figure 7.16. Total flow angle β_i by different codes at different tip speed ratio for turbine case study5.

Table 7.6. Comparison of C_Q and C_P by different codes at different tip speed ratio for turbine case study5.

	$\lambda = 4$		$\lambda = 6$		$\lambda = 10$	
	PVLt	OptRotor	PVLt	OptRotor	PVLt	OptRotor
C_Q	-0.102	-0.105	-0.073	-0.075	-0.046	-0.048
C_P	-0.408	-0.420	-0.438	-0.451	-0.461	-0.475

The last case study is to demonstrate the additional capability of the OptRotor code for turbine optimization with constraints. Although there is no requirement on the thrust of a turbine, there are other considerations that lead to some constraints. For example, due to structural or manufacturing considerations, the hub region of the blade is usually designed in the shape of a cylindrical rod. There is no lift generated by a cylinder and thus the loading at the cylindrical rod region is always zero regardless of the inflow velocities and rotation speed. This loading constraint can be easily specified in OptRotor. Case study6 is the same as Case study5 ($Z = 3$, $r_h = 0.1R$ with hub model, non-uniform inflow $V_a/V_f = 1 - 0.1\left(r/R\right)^2$ and $V_t/V_f = 0$), except that from blade hub 0.1R to 0.2R the blade is in the shape of a cylindrical rod and thus the bound circulation is always zero. At tip speed ratio $\lambda = 6$, the bound circulation distribution for case study5 and case study6 are compared in Figure 7.17. The results show that the loading constraints from 0.1R to 0.2R affect the optimized circulation distribution up to 0.4R.

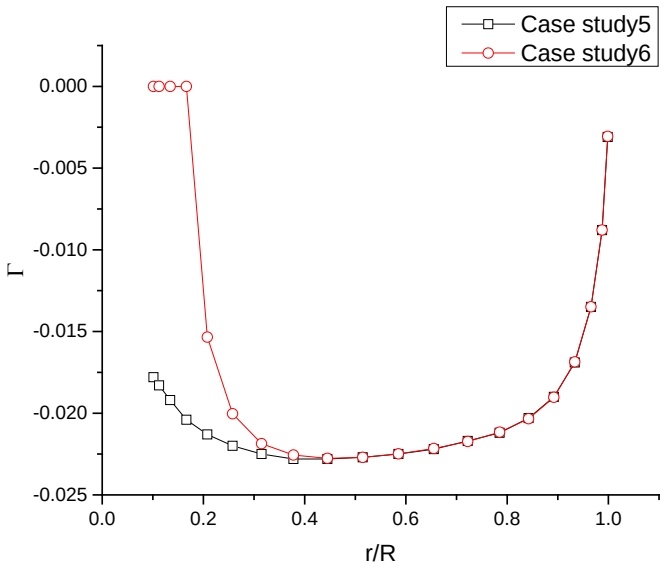

Figure 7.17. Optimized circulation distributions with constrains (case study6) and without constrains (case study5).

7.3 Comments on the OptRotor Code

OptRotor uses the Matlab internal function fmincon to do optimization based on the Interior point method. Besides the basic rotor parameters (blade number Z, hub radius r_h and tip speed ratio λ or advance coefficient J) and inflow conditions (V_a and V_t), other parameters for numerical calculation need to be specified such as an initial guess x_0, the lower bound *lb* and upper bound *ub*, and number of the discretization panels M. Convergence tests have been conducted and show that 20 panels are sufficient to give an accurate result for most cases. Convergence tests also show that OptRotor is not sensitive to the initial guess. A physically reasonable guess (for example, simply a positive number) always leads to the optimized result. The lower the upper bound suggested in Section 2.6 are good enough to achieve an optimized result rapidly for most cases. The bound range needs to be increased a bit when an extra constraints is specified. For example, in turbine case study6, the upper bound is increased to $5\tan\beta$ to obtain the optimized result. The default maximum number of function evaluation is 3000 in fmincon. For some cases (especially low tip speed ratio or high advance coefficient),

more iterations are needed to converge to the optimized result. The maximum number of function evaluations can be increased by using Matlab internal function optimoptions.
Since normally there is no constraint for horizontal-axis turbine optimization, another Matlab internal function fminsearch was considered. fminsearch is an unconstrained nonlinear optimization function based on Nelder-Mead simplex algorithm. Several turbine design case studies have been conducted with fminsearch. fmincon based on Interior point method works much better than fminsearch in terms of number of iterations and the final physically reasonable optimized solution. In addition, fmincon is more versatile by being able to specify more constraints if necessary.

7.4 Summary

In this chapter, detailed validation and case studies are conducted for the newly developed OptRotor code and the new implementation of the PVL code, PVLt. The OptRotor code is first validated with results from both PVL and the OpenProp code for propeller design with uniform inflow and also with non-uniform inflow.

The OptRotor code and PVLt code are then validated with the analytical results given by General Momentum theory for horizontal-axis turbine design. For uniform inflow with hub model, results from the OptRotor code and PVLt code are compared with the results from the OpenRotor code. Good agreement on both optimized bound circulation and total flow angle is observed. Additional validation between OptRotor and PVLt are conducted for the turbine optimization with non-uniform incoming flow with and without hub image. OptRotor gives a better optimization because the assumption $u_t^* \ll \omega r$ used in PVLt gets poorer at small radius and low tip speed ratio. In addition, the capability of specifying extra constraints makes OptRotor a more versatile preliminary design tool.

CHAPTER 8. CONCLUSION AND FUTURE WORK

8.1 Conclusion

This thesis presents four analytical/ semi-analytical models for preliminary design in turbomachinery. They are: 1) a generalized flat plate cascade model for investigating the unsteady aerodynamic of a blade row with non-uniformly spaced blades; 2) a multistage interaction model for investigating rotor-stator interactions; 3) an analytical solution for quantifying the centrifugal compressor impeller wake convection and pressure wave propagating between the impeller and diffuser vane; and 4) a semi-analytical model based lifting line theory for unified propeller and horizontal-axis turbine optimization.

The first three models for unsteady aerodynamics in axial and centrifugal compressors are based on linearized Euler equations. The unsteadiness in the flow is assumed to a small perturbation superimposed on a steady mean flow. The time-averaged steady mean flow is first obtained by solving the non-linear mean flow Euler equations. The unsteady waves in the flow are assumed to be harmonic in time and in the circumferential direction. Their amplitudes are found by solving the linearized Euler equations. The last model for propeller and horizontal-axis turbine optimization is based on the Lifting line theory. The Interior point method is used for optimization. To analyze the aeromechanics problem, the blade section structural dynamics are modelled using a spring-mass model with uncoupled bending and torsion vibrations. Each model is first validated with existing models, and then applied in different case studies.

The generalized flat plate cascade model is applied in several case studies based on the geometry and flow condition of the Purdue Transonic Compressor rotor, to study the effect of different aerodynamically mistuned configurations on rotor forced response, flutter and acoustic behavior. Forced response and flutter analyses show that loading and

aerodamping on the blades of non-uniformly spaced blade rows can be significantly different from the blades on a uniformly spaced blade row. Some blades on a non-uniformly spaced blade row may become unstable at certain interblade phase angles and at certain operating conditions when the corresponding uniformly spaced blade row has no flutter problem. Acoustic analysis shows that the acoustic energy of the propagating pressure waves generated on the rotor due to the excitation of the IGV wake spread out over more frequency components for the non-uniformly spaced blade row than for the uniformly spaced blade row.

The multistage interaction model is applied in a series of case studies based on the geometry and flow conditions of the Purdue 3-Stage Research Compressor to investigate the multistage interactions effects (by varying inter-row spacing and vane clocking positions) on the forced response, flutter and aeroacoustic behavior of the embedded rotor row. The forced response and flutter analyses show that unsteady loading and aerodamping considering multistage interactions are markedly different from the values obtained by a single row analysis. By varying inter-row spacing and vane clocking, the multistage effect can be altered in a favorable way to reduce unsteady loading and increase the aerodamping of the rotor. The acoustic analysis shows that multistage interaction amplifies the existing pressure wave in the single blade row analysis. Additional propagating pressure waves that do not exist in a single blade row analysis are also generated due to the multistage interactions. Both inter-row spacing and vane clocking can greatly affect the amplitude of the propagating pressure waves.

The generalized flat plate cascade model and multistage interaction model are combined to study the effect of non-uniform spaced IGV on the downstream rotor flutter stability based on the Purdue Transonic Compressor's geometry and flow conditions. Case studies show that both the effects of multistage interaction and non-uniformly spaced IGV make the classic flutter analysis of a single rotor inaccurate at certain interblade phase angles.

The analytical solutions for the unsteady waves in a radial duct with mean swirling flow is used to study the propagation of the impeller wake and pressure wave in the vaneless space based on the geometry and flow conditions of the Purdue Low Speed

Centrifugal Compressor. For vorticity wave propagation, results show that the unsteady circumferential velocity and unsteady radial velocity change in different ways over radius. This causes distortion of the wake profile as the impeller wake travels downstream. For pressure wave propagation, results show that the amplitude of the pressure waves always increase as they propagate inwardly due to space contraction and thus the increase of the acoustic energy density. Mean flow velocity has a negligible effect on the pressure wave amplitude growth rate. Opposite to the trend in axial compressors, pressure waves with larger circumferential wave numbers have higher growth rates.

Blade element momentum theory is the current standard preliminary design tool for wind turbines. It models a wind turbine as a rotating actuator disk and assumes there is no aerodynamic interaction between different blade sections. These two assumptions significantly limit the accuracy of the model. By performing a detailed analysis of the Lifting line theory based marine propeller preliminary design tool, the mathematical and physical equivalence of the propeller and horizontal-axis turbine under the Lifting line theory is found. Case studies show that propeller optimization methods can be applied to horizontal-axis turbine optimization directly by sweeping through all possible thrust coefficients and finding the overall minimum negative value for the torque coefficient (which gives maximum power output). By examining the assumptions made in the Lagrange multiplier based optimization method, a new unified propeller and horizontal-axis turbine optimization code based on the Interior point method is developed. Case studies show the new code is a very versatile preliminary design tool with the capability of hub modelling, working with non-uniform inflow and including extra user specified constraints.

8.2 Future Work

The theoretical framework of the models developed in this study is very general and can be extended for additional features and applications. The following areas are those that the author recommends for future work

8.2.1 Unintentional Aerodynamic Mistuning

The generalized flat plate cascade model developed in this study is used to explore the potential of intentionally aerodynamically mistuning a blade row as a passive control technique. Unintentional aerodynamic mistuning due to operational wear and damage is also of great interest because it can change unsteady loading on each blade randomly. The associated small blade-to-blade non-uniform stagger angles and chord length can be easily included as they are just another form of non-uniform spacing at different chordwise positions for the flat plate cascade model. A statistical analysis would be able to quantify the unintentional aerodynamic mistuning effect on the unsteady loading of a blade row.

8.2.2 Structural Mistuning

Structural mistuning in terms of blade-to-blade natural frequency variations can be easily included in the mass-spring structural dynamic model of the blade section in Section 2.1. The response blade vibration amplitude can be treated as the summation of all possible fundamental harmonic modes by discrete Fourier transform. In this way, aerodynamically mistuned blade rows, structurally mistuned blade rows and multistage interaction are all based on the same theoretical framework of using cascade waves to model the unsteady waves, unsteady loading and blade vibration. In this study, the aerodynamically mistuned blade row has been incorporated into the multiage interaction model. The extension to include structural mistuning can result in a complete unsteady aerodynamic model for aeromechanic problems in axial compressors.

8.2.3 Radial Cascade Model

The analytical unsteady radial wave solution is a fundamental characteristic of the unsteady flow field in a radial duct. Based on these analytical unsteady radial wave solutions, the framework developed for a linear flat plate cascade model [11] can be followed to develop a radial flat plate cascade applicable to centrifugal compressors. This semi-analytical radical cascade model can be very helpful in preliminary centrifugal

compressor design because 1) start-of-art aeromechanic analysis methods for centrifugal compressors are very limited, and 2) centrifugal compressor design usually varies based on customer specifications and applications that which prohibit systematic unsteady CFD simulations [19].

8.2.4 Lifting Line Theory Based Novel Horizontal-axis Turbine Design

This study has shown the mathematical and physical equivalence between propellers and horizontal-axis turbines in Lifting line theory. This equivalence enables many existing propeller design tools and design concepts to be used for horizontal-axis turbine design with little additional effort. For example, ducted propellers and contra-rotating propellers have all been designed based on Lifting line theory [46-47]. Corresponding shrouded wind turbines and contra-rotating wind turbines have been proposed and commercialized by several companies [48-49]. The Lifting line theory based optimization method is able to provide a strong theoretical foundation for these novel horizontal-axis turbine designs.

LIST OF REFERENCES

LIST OF REFERENCES

[1] Kaza, K., and Kielb, R. E., 1982, "Flutter and Response of a Mistuned Cascade in Incompressible Flow," *AIAA J.*, 20(8), pp. 1120–1127.

[2] Crawley, E. F., and Hall, K. C., 1985, "Optimization and Mechanisms in Mistuning in Cascades," *ASME J. Eng. Gas Turbines Power*, 108, pp. 418–426.

[3] Mayorca, M. A, 2011, "Numerical Methods for Turbomachinery Aeromechanical Predictions", *PhD Thesis*, Department of Energy Technology, Royal Institute of Technology, Sweden

[4] Scott, S. and Fleeter, S.,1995, "Flutter Stability of a Detuned Cascade in Subsonic Compressible Flow", *Journal of Propulsion and Power*, Vol. 11, No.5

[5] Ekici, E., Kielb, R. and Hall, K. 2010, "Aerodynamic Asymmetry Analysis of Unsteady Flows in Turbomachinery", *Journal of Turbomachinery*, Vol. 132

[6] Crall, D.W. and Manwaring, S.R., 2002, "Periodic Stator Airfoils", *General Electric Co, US Patent*, US6439838 B1

[7] Gautreau, J.C. and Wassynger, S.P., 2010, "Method of Providing Non-uniform Stator Vane Spacing in a Compressor", *General Electric Co, US Patent*, US7743497 B2, June 2010

[8] Delvaux, J.M. and Potter B.D., 2012, "Rotary Machine Having Non-uniform Blade and Vane Spacing", *General Electric Co, US Patent*, US0099961 A1

[9] Hanson, D.B, 1992, "Unsteady Coupled Cascade Theory applied to the Botor/Stator Interaction Noise Problem," *DGLR/AIAA Paper* 92-02-08

[10] Buffum, D.H., 1993, "Blade Row Interaction Effects on Flutter and Forced Response", *AIAA*-93-2084

[11] Smith, S.N., 1971, "Discrete Frequency Sound Generation in Axial Flow Turbomachines",*CUED/ATurbo*/TR29

[12] Hall, K.C., and Sikowaski, P.D., 1997, "The Influence of the Neighboring Blade rows on the Unsteady Aerodynamic Response of Cascades," *Journal of Turbomachinery*, Vol.119, pp.85-93

[13] Silkowski, P.D., 1996, "A Coupled Mode Method for Multistage Aeroelastic and Aeroacoustic Analysis of Turbomachinery", *PhD Thesis*, Department of Mechanical Engineering and Materials Science, Duke University, USA

[14] Key, N., Lawless, P., and Fleeter, S., 2008, "An experimental study of Vane clocking effects on Embedded Compressor Stage Performance," *ASME Paper* GT2008-51087.

[15] Capece,V.R. and Fletter,S., 1987, " Unsteady Aerodynamic Intercations in a Multistage Compressor," *Journal of Turbomachinery*, Vol.109, pp.420-428.

[16] Choi,Y.S., 2008, "Investigation of the resonant response of mistuned rotors", *PhD Thesis*, Department of Mechanical Engineering, Purdue University, USA

[17] Salontay, J.R. and Key,N., 2010, "A Computational Investigation of Vane Clocking Effects on Comrpessor Forced Response", *AIAA Paper* AIAA-2010-746

[18] Konig, S., Petry, N. and Wagner,N.G, 2009, "Aeroacoustic phenomena in high-pressure centrifugal compressors - A possible root cause for impeller failures".*Texas A&M 37th Turbomachinery Symposium Proceedings*

[19] Ranakrishnan, K.,Richards,S.K., Moyroud F., Michelassi V., 2011, "Multi-blade row interactions in a low pressure ratio centrifugal compressor stage with a vaned diffuser" . *Proceedings of ASM Turbo Expo*

[20] Bryan, W.B., 1991, "An investigation of unsteady impeller-diffuser interactions in a centrifugal compressor", *PhD Thesis*, Department of Mechanical Engineering, Purdue University, USA

[21] Gottfried, DA., Fleeter,S., 2002, "Impeller Blade Unsteady Aerodynamic Response to Vaned Diffuser Potential Fields", *Journal of Propulsion and Power*, Vol. 18, No.2

[22] Betz, A., 1920, "Das Maximum der theoretisch möglichen Ausnützung des Windes durch Windmotoren." *Zeitschrift für das gesamte Turbinenwesen* 26: 307–309.

[23] Betz, A., 1919, "Schraubenpropeller mit geringstem energieverlust", K. Ges. Wiss. *Gottingen Nachr. Math.-Phys. Klasse*, pp. 193–217.

[24] Wald, Q.R., 2006, "The aerodynamics of propellers". *Progress in Aerospace Sciences* 42: 85–128

[25] Goldstein, S., 1929, “On the vortex theory of screw propellers.” *Proceedings of the Royal Society of London*, Series A 123:440–465.

[26] Okulov, V.L. and Sørensen. J.N., 2008, “Refined Betz limit for rotors with a finite number of blades”. *Wind Energy* 11:415–26

[27] Kerwin, J. and Hadler, J., 2010, “Principles of Naval Architecture: Propulsion”. *SNAME*.

[28] Epps, B.P. and Kimball, R.W., 2013, “Unified rotor lifting line theory”, *J Ship Res*, 57

[29] Glauert, H., 1935, “Airplane propellers.” In Durand W.(ed) *Aerodynamic Theory: A General Review of Progress*, vol 4, Springer.

[30] Schmitz, G., 1955 “Theorie und Entwurf von Windrädern optimaler Leistung (Theory and design of windwheels with an optimum performance),” *Wiss. Zeitschrift der Universität Rostock*

[31] Lerbs, H., 1952, “Moderately loaded propellers with a finite number of blades and an arbitrary distribution of circulation”. *SNAME Transactions* 60.

[32] Goldstein, M.E., 1978, “Unsteady vertical and entropic distortions of potential flows round arbitrary obstacles”, *Journal of Fluid Mechanics*, vol.89, p. 433-468.

[33] Golubev, V.V. and Atassi, H. M., 2000, “Unsteady swirling flows in annular cascades, part 1: Evolution of incident disturbances.” *AIAA journal*, vol.38, no.7: p. 1142-1149.

[34] Roger, M., 2004, “Analytical Modelling of Wake-Interaction Noise in Centrifugal Compressors with Vaned Diffusers”. *In 10th AIAA/CEAS Aeroacoustics Conference, Manchester*, p. 2994

[35] Manwaring, S.R. and Wisler D.C., 1993, “Unsteady Aerodynamics and Gust Response in Compressors and Turbines”, *J. Turbomach* 115(4), 724-740

[36] Wrench, J.W. 1957, “The calculation of propeller induction factors”. *Tech. Rep. 1116*, David Taylor Model Basin

[37] Retrieved from http://dspace.mit.edu/bitstream/handle/1721.1/39815/2-23Fall-2003/OcwWeb/Mechanical-Engineering/2-23Fall-2003/Tools/index.htm

[38] Retrieved from http://engineering.dartmouth.edu/epps/openprop/index.html

[39] Wang, M.H., 1985, “Hub effects in propeller design and analysis”. *Technical report 85-12*. Department of Ocean Engineering, Massachusetts Institute of Technology, USA

[40] Yim, B., 1976, “Optimum propellers with cavity-drag and frictional drag effects”. *Journal of Ship Research*, 20 .

[41] Coney, W.B., 1989, “A Method for the Design of a Class of Optimum Marine Propulsors”, *PhD Thesis*, Department of Ocean Engineering, Massachusetts Institute of Technology, USA

[42] Gasch, R., Twele, J., 2012, “Wind Power Plants, Fundamentals, Design, Construction and Operation”, Chapter 5, *Springer-Verlag Berlin Heidelberg*

[43] Kinnas, S., Xu, W., Yu, Y.H., and Lei, H., 2012, “Computational methods for the design and prediction of performance of tidal turbines”. *Journal of Offshore Mechanics and Arctic Engineering (OMAE)*, vol 134.

[44] Fulayter, R.D., 2004, “An Experimental Investigation of Resonant Response of Mistuned Fan and Compressor Rotors Utilizing NSMS”, *PhD Thesis*, Department of Mechanical Engineering, Purdue University, USA

[45] Drazin, P.G., and Reid, W.H., 2004, “Hydrodynamic Stability”, *Cambridge University Press*, United Kingdom, p.69-82

[46] Laskos, D., 2010, “Design and cavitation performance of contra-rotating propellers”. *Master Thesis*, Department of Mechanical Engineering, Massachusetts Institute of Technology, USA

[47] Stubblefield, J.M., 2008, “Numerically based ducted propeller design using vortex lattice lifting line theory”, *Master Thesis*, Department of Mechanical Engineering, Massachusetts Institute of Technology, USA

[48] Ogin Inc., http://oginenergy.com/

[49] Poduhvat Hydrokinetics Ltd., http://www.poduhvat-hydrokinetics.co.uk/

APPENDICES

Appendix A Unified Propeller and Horizontal-axis Turbine Code

This is a unified propeller and horizontal-axis turbine optimization code based on Lifting line theory and interior point optimization method. It includes main program, OptRotor.m and 4 functions: Wrench.m, evaluate.m, objective.m and constrain.m.

Main Program: OptRotor.m

```
% This is a unified propeller and horizontal-axis turbine optimization code
% based on Lifting line theory and interior point optimization method.

% It includes 1) main program OptRotor.m and 2) Four functions:
% Wrench.m, evaluate.m, objective.m and constrain.m.
% It also requires Matlab optimization function fmincon.

% Most of the Lifting line theory and numerical implementation is based on:
% [1]Kerwin J.& Hadler J.(2010)“Principles of Naval Architecture: Propulsion”
% SNAME.  AND   [2]B.P. Epps & R.W. Kimball (2013) “Unified rotor lifting
% line theory”, J Ship Res, 57
% Part of the code is based on Kerwin's PVL code and Epps's OpenPropcode.

% In comments Eq.(xx) refers to the Author's PhD thesis
% Kerwin Eq.(xx) refers to equations in Kerwin J.& Hadler J. paper
% Additional theory, model details and case studies are given in the
% Author's PhD thesis, Yujun Leng, 2016 "Preliminary design tools in
% turbomachinery: non-uniformly spaced blade rows, multistage interaction,
% unsteady radial waves, and propeller horizontal-axis turbine
% optimization", Mechanical Engineering, Purdue University, West Lafayette

% Author: Yujun Leng  Email:lengyujun@gmail.com  Last updated: Apr 16, 2016
% This is free software under the terms of the GNU General Public License
% You are welcome to use it. I hope it will be helpful!

%% INPUT-----------------------------------------------------------------
Turbine_flag = 1;      % 0 == propeller, 1 == horizontal-axis turbine
Mp = 20;               % number of vortex panels over the radius
Z  = 3;                % number of blades
L  = 6;                % tip-speed ratio
   Js      = pi/L;    % advance coefficient
Rhub = 0.1;            % hub radius /rotor radius
Hub_flag = 1;          % 0 == no hub model, 1 == with hub model
XR = [0.1 0.15 0.2 0.25 0.3 0.4 0.5 0.6 0.7 0.8 0.9 0.95 1.0];   % r/R
```

```
XVA = -0.1*XR.^2+1;    % Va/Vs
XVT = zeros(size(XR)); % Vt/Vs
% CTdes = 1.0;    %desired thrust coefficient,   for propeller only
% Rhv = 0.25;     %hub vortex radius/hub radius, for marine propeller only

%% Pre-processing------------------------------------------------------------
% ---Calculate Volumetric Mean Inflow Velocity VMIV
XRtemp=linspace(Rhub,1,100); XVAtemp=interp1(XR,XVA,XRtemp,'pchip','extrap');
VMIV = 2*trapz(XRtemp,XRtemp.*XVAtemp)/(1-Rhub^2); % Kerwin eq.(4.4)
% ---Compute cosine spaced vortex & control pt. radial position
RV = zeros(1,Mp+1);
RC = zeros(1,Mp);
DEL = pi/(2*Mp);
Rdif = 0.5*(1 - Rhub);
for m = 1:Mp+1
   RV(m) = Rhub + Rdif*(1-cos(2*(m-1)*DEL));   % Eq. (2.133)
end
for n = 1:Mp
   RC(n) = Rhub + Rdif*(1-cos((2*n-1)*DEL));   % Eq. (2.134)
end
DR = diff(RV);
% ---Interpolate Va, Vt at control points RC
VAC = pchip(XR,XVA   ,RC);
VTC = pchip(XR,XVT   ,RC);
TANBC = VAC./(L*RC + VTC); % tan(Beta) at RC

%% Optimization--------------------------------------------------------------
if Turbine_flag==0
   % efficiency estimate 90% of the actuator disk efficiency, EDISK
   EDISK = 1.8/(1+sqrt(1+CTdes/VMIV^2));  % Eq. (2.154)
   x0 = TANBC/EDISK;       % initial guess of tan(BetaI)
   lb = 0.1*TANBC;         % lower bound of tan(BetaI)
   ub = 10*TANBC;          % upper bound of tan(BetaI)
   % if Rhv is not specified, use Rhv=exp(3) to zero hub drag
   if ~exist('Rhv','var') Rhv  = exp(3); end;
   objectivef=objective(Mp,Z,L,VAC,VTC,VMIV,TANBC,RC,RV,DR,...
      Rhub,Rhv,Hub_flag);
   constrainf=constrain(Mp,Z,L,VAC,VTC,VMIV,TANBC,RC,RV,DR,...
      Rhub,Rhv,Hub_flag,CTdes);
elseif Turbine_flag==1
   x0 = tan(atan(TANBC)*2/3); % initial guess from General Momentum Theory
   lb = zeros(1,Mp);          % lower bound of tan(BetaI)
   ub = 5*TANBC;              % upper bound of tan(BetaI)
   Rhv=exp(3); % use this number to zero hub drag for turbine optimization
   objectivef=objective(Mp,Z,L,VAC,VTC,VMIV,TANBC,RC,RV,DR,Rhub,...
```

```
        Rhv,Hub_flag);
    constrainf=[];
end
% x = fmincon(fun,x0,A,b,Aeq,beq,lb,ub,nonlcon)
% optimoptions may be needed to increase maximum function evaluation times
x = fmincon(objectivef,x0,[],[],[],[],lb,ub,constrainf);

%% Post-processing------------------------------------------------------------
TANBIC = x;
[UASTAR,UTSTAR,G,CT,CQ,CP,CTH,KT,KQ,EFFY] = ...

evaluate(TANBIC,TANBC,Mp,Z,L,VAC,VTC,VMIV,RC,RV,DR,Rhub,Rhv,Hub_flag);
% UASTAR,UTSTAR:induced velocities;G is nondimensionalized bound circulation
% CT,CQ,CP: thrust, torque and power coefficient
% CTH: hub thrust coefficient due to hub drag
% KT,KQ: thrust,torque coefficient based on rotational speed Kerwin eq.(4.8)
% EFFY: propeller efficiency based on VMIV, aka inflow-adapted efficiency
```

Function 1: evaluate.m

```
function [UASTAR,UTSTAR,G,CT,CQ,CP,CTH,KT,KQ,EFFY]=...

evaluate(TANBIC,TANBC,Mp,Z,L,VAC,VTC,VMIV,RC,RV,DR,Rhub,Rhv,Hub_flag)
% ---Calculate horseshoe influence functions
UAHIF = zeros(Mp,Mp); UTHIF = zeros(Mp,Mp);
for n = 1:Mp                % for each control point, n
   for m = 1:Mp             % for each vortex  panel, m
      % Use Epps's wake model, Figure 2.11
      % Velocity induced at RC(n) by a unit vortex shed at RV(m+1)
      [UAW1,UTW1] = Wrench(Z,TANBIC(m)*RC(m)/RV(m+1),RC(n),RV(m+1));
      % Velocity induced at RC(n) by a unit vortex shed at RV(m)
      [UAW2,UTW2] = Wrench(Z,TANBIC(m)*RC(m)/RV(m)  ,RC(n),RV(m)  );
      % Add hub image vortex effect to horseshoe influence functions
      if Hub_flag == 1
         RVH1=Rhub^2/RV(m+1); RVH2=Rhub^2/RV(m); % Eq. (2.135)
         [UAWh1,UTWh1] = Wrench(Z,TANBIC(m)*RC(m)/RVH1,RC(n),RVH1 );
         [UAWh2,UTWh2] = Wrench(Z,TANBIC(m)*RC(m)/RVH2,RC(n),RVH2 );
         UAW1=UAW1-UAWh1; UAW2=UAW2-UAWh2;%negative strength image
vortex
         UTW1=UTW1-UTWh1; UTW2=UTW2-UTWh2;%negative strength image
vortex
      end
      UAHIF(n,m) = UAW1 - UAW2;   % Eq. (2.131)
      UTHIF(n,m) = UTW1 - UTW2;   % Eq. (2.132)
```

```
    end
end
% ---Solve Eq.(2.149) for bound circulation BC based on TANBIC & TANBC
RHS = zeros(Mp,1); LHS = zeros(Mp,Mp);
for n = 1:Mp                        % for each control point, n
    RHS(n) = VAC(n)*((TANBIC(n)/TANBC(n))-1);
    for m = 1:Mp                    % for each vortex  panel, m
        LHS(n,m) = UAHIF(n,m)-UTHIF(n,m)*TANBIC(n);
    end
end
BC = LHS\RHS;   % bound circulation strength
% ---Compute induced velocities at control points
UASTAR = (UAHIF*BC)';   % Eq. (2.129)
UTSTAR = (UTHIF*BC)';   % Eq. (2.130)
% ---Calculate performance coefficients
G = BC/(2*pi);  % nondimensionalized bound circulation: Gamma/(2*pi*R*Vf)
CTP = 4*Z*sum((L*RC + VTC + UTSTAR).*G'.*DR); %propeller thrust coefficient
CQ = 4*Z*sum((VAC + UASTAR).*G'.*RC.*DR);     %torque coefficient
% Compute hub drag effect(negative thrust) on thrust coefficient,
if Hub_flag == 1
    CTH = -0.5*(log(1/Rhv)+3)*(Z*G(1))^2;   % Eq. (2.140)
elseif Hub_flag == 0
    CTH = 0;
end
CT = CTP+CTH;   % total thrust coefficient
Js = pi/L;      % advance coefficient
CP = CQ*pi/Js;  % power coeff. based on torque, Kerwin eq.(4.12)
KT=CT*Js^2*pi/8;  %thrust coeff. based on rotational speed, Kerwin eq.(4.11)
KQ=CQ *Js^2*pi/16;%torque coeff. based on rotational speed, Kerwin eq.(4.11)
EFFY=CT/CP*VMIV; % inflow-adapted efficiency, for propeller only
end
```

Function 2: Wrench.m

```
% Function Wrench calculates influence functions u_barA, u_barT based on
% Wrench, J.W. 1957, “The calculation of propeller induction factors”.
% Tech. Rep. 1116, David Taylor Model Basin
function [u_barA, u_barT] = Wrench(Z,tan_betaW,rc,rv)

if Z > 50 % blade number>50, use the formula for infinite number of blades
   if rc < rv
      u_barA = Z/(4*pi*rv*tan_betaW);    % Eq.(2.125)
      u_barT = 0;                        % Eq.(2.126)
   elseif rc > rv
      u_barA = 0;                        % Eq.(2.127)
      u_barT = Z/(4*pi*rc);              % Eq.(2.128)
   end
else
   y  = rc/(rv*tan_betaW);
   y0 = 1/tan_betaW;
   U  = (y0*(sqrt(1+y^2)-1)*exp(sqrt(1+y^2)-sqrt(1+y0^2))/...
    (y*(sqrt(1+y0^2)-1)))^Z;
   F1 = -1/(2*Z*y0)*((1+y0^2)/(1+y^2))^0.25*((U/(1-U))+1/(24*Z)*...
    ((9*y0^2+2)/(1+y0^2)^1.5+(3*y^2-2)/(1+y^2)^1.5)*log(abs(1+U/(1-U))));
   F2 = 1/(2*Z*y0)*((1+y0^2)/(1+y^2))^0.25*((1/(U-1))- 1/(24*Z)*...
    ((9*y0^2+2)/(1+y0^2)^1.5+(3*y^2-2)/(1+y^2)^1.5)*log(abs(1+1/(U-1))));
   if rc < rv
      u_barA = Z/(4*pi*rc)*(y-2*Z*y*y0*F1);        % Eq.(2.121)
      u_barT = Z^2*y0*F1/(2*pi*rc);                % Eq.(2.122)
   elseif rc > rv
      u_barA = -Z^2*y*y0*F2/(2*pi*rc);             % Eq.(2.123)
      u_barT = Z/(4*pi*rc)*(1+2*Z*y0*F2);          % Eq.(2.124)
   end
end
```

Function 3: objective.m

```
function objectivef = ...
   objective(Mp,Z,L,VAC,VTC,VMIV,TANBC,RC,RV,DR,Rhub,Rhv,Hub_flag)
objectivef = @optimizeobj;
  function obj = optimizeobj(x)
     TANBIC = x;
     [~,~,~,~,CQ,~,~,~,~,~] = evaluate ...
        (TANBIC,TANBC,Mp,Z,L,VAC,VTC,VMIV,RC,RV,DR,Rhub,Rhv,Hub_flag);
     obj = CQ;
  end
end
```

Function 4: constrain.m

```
function constrainf = ...
   constrain(Mp,Z,L,VAC,VTC,VMIV,TANBC,RC,RV,DR,Rhub,Rhv,Hub_flag,CTdes)
constrainf = @nonlinearconstrain;
  function [c1, c2] = nonlinearconstrain(x)
     TANBIC = x;
     [~,~,~,CT,~,~,~,~,~,~] = evaluate...
        (TANBIC,TANBC,Mp,Z,L,VAC,VTC,VMIV,RC,RV,DR,Rhub,Rhv,Hub_flag);
     c1 = []; % the non-linear inequality
     c2 = CT-CTdes; % the non-linear equality
  end
end
```

Appendix B Multistage Interaction Code

This is a multistage interaction code for calculating the unsteady loading and unsteady waves in axial compressors. This code includes main program, Multistage_LINSUB.m and 5 functions: scattergrpC.m, upwashUm.m, coeffXm.m, kernelKm10.m and pressurewavem.m

Main Program: Mulititage_LINSUB.m

```
%%%%%%%%%%%%%%%%%%%%%%%%%%%%%%%%%%%%
%      Multistage LINSUB        %
%%%%%%%%%%%%%%%%%%%%%%%%%%%%%%%%%%%%

% This is a multistage interaction code for calculating the unsteady
% loading and unsteady waves in axial compressors.
% Since Multi-row interactions beyond 3 blades rows have minimum effect.
% This code deals with 2 or 3 blade rows.
% To include the counter-rotating stages case, both rotor and 'stator'
% rotational speed can be specified.

% This code includes main program Multistage_LINSUB.m and 5 functions:
% scattergrpC.m-calculate LINSUB coefficients for the scattering group
% scattergrpC.m calls the following 4 functions
% upwashUm.m----calculate input upwash velocity matrix
% coeffXm.m-----calculate output coefficient matrix
% kernelKm10.m--calculate kernel matrix based on 10 times convergence tests
% pressurewavem.m-----calculate pressure wave & vorticity wave properties

% The major structure of the code is based on the derivation of the paper
% Hall,K.C & Silkowski,P.D:
% "The influence of Neighboring Blade rows on the Unsteady Aerodynamic
% response the unsteady Aerodynamic response of cascades" Journal of
% Turbomachinery, Vol.119/85 (Jan 1997)
% The transmission, reflection and scattering coefficients are calculated
% based on a modified version of the original LINSUB code in papers:
% Whitehead, D. S. "Classical two-dimensional methods."
% In AGARD Aeroelasticity in Axial-Flow Turbomachines. 1 (1987).
% Smith, S. N. "Discrete frequency sound generation in axial flow
% turbomachines."  Reports and Memoranda 3709 (1972)

% In comments Eq.(xx) refers to equation the Author's PhD thesis
% Hall Eq.(xx) refers to equation in Hall,K.C & Silkowski,P.D's paper
```

```
% Smith Eq.(xx) refers to equation in Smith,S. N.'s paper
% Additional theory, model details and case studies are given in the
% Author's PhD thesis, Yujun Leng, 2016 "Preliminary design tools in
% turbomachinery: non-uniformly spaced blade rows, multistage interaction,
% unsteady radial waves, and propeller horizontal-axis turbine
% optimization", Mechanical Engineering, Purdue University, West Lafayette

% Author: Yujun Leng  Email:lengyujun@gmail.com  Last updated:Apr 16, 2016
% This is free software under the terms of the GNU General Public License
% You are welcome to use it. I hope it will be helpful!

%% INPUT-----------------------------------------------------------------

% Input for Purdue 3-stage research compressor
np=20;                          % Number of control points
radius=12;                      % Radius of 2-D slice
nrows=3;                        % Number of blade rows
stag=[-24.3 49.8 -24.3]/180*pi;     % Stagger angle
nbl=[44 33 44];                 % Number of blades
omega_r=[0 -387.46 0];          % Rotation rate (rad/s)
chord=[2.11 2.96 2.22];         % Chord length
gapx=[0.65 0.65];    % Trailing Edge-Leading Edge gap in x direction;
gapy=[0 0];                     % TE-LE gap in y direction;
relvel=[3120 4406 3120];        % Relative velocity along the chord
relma=[0.2331 0.3292 0.2331];   % Relative Mach Number along the chord
xea=15/35;                      % Elastic axis position for torsion mode

excitedrow_number=2;            % Blade row receiving primary excitation
omega_not=17048;                % Excitation frequency (rad/s)
n_not=-44;                      % Excitation Nodal diameters
excite_type=4;     % 1:bending 2:torsion 3:vorticity 4:pressure wave up 5:pdn

% Specify the modes involved in the multistage interaction analysis
% mode[i,j] is the scattering index of ith mode in jth blade row
% If the 3rd row is the repeated blade row of the 1st row, only the
% scattering index in the first 2 rows needs to be specified in the 'mode'.
% If the 3rd row is the repeated blade row of the 1st row, repeated_stage=1
repeated_stage=1;
mode=[-2 -2; -2 -1; -2 0; -2 1; -2 2;...
      -1 -2; -1 -1; -1 0; -1 1; -1 2;...
       0 -2;  0 -1;  0 0;  0 1;  0 2;...
       1 -2;  1 -1;  1 0;  1 1;  1 2;
       2 -2;  2 -1;  2 0;  2 1;  2 2];

%% Calculate transmission, reflection and scattering coefficients----------
```

```
% ---Calculate steady flow properties in each blade row
% LINSUB assumes the axial velocity and axial Ma in different blade rows
% are the same, and thus the sound speed a is the same.

U=relvel(1)*cos(stag(1))*ones(1,nrows); %axial velocity in each row
V=zeros(1, nrows);                  %tangential velocity in each row
V(1)=relvel(1)*sin(stag(1));
for jj1=2:nrows
   V(jj1)=V(jj1-1)-(omega_r(jj1)-omega_r(jj1-1))*radius;
end
W=sqrt(U.^2+V.^2);                  %chord wise velocity in each row
theta=atan(V./U);                   %calculated stagger angle
a=relvel(1)/relma(1);               %sound speed
M=W./a;                             %calculated Mach number

% LINSUB assumes no flow turning in each blade row.
% Check whether the flow angle matches the input stagger angle.
   error_W=max(abs((W-relvel)./W));
   error_theta=max(abs((theta-stag)./theta));
   error_M=max(abs((M-relma)./M));
   if (error_W>0.01)||(error_theta>0.01)||(error_M>0.01)
      warning('flow angle does NOT match the given stagger angle')
      warning('main flow properties are corrected as follow')
      display('flow angles(deg) in each blade row')
      display(theta/pi*180)
      display('chordwise velcoity in each blade row')
      display(W)
      display('chordwise Mach number in each blade row')
      display(a)
   end

% ---Calculate space to chord ratio sc
s=2*pi*radius./nbl;
sc=s./chord;

% NOTE:
% LINSUB Input M, theta,sc is the same for different modes in the same
% blade row. Thus M, theta and sc calculated above are used as common
% LINSUB inputs for different modes in each blade row.
% LINSUB Input phi and lambda are different for different modes. They
% are calculated for each mode in each blade row below.

% ---Calculate interblade phase angle phi based on nodal diameter ND
nmodes=size(mode,1);
```

```
if repeated_stage==1
   %add zero scattering index for the repeated 3rd row in order to use
   %the general 3rows formulation for omega and phi calculation
   mode(:,3)=zeros(nmodes,1);
end
ND=sum(mode.*repmat(nbl,nmodes,1),2)+n_not;   %Eq. (2.100)
ND=repmat(ND,1,nrows);
phi=ND*2*pi./repmat(nbl,nmodes,1);          %interblade phase angle

% ---Calculate reduced frequency lambda based on frequency omega
omega=zeros(nmodes,nrows);
if excitedrow_number==2        %Eq. (2.102)
   omega(:,1)=omega_not+(n_not+mode(:,2)*nbl(2))*(omega_r(1)-omega_r(2));
   if nrows==3
      omega(:,2)=omega_not+(mode(:,1)*nbl(1)+mode(:,3)*nbl(3))...
         *(omega_r(2)-omega_r(1));
   elseif nrows==2
      omega(:,2)=omega_not+(mode(:,1)*nbl(1))*(omega_r(2)-omega_r(1));
   end
elseif (excitedrow_number==1)||(excitedrow_number==3)   %Eq. (2.101)
   omega(:,1)=omega_not+mode(:,2)*nbl(2)*(omega_r(1)-omega_r(2));
   if nrows==3
      omega(:,2)=omega_not+(n_not+mode(:,1)*nbl(1)+mode(:,3)*nbl(3))...
         *(omega_r(2)-omega_r(1));
   elseif nrows==2
      omega(:,2)=omega_not+(n_not+mode(:,1)*nbl(1))*(omega_r(2)-omega_r(1));
   end
else
   error('Wrong blade row which receive the initial excitation')
end
if nrows==3
   omega(:,3)=omega(:,1);
end
lambda=omega./repmat(W, nmodes,1).*repmat(chord, nmodes,1);%reduced freq.

% ---Calculate axial and tangential wave numbers
alpha1=zeros(nmodes,3);
alpha2=zeros(nmodes,3);
alpha3=zeros(nmodes,3);
beta=zeros(nmodes,3);
for jj1=1:nmodes
   [aa1,aa2,aa3, bb,~,~,~,~]=...
      pressurewavem(lambda(jj1,1), M(1), theta(1), sc(1),0,phi(jj1,1));
   alpha1(jj1,1)=aa1/chord(1);%in LINSUB alpha,beta are multiplied by chord
   alpha2(jj1,1)=aa2/chord(1);
```

```
    alpha3(jj1,1)=aa3/chord(1);
    beta(jj1,1)=bb/chord(1);
    [aa1,aa2,aa3, bb,~,~,~,~]=...
        pressurewavem(lambda(jj1,2), M(2), theta(2), sc(2),0,phi(jj1,2));
    alpha1(jj1,2)=aa1/chord(2);
    alpha2(jj1,2)=aa2/chord(2);
    alpha3(jj1,2)=aa3/chord(2);
    beta(jj1,2)=bb/chord(2);
    %only first two blade rows are calculated because in the linear
    %assumption the 3rd row has the same steady flow properties as the 1st
    %row
    alpha1(jj1,3)=alpha1(jj1,1);
    alpha2(jj1,3)=alpha2(jj1,1);
    alpha3(jj1,3)=alpha3(jj1,1);
    beta(jj1,3)=beta(jj1,1);
end

% alpha, beta in different blade rows should be the same.
% i.e. alpha(i,1)=alpha(i,2) beta(i,1)=beta(i,2)
% this serves as a check for the correct input convention
if (mean(abs(alpha1(:,1)./alpha1(:,2)))-1)>1e-3 || ...
   (mean(abs(alpha2(:,1)./alpha2(:,2)))-1)>1e-3 || ...
   (mean(abs(alpha3(:,1)./alpha3(:,2)))-1)>1e-3 || ...
   (mean(abs(beta(:,1)./beta(:,2)))-1)>1e-3
    error('the wave numbers in different blade row are different!')
end

% ---Build up the scattering table and find the scatter group
% Since the scatter range and steady flow conditions are different in each
% row generally, the scatter group in each row are different.
% The mode is given by a matrix of scatter index [n1 n2 n3] for three blade
% rows and [n1 n2] for two blade rows


% Max possible scatter index in all blade rows, nsrange
nsrange=size(unique(mode),1);
% the corresponding scattering modes for a certain mode in each blade row
nscatter=zeros(nmodes, nsrange, nrows);
% the corresponding LINSUB coefficients [5*5] for each scattering mode
nscatterCL=cell(nmodes,nsrange, nrows);

%Build up the scattering table
for jj1=1:nmodes
    n1fix=find(mode(:,1)==mode(jj1,1))';
    n2fix=find(mode(:,2)==mode(jj1,2))';
```

```
    if nrows==2
        n1s=n2fix;
        n2s=n1fix;
        nscatter(jj1,1:size(n1s,2),1)=n1s;
        nscatter(jj1,1:size(n2s,2),2)=n2s;
    elseif nrows==3
        n3fix=find(mode(:,3)==mode(jj1,3))';
        %scattering modes in 1st blade rows have n2 and n3 value fixed
        n1s=intersect(n2fix,n3fix);
        n2s=intersect(n1fix,n3fix);
        n3s=intersect(n1fix,n2fix);
        nscatter(jj1,1:size(n1s,2),1)=n1s;
        nscatter(jj1,1:size(n2s,2),2)=n2s;
        nscatter(jj1,1:size(n3s,2),3)=n3s;
    else
        error('this code only deal with 2 or 3 blade rows')
    end
end

% For each blade row, calculate the corresponding LINSUB coefficients and
% store them in the nscatterCL
for jj1=1:nrows
    nsgroup=unique(nscatter(:,:,jj1),'rows');
    for jj2=1:size(nsgroup,1)
        scattermode=nsgroup(jj2,:);
        scattermode=scattermode(scattermode~=0); %get rid of the empty mode
        nn1=mode(scattermode,jj1)';
        %find the base mode(least scattering number) index number,bmodeIn
        [~, bmodeIn]=min(abs(nn1));
        bmodeI=scattermode(bmodeIn);
        rm=nn1-nn1(bmodeIn);
        rm=-rm;      %negative because in LINSUB, beta=(phi-2*pi*r)/sc;
        [grpC] = scattergrpC(np,lambda(bmodeI,jj1), M(jj1), theta(jj1), ...
            sc(jj1), rm, phi(bmodeI,jj1),xea);
        %load [grpC] into nscatterCL
        for jj3=1:size(scattermode,2)
            for jj4=1:size(scattermode,2)
                nscatterCL{scattermode(jj3),jj4,jj1}=grpC{jj3,jj4};

                %if incoming and outgoing waves have the same mode, add one
                if scattermode(jj3)==scattermode(jj4)
                    %if the incoming wave and outgoing wave are of the same
                    %type, i.e. vo-vo (3,3), pup-pup(4,4), pdn-pdn(5,5),
                    %original excitation needs to be added to the output.
                    jj5=scattermode(jj3);
```

```
                LETEdx=chord(jj1)*cos(stag(jj1));
                LETEdy=chord(jj1)*sin(stag(jj1));
                %wake, input reference to LE, output reference to TE
                LETEvo=exp(1i*alpha3(jj5,jj1)*LETEdx+...
                   1i*beta(jj5,jj1)*LETEdy);
                %pup, input reference to TE, output reference to LE
                LETEpup=exp(1i*alpha1(jj5,jj1)*(-LETEdx)+...
                   1i*beta(jj5,jj1)*(-LETEdy));
                %pdn, input reference to LE, output reference to TE
                LETEpdn=exp(1i*alpha2(jj5,jj1)*LETEdx+...
                   1i*beta(jj5,jj1)*LETEdy);
                nscatterCL{scattermode(jj3),jj4,jj1}(3,3)=...
                   nscatterCL{scattermode(jj3),jj4,jj1}(3,3)+LETEvo;
                nscatterCL{scattermode(jj3),jj4,jj1}(4,4)=...
                   nscatterCL{scattermode(jj3),jj4,jj1}(4,4)+LETEpup;
                nscatterCL{scattermode(jj3),jj4,jj1}(5,5)=...
                   nscatterCL{scattermode(jj3),jj4,jj1}(5,5)+LETEpdn;
             end
          end
       end
    end
end

% If the 3rd row is a repeated blade row, its scattering table and
% corresponding LINSUB coefficients should be the same as 1st blade row
if repeated_stage==1
   nscatter(:,:,3)=nscatter(:,:,1);
   nscatterCL(:,:,3)=nscatterCL(:,:,1);
end

%% Build up the Left hand side of the governing matrix--------------------
% The whole governing matrix is shown in Hall Eq.(20)
LHS=zeros(nmodes*nrows*6,nmodes*nrows*6);

% ---Build up the transmission reflection coefficient matrix
% load matrix AB, column by column, blade row by blade row
for jj1=1:nrows
   for jj2=1:nmodes    %jj2 is the input mode
      scattermode=nscatter(jj2,:,jj1);
      scattermode=scattermode(scattermode~=0);
      for jj3=1:size(scattermode,2)   %jj3 is the output mode
         CL=nscatterCL{jj2,jj3,jj1};
         CC=[CL(4,4) CL(4,5) CL(4,3);...
            CL(5,4) CL(5,5) CL(5,3);...
            CL(3,4) CL(3,5) CL(3,3)];
```

```
            AB=[0 -CC(1,2) -CC(1,3) -CC(1,1) 0 0;...
               0 -CC(2,2) -CC(2,3) -CC(2,1) 0 0;...
               0 -CC(3,2) -CC(3,3) -CC(3,1) 0 0];
            % if the incoming and outgoing waves are of the same mode,
            % add delta function
            if jj2==scattermode(jj3)
               d=[1 0 0 0 0 0 ;0 0 0 0 1 0;0 0 0 0 0 1];
               AB=AB+d;
            end
            leftop=[(scattermode(jj3)-1)*nrows*6+1 (jj2-1)*nrows*6+1];
            LHS((leftop(1)+(jj1-1)*6):(leftop(1)+(jj1-1)*6+2),...
               (leftop(2)+(jj1-1)*6):(leftop(2)+(jj1-1)*6+5))=AB;
         end
      end
   end

% ---Build up inter-row coupling matrix and sublunary conditions
% Calculate matrix E,I,C,D
EI12=zeros(3,6,nmodes); EI23=zeros(3,6,nmodes);

for jj1=1:nmodes
   % non-dimensionalization for the unsteady waves in different blade rows
   % is based on the flow conditions and blade geometry of the specific row.
   EI12(:,:,jj1)=...
   [-exp(1i*alpha1(jj1,1)*gapx(1)+1i*beta(jj1,1)*gapy(1))*...
   (W(1)/W(2))^2 0 0 1 0 0;
    0 -exp(1i*alpha2(jj1,1)*gapx(1)+1i*beta(jj1,1)*gapy(1))*...
    (W(1)/W(2))^2 0 0 1 0;
    0 0 -exp(1i*alpha3(jj1,1)*gapx(1)+1i*beta(jj1,1)*gapy(1))...
    *(W(1)/W(2)*chord(2)/chord(1)) 0 0 1];
   if nrows==3  %three blade rows case
      EI23(:,:,jj1)=...
      [-exp(1i*alpha1(jj1,2)*gapx(2)+1i*beta(jj1,2)*gapy(2))...
      *(W(2)/W(3))^2 0 0 1 0 0;...
       0 -exp(1i*alpha2(jj1,2)*gapx(2)+1i*beta(jj1,2)*gapy(2))...
       *(W(2)/W(3))^2 0 0 1 0;
       0 0 -exp(1i*alpha3(jj1,2)*gapx(2)+1i*beta(jj1,2)*gapy(2))...
       *(W(2)/W(3)*chord(3)/chord(2)) 0 0 1];
   end
end
C=[0 0 0;0 1 0;0 0 1]; D=[1 0 0;0 0 0;0 0 0];

% Load matrix E,I,C,D, along the diagonal
for jj1=1:nmodes
   leftop=[(jj1-1)*nrows*6+1 (jj1-1)*nrows*6+1];
```

```
    LHS((leftop(1)+3):(leftop(1)+3+2),(leftop(2)+3):(leftop(2)+3+5))...
        =EI12(:,:,jj1);
    if nrows==3  %three blade rows case
        LHS((leftop(1)+9):(leftop(1)+9+2),(leftop(2)+9):(leftop(2)+9+5))...
            =EI23(:,:,jj1);
    end
    LHS((leftop(1)+(2*nrows-1)*3):(leftop(1)+(2*nrows-1)*3+2),...
        leftop(2):(leftop(2)+2))=C;
    LHS((leftop(1)+(2*nrows-1)*3):(leftop(1)+(2*nrows-1)*3+2),...
        (leftop(1)+(2*nrows-1)*3):(leftop(1)+(2*nrows-1)*3+2))=D;
end

%% Build up the Right hand side of the governing matrix----------------------
% The whole governing matrix is shown in Hall Eq.(20)
RHS=zeros(nmodes*nrows*6,1);

% NOTE:
% Since LINSUB is a linearized model, if there are multiple excitations,
% each excitation can be treated separately. The responses can be
% added together to obtain the total response.
% The mode family is specified in a way that the initial excitation is
% always the [0,0] mode or [0,0,0] for 3 blade row cases.

% find [0,0] or [0,0,0] mode index InitialmodeI
[~,InitialmodeI]=min(sum(abs(mode),2));
rightop=(InitialmodeI-1)*nrows*6+1;

% ---Specify external excitation
if excite_type==3    %vorticity wave, i.e. wake from upstream row
    if excitedrow_number==1 %far upstream wake excites the 1st row
        RHS(rightop+(nrows-1)*6+5)=1;
    else
        RHS(rightop+((excitedrow_number-1)-1)*6+2)=1;
    end
elseif excite_type==4   %upstream going pressure wave from downstream row
    if excitedrow_number==nrows
    %upstream going pressure wave excites the last row from far downstream
        RHS(rightop+(nrows-1)*6+3)=1;
    else
        RHS(rightop+((excitedrow_number+1)-1)*6+0)=1;
    end
elseif excite_type==5   %downstream going pressure wave from upstream row
    if excitedrow_number==1
    %downstream going pressure wave excites the 1st row from far upstream
        RHS(rightop+(nrows-1)*6+4)=1;
```

```
    else
        RHS(rightop+((excitedrow_number-1)-1)*6+1)=1;
    end

% ---Specify internal excitation
else
    %load initial excitation and its scattering mode into LHS one by one.
    scattermode=nscatter(InitialmodeI,:,excitedrow_number);
    scattermode=scattermode(scattermode~=0);
    for jj1=1:size(scattermode,2)
        rightop=(scattermode(jj1)-1)*nrows*6+1;
        CL=nscatterCL{InitialmodeI,jj1,excitedrow_number};
        if excite_type==1   %bending
            rhsb=[CL(4,1); CL(5,1); CL(3,1)];
        elseif excite_type==2   %torsion
            rhsb=[CL(4,2); CL(5,2); CL(3,2)];
        end
        RHS((rightop+(excitedrow_number-1)*6):...
            (rightop+(excitedrow_number-1)*6)+2)=rhsb;
    end
end

%% Solve the governing matrix and post-processing-------------------------
% The whole governing matrix is shown in Hall Eq.(20)

U=LHS\RHS;
U_nrows_nmodes=reshape(U,6,nrows,nmodes);

% ---Post-processing to find the five outputs:
% 1.total upstream going pressure wave for each mode, C_pup
% 2.total downstream going pressure wave for each mode, C_pdn
% 3.total downstream going vorticity wave for each mode, C_vo
% 4.unsteady lift on each blade row for each mode, C_lift
% 5.unsteady moment on each blade row for each mode, C_moment

% upstream going pressure wave from the 1st row C_pup[nmodes,1]
C_pup=reshape(U_nrows_nmodes(1,1,:),nmodes,1);
% downstream going pressure wave from the last row C_pdn[nmodes,1]
C_pdn=reshape(U_nrows_nmodes(5,nrows,:),nmodes,1);
% downstream going vorticity wave from the last row C_vo[nmodes,1]
C_vo=reshape(U_nrows_nmodes(6,nrows,:),nmodes,1);


% unsteady lift on each row due to the 3 incoming excitation waves
% of each mode, C_lift[nmodes,nrows]
```

```
C_lift=zeros(nmodes, nrows);
% unsteady moment on each row due to the 3 incoming excitation waves
% of each mode C_moment[nmodes,nrows]
C_moment=zeros(nmodes, nrows);

for jj1=1:nmodes
    for jj2=1:nrows
       Pu=U_nrows_nmodes(4,jj2,jj1);
       Pd=U_nrows_nmodes(2,jj2,jj1);
       Vo=U_nrows_nmodes(3,jj2,jj1);
       scattermode=nscatter(jj1,:,jj2);
       %find the non-scattering fundamental mode index, fmodeI
       fmodeI=find(scattermode==jj1);
       CL=nscatterCL{jj1,fmodeI,jj2}; %#ok<FNDSB>
       C_lift(jj1,jj2)=CL(1,4)*Pu+CL(1,5)*Pd+CL(1,3)*Vo;
       C_moment(jj1,jj2)=CL(2,4)*Pu+CL(2,5)*Pd+CL(2,3)*Vo;
    end
end

% Add unsteady lift and moment due to the inertial internal excitation
% As calculated before, the inertial mode index is InitialmodeI
scattermode=nscatter(InitialmodeI,:,excitedrow_number);
fmodeI=find(scattermode==InitialmodeI);
CL=nscatterCL{InitialmodeI,fmodeI,excitedrow_number};
if excite_type==1   %bending
   C_lift(InitialmodeI,excitedrow_number)=...
      C_lift(InitialmodeI,excitedrow_number)+CL(1,1);
   C_moment(InitialmodeI,excitedrow_number)=...
      C_moment(InitialmodeI,excitedrow_number)+CL(2,1);
elseif excite_type==2   %torsion
   C_lift(InitialmodeI,excitedrow_number)=...
      C_lift(InitialmodeI,excitedrow_number)+CL(1,2);
   C_moment(InitialmodeI,excitedrow_number)=...
      C_moment(InitialmodeI,excitedrow_number)+CL(2,2);
end

%% OUTPUT----------------------------------------------------------------
% All output are organized in outputC_original[nmodes * (4*nrows+4)]
% where columns are [mode_index(1) omega(nrows) mode(nrows) C_lift(nrows)
% C_moment(nrows) C_pup(1) C_pdn(1) C_vo(1)]
outputC_original=[(1:nmodes)' omega mode C_lift C_moment C_pup C_pdn C_vo];
```

Function 1: scattergrpC.m

```
% Function scattergrpC calculates the transmission reflection coefficient
% matrix for the whole scattering group using LINSUB.

% It calls the following functions:
% upwashUm.m----calculate input upwash velocity matrix
% coeffXm.m-----calculate output coefficient matrix
% kernelKm10.m--calculate kernel matrix based on 10 times convergence tests
% pressurewavem.m-----calculate pressure wave & vorticity wave properties

% The transmission reflection coefficients are calculated based on a
% modified Matlab version of the LINSUB code in the paper:
% Whitehead, D. S. "Classical two-dimensional methods."
% In AGARD Aeroelasticity in Axial-Flow Turbomachines. 1 (1987).
% The code follows closely the derivation in the paper:
% Smith, S. N.
% "Discrete frequency sound generation in axial flow turbomachines."
% Reports and Memoranda 3709 (1972).

% The modified Matlab version LINUSB is coded directly based on the
% physical model equations that appear in the Smith's 1972 paper.
% This makes the code much easier to be understood and modified.

% The output is:
% LINSUB coefficients matrix CL(5*5) store in cell of grpC{rm*rm}:
% LINSUB coefficient matrix CL(i,j):
% i: normalized output:
% 1.lift 2.moment 3. shed vorticity wave
% 4.upstream going Pressure wave 5. downstream going pressure wave
% j: normalized input:
% 1.bending 2.torsion 3.shed vorticity wave
% 4.upstream going Pressure wave 5. downstream going pressure wave
% The LINSUB coefficients reference points are defined as following
% input upwash velocity: Pup-TE, Pdn-LE, Vo-LE
% output response waves: Pup-LE, Pdn-TE, Vo-TE
% (LE: leading edge, TE: trailing edge)

% The modified matlab version LINUSB has the following changes in order to
% correct some minor error in the original LINSUB code and in order to be
% used in the multistage interaction model.
% 1. correctly handle the decaying pressure waves
% 2. ensure the correct pressure waves propagating direction for
%    negative frequency cases which occur in multistage interaction analysis
% 3. add elastic axis for torsion mode
```

```
% 4. change the input-output LINSUB coefficient reference points in the
%    above mentioned way in order to reduce the magnitude of the LINSUB
%    coefficient for the decaying wave. This helps to prevent the ill
%    conditioning of the governing matrix in multistage interaction model
% 5. convergence check of the kernel functions for pressure wave
%    is increased to 10 times in order to correctly calculate the spinning
%    modes with negative frequency and high scattered index.
% 6. output shed vortex sheet is changed to output shed vorticity wave
% 7. input wake upwash velocity is changed to input shed vorticity wave
% 8. input pressure wave upwash velocity is changed to input pressure wave
%    pressure
% 9. additional capability to calculate the scattered pressure wave

% Author: Yujun Leng  Email:lengyujun@gmail.com   Last updated: Apr16, 2016
% This is free software under the terms of the GNU General Public License
% You are welcome to use it. I hope it will be helpful!

%% Function scattergrpC-----------------------------------------------------
function [grpC] = scattergrpC(n,lambda, M, theta, sc, rm,phi,xea)
ns=size(rm,2);
grpC=cell(ns,ns);

% ---build up the kernel matrix K
[K]=kernelKm10(n,lambda, M, theta, sc, 0,phi);

for j1=1:ns
   r1=rm(j1);
   % ---build up input upwash velocity matrix U
   [U]=upwashUm(n,lambda, M, theta, sc, r1,phi,xea);
   for j2=1:ns
      r2=rm(j2);
      % ---build up the output coefficient matrix X
      [X]=coeffXm(n,lambda, M, theta, sc, r2,phi,xea);
      % ---calculate bound vorticity B
      B=K\U;
      % ---calculating LINSUB coefficient CL
      CL=X*B;
      grpC{j1,j2}=CL;
   end
end
```

Function 2: upwashUm.m

```
% Function upwashUm calculates the upwash velocity matrix U in the
% modified matlab version LINUSB

% Author: Yujun Leng  Email:lengyujun@gmail.com  Last updated: Apr 16, 2016
% This is free software under the terms of the GNU General Public License
% You are welcome to use it. I hope it will be helpful!

%% Function upwashUm----------------------------------------------------
function [U]=upwashUm(n,lambda, M, theta, sc, r,phi, xea)
U=zeros(n,5);

% Calculate unsteady waves axial and tangential wave numbers
[alpha1, alpha2,alpha3, beta, vp1db, vp2db, up1, up2]...
   =pressurewavem(lambda, M, theta, sc, r, phi);

%  Calculates the upwash velocity matrix U,  Smith bewtween Eq.(50-51)
for m=0:(n-1)
   epsilon=pi*(2*m+1)/2/n;     % Smith bewtween Eq.(45-46)
   z=0.5*(1-cos(epsilon));     % Control point position, Smith Eq.(44)
   U((m+1),1)=1;               % bending
   %the elastic axis of torsion mode is at z=xea
   U((m+1),2)=1+1i*lambda*(z-xea);   %torsion
   %modified the shed vortex upwash velocity such that vorticity*c/W=1
   vorticitytow=(alpha3*cos(theta)+beta*sin(theta))/1i/(alpha3^2+beta^2);
   %vorticity input reference to leading edge
   U((m+1),3)=-exp(-1i*lambda*z)*vorticitytow;
   % upstream going pressure wave input reference to trailing edge
   % unit nondimensionalized pressure assumed, Smith Eq.(10), Eq.(38)
   U((m+1),4)=(cos(theta)*beta-sin(theta)*alpha1)...
      /(lambda+cos(theta)*alpha1+sin(theta)*beta)...
      *exp(1i*(alpha1*cos(theta)+beta*sin(theta))*(z-1));
   % downstream going pressure wave input reference to leading edge
   % unit nondimensionalized pressure assumed, Smith Eq.(10), Eq.(38)
   U((m+1),5)=(cos(theta)*beta-sin(theta)*alpha2)...
      /(lambda+cos(theta)*alpha2+sin(theta)*beta)...
      *exp(1i*(alpha2*cos(theta)+beta*sin(theta))*z);
end
```

Function 3: coeffXm.m

```
% Function coeffXm calculates the output coefficient matrix X in the
% modified matlab version LINUSB

% Author: Yujun Leng  Email:lengyujun@gmail.com  Last updated: Apr 16, 2016
% This is free software under the terms of the GNU General Public License
% You are welcome to use it. I hope it will be helpful!

%% Function coeffXm----------------------------------------------------------
function [X]=coeffXm(n,lambda, M, theta, sc, r,phi,xea)
X=zeros(5,n);

% Calculate unsteady waves axial and tangential wave numbers
[alpha1, alpha2,alpha3, beta, vp1db, vp2db, up1, up2]...
   =pressurewavem(lambda, M, theta, sc, r, phi);

% Calculates the output coefficient matrix X, Smith between Eq.(62-43)
for l=0:(n-1)
   psi=pi*l/n;     % Smith between Eq.(45-46)
   z0=0.5*(1-cos(psi));    % Bound vortex position, Smith Eq.(44)
   X(1,(l+1))=-1;              %lift
   %the elastic axis of torsion mode is at z=xea
   X(2,(l+1))=-(z0-xea);       %moment
   % modify the shed vortex output to be vorticity*c/W
   % vorticity wave reference to trailing edge
   X(3,(l+1))=-1i*lambda*exp(1i*lambda*(z0-1))/cos(theta)/sc;

   % input pressure wave upwash velocity is changed to input pressure wave
   % pressure, Smith Eq.(53)
   % output upstream going pressure wave reference to leading edge
   X(4,(l+1))=-1/sc*vp1db*(lambda+alpha1*cos(theta)+beta*sin(theta))...
    *exp(-1i*(alpha1*cos(theta)+beta*sin(theta))*z0);
   % output downstream going pressure wave reference to trailing edge
   X(5,(l+1))=-1/sc*vp2db*(lambda+alpha2*cos(theta)+beta*sin(theta))...
    *exp(-1i*(alpha2*cos(theta)+beta*sin(theta))*(z0-1));
end
```

Function 4: kernelKm10.m

```
% Function kernelKm10 calculates the kernel matrix K ( based on 10 times
% convergence tests) in the  modified matlab version LINUSB

% Kernel function is given in Smith Eq.(30) and Eq.(31),
% after discretization it becomes Smith Eq.(45).
% Each kernel function (induced upwash velocity at z by bound vorticity
% at z0) contains infinite number of the cascade waves(vorticity wave and
% pressure wave) with different tangential wavenumbers, ie. r=-inf to +inf
% The summation for vorticity wave is done analytically by Smith Eq.(43).
% The summation for pressure wave is done one by one (r=0, plus r=1,
% plus r=-1,plus r=2, plus r=-2 ...) until 10 additional terms doesn't
% change the kernel function value.
% The log singularity of the kernel function when z is very close to z0 is
% handled by a correction given in Smith Eq.(46), Eq.(47) and Eq.(48).
% The log correction only needs to be done once since the correction
% doesn't depend on cascade wave index r.
% Correction for log singularity and the summation for the vorticity wave
% are added after the pressure waves are converged
% K(i,j) is K(z_i,z0_j) which is the induced upwash velocity at z_i by the
% bound vorticity at z0_j.

% Author: Yujun Leng  Email:lengyujun@gmail.com  Last updated: Apr 16, 2016
% This is free software under the terms of the GNU General Public License
% You are welcome to use it. I hope it will be helpful!

%% Function kernelKm10-------------------------------------------------
function [K]=kernelKm10(n,lambda, M, theta, sc, r,phi)
K=zeros(n,n);              % initialize the kernel matrix
icheck=zeros(n,n);          % icheck=10 means it has converged
icount=0;                  % icount=n*n means all points has converged
term=0;                    % the new cascade wave
r=0;                     % cascade wave index

% Calculate unsteady waves axial and tangential wave numbers
[alpha1, alpha2,alpha3, beta, vp1db, vp2db, up1, up2]...
   =pressurewavem(lambda, M, theta, sc, r, phi);

% Calculate pressure cascade wave summation
while icount<n*n  %all n*n Kernel function entries are converged
for m=0:(n-1)
   epsilon=pi*(2*m+1)/2/n;
   z=0.5*(1-cos(epsilon));     % control point position, Smith Eq.(44)
   for l=0:(n-1)
```

```
psi=pi*l/n;
z0=0.5*(1-cos(psi));    % bound vortex position, Smith Eq.(44)

%pass the point if it is converged already
if abs(icheck((m+1),(l+1))-10)<1e-6
   continue %if icheck=10, the Kernel function entry is converged
end

eta=z-z0;
%induced upwash velocity by pressure waves, Smith Eq.(29)
if eta>0              %downstream going pressure wave
   term=(vp2db*beta*cos(theta)-up2*sin(theta))...  %
    *exp(1i*(alpha2*cos(theta)+beta*sin(theta))*eta)/sc;
   K((m+1),(l+1))=K((m+1),(l+1))+term;
elseif eta<0          %upstream going pressure wave
   term=(vp1db*beta*cos(theta)-up1*sin(theta))...
    *exp(1i*(alpha1*cos(theta)+beta*sin(theta))*eta)/sc;
   K((m+1),(l+1))=K((m+1),(l+1))+term;
end

%check convergence of cascade waves
if (abs(term)/abs(K((m+1),(l+1))))<1e-10
   if abs(icheck((m+1),(l+1))-9)<1e-6
      icheck((m+1),(l+1))=10;
      icount=icount+1;

      %correct for log singularity
      sum=0;
      for jr=1:n
         sum=sum+cos(jr*epsilon)*cos(jr*psi)/jr;
      end
      b2=1-M^2;
      d0=1i;  %Smith Eq.(IV.6)
      d1=(1-M^2/2/b2)*lambda;                %Smith Eq.(IV.6)
      d2=-1i*(1-1/2/b2+M^2/4/b2^2)*lambda^2;    %Smith Eq.(IV.6)
      d3=-0.5*(1-1/b2+M^2/6/b2^2+1/3/b2^2 ...
       -3/8*M^4/b2^3+M^6/6/b2^3)*lambda^3;      %Smith Eq.(IV.6)
      %Smith Eq.(IV.6) for f
      f=-lambda/2/pi/sqrt(b2)*(d0+d1*eta+d2*eta^2+d3*eta^3);
      K((m+1),(l+1))=K((m+1),(l+1))...
         -f*(2*log(2)+2*sum+log(abs(eta))); %Smith Eq.(48),(47)

      %add vorticity wave
      if eta>0
         vort=sinh(lambda*sc*cos(theta))/...
```

```
                (cosh(lambda*sc*cos(theta))...
                -cos(phi+lambda*sc*sin(theta)));
               K((m+1),(l+1))=K((m+1),(l+1))...
                +0.5*lambda*vort*exp(-1i*lambda*eta);  %Smith Eq.(43)
            end
         else
            icheck((m+1),(l+1))=icheck((m+1),(l+1))+1;
            continue
         end
      end
   end
end

if r>0
   r=-r;
else
   r=-r+1;
end
[alpha1, alpha2,alpha3, beta, vp1db, vp2db, up1, up2]...
   =pressurewavem(lambda, M, theta, sc, r, phi);
end
```

Function 5: pressurewavem.m

```
% Function pressurewavem calculates pressure wave and vorticity wave
% properties in the modified matlab version LINUSB

% Author: Yujun Leng  Email:lengyujun@gmail.com  Last updated: Apr 16, 2016
% This is free software under the terms of the GNU General Public License
% You are welcome to use it. I hope it will be helpful!

%% Function pressurewavem-------------------------------------------------
function [alpha1, alpha2,alpha3, beta, vp1db, vp2db, up1, up2]=...
   pressurewavem(lambda, M, theta, sc, r,phi)

beta=(phi-2*pi*r)/sc;  % tangential wave number, Simith Eq.(18)
A=lambda^2+beta^2+2*lambda*sin(theta)*beta;    %Smith bewtween Eq.(24-25)
radical=-beta^2+M^2*A;

% Calculating axial wave number, Smith Eq.(11)
if radical>0              %propagating case
   alpha1=(M^2*(lambda+beta*sin(theta))*cos(theta)+sqrt(radical))...
      /(1-(M*cos(theta))^2);
   alpha2=(M^2*(lambda+beta*sin(theta))*cos(theta)-sqrt(radical))...
```

```
        /(1-(M*cos(theta))^2);
    % ensure that upstream going pressure wave has larger axial wave number
    if abs(alpha1)<abs(alpha2)
        aaaa=alpha1;alpha1=alpha2;alpha2=aaaa;
    end

elseif radical<0          %decaying case
    alpha1=(M^2*(lambda+beta*sin(theta))*cos(theta)-sqrt(radical))...
        /(1-(M*cos(theta))^2);
    alpha2=(M^2*(lambda+beta*sin(theta))*cos(theta)+sqrt(radical))...
        /(1-(M*cos(theta))^2);
else
    warning('resonance happens!');
end
alpha3=-lambda/cos(theta)-tan(theta)*beta;

% Calculate the corresponding v', u' of a cascade wave, Smith Eq.(23),(28)
% vp1db,vp2db : v'/beta in order to remove the singularities when beta=0
vp1db=1/2/A*(beta*lambda*cos(theta)/sqrt(-radical)*1i-...
    (beta+lambda*sin(theta)));
vp2db=1/2/A*(beta*lambda*cos(theta)/sqrt(-radical)*1i+...
    (beta+lambda*sin(theta)));
up1=alpha1*vp1db;   % Smith Eq.(10)
up2=alpha2*vp2db;   % Smith Eq.(10)
```

Appendix C Generalized Flat Plate Cascade Code

This is a generalized flat plate cascade model code calculating the unsteady loading and unsteady waves for a blade row with general uniform/non-uniform spacing. This code includes main program, Aeromistuning_LINSUB.m and 4 functions: upwashUm.m, coeffXm.m, kernelKm10.m and pressurewavem.m. The four functions are the same as the ones used in multistage interaction code in Appendix B.

Main Program: Aeromistuning_LINSUB.m

```
%%%%%%%%%%%%%%%%%%%%%%%%%%%%%%%%%%%%%%%%%%%
%%%%%%%%%%%%%%%%%%%%%%%%%%%
%      Generalized LINSUB with non uniformly spaced blade row        %
%%%%%%%%%%%%%%%%%%%%%%%%%%%%%%%%%%%%%%%%%%%
%%%%%%%%%%%%%%%%%%%%%%%%%%%

% This is a generalized flat plate cascade model code calculating
% the unsteady loading and unsteady waves for a blade row with general
% non-uniform spacing.

% This code includes main program Aeromistuning_LINSUB.m and 4 functions:
% upwashUm.m----calculate input upwash velocity matrix
% coeffXm.m-----calculate output coefficient matrix
% kernelKm10.m--calculate kernel matrix based on 10 times convergence tests
% presssurewavem.m-----calculate pressure wave & vorticity wave properties

% This code is an extension of the LINSUB code for blade row with
% non-uniform spacing. The original LINSUB model and code is based on
% Whitehead, D. S. "Classical two-dimensional methods."
% In AGARD Aeroelasticity in Axial-Flow Turbomachines. 1 (1987).
% Smith, S. N. "Discrete frequency sound generation in axial flow
% turbomachines."  Reports and Memoranda 3709 (1972)

% LINSUB coefficient matrix CL(i,j), is defined as
% i: normalized output:
% 1.lift 2.moment 3. shed vorticity wave
% 4.upstream going Pressure wave 5. downstream going pressure wave
% j: normalized input:
% 1.bending 2.torsion 3.shed vorticity wave
% 4.upstream going Pressure wave 5. downstream going pressure wave
```

```
% The LINSUB coefficients reference points are defined as following
% input upwash velocity: Pup-TE, Pdn-LE, Vo-LE
% output response waves: Pup-LE, Pdn-TE, Vo-TE
% (LE: leading edge, TE: trailing edge)

% The original LINUSB code has been modified, improved and rewritten in
% Matlab. It has the following changes in order to correct some minor error
% in the original LINSUB code and in order to be used in the multistage
% interaction model.
% 1. correctly handle the decaying pressure waves
% 2. ensure the correct pressure waves propagating direction for
%    negative frequency cases which occur in multistage interaction analysis
% 3. add elastic axis for torsion mode
% 4. change the input-output LINSUB coefficient's reference point to in the
%    above mentioned way
% 5. convergence check of the kernel functions for pressure wave
%    is increased to 10 times in order to correctly calculate the spinning
%    modes with negative frequency and high scattered index.
% 6. output shed vortex sheet is changed to output shed vorticity wave
% 7. input wake upwash velocity is changed to input shed vorticity wave
% 8. input pressure wave upwash velocity is changed to input pressure wave
%    pressure
% 9. additional capability to calculate the scattered pressure wave

% In comments, Eq.(xx) refers to the equation the Author's PhD thesis
% Smith Eq.(xx) refers to the equation in Smith,S. N.'s paper
% Additional theory, model details and case studies are given in the
% Author's PhD thesis, Yujun Leng, 2016 "Preliminary design tools in
% turbomachinery: non-uniformly spaced blade rows, multistage interaction,
% unsteady radial waves, and propeller horizontal-axis turbine
% optimization", Mechanical Engineering, Purdue University, West Lafayette

% Author: Yujun Leng  Email:lengyujun@gmail.com  Last updated:Apr 16, 2016
% This is free software under the terms of the GNU General Public License
% You are welcome to use it. I hope it will be helpful!

%% INPUT----------------------------------------------------------------

% Input for case studies based on Purdue transonic compressor rotor
NB=108;          %number of total blades (real + imaginary)
% Sinusoidal Spacing
ss=round(6+4*sin((0:17)/18*4*pi));   % blade-to-blade spacing with 2 cycles
pbr=zeros(18,1);    % real blade potions
pbr(1)=1;          % The first blade is always a real blade
for i=1:17
```

```
   pbr(i+1)=1+sum(ss(1:i));
end
pbi=(1:108)';
pbi(pbr)=[];       % imaginary blade positions


np=20;          % Number of control points
phi=2*pi/NB;    % The fundamental interblade phase angle in radian
             % NB possible interblade phase angle are phi*[0:(NB-1)]
lambda=6.5153;  % Reduced frequency
sc=0.16872;     % Space to chord ratio based on total blades
theta=71/180*pi;     % Stag angle in radian
ND=20;               % Nodal diameter of the excitation
phi_in=ND*2*pi/NB;     % Inter blade phase angle of the excitation
M=0.822;         % Chordwise Mach number
xea=0;           % Elastic axis position for torsional vibration

%% Build up the governing matrix----------------------------------------
% The whole governing matrix is shown in Eq.(2.91)

% ---Build up the Left hand side of the governing matrix for real blades
% Eq. (2.87)

% First rows containing the kernel of all possible interblade phase angle
% Kernel matrix for each mode is of size [np*np]
% NB blades gives NB fundamental modes
nbr=size(pbr, 1);      % number of real blades
nbi=size(pbi, 1);      % number of imaginary blades
Kall=zeros(np*NB,np*NB);
Kbase=zeros(np, np*NB);
for i=1:NB     % go through all NB fundamental modes
   pcol=(i-1)*np+1;
   [K]=kernelKm10(np,lambda, M, theta, sc, 0,phi*(i-1));
   Kbase(1:np,pcol:(pcol+np-1))=K;
end
Kall(1:np,1:(np*NB))=Kbase;

for i=2:nbr
   % The induced velocity on the blades other than the first blade has a
   % phase which is a multiple of the interblade phase angle of each
   % fundamental mode
   phishift=zeros(np, np*NB);
   for j=1:NB
      pcol=(j-1)*np+1;
      phishift(1:np, pcol:(pcol+np-1))...
```

```
        =ones(np,np)*exp(1i*(pbr(i)-1)*(j-1)*phi);
    end
    prow=(pbr(i)-1)*np+1;
    Kall(prow:(prow+np-1),1:np*NB)=Kbase.*phishift;
end


% ---Build up the Left hand side of the governing matrix for imaginary
% blades, Eq. (2.89)

for i=1:nbi
    j=pbi(i);
    wj=exp(2*pi*1i*(j-1)/NB);
    prow=(j-1)*np+1;
    for k=1:NB
        pcol=(k-1)*np+1;
        Kall(prow:(prow+np-1),pcol:(pcol+np-1))=wj^(k-1)*eye(np);
    end
end


% ---Build up the Right hand side of the governing matrix, Eq.(2.87),(2.89)

[U]=upwashUm(np,lambda, M, theta, sc, 0,phi_in,xea);
% U(i,j), i:control points along the cord
% j:excitation type, 1.bending 2. torsion 3.vorticity 4. pup 5. pdown
Ubase=U;
Uall=zeros(np*NB,5);
for i=1:nbr
    phishift=exp(1i*(pbr(i)-1)*phi_in)*ones(np,5);
    prow=(pbr(i)-1)*np+1;
    Uall(prow:(prow+np-1),1:5)=Ubase.*phishift;
end

%% Solve the governing matrix and post-processing-------------------------

% ---Solve for strength of each mode (or interpreted as bound vorticity of
% each mode on the first blade)
B=Kall\Uall;
% B(1:np,j): mode1 at n control points
% B(n+1:2n,j): mode2 at n control points
% B(n*(NB-1)+1:NB,j): modeNB at n control points
% j is the excitation type, 1.bending 2. torsion 3.vorticity 4. pup 5. pdown

% Change matrix B to 3D matrix B3 with B3(:,:,k), k is the mode index
```

```
B3=zeros(np,5,NB);
for i=1:NB      %go through NB modes
   B3(:,:,i)=B(((i-1)*np+1):(i*np),:);
end

% B3 are mode strengths on the first blade, mode strengths on the other
% blades are calculated by phase shift for each mode depending on its mode
% interblade phase angle
interblade_phaseshift=zeros(np,5,NB);
for i=0:(NB-1)      % go through NB modes
   interblade_phaseshift(:,:,i+1)=ones(np,5)*exp(1i*2*pi/NB*i);
end

B4=zeros(np,5,NB,NB);   % B4 [np, 5upwash, modes, NBblades]
for i=0:(NB-1)      % go through NB blades
  B4(:,:,:,i+1)=B3.*(interblade_phaseshift.^i);
end

% ---Post processing
% Calculate unsteady surface pressure difference dp/(ro*w^2) for each mode
% on each blade, dp and bound vorticity has a one to one relationship from
% control point 2 to point np
l=repmat((1:(np-1))',[1,5,NB,NB]);
dp=B4(2:np,:,:,:)./(pi/2/np*sin(pi*l/np));

% Calculate unsteady aerodynamic coefficients for each mode on each blade
CL=zeros(5,5,NB,NB); % LINSUB coefficient CL[5,5,NBmode, NBblades]
for i=1:NB      %go through NB modes
   %build up the output coefficient matrix X for each mode
   phi=2*pi/NB*(i-1);
   [X]=coeffXm(np,lambda, M, theta, sc, 0,phi,xea);
   for j=1:NB  %go through NB blades
      B2=B4(:,:,i,j);
      %calculating LINSUB coefficient CL
      CL(:,:,i,j)=X*B2;
   end
end

%% OUTPUT-----------------------------------------------------------------
% In a linearized analysis, each mode is independent from each other
% They can be treated individually and then summed together to get the total
% effect.

% Total unsteady surface pressure difference, dptotal, is the summation of
% the unsteady surface pressure difference of all modes
```

```
dptotal=sum(dp,3);
dptotal_vo=reshape(dptotal(:,3,1,:), 19,108);    % dptotal due to wake
dptotal_vo_rb=dptotal_vo(:,pbr);      % dptotal due to wake at real blades

CLtotal=sum(CL,3);
% Total unsteady lift due to wake on each blade, C_lift
C_lift=reshape(CLtotal(1,3,1,:),108,1);
% Total unsteady moment due to wake on each blade, C_moment
C_moment=reshape(CLtotal(2,3,1,:),108,1);

% Upstream going pressure wave due to wake for each mode, C_pup
C_pup=reshape(CL(4,3,:,1), 108,1);
% Downstream going pressure wave due to wake for each mode, C_pdn
C_pdn=reshape(CL(5,3,:,1), 108,1);
```

VITA

VITA

Yujun Leng was born in Yantai, China in 1983, and received his BS in Bioengineering from National University of Singapore in 2006. He began his graduate study in Biomedical Engineering at Purdue University in August 2007. With a strong passion in flight and aeronautics, he transferred to Aeronautical and Astronautical Engineering in August 2008 and received a Master degree in August 2009. He continued to pursue his PhD study with Prof. Sanford Fleeter in the area of unsteady aerodynamics in turbomachinery. He will receive his Ph.D from the School of Mechanical Engineering in May 2016.